University of California
Santa Barbara

Importance learning: new methods to efficiently model heterogeneous catalysts with quenched disorder

A dissertation submitted in partial satisfaction
of the requirements for the degree

Doctor of Philosophy
in
Chemical Engineering

by

Craig Austin Vandervelden

Committee in charge:

Professor Baron G. Peters, Chair
Professor Susannah L. Scott
Professor Phillip Christopher
Professor Linda Petzold

September 2021

The Dissertation of Craig Austin Vandervelden is approved.

Professor Susannah L. Scott

Professor Phillip Christopher

Professor Linda Petzold

Professor Baron G. Peters, Committee Chair

June 2021

Importance learning: new methods to efficiently model heterogeneous catalysts with quenched disorder

by

Craig Austin Vandervelden

Acknowledgements

First, I want to thank my advisor, Baron Peters, for all of his support. Baron's magnetic passion towards science and research was a major driving force for attending UCSB. Working with Baron over the past five years, I have learned more than I could have imagined. Baron taught me all the theoretical and computational tools for catalysis, the importance and how to effectively communicate my ideas, and to always bring a jacket when going over a mountain pass. But most importantly, Baron taught me how to think about research problems and dissect them to answer the most important questions. Most of these skills were not only essential to learn as a graduate student, but will be invaluable in my future endeavors.

I could not have asked for a better group of colleagues and friends to work with, either. Geoff Poon, Xijun Wang, Kartik Kamat, and Christian Leitold all helped me get started in the group, from running electronic structure calculations to exiting vim on our cluster. Salman Khan has also been a fantastic partner to work with on our catalysis projects. In addition, I am grateful to have worked with and become friends with everyone else in our group: Ryan Yappert, Armin Shayesteh Zadeh, Ziqiu Chen, Howard Weatherspoon, and Hossam Farag. I am also grateful to the members of the Shell group, with whom we shared an office with at UCSB. The whiteboard discussions with Jacob Monroe, Tanmoy Sanyal, Dave Smith, and Nick Sherck. I am also thankful for the stimulating and fruitful collaborations with Susannah Scott, Marco Caricato, Brian Laird, and Ward Thompson.

I have been fortunate to have made such amazing friends during graduate school, especially Nick Scherk, Tsatsa Battsengel, Susen Green, Nicole Gunther, Takumi Kobiyashi, Tiffany Lee, and my roommates Cam Sheth, Brett Aho, Varun Hegde, and Boris Sadykoff. From runs along the beach, tabletop game sessions, catching lightning in a bottle, sharing obscure albums, or clearing the latest raid tier, I am grateful to them for

all the wonderful memories we made and I look forward to the adventures we will have in the future.

Finally, none of this would have been possible without my parents, Trish and Paul Vandervelden. They taught me the importance of kindness, perseverance, and not procrastinating. They nurtured my curiosity at every step and have been my biggest allies at every step of my life. From driving me to summer nature camps when I was young to driving across the country with me when I moved to Santa Barbara, they gave me the freedom and support to pursue my passions. They have always been there to celebrate the good times or help me when I was feeling down. I cannot thank them enough for everything they have done or express how much they mean to me.

Curriculum Vitæ

Craig Austin Vandervelden

Education

2021	Ph.D. in Chemical Engineering (Expected), University of California, Santa Barbara.
2016	B.S. in Chemical Engineering, University of Kansas.

Publications

1. Feroz, H. *et al.* Concentrating membrane proteins using ultrafiltration without concentrating detergents. *Biotechnol. Bioeng.* **113,** 2122–2130. https://doi.org/10.1002/bit.25973 (2016).
2. Kampen, E. V. *et al.* Design of Hollow Hyaluronic Acid Cylinders for Sustained Intravitreal Protein Delivery. *J. Pharm. Sci* **107,** 2354–2365. https://doi.org/10.1016/j.xphs.2018.04.024 (2018).
3. Fong, A., Vandervelden, C., Scott, S. L. & Peters, B. Computational Support for Phillips Catalyst Initiation via Cr–C Bond Homolysis in a Chromacyclopentane Site. *ACS Catal.* **8,** 1728–1733. https://doi.org/10.1021/acscatal.7b03724 (2018).
4. Khan, S. A., Vandervelden, C. A., Scott, S. L. & Peters, B. Grafting metal complexes onto amorphous supports: From elementary steps to catalyst site populations: Via kernel regression. *React. Chem. Eng.* **5,** 66–76. https://doi.org/10.1039/c9re00357f (2020).
5. Vandervelden, C. A., Khan, S. A., Scott, S. L. & Peters, B. Site-averaged kinetics for catalysts on amorphous supports: An importance learning algorithm. *React. Chem. Eng.* **5,** 77–86. https://doi.org/10.1039/c9re00356h (2020).
6. Vandervelden, C. A., Khan, S. A. & Peters, B. Importance learning estimator for the site-averaged turnover frequency of a disordered solid catalyst. *J. Chem. Phys.* **153,** 244120. https://doi.org/10.1063/5.0037450 (2020).
7. Vandervelden, C., Jystad, A., Caricato, M. & Peters, B. Predicted Properties of Active Catalyst Sites on Amorphous Silica: Impact of Silica Pre-Optimization Protocol. *Submitted* (2021).
8. Zhang, F., Vandervelden, C., Peters, B. & Scott, S. L. Elucidating the activation mechanism for ReO_x/Al_2O_3 in olefin metathesis: Pseudo-Wittig or allylic C-H activation path? *In preparation* (2021).

Conferences

- UCSB Chemical Engineering 50th Anniversary Poster Session, April 2017 (Poster)
- UCSB Graduate Student Symposium, October 2018 (Poster)
- Chicago Catalysis Club Spring Symposium, British Petroleum, Naperville, IL, April 2019 (Talk)
- Midwest Thermodynamics and Statistical Mechanics Conference, UIUC, June 2019 (Poster)
- University of Kansas Seminar, Lawrence, Kansas, October 2019 (Talk)
- UIUC Graduate Research Symposium, Urbana-Champaign, IL October 2019 (Talk)
- AIChE Annual Meeting, Orlando, FL November 2019 (Talk)
- AIChE Midwest Regional Conference, Chicago, IL, March 2020 (Talk)

Abstract

Importance learning: new methods to efficiently model heterogeneous catalysts with quenched disorder

by

Craig Austin Vandervelden

Over the past few decades there have been tremendous advances in the accuracy of electronic structure calculations, rigorous methods to assess proposed reaction mechanisms, and techniques to create representative models of active sites for homogeneous and ordered heterogeneous catalysts. Advances on all these fronts have greatly improved our understanding of numerous catalysts. However, most of these methods assume that the active sites are both well-defined and uniform (or are in an ensemble of uniform sites). Catalysts with quenched disorder have non-uniform active sites. Most established modeling techniques are inapplicable and many important catalysts in this category remain poorly understood. The major challenges of modeling catalysts with quenched disorder are (i) the nature of the disorder is out-of-equilibrium and unknown; (ii) each active site has a different local environment and activity; (iii) active sites are rare, often less than $\sim$20% of potential sites, depending on the catalyst and preparation method.

In this thesis, we develop new methods to efficiently predict kinetic properties of the distribution of quenched-disordered sites and how they affect different steps of catalyst operation. We combine population balance modeling techniques with machine learning methods to learn how the population of grafted sites evolves in time. We develop a new algorithm to efficiently converge site-averaged kinetics for a given distribution of grafted sites, the Importance Learning algorithm. A combination of *Importance* sampling and machine *Learning* are used to efficiently and accurately learn activation parameters of

rare sites that dominate site-averaged kinetics. Finally, we develop a protocol to create cluster models of active sites that most accurately preserve quenched degrees of freedom.

Contents

Chapter 1

Introduction

1.1 Overview

Catalysts play a crucial role in chemical technologies. Approximately 90% of chemical processes utilize catalysts to annually produce 2–4 trillion USD of chemicals.[1] Viable industrial catalysts require sufficient activity, selectivity, stability (mechanical and thermal), and most importantly commercial feasibility.[2] There has also been an emphasis to decrease reliance on precious metals and use more environmentally benign processes, *e.g.* less byproducts, milder operating conditions, or non-toxic catalytic materials.[3] Efforts to engineer better catalysts often involve a trial-and-error approach, and usually require numerous (sometimes hundreds of thousands!) experiments.[4] Over the past couple decades there has been a surge in "rational catalyst design", which aims to engineer better catalysts through understanding the governing physical phenomena. Examples include increasing the activity and/or selectivity of nanoparticles by changing the composition[5] or morphology,[6] designing sinter-resistant heterogeneous catalysts by chemically or physically modifying the catalyst surface,[7] and increasing the efficiency or selectivity of enzymes by modifying their protein sequences.[8] Computations have played an increas-

ing role in better understanding the underlying phenomena of catalysts. The increasing presence of computational catalysis can be attributed to three factors: (i) computing power has drastically increased, in correspondence with Moore's Law,[9] (ii) the computational methods used to predict catalyst properties have greatly increased in accuracy, and (iii) methods to create representative models of catalysts and compute their kinetics have been developed for many categories of catalysts.

1.2 Computational catalysis

The most common applications of modeling catalysts include testing hypothesized mechanisms[10], high-throughput screening,[11] and engineering catalysts with known mechanisms to be more active, selective, and/or stable.[12,13] Modeling a catalytic cycle requires a model of the active site, a means to compute the relative energies of reactants, products, intermediates and transition states, and a means convert and compare the computed energies of the catalytic cycle to experimentally observable quantities.

Active site models can vary in their complexity, which usually balances computational cost with model accuracy. For example, many industrial processes use heterogeneous catalysts consisting of a nanoparticles supported on a high-surface area support like alumina.[14] The earliest and simplest catalyst models consists of a single crystal face, which represented a face of the nanoparticle. More complex catalyst models including steps and/or defects in crystal faces. Current catalyst models can include entire nanoparticles and a portion of the support.[15] Many other classes of catalysts like zeolites, organometallic complexes, and metal oxides all have established methods for creating representative active site models.[16–18]

Electronic structure methods are almost exclusively used to compute energies of a catalytic cycle because bond-formation and bond-breaking steps of a catalytic cycle are

inherently quantum-chemical. Density functional theory (DFT) is by far the most common method for computing relative energies because it has a desirable balance of computational cost and accuracy.[19,20] Wavefunction-based methods like coupled cluster theory have excellent accuracy, but are much less common due to their high computational cost.[21] Electronic structure calculations are used in conjunction with optimization algorithms to optimize the energy of a species to a stationary point (*i.e.*, a minimum and saddle point) by changing the atomic structure. Performing structure optimizations is well-studied and robust algorithms are available in many quantum chemistry software packages.[22–24]

Once the relative energies of reactants, intermediates, transition states, and products are computed, they must be converted into quantities that can be compared with experimental observables. One of the most common methods is to compute a rate law by constructing a microkinetic model from the elementary steps of the mechanism.[10,25] Rate constants are usually computed using harmonic transition state theory,[26] which parameterized by the relative free energies. If a microkinetic model is derived from the correct mechanism, the predicted rates, intermediate abundancies, and selectivities will be consistent with experimental data over a range of species concentrations and temperatures. The results of electronic structure calculations can also be used to compute IR,[27] NMR,[28–30] or Raman[31] spectra of abundant intermediates, which can be compared to experimentally measured spectra.

In addition to methods to assess mechanisms, there are frameworks to help engineer and discover more effective catalysts. For example, Campbell's degree of rate control formalism identifies the rate determining step of complex, multistep mechanisms.[32] Understanding which step is rate determining is crucial before attempting to design a better catalyst. Nørskov and coworkers also developed a framework for catalyst screening/discovery.[33] The adsorption energy of adatoms (*e.g.*, C) is linearly related to the

adsorption energy of molecules containing said adatom (*e.g.*, CH_x, x = 1, 2, 3). Correlated adsorption and dissociation energies can be used with reaction stoichiometries to compute heats of formation. Free energy relations from Bell, Evans, and Polanyi (BEP relations)[34] linearly relate quantities like dissociation energies and heats of formation to activation barriers, the latter being far more difficult to compute. When paired with a microkinetic model, there is a direct route to compute the turnover frequency as a function of atomic adsorption energy. While these energy relations are only qualitatively accurate, they can quickly screen the periodic table for candidate materials, dopants, or supports to investigate with more accurate methods.[35]

Developments in all these areas have greatly advanced our understanding of many types of catalysts through computation. Although many computational catalysis is still an active field of research, most types of catalysts at least have established protocols for modeling them.

1.3 Heterogeneous catalysts with quenched disorder

Most of the methodological developments discussed above leverage the fact that catalysts have uniform (or an ensemble of uniform) sites. One class of catalysts, heterogeneous catalysts with quenched disorder, has unique properties which violate the assumptions invoked in most modeling techniques. Currently, there are no rigorous methods to model this class of catalysts and they remain poorly understood.

Heterogeneous catalysts with quenched disorder, *i.e.*, non-equilibrium disorder that does not vary in time, present special challenges for experimental and computational studies. Examples of some heterogeneous catalysts with quenched disorder include metallic glasses,[36–38] high-entropy alloys,[39,40] mixed metal oxides,[41] and single metal atoms grafted to amorphous supports like silica or silica-alumina.[42–45] The latter, single metal atoms

catalysts, can be encountered in industrial processes and will be the focus of this thesis. Some well-studied single metal atoms grafted onto amorphous silica include chromocenes or chromates for olefin polymerization,[46–48] titanium and tantalum complexes for olefin epoxidation,[49] molybdates for methanol dehydration,[50] and vanadates for partial oxidation of methanol.[51] A typical active site consists of a metal center grafted to surface hydroxyls on the amorphous support. The resulting sites are non-uniform on two accounts. First, the amorphous support has both structural and topological disorder, so each site has a different local environment. Structural disorder is frequently characterized by bond-length and bond-angle distributions. An example of topological disorder is the distribution siloxane rings in amorphous silica.[52] Different support preparation methods (sol-gel,[53,54] pyrolysis,[55] or precipitation[56]) also leads to amorphous oxides with different disorder characteristics.[57] Second, different surface hydroxyl groups (isolated, geminal, vicinal, and proximal) can lead to qualitatively different sites.[57] For example, a metal center grafted to an isolated silanol will have a fundamentally different coordination environment than one grafted to a pair of vicinal silanols. The two sources of non-uniformity and a schematic of different surface OH types are shown in Figure 1.1

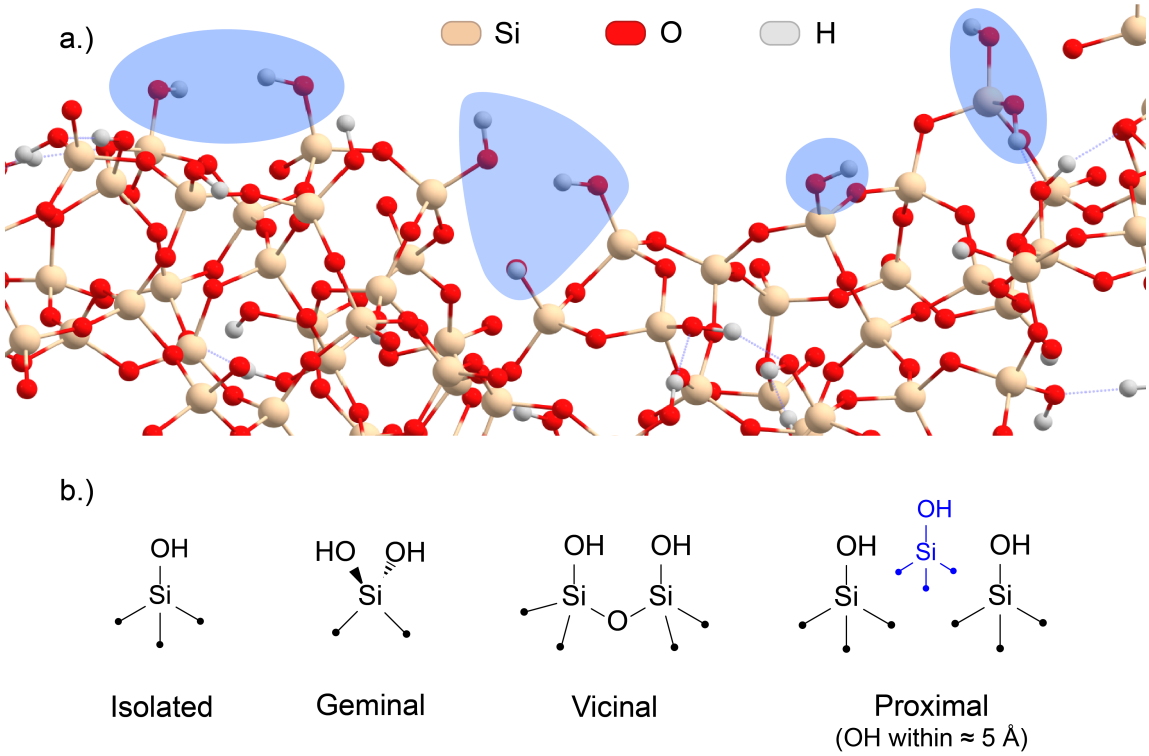

Figure 1.1: Sources of non-uniformity for sites on an amorphous support. Figure (1.1a) shows the structural and topological disorder for different OH groups (highlighted in blue) on an amorphous SiO_2 model. Figure (1.1b) shows the different type of surface OH groups that can populate a silica surface. Proximal groups refer to pairs of isolated surface OH groups which are close enough to graft a metal to. Note that proximal OH groups can occur as tuples, triplets, etc.

Both types of non-uniformity are important in catalysis. Specific metal precursors may only be able to graft to certain types of OH groups. Furthermore, sites where grafting is possible will not necessarily produce a catalytically active site. The structural and topological disorder of the support also gives rise to a distribution of non-uniform sites, where each site has exponentially different kinetic and thermodynamic properties.[58] Any observed kinetics are averages over the quenched distribution of sites, referred to as site-averaged kinetics. Furthermore, only a small fraction of sites are active, typically less than ca. 20%, depending on the catalyst and preparation method.[48,59–61] This makes studying disordered heterogeneous catalysts tremendously challenging, both experimentally

and computationally. Characterization techniques that probe the structure, oxidation state, and coordination environment of catalytic sites likely scan inactive sites. Testing mechanisms and discovering features of active sites is difficult because these rare active sites present a "needle in a haystack"-type challenge. On the computational side, most challenges stem from creating a representative distribution of active models or efficiently averaging kinetics over the distribution of sites.

Models of active sites

Creating a distribution of active site models that accurately matches the real distribution of sites for amorphous oxides is difficult because because they are out of equilibrium, so sampling techniques like Monte Carlo cannot be used. For studies that investigate how site heterogeneity affects a sites activity, the ensemble of active site models usually consists of cluster models carved from periodic slab models of amorphous oxide surfaces.[62–68] The cluster models are much smaller than the entire slab, which makes them amenable to more accurate electronic structure calculations.

However, assessing how accurately cluster and slab models resemble real amorphous oxides like silica is an outstanding challenge because atomically resolved structural data is unavailable. Present amorphous oxide models are also created with approximate methods because mimicking experimental synthesis methods like sol-gel or pyrolysis is currently intractable.[53,55] This further makes it challenging to compare which computational protocol yields a more realistic model because all are based on *ad hoc* methods. Nevertheless, most modern slab models are able to reproduce many average quantities, *e.g.*, average Si−OH surface converge, the average Si−O bond distance, the average O−Si−O bond angle, etc.[68]

The procedures to create these cluster models of amorphous oxides[69,70] resemble those used to create cluster models of crystalline zeolites.[16,71] The cluster encompasses all atoms

within some cutoff away from a site of interest, all "peripheral" Si-O-Si linkages beyond the cutoff are cut, and dangling bonds are terminated with capping atoms like F, H, or OH groups. The peripheral atoms are often constrained in place during subsequent analyses of grafting and reactivity to mimic the structural constraints imposed by the silica matrix.[66,68,72–74] An example of carving a silica cluster model from a periodic slab is shown in Figure 1.2.

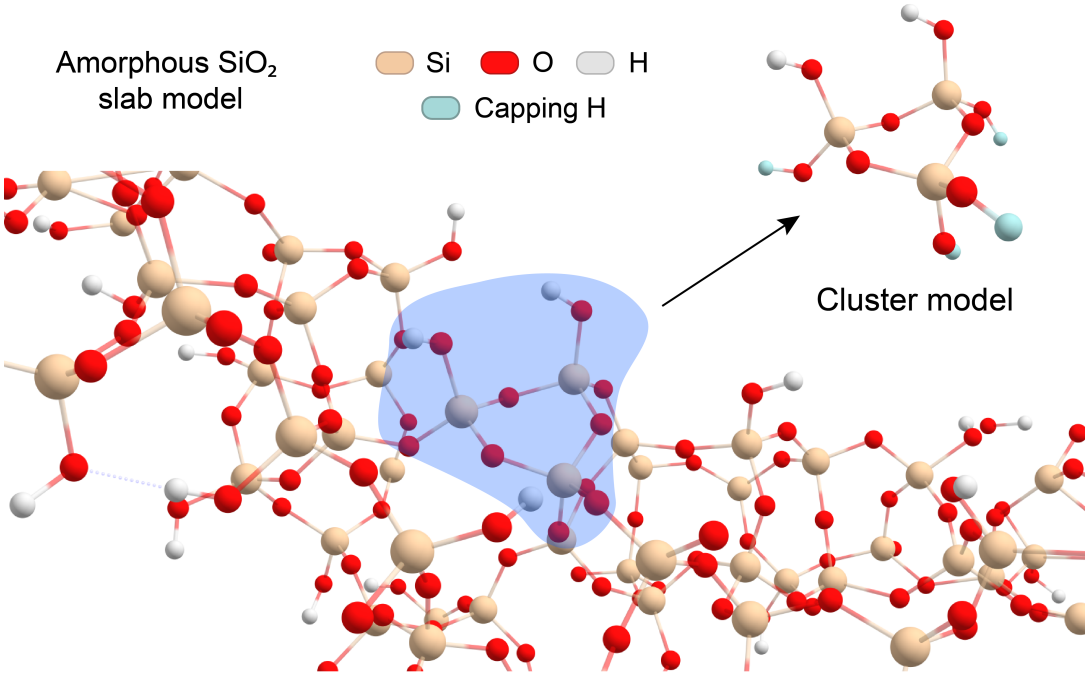

Figure 1.2: Example of carving a small cluster model (outlined in blue) from an periodic SiO_2 slab model. Dangling O bonds are capped with H atoms, which are aligned along the Si−O bond and rescaled to an equilibrium distance.

Cluster models are also a reasonable model choice because oxides are insulators, so long-range electronic interactions should have a negligible effect.[75,76] The size of the cluster can also be adjusted to provide an acceptable cost-accuracy balance. The cluster size should be large enough so that key interactions (including steric effects, electrostatic/dispersion attraction, and H-bonding) present catalytic sites are accurately captured.[77–79] However, the cluster model should also be small enough so accurate electronic

methods and basis sets remain computationally tractable. While calculations using periodic slab models as active sites are possible, they require a large simulation cell to accurately capture the quenched disorder.[68] This limits the number of sites that can be used in an ensemble and also the accuracy of the level of theory that can be employed (*e.g.*, using accurate hybrid or double-hybrid functionals is not feasible).

Site-averaged kinetics

In addition to difficulties in creating and assessing realistic active site models, averaging kinetics over the distribution of sites has its own statistical challenges. For single metal atom catalysts, the metal center first has to be grafted to the support by reacting an organometallic precursor with surface hydroxyls on the support.[44] Because every site is different, sites will graft at different rates. Different grafted populations can be obtained by changing the grafting reaction conditions or how long the grafting reaction is conducted. Once grafted, the site may also undergo an activation step before the catalytic cycle can proceed. Only once the distribution of activated sites is obtained can site-averaged kinetics be computed, which will likely depend on all prior steps. However, converging estimates of site-averaged kinetics involves computing exponential averages,[58] which are notoriously difficult to converge.[80–82] It was estimated that converging site-averaged kinetics within 10% of their actual values may require thousands of sites when standard sampling methods are used.[44] Because each sample is a handful of expensive electronic structure calculations, randomly sampling the quenched distribution of sites is an infeasible strategy.

For example, the Phillips catalyst (Cr/SiO_2 for olefin polymerization) is believed to activate by forming $(\equiv SiO)_2Cr(III)alkyl$ sites from Cr(II) sites exposed to ethylene.[48] From a given population of grafted sites, only a subset of these might activate or be catalytically active due to differences in a site's local environment. Only from the final

distribution of active sites can site-averaged kinetics be computed. A schematic illustrating grafting, activation, and polymerization steps steps in the Phillips catalyst, along with how the distribution of sites changes in each step, is shown in Figure 1.3.

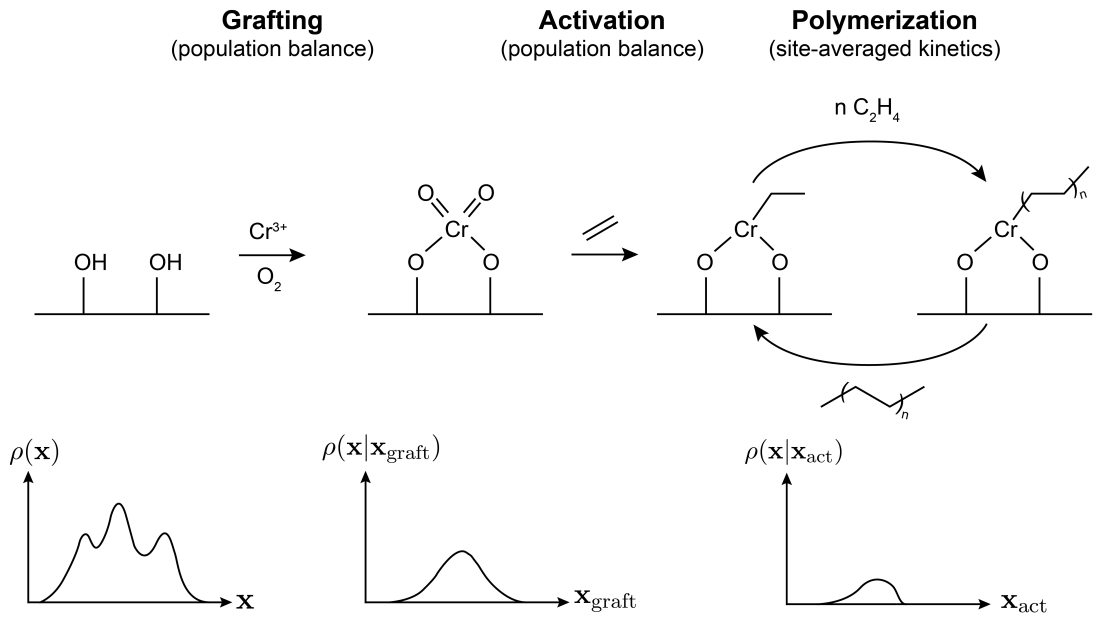

Figure 1.3: Schematic showing grafting, activation, and polymerization steps in the Phillips catalyst. The plots below graphically represents the population of sites, denoted at $\mathbf{x}$, as conditional probability distributions. A Cr precursor grafts to a subpopulation of all sites as dioxoCr(VI), $\rho(\mathbf{x}|\mathbf{x}_{\text{graft}})$. An even smaller subpopulation forms catalytically active sites, $\rho(\mathbf{x}|\mathbf{x}_{\text{act}})$. The catalytic cycle proceeds from the population of active sites.

Prior computational studies have used one[83,84] or a small number (< 10)[66,74,85–90] of active site models. Most studies also focused on qualitatively assessing the plausibility of mechanisms or illustrated how site diversity affects the kinetic and thermodynamic properties of a site. No studies have attempted to rigorously compute site-averaged kinetics. While these studies provide useful mechanistic insight, the conclusions drawn are limited because only a small number of sites are considered. One of the biggest challenges with this modeling approach is distinguishing unviable mechanisms from inactive site models. Because only a small fraction of sites are active, most randomly selected sites

might appear inactive, even according the correct mechanism. Another related challenge is computing the relative abundance of active sites. If a site model is catalytically active, is that site abundant enough to contribute to the observed kinetics? With increasingly realistic amorphous oxide models being developed, site-averaged kinetics can address these issues by accounting for the activity and relative abundance of the non-uniform sites. However, efficient methods to accurately estimate site-averaged kinetics are necessary.

1.4 Outline

The main goal of this dissertation is to develop new methods to model catalysts with quenched disorder. Chapter 2 assesses an activation mechanism involving pairs of active sites for the Phillips catalyst. This chapter can be thought of an application of current methods to model catalysts with quenched disorder in the sense that one local environment is considered with a minimal cluster model. We then develop a statistical model that accounts for the spatial distribution of sites to estimate the total fraction of sites that can activate.

Chapters 3 – 5 focuses on new methods to efficiently model catalysts with quenched disorder. We developed a structurally disordered, functionalized lattice model to mimic the surface of amorphous SiO_2: the quenched disorder lattice model. The quenched disorder lattice model serves as a platform for method development. The model contains sites for grafting and catalysis reactions, along with a simple model chemistry that allows for reaction energies to be computed as a function of the local environment. The simple model chemistry also allows for site-averaged kinetics to be exhaustively computed for all sites, enabling new methods to be benchmarked against standard sampling methods.

Chapter 3 develops tools to efficiently model the grafting step. A small set of expensive electronic structure calculations are used to construct a training set for a kernel regression

(KR) model. The trained KR model is used to predict the grafting barriers for the entire distribution of sites. The trained kernel regression model is paired with a population balance model to predict how population of grafted sites evolves in time. Chapter 4 presents an algorithm combining of *importance* sampling and KR-based machine *learning* methods to efficiently estimate the site-averaged kinetics of a catalytic cycle given a distribution of grafted sites, the Importance Learning algorithm. Chapter 5 presents an efficient estimator for the site-averaged turnover frequency (TOF) using the Importance Learning algorithm. The site-averaged TOF estimator requires no calculations in addition to the ones used in the Importance Learning algorithm. We also show how to account for errors in the trained KR model, which provides more accurate estimates of site-averaged kinetics.

Finally, Chapter 6 presents a protocol for carving cluster models from slab models that most accurately preserve the quenched disordered degrees of freedom. We demonstrate the protocol with the simple quenched disorder lattice model, which allows us to use large cluster models and collect many statistics. We also use large atomistic cluster models of SiO_2 with electronic structure calculations to model the grafting step in the Phillips catalyst as a realistic example.

Bibliography

1. Dumesic, J. A., Huber, G. W. & Boudart, M. *Principles of Heterogeneous Catalysis* ISBN: 9781847559906. http://doi.wiley.com/10.1002/9783527610044.hetcat0001 (2008).

2. Dingerdissen, U., Martin, A., Herein, D. & Wernicke, H. J. *The Development of Industrial Heterogeneous Catalysis* 37–56. https://onlinelibrary.wiley.com/doi/abs/10.1002/9783527610044.hetcat0003 (Wiley-VCH, 2008).

3. Nørskov, J. K., Bligaard, T., Rossmeisl, J. & Christensen, C. H. Towards the computational design of solid catalysts. *Nat. Chem.* **1,** 37–46. https://www.doi.org/10.1038/nchem.121 (2009).

4. Yaccato, K. *et al.* High Throughput Discovery of Families of High Activity WGS Catalysts: Part I - History and Methodology. *Comb. Chem. High Throughput Screening* **13,** 318–330. https://doi.org/10.2174/138620710791054286 (2010).

5. Nørskov, J. K. *et al.* The nature of the active site in heterogeneous metal catalysis. *Chem. Soc. Rev.* **37,** 2163–2171. https://www.doi.org/10.1039/b800260f (2008).

6. Jin, R., Li, G., Sharma, S., Li, Y. & Du, X. Toward Active-Site Tailoring in Heterogeneous Catalysis by Atomically Precise Metal Nanoclusters with Crystallographic

Structures. *Chem. Rev.* **121,** 567–648. https://www.doi.org/10.1021/acs.chemrev.0c00495 (2020).

7. Goodman, E. D., Schwalbe, J. A. & Cargnello, M. Mechanistic Understanding and the Rational Design of Sinter-Resistant Heterogeneous Catalysts. *ACS Catal.* **7,** 7156–7173. https://www.doi.org/10.1021/acscatal.7b01975 (2017).

8. Chen, K. & Arnold, F. H. Engineering new catalytic activities in enzymes. *Nat. Catal.* **3,** 203–213. https://www.doi.org/10.1038/s41929-019-0385-5 (2020).

9. Theis, T. N. & Wong, H. .-. P. The End of Moore's Law: A New Beginning for Information Technology. *Comput. Sci. Eng.* **19,** 41–50. https://doi.org/10.1109/MCSE.2017.29 (2017).

10. Motagamwala, A. H., Ball, M. R. & Dumesic, J. A. Microkinetic analysis and scaling relations for catalyst design. *Annu. Rev. Chem. Biomol. Eng.* **9,** 413–450. https://www.doi.org/10.1146/annurev-chembioeng-060817-084103 (2018).

11. Greeley, J., Jaramillo, T. F., Bonde, J., Chorkendorff, I. & Nørskov, J. K. Computational high-throughput screening of electrocatalytic materials for hydrogen evolution. *Nat. Mater.* **5,** 909–913 (2006).

12. *Computational Modeling for Homogeneous and Enzymatic Catalysis* (eds Morokuma, K. & Musaev, D. G.) 1–378. https://doi.org/10.1002/9783527621965.fmatter (John Wiley & Sons, Ltd, 2008).

13. *Computational Catalysis* (eds Asthagiri, A. & Janik, M. J.) P001–266. http://dx.doi.org/10.1039/9781849734905 (The Royal Society of Chemistry, 2014).

14. Bartholomew, C. H. & Farrauto, R. J. *Fundamentals of Industrial Catalytic Processes: Second Edition* 1–966. https://doi.org/10.1002/9780471730071 (2010).

15. Jørgensen, M. & Grönbeck, H. Perspectives on Computational Catalysis for Metal Nanoparticles. *ACS Catal.* **9,** 8872–8881. https://doi.org/10.1021/acscatal.9b02228 (2019).

16. Migues, A. N., Muskat, A., Auerbach, S. M., Sherman, W. & Vaitheeswaran, S. On the rational design of zeolite clusters. *ACS Catal.* **5,** 2859–2865. https://doi.org/10.1021/cs501827p (2015).

17. Harvey, J. N., Himo, F., Maseras, F. & Perrin, L. Scope and Challenge of Computational Methods for Studying Mechanism and Reactivity in Homogeneous Catalysis. *ACS Catal.* **9,** 6803–6813. https://doi.org/10.1021/acscatal.9b01537 (2019).

18. Chen, B. W., Xu, L. & Mavrikakis, M. Computational Methods in Heterogeneous Catalysis. *Chem. Rev.* **121,** 1007–1048. https://doi.org/10.1021/acs.chemrev.0c01060 (2021).

19. Iron, M. A. & Janes, T. Evaluating Transition Metal Barrier Heights with the Latest Density Functional Theory Exchange-Correlation Functionals: The MOBH35 Benchmark Database. *Journal of Physical Chemistry A.* https://doi.org/10.1021/acs.jpca.9b01546 (2019).

20. Chan, B., Gill, P. M. & Kimura, M. Assessment of DFT Methods for Transition Metals with the TMC151 Compilation of Data Sets and Comparison with Accuracies for Main-Group Chemistry. *J. Chem. Theory Comput.* **15,** 3610–3622. https://doi.org/10.1021/acs.jctc.9b00239 (2019).

21. Jensen, F. *Introduction to Computational Chemistry* 624 (2007).

22. Valiev, M. *et al.* NWChem: A comprehensive and scalable open-source solution for large scale molecular simulations. *Comput. Phys. Commun.* **181,** 1477–1489. https://doi.org/10.1016/j.cpc.2010.04.018 (2010).

23. Shao, Y. *et al.* Advances in molecular quantum chemistry contained in the Q-Chem 4 program package. *Mol. Phys.* **113,** 184–215. https://doi.org/10.1080/00268976.2014.952696 (2015).

24. Frisch, M. J. *et al.* Gaussian16. Gaussian Inc. Wallingford CT 2016.

25. Boudart, M. & Djega-Mariadassou, G. *Kinetics of Heterogeneous Catalytic Reactions* https://books.google.com/books?id=iqf_AwAAQBAJ (Princeton University Press, Princeton, 2014).

26. Peters, B. *Reaction Rate Theory and Rare Events* **20178817,** xiv, 619 pages (Elsevier, Amsterdam ; Cambrige, MA, 2017).

27. Wilson, E. B., Decius, J. C. & Cross, P. C. *Molecular Vibrations: The Theory of Infrared and Raman Vibrational Spectra* ISBN: 9780486639413. https://books.google.com/books?id=yKVPDwAAQBAJ (Dover Publications, 1980).

28. Yates, J. R., Pickard, C. J. & Mauri, F. Calculation of NMR chemical shifts for extended systems using ultrasoft pseudopotentials. *Phys. Rev. B: Condens. Matter Mater. Phys.* **76,** 024401. https://doi.org/10.1103/PhysRevB.76.024401 (2007).

29. Pickard, C. J. & Mauri, F. All-electron magnetic response with pseudopotentials: NMR chemical shifts. *Phys. Rev. B: Condens. Matter Mater. Phys.* **63,** 245101. https://doi.org/10.1103/physrevb.63.245101 (2001).

30. Bonhomme, C. *et al.* First-principles calculation of NMR parameters using the gauge including projector augmented wave method: A chemists point of view. *Chem. Rev.* **112,** 5733–5779. https://doi.org/10.1021/cr300108a (2012).

31. Fairchild, S. Z., Bradshaw, C. F., Su, W. & Guharay, S. K. Predicting Raman Spectra Using Density Functional Theory. *Appl. Spectrosc.* **63,** 733–741. http://as.osa.org/abstract.cfm?URI=as-63-7-733 (July 2009).

32. Campbell, C. T. The Degree of Rate Control: A Powerful Tool for Catalysis Research. *ACS Catal.* **7,** 2770–2779. https://doi.org/10.1021/acscatal.7b00115 (2017).

33. *Fundamental Concepts in Heterogeneous Catalysis* i–ix. ISBN: 9781118892114. https://onlinelibrary.wiley.com/doi/abs/10.1002/9781118892114.fmatter (John Wiley & Sons, Ltd, 2014).

34. Evans, M. G. & Polanyi, M. Inertia and driving force of chemical reactions. *Trans. Faraday Soc.* **34,** 11–24. https://doi.org/10.1039/TF9383400011 (1938).

35. Andersson, M. P. *et al.* Toward computational screening in heterogeneous catalysis: Pareto-optimal methanation catalysts. *J. Catal.* **239,** 501–506. https://doi.org/10.1016/J.JCAT.2006.02.016 (Apr. 2006).

36. Tanaka, S. *et al.* A nanostructured skeleton catalyst: Suzuki-coupling with a reusable and sustainable nanoporous metallic glass Pd-catalyst. *Chem. Commun.* **27,** 5985–5987. https://www.doi.org/10.1039/c1cc10710k (2011).

37. Hasannaeimi, V. & Mukherjee, S. Noble-Metal based Metallic Glasses as Highly Catalytic Materials for Hydrogen Oxidation Reaction in Fuel Cells. *Sci. Rep.* **9,** 12136. https://www.doi.org/10.1038/s41598-019-48582-7 (2019).

38. Jia, Z. *et al.* Attractive In Situ Self-Reconstructed Hierarchical Gradient Structure of Metallic Glass for High Efficiency and Remarkable Stability in Catalytic Performance. *Adv. Funct. Mater.* **29,** 1807857. https://www.doi.org/10.1002/adfm.201807857 (2019).

39. Nellaiappan, S. *et al.* High-Entropy Alloys as Catalysts for the CO2 and CO Reduction Reactions: Experimental Realization. *ACS Catal.* **10,** 3658–3663. https://www.doi.org/10.1021/acscatal.9b04302 (2020).

40. Pedersen, J. K., Batchelor, T. A. A., Bagger, A. & Rossmeisl, J. High-entropy alloys as catalysts for the CO2 and CO reduction reactions. *ACS Catal.* **10,** 2169–2176. https://www.doi.org/10.1021/acscatal.9b04343 (2020).

41. Bui, L. & Bhan, A. Mechanisms for C-C bond cleavage and formation during acrolein production on a mixed metal oxide catalyst. *Appl. Catal., A* **546,** 87–95. https://www.doi.org/10.1016/j.apcata.2017.08.011 (2017).

42. Thomas, J. M., Raja, R. & Lewis, D. W. Single-site heterogeneous catalysts. *Angew. Chem., Int. Ed.* **44,** 6456–6482. https://www.doi.org/10.1002/anie.200462473 (2005).

43. Coperet, C. *et al.* Surface Organometallic and Coordination Chemistry toward Single-Site Heterogeneous Catalysts: Strategies, Methods, Structures, and Activities. *Chem. Rev.* **116,** 323–421. https://www.doi.org/10.1021/acs.chemrev.5b00373 (2016).

44. Goldsmith, B. R., Peters, B., Johnson, J. K., Gates, B. C. & Scott, S. L. Beyond Ordered Materials: Understanding Catalytic Sites on Amorphous Solids. *ACS Catal.* **7,** 7543–7757. https://www.doi.org/10.1021/acscatal.7b01767 (2017).

45. Wang, A., Li, J. & Zhang, T. Heterogeneous single-atom catalysis. *Nat. Rev. Chem.* **2,** 65–81. https://doi.org/10.1038/s41570-018-0010-1 (2018).

46. Carrick Wayne, L. *et al.* Ethylene polymerization with supported bis(triphenylsilyl) chromate catalysts. *J. Polym. Sci., Part A-1: Polym. Chem.* **10,** 2609–2620. https://www.doi.org/10.1002/pol.1972.150100909 (1972).

47. Theopold, K. H. Organochromium(III) Chemistry: A Neglected Oxidation State. *Acc. Chem. Res.* **23,** 263–270. https://www.doi.org/10.1021/ar00176a005 (1990).

48. McDaniel, M. P. A Review of the Phillips Supported Chromium Catalyst and Its Commercial Use for Ethylene Polymerization. English. *Adv. Catal.* **53,** 123–606. https://www.doi.org/https://doi.org/10.1016/S0360-0564(10)53003-7 (2010).

49. Ruddy, D. A. & Tilley, T. D. Kinetics and mechanism of olefin epoxidation with aqueous H_2O_2 and a highly selective surface-modified TaSBA15 heterogeneous catalyst. *J. Am. Chem. Soc.* **130,** 11088–11096. https://www.doi.org/10.1021/ja8027313 (2008).

50. Shannon, I. J. *et al.* Metallocene-derived, isolated Mo(VI) active centres on mesoporous silica for the catalytic dehydrogenation of methanol. *J. Chem. Soc., Faraday Trans.* **94,** 1495–1499. https://www.doi.org/10.1039/a800054i (1998).

51. Vining, W. C., Strunk, J. & Bell, A. T. Investigation of the structure and activity of $VO_x/CeO_2/SiO_2$ catalysts for methanol oxidation to formaldehyde. English. *J. Catal.* **281,** 222–230. https://www.doi.org/10.1016/j.jcat.2011.09.024 (2012).

52. Lichtenstein, L. *et al.* The atomic structure of a metal-supported vitreous thin silica film. *Angew. Chem., Int. Ed.* **116,** 20429–20432. https://doi.org/10.1002/anie.201107097 (2012).

53. White, L. & Duffy, G. STAFF-INDUSTRY COLLABORATIVE REPORT Vapor-Phase Production of Colloidal Silica. *Ind. Eng. Chem.* **51,** 232–238. https://pubs.acs.org/doi/abs/10.1021/ie51394a019 (Mar. 1959).

54. Rahman, I. A. & Padavettan, V. Synthesis of Silica nanoparticles by Sol-Gel: Size-dependent properties, surface modification, and applications in silica-polymer nanocompositesa review. *J. Nanomater.* **2012,** 132424. https://doi.org/10.1155/2012/132424 (2012).

55. Barthel, H., Rösch, L. & Weis, J. *Fumed Silica - Production, Properties, and Applications* 761–778. https://doi.org/10.1002/9783527620777.ch91a (2005).

56. Garrett, P. R. *Defoaming: Theory and industrial applications* 329. https://doi.org/10.1201/9781315140827 (CRC Press, Boca Raton, 1992).

57. Vansant, E. E., Van Der Voort, P. & Vrancken, K. C. *Characterization and Chemical Modification of the Silica Surface* (1995).

58. Peters, B. & Scott, S. L. Single Atom Catalysts on Amorphous Supports: A Quenched Disorder Perspective. *J. Chem. Phys.* **142,** 104708. https://www.doi.org/10.1063/1.4914145 (2015).

59. Chauvin, Y. & Commereuc, D. Chemical counting and characterization of the active sites in the rhenium oxide/alumina metathesis catalyst. *J. Chem. Soc., Chem. Commun.* **6,** 462–464. https://doi.org/10.1039/C39920000462 (1992).

60. Amakawa, K. *et al.* Active Sites in Olefin Metathesis over Supported Molybdena Catalysts. *ChemCatChem* **7,** 4059–4065. https://www.doi.org/10.1002/cctc.201500725 (2015).

61. Howell, J. G., Li, Y. P. & Bell, A. T. Propene Metathesis over Supported Tungsten Oxide Catalysts: A Study of Active Site Formation. *ACS Catal.* **6,** 7728–7738. https://doi.org/10.1021/acscatal.6b01842 (2016).

62. Gulmen, T. S. & Thompson, W. H. Testing a two-state model of nanoconfined liquids: Conformational equilibrium of ethylene glycol in amorphous silica pores. *Langmuir* **22,** 10919–10923. https://www.doi.org/10.1021/la062285k (2006).

63. Ugliengo, P. *et al.* Realistic models of hydroxylated amorphous silica surfaces and MCM- 41 mesoporous material simulated by large-scale periodic B3LYP calculations. *Adv. Mater.* **20,** 4579–4583. https://www.doi.org/10.1002/adma.200801489 (2008).

64. Tielens, F., Gervais, C., Lambert, J. F., Mauri, F. & Costa, D. Ab initio study of the hydroxylated surface of amorphous silica: A representative model. *Chem. Mater.* **20,** 3336–3344. https://www.doi.org/10.1021/cm8001173 (2008).

65. Chizallet, C. l. & Raybaud, P. Pseudo-Bridging Silanols as Versatile Brønsted Acid Sites of Amorphous Aluminosilicate Surfaces. *Angew. Chem., Int. Ed.* **48,** 2891–2893. https://doi.org/10.1002/anie.200804580 (2009).

66. Jystad, A. M., Biancardi, A. & Caricato, M. Simulations of Ammonia Adsorption for the Characterization of Acid Sites in Metal-Doped Amorphous Silicates. *J. Phys. Chem. C* **121,** 22258–22267. https://www.doi.org/10.1021/acs.jpcc.7b08113 (2017).

67. Comas-Vives, A. Amorphous SiO_2 surface models: Energetics of the dehydroxylation process, strain, ab initio atomistic thermodynamics and IR spectroscopic signatures. *Phys. Chem. Chem. Phys.* **18,** 7475–7482. https://www.doi.org/10.1039/c6cp00602g (2016).

68. Tielens, F., Gierada, M., Handzlik, J. & Calatayud, M. Characterization of amorphous silica based catalysts using DFT computational methods. *Catal. Today* **354,** 3–18. https://www.doi.org/10.1016/j.cattod.2019.03.062 (2020).

69. Sautet, P. & Delbecq, F. Catalysis and surface organometallic chemistry: A view from theory and simulations. *Chem. Rev.* **110,** 1788–1806. https://doi.org/10.1021/cr900295b (2010).

70. Catlow, C. R., French, S. A., Sokol, A. A. & Thomas, J. M. Computational approaches to the determination of active site structures and reaction mechanisms in heterogeneous catalysts. *Philos. Trans. R. Soc. A: Math. Phys. Eng. Sci.,* 913–936 (2005).

71. Fermann, J. T. *et al.* Modeling proton transfer in zeolites: Convergence behavior of embedded and constrained cluster calculations. *J. Chem. Theory Comput.* **1,** 1232–1239 (2005).

72. Handzlik, J. & Ogonowski, J. Structure of Isolated Molybdenum(VI) and Molybdenum(IV) Oxide Species on Silica: Periodic and Cluster DFT Studies. *J. Chem. Phys. C* **116,** 5571–5584. https://www.doi.org/10.1021/jp207385h (2012).

73. Goldsmith, B. R., Sanderson, E. D., Bean, D. & Peters, B. Isolated Catalyst Sites on Amorphous Supports: A Systematic Algorithm for Understanding Heterogeneities in Structure and Reactivity. *J. Chem. Phys.* **138,** 204105. https://www.doi.org/10.1063/1.4807384 (2013).

74. Fong, A., Yuan, Y., Ivry, S. L., Scott, S. L. & Peters, B. Computational Kinetic Discrimination of Ethylene Polymerization Mechanisms for the Phillips (Cr/SiO_2) Catalyst. English. *ACS Catal.* **5,** 3360–3374. https://www.doi.org/10.1021/acscatal.5b00016 (2015).

75. Van Santen, R. A. & Kramer, G. J. Reactivity Theory of Zeolitic Broensted Acidic Sites. *Chem. Rev.* **95,** 637–660. https://doi.org/10.1021/cr00035a008 (1995).

76. in. *Catalysis: An Integrated Approach* (eds van Santen, R., van Leeuwen, P., Moulijn, J. & Averill, B.) 433–457 (Elsevier, 1999). https://doi.org/10.1016/S0167-2991(99)80012-3.

77. Sauer, J. Molecular models in ab initio studies of solids and surfaces: from ionic crystals and semiconductors to catalysts. *Chem. Rev.* **89,** 199–255. https://doi.org/10.1021/cr00091a006 (1989).

78. Sauer, J., Ugliengo, P., Garrone, E. & Saunders, V. R. Theoretical Study of van der Waals Complexes at Surface Sites in Comparison with the Experiment. *Chem. Rev.* **94,** 2095–2160. https://doi.org/10.1021/cr00031a014 (1994).

79. Van Santen, R. A. & Neurock, M. *Molecular Heterogeneous Catalysis* https://www.doi.org/10.1002/9783527610846.ch2 (Wiley-VCH, Weinheim, Germany, 2007).

80. Başтuğ, T. & Kuyucak, S. Application of Jarzynski's equality in simple versus complex systems. *Chem. Phys. Lett.* **436,** 383–387. https://www.doi.org/10.1016/j.cplett.2007.01.078 (2007).

81. Bustamante, C., Liphardt, J. & Ritort, F. The Nonequilibrium Thermodynamics of Small Systems. *Phys. Today* **58,** 43–48. https://doi.org/10.1063/1.2012462 (2005).

82. Sear, R. P. Non-self-averaging nucleation rate due to quenched disorder. *J. Phys.: Condens. Matter* **24,** 052205. https://doi.org/10.1088/0953-8984/24/5/052205 (2012).

83. Espelid, Ø. & Børve, K. J. Theoretical Models of Ethylene Polymerization over a Mononuclear Chromium(II)/Silica Site. *J. Catal.* **195,** 125–139. https://www.doi.org/10.1006/jcat.2000.2986 (2000).

84. Fong, A., Vandervelden, C., Scott, S. L. & Peters, B. Computational Support for Phillips Catalyst Initiation via Cr-C Bond Homolysis in a Chromacyclopentane Site. *ACS Catal.* **8,** 1728–1733. https://doi.org/10.1021/acscatal.7b03724 (2018).

85. Floryan, L., Borosy, A. P., Nunez-Zarur, F., Comas-Vives, A. & Coperet, C. Strain Effect and Dual Initiation Pathway in Cr(III)/SiO_2 Polymerization Catalysts from Amorphous Periodic Models. English. *J. Catal.* **346,** 50–56. https://www.doi.org/10.1016/j.jcat.2016.11.037 (2017).

86. Handzlik, J. Properties and metathesis activity of monomeric and dimeric Mo centres variously located on γ-alumina - A DFT study. *Surf. Sci.* **601,** 2054–2065. https://www.doi.org/10.1016/J.SUSC.2007.03.002 (2007).

87. Guesmi, H. & Tielens, F. Chromium oxide species supported on silica: A representative periodic DFT model. *J. Phys. Chem. C* **116,** 994–1001. https://doi.org/10.1021/jp209680r (2012).

88. Delley, M. F. *et al.* Proton Transfers Are Key Elementary Steps in Ethylene Polymerization on Isolated Chromium(III) Silicates. *Proc. Natl. Acad. Sci.* **111,** 11624–11629. https://www.doi.org/10.1073/pnas.1405314111 (2014).

89. Gierada, M. & Handzlik, J. Active Sites Formation and Their Transformations During Ethylene Polymerization by the Phillips CrO_x/SiO_2 Catalyst. *J. Catal.* **352,** 314–328. https://www.doi.org/10.1016/j.jcat.2017.05.025 (2017).

90. Ewing, C. S., Bhavsar, S., Veser, G., McCarthy, J. J. & Johnson, J. K. Accurate amorphous silica surface models from first-principles thermodynamics of surface dehydroxylation. *Langmuir* **30,** 5133–5141. https://doi.org/10.1021/la500422p (2014).

Chapter 2

Computational Support for Phillips Catalyst Initiation via Cr-C Bond Homolysis in a Chromacyclopentane Site

Reproduced in part with permission from:

. Fong, A., Vandervelden, C., Scott, S. L. & Peters, B. Computational Support for Phillips Catalyst Initiation via Cr–C Bond Homolysis in a Chromacyclopentane Site. *ACS Catal.* **8,** 1728–1733. https://doi.org/10.1021/acscatal.7b03724 (2018).

The Phillips catalyst (Cr/SiO_2) is used to produce about 30 million tons of high density polyethylene annually. Despite its long history and continuing industrial importance,[1,2] the mechanism by which the active sites are initially formed remains incompletely understood. In industrial practice,[2] Cr(VI) sites are reduced by either CO[3] or

ethylene[4] to $(\equiv SiO)_2Cr(II)$ sites. Upon exposure to ethylene at ca. 100 C, the active sites (which are widely believed to be $(\equiv SiO)_2Cr(III)$-alkyls)[2] form spontaneously without the assistance of an alkylating co-catalyst. For typical industrial catalysts, estimates of the fraction of Cr sites that is eventually activated vary from 7 to 32 %.[2] According to McDaniel's authoritative review of the commercial Phillips catalyst: "The CO-reduced catalyst, much like its hexavalent parent, polymerizes ethylene under commercial conditions, producing similar polymer".[2] Furthermore, McDaniel shows that activation profiles of Phillips catalysts reduced by either CO or ethylene are very similar,[2,3] strongly suggesting that they follow the same activation mechanism with the same kinetic barrier. Thus while the distribution of Cr coordination numbers and local environments may differ in Phillips catalysts subjected to different treatments,[5–7] and may be manifested in their average spectroscopic properties, there is no evidence that such differences influence reactivity. Based on published observations that approx. one hour is needed to achieve full catalytic activity from either reduced catalyst in an industrial reactor at 373 K,[2] and using transition state theory, we estimated the overall barrier for initiation to be approx. 120 kJ/mol.[8]

Many mechanistic proposals and active site models for the Phillips catalyst have been put forth, some despite ambiguous evidence or even considerable counter-evidence (as discussed extensively by McDaniel).[2] Peters et al. emphasized the need to evaluate computational results more critically for consistency, offering the following three guidelines:[9]

1. The complete catalytic cycle should be considered (initiation, propagation, and termination). A viable mechanism and active site model should distinguish between the preliminary reduction of Cr(VI), slow initiation of the first chain, and chain termination with rapid re-initiation of subsequent chains. In the words of

McDaniel,[2] "...termination of a typical chain must not leave the site in the virgin state, requiring full re-alkylation."

2. Computational studies should distinguish between plausible and implausible departures from experiment.[9] Computationally-predicted polymerization rates and polymer molecular weights are not expected to have "chemical" accuracy, particularly for heterogeneous catalysts whose active site structures are not well-defined. However, benchmark DFT calculations[10] suggest that discrepancies in computed rates that exceed factors of ca. 10^5 are likely due to problems in the active site model and/or proposed mechanism, rather than to inherent inaccuracies in DFT.

3. There should be a viable pathway (based on experimental synthesis protocols) to obtain the sites proposed in computational models.[11] This point is especially important in mechanistic proposals that invoke highly strained sites/unusual metal coordination environments,[12] or support defects.[13] Certainly, site variability can influence the properties of metal sites grafted onto amorphous supports.[5,14] However, proposals that invoke unusual sites must also demonstrate sufficient site abundance to explain the observed catalyst activity and/or active site counting results. Computational proposals which invoke undetectably rare sites must also quantify their abundance in order to make falsifiable predictions about their kinetic viability.

Recently, Gierada et al.[13,15] examined a proposed mechanism in which hydroxyl ligands associated with rare $(\equiv SiO)_2Cr(III)-OH$ sites abstract a proton from ethylene to give $(\equiv SiO)_2Cr(III)(OH_2)(vinyl)$ sites. Since the partial pressure of water is extremely low under polymerization conditions, the subsequent desorption of H_2O from such sites would generate polymerization-active $(\equiv SiO)_2Cr(III)-vinyl$ sites. However, this proposed initiation mechanism is not supported by any experimental evidence for the existence of the putative $(\equiv SiO)_2Cr(III)-OH$ sites;[15] instead, the polymerization activity of

the catalyst is inversely correlated with hydroxyl content of the catalyst.[2]

In another recent paper, Floryan et al.[12] revisited a proposed initiation mechanism involving highly energetically unfavorable proton transfer from ethylene to a bridging oxygen atom on a purported $(\equiv SiO)_3Cr(III)$ site. The authors examined several versions of this site computationally in order to show that very highly strained sites can spontaneously deprotonate ethylene and thereby initiate polymerization. However, the most highly strained sites also have markedly different energetics than the previously proposed site for the same mechanism (*e.g.*, their proton transfer energies differ by ca. 150 kJ/mol, compared to the original study).[16] In addition, the strained sites were obtained by computational alchemy,[17] *i.e.*, hand replacement of an $\equiv SiOH$ site by a Cr(III) ion.[12] In this respect, the model violates guideline (3) above: the authors do not show that their grafting strategy using a molecular Cr(III) complex and mild calcination could generate such highly strained sites on silica, nor do they predict the abundance of the model sites. Furthermore, their computational findings were reported to be based in part on incompletely optimized structures, with multiple imaginary frequencies.[12]

Our recent studies,[18] as well as earlier calculations by Espelid and Børve,[19,20] confirmed that alkylCr(III) sites interacting with silica via two anionic silanolate ligands (and possibly additional neutral siloxane ligands) are viable propagating sites for olefin polymerization, but the mechanism by which they could form has not yet been fully resolved. Using a simple cluster model ($^{5}\mathbf{I}$ in Figure 2.1),[8] our previous work examined several hypothesized initiation pathways that begin with reduced $(\equiv SiO)_2Cr(II)$ sites. Nearly all were excluded on the basis of very high activation barriers and/or rapid termination after initiation. Ethylene disproportionation to give $(\equiv SiO)_2Cr(IV)(CH_2CH_3)(CH{=}CH_2)$ sites followed by ethyl radical extrusion was found to be consistent with the observed formation of organic radicals during initiation.[21,22]

Thus *ab initio* calculations[8] as well as experimental observations[21,22] and precedents

from molecular chromium chemistry[23,24] all suggest a probable role for homolysis pathways in the initiation mechanism. However, our previous computational investigation using simple, rigid cluster models predicted that a two-step mechanism involving activation of coordinated ethylene to give an (ethyl)(vinyl)Cr(IV) site followed by homolytic Cr-C bond cleavage would require hemilabile coordination of siloxane ligands, and no suitable arrangement of ligands was found to allow both steps to proceed at appreciable rates.[88] In this work, we explore a modified Cr-C bond homolysis mechanism, beginning from readily accessible chromacyclopentane sites. Of course, different homolysis pathways may be favored at various sites in the heterogeneous catalyst due to differences in the local Cr geometry.

Our calculations begin with the same cluster model used in our previous works:[8] a small chromasiloxane ring with fixed OH capping groups. The small model assumes only minimal information about the local environment around the Cr site. Larger models rely on more detailed assumptions and, for the Phillips catalyst, there is evidence in many cases that they provide similar results.[13] Also following our previous work, intermediates and transition states were optimized using the ωB97X-D functional[25,26] with a def2-TZVP basis for Cr[27–29] and a TZVP basis for all other atoms.[30] All free energies include translational, rotational, and vibrational contributions. Further details on the cluster model and computational methods can be found in Appendix A.

The most stable form of the *bis*(ethylene)Cr(II) complex has quintet spin multiplicity, and is denoted ^{5}**III** in Figure 2.1. Its preferred reaction with ethylene is cycloaddition to give a chromacyclopentane. We and others previously reported computational evidence for facile chromacyclopentane formation in Phillips catalyst models by ethylene oxidative addition,[8,19] and many chromacycles have been described in molecular chromium chemistry,[31–33] particularly in homogeneous catalysts for ethylene oligomerization.[34,35] Spectroscopic evidence for chromacyclopentane formation in the Phillips catalyst has

also been reported,[36,37] although this intermediate is considered unlikely to be involved in the polymerization mechanism.[18,19,38] Direct conversion of ^{5}**III** to the quintet metallacycle ^{5}**IV** requires a free energy barrier of 177 kJ/mol, while a spin crossing route to the triplet metallacycle ^{3}**IV** requires only 81 kJ/mol (*i.e.*, 57+24 kJ/mol).[8] Non-adiabatic rate estimates from Landau-Zener theory suggest that the spin crossing step (67 kJ/mol) and the adiabatic barrier crossing step (81 kJ/mol) allow both rapid formation of the metallacycle ring **IV** and its cycloreversion. These paths, shown in Figure 2.1, include the Cr(II) and Cr(IV) starting points for each of the mechanisms discussed below.

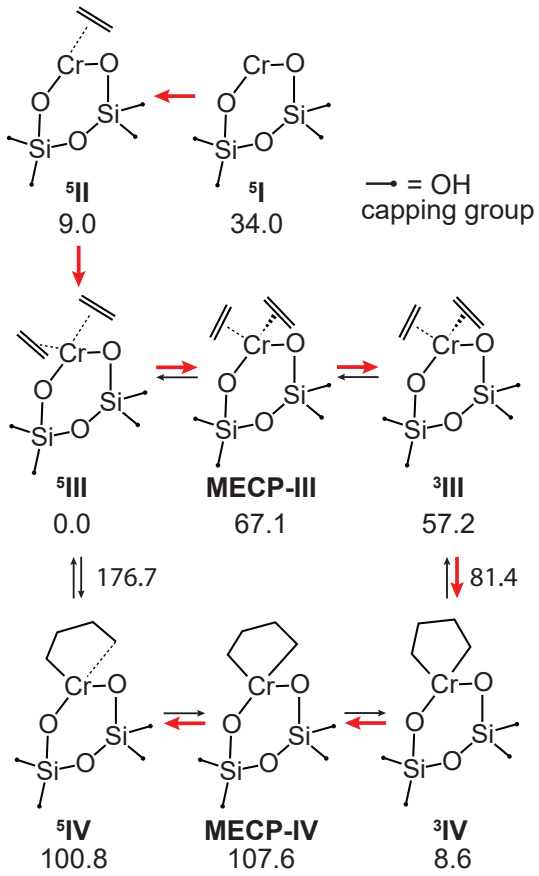

Figure 2.1: Stationary points and minimum energy crossing points (MECPs) in chromacyclopentane formation. The preferred path is indicated in red (geometries shown in Appendix Figure A.1) . Dangling Si- bonds were capped with OH groups. Free energies (kJ/mol) for all species are given relative to the *bis*(ethylene)Cr(II) complex, ^{5}**III**, at 373 K. Numbers next to arrows represent free energies of transition states. Quintet spin species: ^{5}**IV**, chromacyclopentane; Triplet spin species: ^{3}**III**, *bis*(ethylene)Cr(II) complex; ^{3}**IV**, chromacyclopentane.

The chromacyclopentane site **IV** can undergo direct homolysis of a Cr-C bond, resulting in a tethered *n*-butyl radical, **V**. Homolysis can occur from either ^{3}**IV** or ^{5}**IV**, with the latter requiring a spin-crossing through **MECP-IV**. In either case, the overall effective free energy to form the tethered radical ^{5}**V** is 123 kJ/mol relative to the *bis*(ethylene)Cr(II) resting state, ^{5}**III**, Figure 2.2. Once created, ^{5}**V** could react in one of four ways:

1. Ethylene could coordinate and insert into the remaining Cr-C bond, with an additional barrier of 71 kJ/mol (Appendix Figure A.2) , thereby extending the length of the tethered radical chain. However, the high overall barrier (homolysis+insertion), at 194 kJ/mol, makes this pathway unlikely.

2. Gas phase (*i.e.*, uncoordinated) ethylene could react with the dangling *n*-butyl radical chain end to create an *n*-hexyl radical chain. We estimate that this pathway requires an additional 80 kJ/mol, based on the barrier computed for reactions between gas phase alkyl radicals and olefins (Appendix A, Figure A.3). This pathway is consequently also unlikely, because of its high overall barrier of 204 kJ/mol.

3. The tethered *n*-butyl radical in site ^{5}**V** could reattach to the Cr center that generated it, with no additional barrier. Reattachment is therefore the most likely fate of the tethered *n*-butyl radical on most sites.

4. If ^{5}**V** is sufficiently close to another Cr(II) with an open coordination site, the dangling radical could react with that site to form an *n*-butyl bridge, shown as ^{3}**BB** (Figure 2.2). Based on our previous work,(Fong, Yuan et al. 2015) both of the resulting alkylCr(III) sites would be capable of facile ethylene polymerization. Similarly, Espelid and Børve showed that Cr(III)-O-Cr(III) sites connected by an *n*-butyl chain, can incorporate ethylene at both Cr-C bonds.[20] As shown below, the computed overall barrier for this initiation pathway is comparable to the estimated initiation barrier for the industrial Phillips catalyst.

The reactions of the organic radical in ^{5}**V** with a neighboring Cr(II) site lacking ethylene ligands, or with a *mono*(ethylene)Cr(II) site (^{5}**II**), have no barrier. However, our model predicts that most Cr(II) sites exist in the resting *bis*(ethylene) state (^{5}**III**) under reaction conditions (*i.e.*, high ethylene pressure). An additional 9 kJ/mol is needed

to create the ^{5}**II** site from ^{5}**III** at $P_{C_2H_4}$ = 1 atm (Figure 2.2). Thus the overall free energy barrier to create the *n*-butyl-bridged alkylCr(III) sites from two neighboring ^{5}**III** sites is 132 kJ/mol.

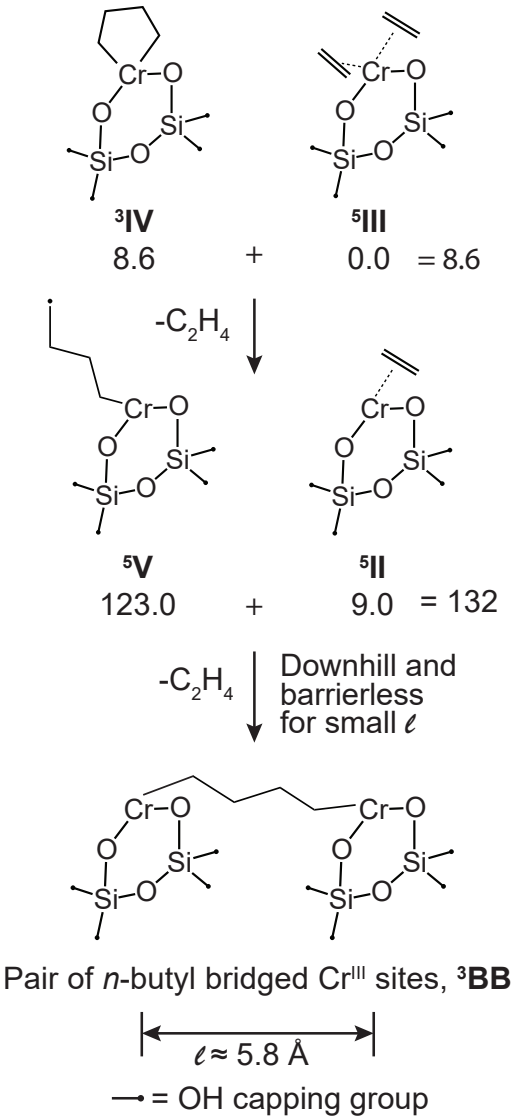

Figure 2.2: A tethered *n*-butyl radical attached to a Cr(III) site can attack a neighboring Cr(II) site co-located within a distance ℓ to create a pair of Cr(III) sites connected by an *n*-butyl chain (see the full free energy path in the Appendix A Figure A.6). Numbers below structures represent free energies; the combined free energies of ^{5}**V** and ^{5}**II** provide an estimate of the overall initiation barrier.

Phillips catalyst initiation mechanisms that involve the formation of bridging alkyl

chains (and specifically n-butyl bridges) between Cr sites have been proposed previously. For example, Rebenstorf et al. proposed direct cycloaddition of two ethylene molecules to form an n-butyl bridge across a [Cr(II)-O-Cr(II)] site.[39] Espelid and Børve proposed an n-butyl-bridged site could form from a chromacycle connected via an oxo bridge to a Cr(II) site.[20] Although they attempted a coordinate-driving calculation, they were not successful in determining the barrier. Our work establishes 132 kJ/mol as a computational upper bound on the free energy barrier to form n-butyl-bridged Cr(III) sites. The barrier may be further lowered by coordination of nearby siloxanes from the silica surface to the chromacyclopentane site,[8] or by sharing of electron density from the dangling n-butyl radical with the Cr orbitals of the neighboring Cr(II) site as the radical migrates from one Cr atom to the other.

To further explore the plausibility of initiation by formation of an n-butyl chain between neighboring sites, we estimated the fraction of sites that could be activated by chromacyclopentane homolysis. To form the ^{3}**BB** site, the two Cr atoms can be no further apart than the distance ℓ. Assuming that all Cr sites are randomly distributed at a surface Cr density σ_{Cr} [Cr atoms per surface area], the average number of Cr ions within bonding range of the n-butyl chain is given by the Poisson distribution:[40]

$$p\,(m) = \exp(-\lambda)\lambda^{m}/m! \tag{2.1}$$

with Poisson parameter $\lambda = \pi\ell^{2}\sigma_{Cr}$. For industrial Phillips catalysts, a typical loading σ_{Cr} is 0.4 Cr/nm^{2} (corresponding to 0.6 - 1.0 wt% Cr, depending on the silica surface area).[2] Based on eqn. 2.1, and the ideal distance between Cr atoms in the bridged Cr(III) cluster of ca. ℓ = 5.8 Å(Figures 2.2 and A.5), we estimate $\lambda \approx 0.42$. Accordingly, eqn. 2.1 predicts that 66% of Cr sites are isolated with zero nearby neighbors, 27% of Cr sites have a single neighbor within distance ℓ, and about 7% of Cr sites have two or more

neighbors within distance ℓ. Chromacyclopentane homolysis should be able to activate all of the sites with a single neighbor and some sites with multiple neighbors, *i.e.* between 27% and 34% of sites. Thus the tethered homolysis mechanism could fully account for the fraction of active sites in the industrial catalyst, which has been estimated to be in the range 7 - 32 %.[2]

Finally, we developed a simple kinetic model to estimate the time scale for initiation by chromacyclopentane homolysis. Initially, all sites are dormant (D), but an approximate fraction $\lambda \exp[-\lambda]$ of sites (those paired with a single neighbor at a distance ℓ or less, *e.g.*, 27% for a typical industrial catalyst) can become active (A). A full derivation of the kinetic model is provided in Section A.3 of Appendix A. Here we summarize the main results. According to our DFT calculations, the fraction of activated sites θ_A as a function of time t after exposure of reduced Cr(II)/SiO_2 sites to ethylene is

$$\theta_A = \lambda \exp[-\lambda](1 - \exp[-t/\tau_{ind}]) \tag{2.2}$$

where the induction time τ_{ind} depends on the overall free energy to reach the approximate transition state configuration, as depicted in Figure 2.2. Specifically, activation requires conversion of two ^{5}**III** sites (the most abundant dormant state) into one site ^{5}**V**, one site ^{5}**II**, and one gas phase ethylene molecule. The predicted induction time is

$$\tau_{ind} = 1/\left(\theta_{^{5}\mathbf{IV}|D}\theta_{^{5}\mathbf{II}|D}k_{^{5}\mathbf{IV}\rightarrow{}^{5}\mathbf{V}}\right) \tag{2.3}$$

where $\theta_{^{5}\mathbf{IV}|D}$ and $\theta_{^{5}\mathbf{II}|D}$ are fractions of the dormant site population in states ^{5}**IV** and ^{5}**II**, respectively. The rate constant $k_{^{5}\mathbf{IV}\rightarrow{}^{5}\mathbf{V}}$ is the frequency of Cr-C bond homolysis in state ^{5}**IV**. Inserting the computed free energies and using transition state theory gives

the expression

$$\tau_{ind} = P_{C_2H_4} \Big/ \left(\frac{k_B T}{h} e^{-(132 kJ/mol)/k_B T} \right) \tag{2.4}$$

which predicts an induction time of ca. 100 hours at 373 K and $P_{C_2H_4} = 1$ atm. This estimate is plausible, compared to the observed induction time of ca. 1 hour,[2] and given the current limitations of DFT. The dependence on ethylene pressure emerges from the pre-equilibrium between sites ^{5}**III** and ^{5}**II**.

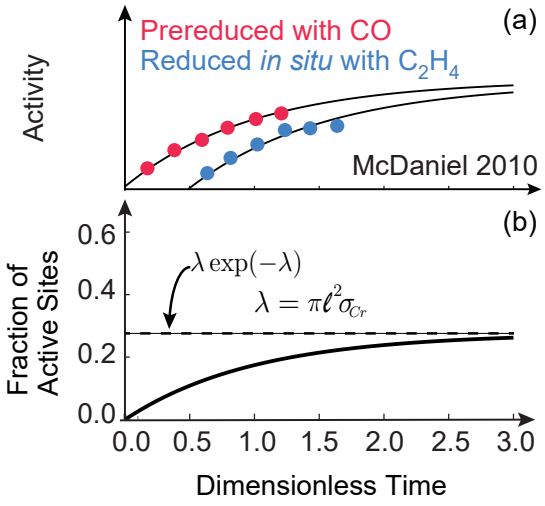

Figure 2.3: Comparison of (a) activity profiles of catalysts pre-reduced by CO (red) or reduced *in situ* by ethylene (blue), taken from data reported by McDaniel.[2] Exponential rise curves are shown to aid in comparing the data to the simulated kinetic profile, and (b) simulated kinetic profile based on the mechanism of initiation proposed in this work. The fraction of sites that can be activated within the induction time is comparable to active site counting experiments for commercial catalysts.[2]

Our bichromium initiation mechanism predicts that fewer sites should activate at lower Cr loadings. However, the average per-site polymerization activity in Phillips catalysts increases as the Cr loading decreases, down to 0.01 Cr/nm^2.[2,41] Most, but not all,[20,39,42–44] researchers have interpreted this trend to mean that initiation does not involve more than one Cr site. In some studies, the apparent increase of activity at low loading may be due in part to formation of extended Cr_2O_3 domains at high loadings.

Even at low loadings, pairing might result from associations between Cr sites. Our Poisson analysis does not account for the presence of associated sites and/or extended Cr_2O_3 domains.

Alternative explanations for the increased activity per site at low loadings might involve additional initiation pathways that amplify the number of active sites. One such mechanism we considered is chromacyclopentane ring expansion prior to homolysis, which could extend the reach of the radical-terminated chain to more distant Cr(II) sites. This mechanism requires a significant additional barrier beyond the 132 kJ/mol for the required steps in Figure 2.2, as shown in the Supporting Information (Figure A.9). Thus we conclude that ring expansion prior to homolysis is unimportant for initiation, like ethylene insertion into the Cr-C bond of the *n*-butyl radical, and coupling of the dangling *n*-alkyl radical with ethylene (see above).

A potentially viable way to amplify the number of Cr sites that can be initiated by the tethered homolysis mechanism involves the dangling bonds ($\equiv$Si$\cdot$ and/or SiO$\cdot$ radicals) present on silica fracture surfaces. Such sites are likely to be created as a result of stresses caused by early stages of polymer production in the silica pores.[45] The forces induced by polymer formation (see section A.5 of Appendix A) can fracture pores with widths down to ca. 15 nm in silica,[46] and these fractures might lead to increased activity[47,48] by abstracting hydrogen atoms from ethylene or from polyethylene (Figure A.10) to create alkyl and/or vinyl radicals. These radicals would readily interact with Cr(II) sites that have not yet been activated, converting them to polymerization-ready alkylCr(III) sites. As yet, this possibility is speculative, and similar catalysts on different support materials can initiate without fracturing.[2] However, the possible amplification of the active site population as the support fractures should be amenable to experimental[49,50] and computational[51] study.

In conclusion, a viable route to alkylCr(III) sites that are capable of ethylene poly-

merization was identified using density functional theory calculations and small cluster models for the active sites of the Phillips catalyst. According to our calculations, *bis*(ethylene)Cr(II) sites readily form chromacyclopentane sites, which undergo homolysis to create tethered butyl radicals, and these radicals can react with neighboring Cr(II) sites. The overall barrier for this initiation mechanism is ca. 132 kJ/mol, in approximate agreement with the experimental barrier estimated from the observed induction time. The tethered homolysis mechanism could cause the activation of about 35% of the Cr sites present at a typical Cr loading of 1.0 wt%, assuming the Cr sites are randomly distributed on the silica surface.

We emphasize that questions about the details of the initiation mechanism remain. Our previous work proposed that hemilabile siloxane ligands at some Cr(II) sites may decoordinate to allow oxidative addition of ethylene to give (ethyl)(vinyl)Cr(IV) sites, then recoordinate to facilitate Cr-C bond homolysis to give vinylCr(III) sites.[8] That two-step mechanism is consistent with several key experimental observations. If a suitable ligand coordination environment were found, it might also explain the low temperature initiation of polymerization by an unspecified number of sites reported in academic studies.[21,37] However, it is not necessary to invoke such sites in order to fully account for activation profiles recorded under industrial conditions (Figure 2.3).[2,3] Without hemilability of the siloxanes, the computed barrier always exceeds 200 kJ/mol for one of the two steps. This work proposes an alternative initiation step involving Cr-C bond homolysis in a chroma(IV)cyclopentane ring near a Cr(II) site. This alternative mechanism does not require a change in Cr coordination number, and appears to be viable without invoking any unusual Cr coordination environments, leading to much faster rates due to its lower computed barrier. However, the need for adjacent Cr sites means that it does not explain the higher per-site activity at lower Cr loadings.[41]

Bibliography

1. Hogan, J. P. & Banks, R. L. US57387756A (United States)

2. McDaniel, M. P. A Review of the Phillips Supported Chromium Catalyst and Its Commercial Use for Ethylene Polymerization. English. *Adv. Catal.* **53,** 123–606. https://www.doi.org/https://doi.org/10.1016/S0360-0564(10)53003-7 (2010).

3. Merryfield, R., McDaniel, M. & Parks, G. An XPS study of the Phillips Cr/silica polymerization catalyst. *J. Catal.* **77,** 348–359. https://www.doi.org/10.1016/0021-9517(82)90178-6 (1982).

4. Baker, L. M. & Carrick, W. L. Oxidation of Olefins by Supported Chromium Oxide. English. *J. Org. Chem.* **33,** 616–618. https://doi.org/10.1021/jo01266a030 (1968).

5. Demmelmaier, C. A., White, R. E., van Bokhoven, J. A. & Scott, S. L. Evidence for a chromasiloxane ring size effect in Phillips (Cr/SiO_2) polymerization catalysts. *J. Catal.* **262,** 44–56. https://www.doi.org/10.1016/j.jcat.2008.11.024 (2009).

6. Zhong, L. *et al.* Spectroscopic and structural characterization of $Cr(II)/SiO_2$ active site precursors in model Phillips polymerization catalysts. *J. Catal.* **293,** 1–12. https://www.doi.org/10.1016/j.jcat.2012.05.014 (2012).

7. Barzan, C. *et al.* Ligands Make the Difference! Molecular Insights into CrVI/SiO_2 Phillips Catalyst during Ethylene Polymerization. *J. Am. Chem. Soc.* **139,** 17064–17073. https://www.doi.org/10.1021/jacs.7b07437 (2017).

8. Fong, A., Peters, B. & Scott, S. L. One-Electron-Redox Activation of the Reduced Phillips Polymerization Catalyst, via Alkylchromium (IV) Homolysis: A Computational Assessment. English. *ACS Catal.* **6,** 6073–6085. https://www.doi.org/10.1021/acscatal.6b01728 (2016).

9. Peters, B., Scott, S. L., Fong, A., Wang, Y. & Stiegman, A. E. Reexamining the Evidence for Proton Transfers in Ethylene Polymerization. *Proc. Natl. Acad. Sci. USA* **112,** E4160–E4161. https://www.doi.org/10.1073/pnas.1422589112 (2015).

10. Harvey, J. N. On the Accuracy of Density Functional Theory in Transition Metal Chemistry. *Ann. Rep. Prog. Chem. C* **102,** 203–226. https://www.doi.org/10.1039/B419105F (2006).

11. Peters, B. & Scott, S. L. Single Atom Catalysts on Amorphous Supports: A Quenched Disorder Perspective. *J. Chem. Phys.* **142,** 104708. https://www.doi.org/10.1063/1.4914145 (2015).

12. Floryan, L., Borosy, A. P., Nunez-Zarur, F., Comas-Vives, A. & Coperet, C. Strain Effect and Dual Initiation Pathway in Cr(III)/SiO_2 Polymerization Catalysts from Amorphous Periodic Models. English. *J. Catal.* **346,** 50–56. https://www.doi.org/10.1016/j.jcat.2016.11.037 (2017).

13. Gierada, M. & Handzlik, J. Active Sites Formation and Their Transformations During Ethylene Polymerization by the Phillips CrO_x/SiO_2 Catalyst. *J. Catal.* **352,** 314–328. https://www.doi.org/10.1016/j.jcat.2017.05.025 (2017).

14. Han, K., Goldsmith, B. R., Fong, A. & Peters, B. in, 213–22 (RSC Publishing, Cambridge, 2013). https://www.doi.org/10.1039/9781849737753.

15. Chakrabarti, A., Gierada, M., Handzlik, J. & Wachs, I. E. Operando Molecular Spectroscopy During Ethylene Polymerization by Supported CrOx/SiO_2 Catalysts: Active Sites, Reaction Intermediates, and Structure-activity Relationship. English. *Top. Catal.* **59,** 725–739. https://www.doi.org/10.1007/s11244-016-0546-6 (2016).

16. Delley, M. F. *et al.* Proton Transfers Are Key Elementary Steps in Ethylene Polymerization on Isolated Chromium(III) Silicates. *Proc. Natl. Acad. Sci.* **111,** 11624–11629. https://www.doi.org/10.1073/pnas.1405314111 (2014).

17. Straatsma, T. P. & McCammon, J. A. Computational Alchemy. *Ann. Rev. Phys. Chem.* **43,** 407–35. https://www.doi.org/10.1146/annurev.pc.43.100192.002203 (1992).

18. Fong, A., Yuan, Y., Ivry, S. L., Scott, S. L. & Peters, B. Computational Kinetic Discrimination of Ethylene Polymerization Mechanisms for the Phillips (Cr/SiO_2) Catalyst. English. *ACS Catal.* **5,** 3360–3374. https://www.doi.org/10.1021/acscatal.5b00016 (2015).

19. Espelid, Ø. & Børve, K. J. Theoretical Models of Ethylene Polymerization over a Mononuclear Chromium(II)/Silica Site. *J. Catal.* **195,** 125–139. https://www.doi.org/10.1006/jcat.2000.2986 (2000).

20. Espelid, Ø. & Børve, K. J. Molecular-Level Insight into Cr/Silica Phillips-Type Catalysts: Polymerization-Active Dinuclear Chromium Sites. *J. Catal.* **206,** 331–338. https://www.doi.org/10.1006/jcat.2001.3499 (2002).

21. Brown, C. *et al.* Mechanism of Initiation in the Phillips Ethylene Polymerization Catalyst: Ethylene Activation by Cr(II) and the Structure of the Resulting Active Site. *ACS Catal.* **7,** 7442–7455. https://doi.org/10.1021/acscatal.7b02677 (2017).

22. Pan, Q., Li, L., Shaikhutdinov, S. & Freund, H.-J. Planar model system of the Phillips (Cr/SiO_2) catalyst based on a well-defined thin silicate film. *J. Catal.* **357,** 12–19. https://www.doi.org/10.1016/j.jcat.2017.10.026 (2018).

23. Katsuyama, T., Bakac, A. & Espenson, J. H. Oxidative homolysis of penta-aquoorganochromium(III) cations induced by macrocyclic nickel(III) complexes. *Inorg. Chem.* **28,** 339–341. https://www.doi.org/10.1021/ic00301a037 (1989).

24. Espenson, J. H. Chemistry of organochromium(III) complexes. *Acc. Chem. Res.* **25,** 222–227. https://www.doi.org/10.1021/ar00017a003 (1992).

25. Chai, J.-D. & Head-Gordon, M. Long-range corrected hybrid density functionals with damped atom-atom dispersion corrections. *Phys. Chem. Chem. Phys.* **10,** 6615–6620. https://www.doi.org/10.1039/B810189B (2008).

26. Goerigk, L. & Grimme, S. A thorough benchmark of density functional methods for general main group thermochemistry, kinetics, and noncovalent interactions. *Phys. Chem. Chem. Phys.* **13,** 6670–6688. https://www.doi.org/10.1039/C0CP02984J (2011).

27. Feller, D. The role of databases in support of computational chemistry calculations. *J. Comput. Chem.* **17,** 1571–1586. https://www.doi.org/10.1002/(SICI)1096-987X(199610)17:13%3C1571::AID-JCC9%3E3.0.CO;2-P (1996).

28. Schuchardt, K. L. *et al.* Basis Set Exchange: A Community Database for Computational Sciences. *J. Chem. Inf. Model.* **47,** 1045–1052. https://www.doi.org/10.1021/ci600510j (2007).

29. Weigend, F. & Ahlrichs, R. Balanced Basis Sets of Split Valence, Triple Zeta Valence and Quadruple Zeta Valence Quality for H to Rn: Design and Assessment of Accuracy. *Phys. Chem. Chem. Phys.* **7,** 3297–3305. https://www.doi.org/10.1039/b508541a (2005).

30. Schäfer, A., Horn, H. & Ahlrichs, R. Fully optimized contracted Gaussian basis sets for atoms Li to Kr. *J. Chem. Phys.* **97,** 2571–2577. https://www.doi.org/10.1063/1.463096 (1992).

31. Briggs, J. R. The selective trimerization of ethylene to hex-1-ene. *J. Chem. Soc., Chem. Commun.,* 674–675. https://www.doi.org/10.1039/C39890000674 (1989).

32. Emrich, R., Heinemann, O., Jolly, P. W., Krüger, C. & Verhovnik, G. P. J. The Role of Metallacycles in the Chromium-Catalyzed Trimerization of Ethylene. *Organometallics* **16,** 1511–1513. https://www.doi.org/10.1021/om961044c (1997).

33. Rozenel, S. S., Chomitz, W. A. & Arnold, J. Chromium Complexes Supported by the Multidentate Monoanionic N2P2 Ligand: Reduction Chemistry and Reactivity with Ethylene. *Organometallics* **28,** 6243–6253. https://www.doi.org/10.1021/om900695s (2009).

34. Tomov, A. K., Chirinos, J. J., Jones, D. J., Long, R. J. & Gibson, V. C. Experimental Evidence for Large Ring Metallacycle Intermediates in Polyethylene Chain Growth Using Homogeneous Chromium Catalysts. *J. Am. Chem. Soc.* **127,** 10166–10167. https://www.doi.org/10.1021/ja051523f (2005).

35. McGuinness, D. S. Olefin Oligomerization via Metallacycles: Dimerization, Trimerization, Tetramerization, and Beyond. *Chem. Rev.* **111,** 2321–2341. https://www.doi.org/10.1021/cr100217q (2011).

36. Ruddick, V. J. & Badyal, J. P. S. Early Stages of Ethylene Polymerization Using the Phillips CrOx/Silica Catalyst. *J. Phys. Chem. B* **102,** 2991–2994. https://www.doi.org/10.1021/jp963318f (1998).

37. Groppo, E., Lamberti, C., Bordiga, S., Spoto, G. & Zecchina, A. In situ FTIR spectroscopy of key intermediates in the first stages of ethylene polymerization on the Cr/SiO_2 Phillips catalyst: Solving the puzzle of the initiation mechanism? *J. Catal.* **240,** 172–181. https://www.doi.org/10.1016/j.jcat.2006.03.006 (2006).

38. McGuinness, D. S., Davies, N. W., Horne, J. & Ivanov, I. Unraveling the Mechanism of Polymerization with the Phillips Catalyst. *Organometallics* **29,** 6111–6116. https://www.doi.org/10.1021/om100883n (2010).

39. Rebenstorf, B. On the Phillips Catalyst Site with High Catalytic Activity. *J. Mol. Catal.* **56,** 170–182. https://www.doi.org/10.1016/0304-5102(89)80181-6 (1989).

40. Dekking, F. M., Kraaikamp, C., Lopuhaa, H. P. & Meester, L. E. in. 1st ed. (Springer, Heidelberg-Berlin, 2005). https://www.doi.org/10.1007/1-84628-168-7.

41. Leach, B. & Hogan, J. P. *Catalysis of the Phillips Petroleum Company Polyethylene Process* 149–176. https://www.doi.org/10.1016/B978-0-12-440201-0.50011-4 (Academic Press, New York, 1983).

42. Spitz, R. Supported Chromium Oxide Catalysts for Olefin Polymerization. *J. Catal.* **35,** 345–352. https://www.doi.org/10.1016/0021-9517(74)90215-2 (1974).

43. Groeneveld, C., Wittgen, P. P. M. M., Swinnen, H. P. M., Wernsen, A. & Schuit, G. C. A. Hydrogenation of Olefins and Polymerization of Ethene over Chromium Oxide/Silica Catalysts. *J. Catal.* **83,** 346–361. https://www.doi.org/10.1016/0021-9517(83)90060-X (1983).

44. Xia, W. *et al.* Multinuclear Solid-State NMR Study of the Coordinative Nature of Alkylaluminum Cocatalyst on Phillips CrOx/SiO_2 Catalyst. *Appl. Catal., A* **389,** 186–194. https://www.doi.org/10.1016/j.apcata.2010.09.023 (2010).

45. McDaniel, M. P. Influence of Catalyst Porosity on Ethylene Polymerization. *ACS Catal.* **1,** 1394–1407. https://www.doi.org/10.1021/cs2003033 (2011).

46. Aguado, J., Calleja, G., Carrero, A. & Moreno, J. Morphological Modifications of Cr/SBA-15 and Cr/Al-SBA-15 Ethylene Polymerization Catalysts: Influence on Catalytic Behaviour and Polymer Properties. *Microporous Mesoporous Mater.* **131,** 294–302. https://www.doi.org/10.1016/j.micromeso.2010.01.006 (2010).

47. Schmeal, W. R. & Street, J. R. Polymerization in Expanding Catalyst Particles. *AIChE J.* **17,** 1188–1197. https://www.doi.org/10.1002/aic.690170526 (1971).

48. McKenna, T. F. & Soares, J. B. P. Single Particle Modelling for Olefin Polymerization on Supported Catalysts: A Review and Proposals for Future Developments. *Chem. Eng. Sci.* **56,** 3931–3949. https://www.doi.org/10.1016/S0009-2509(01)00069-0 (2001).

49. D'Souza, A. S. & Pantano, C. G. Mechanisms for Silanol Formation on Amorphous Silica Fracture Surfaces. *J. Am. Ceram. Soc.* **82,** 1289–1293. https://www.doi.org/10.1111/j.1151-2916.1999.tb01909.x (1999).

50. Musso, F., Ugliengo, P., Solans-Monfort, X. & Sodupe, M. Periodic DFT Study of Radical Species on Crystalline Silica Surfaces. *J. Phys. Chem. C* **114,** 16430–16438. https://www.doi.org/10.1021/jp103342b (2010).

51. Rountree, C. L. *et al.* Atomistic Aspects of Crack Propagation in Brittle Materials: Multimillion Atom Molecular Dynamics Simulations. *Ann. Rev. Mater. Res.* **32,** 377–400. https://www.doi.org/10.1146/annurev.matsci.32.111201.142017 (2002).

Chapter 3

Grafting metal complexes onto amorphous supports: from elementary steps to catalyst site populations via kernel regression

Reproduced in part with permission from:

. Khan, S. A., Vandervelden, C. A., Scott, S. L. & Peters, B. Grafting metal complexes onto amorphous supports: From elementary steps to catalyst site populations: Via kernel regression. *React. Chem. Eng.* **5,** 66–76. https://doi.org/10.1039/c9re00357f (2020).

3.1 Introduction

Most *ab initio* computational catalysis studies focus on homogeneous catalysts,[1–3] enzymes,[4–6] or heterogeneous catalysts with ordered structures such as metals,[7–11] zeo-

lites,[12–14] and crystalline metal oxides.[15–17] All of these materials have in common the advantage that many features of the catalyst structure are known. Even for molecular catalysts and enzymes, where the active site resides within a fluctuating environment, there are systematic computational frameworks for averaging over the fluctuations.[18–20] In contrast, amorphous catalysts cannot be modelled with small, periodically repeating solid structures, nor by sampling a well-defined ensemble for liquid phase disorder. Instead, the quenched disorder in an amorphous heterogeneous catalyst[21,22] is a permanent signature of its non-equilibrium preparation history. Examples within this family include the Phillips catalyst (Cr/SiO_2) for ethylene polymerization,[23] molybdenum (Mo/SiO_2) and tungsten (W/SiO_2) catalysts for olefin metathesis,[24] and titanium catalysts (Ti/SiO_2) for alkene epoxidation.[25]

Because of these difficulties, amorphous catalysts have mostly been avoided in *ab initio* computational studies. Those exceptions in which calculations on amorphous catalysts were attempted were forced to rely on questionable assumptions.[22,26–34] For example, are the model sites representative of the real material? Do the models accurately represent the most active sites? Can reliable conclusions about the reaction kinetics be drawn from a single-site computational model? At present, none of these questions can be satisfactorily answered with *ab initio* calculations.

These questions are addressed in two papers, this one and a companion. They provide a computational framework that combines machine learning, statistical importance sampling, and population balance modeling techniques. To illustrate the concepts and methods, we begin with a model for an atomically-dispersed catalyst on an amorphous support. The essential features of the model are a quenched disordered support scaffold (to represent an amorphous silica matrix), surface silanol sites where precursors can be attached (to represent surface hydroxyl groups), and a microkinetic model for grafting at each silanol site. These microkinetic models have rate parameters that depend on the

individual grafting site characteristics. The rate parameters at each grafting site will be determined, much like in a real *ab initio* calculation, by structural optimization of the intermediates using a simple force field.

This first paper deals with how the active sites are generated during catalyst preparation. In particular, we show how the populations of both grafted sites and the unreacted grafting sites evolve during an idealized grafting process. If the surface reactions are irreversible, the final metal site distribution will be determined by those surface grafting sites with the fastest grafting kinetics. However, if the surface reactions are reversible, the final grafted site distribution will favor grafted sites that lead to the most stable grafted species. To enable *ab initio* studies in the future, the algorithm must efficiently predict the characteristics of the most reactive grafting sites and their abundances, without performing exhaustive *ab initio* calculations for many thousands of grafting sites. We demonstrate how kernel regression can learn to anticipate the outcomes of these optimizations. Then, by applying the kernel regression model to thousands of grafting sites, we can construct a population balance model for the grafting process. The simplicity of our model system allows us to test the accelerated predictions against an exhaustive parameterization from structure optimizations at thousands of grafting sites.

The companion paper uses a grafted site population that reflects both the disordered support and the superimposed grafting kinetics to predict site-averaged kinetics. Because turnover frequencies at individual grafting sites depend exponentially on their activation energies, site-averaged kinetics are difficult to converge without rare events sampling methods. The second paper deals with averaging over the non-uniform distribution of grafted sites to predict the overall kinetics.

The remainder of this paper is as follows. First, we introduce simple models for the amorphous support and grafting kinetics. Next, we use kernel regression tools to predict the grafting thermodynamics and kinetics based on a concise list of grafting

site characteristics. Finally, we use the kernel regression results and kinetic models to parameterize the population balance model for grafting.

3.2 Amorphous silica

Amorphous silica is a commonly used catalyst support because of its thermal and mechanical stability, large surface area, and its chemical inertness. The surface of silica is terminated by silanol groups which may be categorized as isolated, geminal, vicinal etc. Real amorphous silicas are created via sol-gel synthesis, spray drying, pyrolysis, or precipitation methods. Silica can be calcined to increase its mechanical strength and to remove adsorbed water.[35–40] The calcination temperature also determines the residual surface silanol density, which in turn influences the activity of the supported catalyst.[23,41,42]

Many studies have used spectroscopic techniques like IR, NMR, and EPR to investigate the populations of different silanol types.[43,44] However, in contrast to crystalline materials, the absence of long-range order results in broad peaks that complicate the precise characterization of silica.

Silicas of different types exhibit different ring size distributions,[45–47] and silanols of the same type can have different bond angles and different dihedral angles.[35,44] These subtle structural differences between silanols and their environments are likely to influence their reactivity. Many investigators have grafted metal atoms to silica via reactions between silanols and molecular complexes like $AlCl_3$,[48] GaR_3,[49,50] $TiCl_4$,[51–53] and $VOCl_3$.[54,55] These grafting reactions are useful both as probes of local structure and as routes to supported organometallic catalysts.

In a typical grafting experiment, a fluid phase molecular precursor reacts with amorphous silica.[49,55,56] A protonolysis reaction between the precursor and surface silanols

results in a metal atom grafted to the silica surface with one, two, or three M-O-Si linkages, sometimes called monopodal, bipodal, or tripodal species, Figure 3.1.[24,57–60]

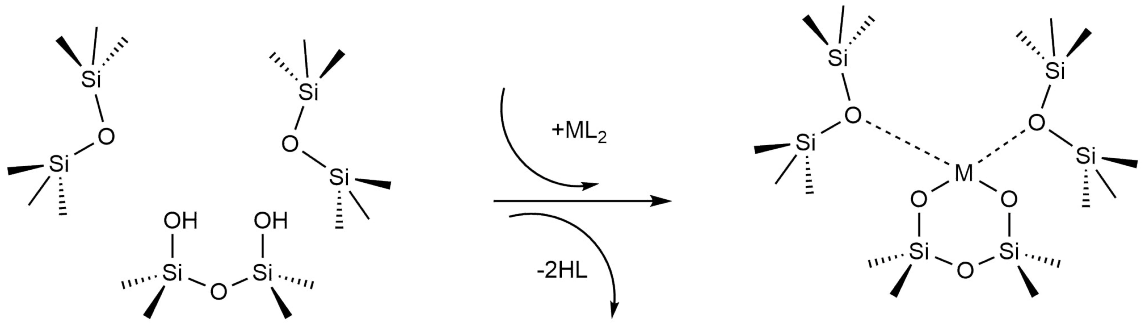

Figure 3.1: Scheme showing the grafting of a molecular $\mathbf{ML_2}$ complex to a vicinal silanol pair. The metal forms two bonds to the silanolate oxygens while two **HL** molecules are eliminated. The metal may also coordinate to nearby siloxane oxygens.

Computational studies of atomically-dispersed metals on silica often use cluster models terminated by hydroxyl groups or hydrogen atoms. These models generally range in sizes from a few to tens of silicon atoms.[28,29,34,61–67] The cluster models are often carved from crystalline materials like zeolites[68] or β-cristobalite.[66,69] In such clusters, the peripheral atoms are fixed at positions characteristic of the crystalline material. The de facto assumption is that larger cluster models are more representative of the real amorphous catalyst. Indeed large cluster models more accurately account for elasticity of the silica matrix and for dispersion interactions between adsorbates and the support.[33,70] However, each layer of silica requires additional and unjustified assumptions about the environment. In this sense, large cluster models are overly specific, while small cluster models are amenable to systematic investigation of the effects of local grafting site geometry.[22]

In the past decade, some computational studies generated amorphous silica surfaces that attempt to reproduce experimental observables like surface silanol density and the IR spectrum.[71–74] Typically, such surfaces are prepared by molecular dynamics simulations, in which crystalline models are heated to high temperatures followed by rapid quenching to generate disordered structures. Then the bulk amorphous structure is cleaved to cre-

ate the surface. Unsaturated oxygens are capped with hydrogen atoms, and unsaturated silicons are capped with hydroxyl groups. Finally, pairs of proximal silanols are condensed to achieve the correct surface silanol density. These methods generate atomistic amorphous models of silica with a non-uniform structural distribution of surface silanols. However, such in silico preparation routes for amorphous silica do not correspond to experimental synthesis procedures. In particular, the high surface area of a real silica does not result from cleavage and subsequent functionalization. In addition, the system sizes modelled are typically quite small (100-200 silanols). For comparison, a 10 mg sample of silica with area 350 m^2g^{-1} and 1.0 silanols/nm^2 contains about 10^{18} silanols.

3.2.1 A simple model for amorphous silica

The mechanisms of grafting, activation, and catalytic reactions are still debated for many amorphous catalysts.[26,30,50,58,69,75–77] To resolve the outstanding questions, we need methods that can predict the kinetics at each grafting site and estimate proper site-averaged kinetic properties. Then a given support model (if large enough) and proposed mechanism will yield well-defined, site-averaged predictions to be tested against experiments. To develop such methods, we selected a simple example system for which benchmark calculations can be performed exhaustively, for the full ensemble of non-uniform sites. In this section, we propose a simple abstract model of the amorphous support.

We model the amorphous support as a 2D lattice with quenched disorder, Figure 3.2. Note the loose similarity to the qualitative model of Peri and Hensley.[48] First, a uniform lattice is created in which nearest neighbors are separated by a unit (dimensionless) distance. Each site is randomly displaced (δ) from the uniform lattice by random displacements along the x and y directions to create a disordered lattice. Displacements are drawn from an isotropic 2-D Gaussian distribution (described in Section B.1.4). The

lattice is then "functionalized" with hydroxyl (-OH), siloxane (≡SiOSi≡), and empty sites with probabilities p_{OH}, p_{siloxane}, and p_{empty}.

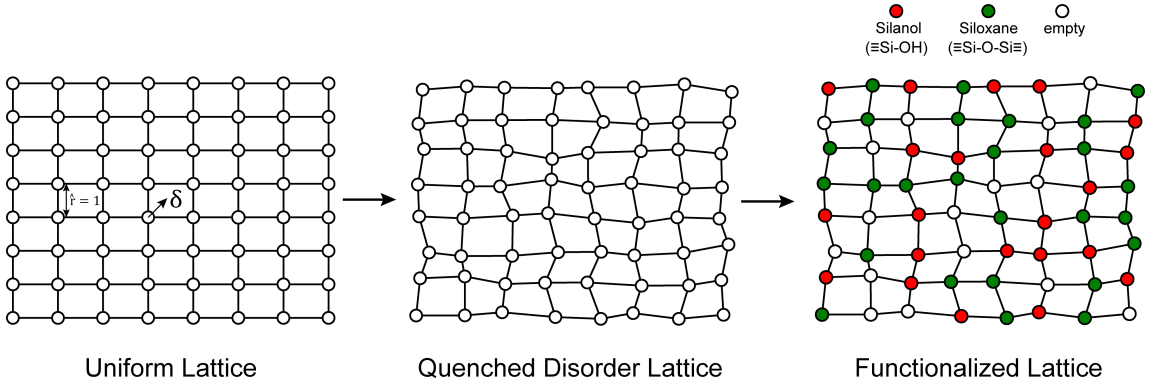

Figure 3.2: Steps to form a functionalized, quenched disorder lattice.

3.2.2 Grafting molecular metal complexes: a simple model

Grafting sites in our model are empty sites surrounded by a pair of vicinal hydroxyls on one axis and a pair of siloxanes on the other axis. Figure 3.3 shows a grafting site located between vicinal silanols $(\equiv\mathrm{SiOH})_2$ and two siloxanes (≡SiOSi≡). The precursor $\mathbf{ML}_2$, a molecular complex, in our model has two displaceable ligands. A real catalyst precursor may have additional ligands like chloride, oxo, or methyl groups that remain bonded to the metal **M** after grafting. The metal is grafted as a bipodal species (≡SiO**M**OSi≡) upon reaction of $\mathbf{ML}_2$ with the vicinal hydroxyls to eliminate two **HL** molecules. The metal may also interact with neighboring siloxanes to form $\mathbf{M}\cdots\mathrm{O}(\mathrm{Si}\equiv)_2$ bonds. The strengths of the ≡SiO-**M** and $\mathbf{M}\cdots\mathrm{O}(\mathrm{Si}\equiv)_2$ bonds depend on the local geometry near the grafting site.

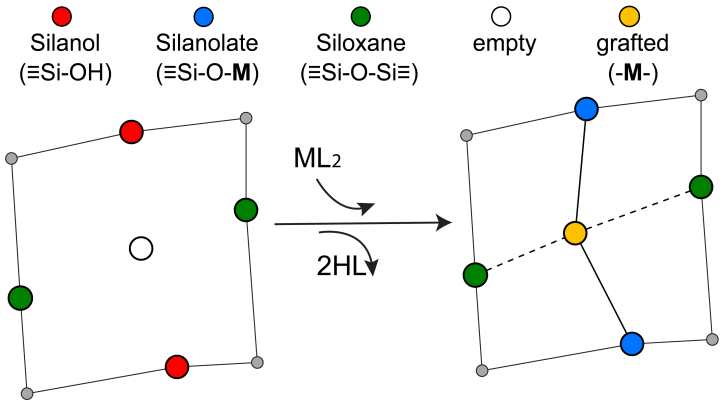

Figure 3.3: Grafting sites on the amorphous 2-D lattice model. One set of opposite nearest neighbor sites are hydroxyl groups, while the other set is siloxanes. $\mathbf{ML}_2$ reacts with two hydroxyls and interacts with the siloxanes to create a grafted $\mathbf{M}$ atom as shown.

3.2.3 Computing grafting rates on the amorphous silica model

To model grafting kinetics of vicinal silanol sites on the amorphous 2D lattice, we consider the grafting mechanism outlined in Sec. 3.2.2. The grafting process at each vicinal silanol site is assumed to be irreversible with the following rate law:

$$r(\mathbf{x}) = [\mathbf{ML}_2]. \tag{3.1}$$

Here $[\mathbf{ML}_2]$ is the gas phase concentration of $\mathbf{ML}_2$, $\mathbf{x}$ represents the local environment of the vicinal silanol site, and $k(\mathbf{x})$ is a site-dependent rate constant.[78] We use concentration to construct rate laws in this work. One can instead use the precursor partial pressure, but note that one must beware of the resulting complications in extracting activation energies. For example, when precursor pressure is set by its T-dependent vapor pressure, as in CrO_2Cl_2 grafting,[58] the pressure and temperature cannot be separately controlled. We use transition state theory (TST) to model the temperature and site-geometry dependence of the grafting rate constant. TST rate constants are widely used

to predict and interpret activation barriers and kinetics across a wide range of catalysis applications.[79–83] TST rate constants are now readily computed from electronic structure calculations.[84] The TST rate constant is:

$$k(\mathbf{x}) = \frac{k_B T}{h} \hat{V}_0 \exp[-\beta \Delta G^{\ddagger}(\mathbf{x})]. \tag{3.2}$$

Here $\Delta G^{\ddagger}(\mathbf{x})$ is the grafting barrier as computed with $[\mathbf{ML_2}]$ at the reference volume ($\hat{V}_0$) per particle. Next, we use a Linear Free Energy Relationship (LFER) to model the grafting free energy barrier. Specifically, we assume that the free energy of grafting is linearly related to the activation barrier for grafting:[78]

$$\Delta G^{\ddagger}(\mathbf{x}) = \Delta G^{\ddagger}_{ref} + \alpha \Delta G^{o}(\mathbf{x}). \tag{3.3}$$

Here α ($0 < \alpha < 1$) is the Brønsted coefficient and $\Delta G^{\ddagger}_{ref}$ is the grafting barrier for a reference grafting site with a thermoneutral grafting free energy ($\Delta G^{o}(\mathbf{x}) = 0$). The value of α indicates the position of the transition state between the reactant and product states. Small values of α (near 0) indicate an early transition state that resembles the reactants. Large values of α (near 1) indicate a transition state that resembles the products. In practice, intermediate values of α are common, so we have chosen $\alpha = 1/2$.[85] The value of $\Delta G^{\ddagger}_{ref}$ determines the time scale for grafting, but it will have no bearing on results after non-dimensionalization. Thus, to complete the kinetic model, including the effects of non-uniform grafting sites, we only need a model for $\Delta G^{o}(\mathbf{x})$. The energy to graft the precursor at an empty site is

$$\Delta E(\mathbf{x}) = 2\epsilon_{\mathbf{HF}} + V_{\mathbf{M*}}(\mathbf{x}) - V_{*} - 2\epsilon_{\mathbf{ML}}. \tag{3.4}$$

Here $V_{\mathbf{M}*}(\mathbf{x})$ is the energy of the grafted metal site, V_* is the energy of the unreacted silica site, $\epsilon_{\mathbf{ML}}$ is the energy of the M-L bond, and $\epsilon_{\mathbf{HL}}$ is the energy of the **H-L** bond. V_* is twice the O-H bond energy,

$$V_* = 2\epsilon_{OH} \tag{3.5}$$

Here ϵ_{OH} is the O-H bond energy. To compute $V_{\mathbf{M}*}(\mathbf{x})$, the **M**-OSi≡ bond energy and **M**...O(Si≡)$_2$ bond energy are modelled as Morse potentials:

$$\epsilon_i(r) = D_i(1 - \exp[-a_i(r - r_{i,rq})])^2 - D_i. \tag{3.6}$$

Here i is the interaction type (**M**-OSi≡ or **M**$\cdots$O(Si≡)$_2$), Di is the equilibrium energy of the interaction, a_i is related to the width of the potential well, $r_{i,eq}$ is the equilibrium distance, and r is the metal-oxygen bond length. All constants defined in this section are shown in Table 3.1. $V_{\mathbf{M}*}(\mathbf{x})$ is computed by optimizing the position of the metal with surrounding hydroxyl and siloxane positions fixed:

$$V_{\mathbf{M}*}(\mathbf{x}) = \underset{\mathbf{x_M}}{min}(\epsilon_{\mathbf{M}-O}(r_{\mathbf{M}-O_1}) + \epsilon_{\mathbf{M}-O}(r_{\mathbf{M}-O_2}) + \epsilon_{\mathbf{M}-O}(r_{\mathbf{M}\cdots O'_1}) + \epsilon_{\mathbf{M}-O}(r_{\mathbf{M}\cdots O'_2})). \tag{3.7}$$

Here, $r_{\mathbf{M}-O_i}$ is a metal-oxygen bond distance, and $r_{\mathbf{M}\cdots O'_i}$ is a metal-siloxane coordination distance, as shown in Figure 3.4a. The bond lengths are functions of the (variable) metal atom position $\mathbf{x_M}$ and the (quenched/fixed) peripheral siloxane and silanol locations in x. The optimization indicated in Eq. 3.7 therefore involves optimization of the metal atom position within the fixed peripheral environment.

Finally, the free energy of grafting is computed using

$$\Delta G^o(\mathbf{x}) = \Delta E(\mathbf{x}) + \Delta PV - T\Delta S^o. \tag{3.8}$$

Table 3.1: Constants used in computing grafting barriers and defining the quenched disorder lattice (see Section B.1 for further explanations)

Parameter	**Value**
T	298.15K
$r_{\mathbf{M}-O,eq}$	1.0
$r_{\mathbf{M}\cdots O,eq}$	1.16
$\sigma^2_{lattice}$	0.00022
p_{OH}	0.3
$p_{siloxane}$	0.3
p_{empty}	0.4
$D_{\mathbf{M}-O}$	524.4 kJ mol^{-1}
$a_{\mathbf{M}-O}$	1.9
$D_{\mathbf{M}\cdots O}$	120.0 kJ mol^{-1}
$a_{\mathbf{M}\cdots O}$	2.3
$2\epsilon_{\mathbf{HL}} - (V_* + 2\epsilon_{\mathbf{ML}}) + \Delta PV + \Delta S^o$	1229.56 kJ mol^{-1}
M	0.026
α	0.5
$\Delta G^o_{unperturbed}$	-30 kJ mol^{-1}
$\Delta G^{\ddagger}_{ref}$	131.3 kJ mol^{-1}

Here ΔS^o is the entropy of the grafting reaction and $\Delta E(\mathbf{x}) + \Delta PV$ is the enthalpy. The entropy changes are predominantly from site-independent contributions like translational and rotational degrees of freedom of the $\mathbf{ML}_2$ and **HL** species. As noted for the parameter $\Delta G^{\ddagger}_{ref}$, the site-independent terms in Eq. 3.8 have no bearing on the results after non-dimensionalization.

3.3 Kernel regression model for grafting barriers

Because *ab initio* calculations are costly, computational studies of catalyst grafting have been based on single sites, or at most a few sites. Ultimately, one hopes to make predictions about grafting across the entire distribution of non-uniform sites. In this section, we propose a machine learning method (kernel regression) to learn structure-property relations from a modest number of training calculations.[86–88] Kernel regression

was chosen because it is a non-parametric method; hence it does not need a predefined form for the fitting function. Specifically, we will use calculations at a small collection of grafting sites to predict barriers and kinetics for all grafting sites.

The training data includes a collection of computed barriers, $\Delta\hat{G}^{\ddagger}(\mathbf{x}_1)$, $\Delta\hat{G}^{\ddagger}(\mathbf{x}_2)$, $\Delta\hat{G}^{\ddagger}(\mathbf{x}_3)$, etc. The estimated barrier for a new peripheral environment $\mathbf{x}$ is a kernel-weighted average of the training data:

$$\Delta\hat{G}^{\ddagger} = \sum_{i=1}^{N_{train}} w(\mathbf{x}, \mathbf{x}_i)\Delta G^{\ddagger}(\mathbf{x}_i). \tag{3.9}$$

Here, $\Delta\hat{G}^{\ddagger}(\mathbf{x})$ is the prediction for a grafting site with local geometry $\mathbf{x}$, $\Delta\hat{G}^{\ddagger}(\mathbf{x}_i)$ values represent the barriers of grafting sites in the training set, N_{train} is the number of training examples, and $w(\mathbf{x}, \mathbf{x}_i)$ are the weights. The weights are represented using a Gaussian kernel:[89]

$$w(\mathbf{x}, \mathbf{x}_i) = \frac{\exp[-d^2(\mathbf{x}, \mathbf{x}_i)]}{\sum_{i=1}^{N_{train}} \exp[-d^2(\mathbf{x}, \mathbf{x}_i)]}. \tag{3.10}$$

Here $d^2(\mathbf{x}, \mathbf{x}')$ is a squared non-Euclidean Mahalanobis distance between structures $\mathbf{x}$ and $\mathbf{x}$'

$$d^2(\mathbf{x}, \mathbf{x}') = (\mathbf{x} - \mathbf{x}')^T \mathbf{S} (\mathbf{x} - \mathbf{x}'). \tag{3.11}$$

$\mathbf{S}$ is a square, symmetric, and positive definite matrix. To ensure that $\mathbf{S}$ remains positive definite while being optimized/learned, we write $\mathbf{S}$ as

$$\mathbf{S} = \mathbf{A}\mathbf{A}^T. \tag{3.12}$$

Here $\mathbf{A}$ is a lower triangular matrix.[90] Matrix A should be optimized so that Eq. 3.9 accurately predicts $\Delta\hat{G}^{\ddagger}(\mathbf{x})$ at new grafting sites. The training data from optimization

of a small collection of grafting sites is used in a leave-one-out objective function

$$L = \sum_{i=1}^{N_{train}} (\Delta G^{\ddagger}(\mathbf{x}_i) - \Delta \hat{G}^{\ddagger}(\mathbf{x}_i))^2. \tag{3.13}$$

to determine $\mathbf{A}$. In L, $\Delta \hat{G}^{\ddagger}(\mathbf{x}_i)$ is a weighted average of all data points in the training set excluding itself:

$$\Delta \hat{G}^{\ddagger}(\mathbf{x}_i) = \sum_{\substack{j=1 \\ j \neq i}}^{N_{train}} \Delta G^{\ddagger}(\mathbf{x}_j) w(\mathbf{x}_i, \mathbf{x}_j). \tag{3.14}$$

The Gaussian kernel in Eq. 3.10 generates a continuous and differentiable model of $\Delta \hat{G}^{\ddagger}(\mathbf{x})$, so the leave-one-out error function is easily minimized with conjugate gradient methods or other superlinear minimization schemes.[91] We use kernel regression as implemented in the metric-learn Python library.[92] The library minimizes L using the conjugate gradient method with analytical derivatives of L.

3.4 Local coordinates

The Gaussian kernel function in Eq. 3.9 can be constructed from the complete set of internal coordinates for the local environment. However, a subset of the internal coordinates will usually be sufficient to predict the activation barriers. We do not know a priori which coordinates are most important, but these can be identified as illustrated below.

The local environment of silanol and siloxane groups in our model is specified by five coordinates (2 dimensions $\times$ 4 "atoms" - 1 rotation - 2 centre-of-mass translations). We use three of the five coordinates to construct the kernel regression model: (1) distance between OH groups (d1), (2) distance between siloxane groups (d2), and (3) angle between the OH-siloxane groups (θ), Figure 3.4.

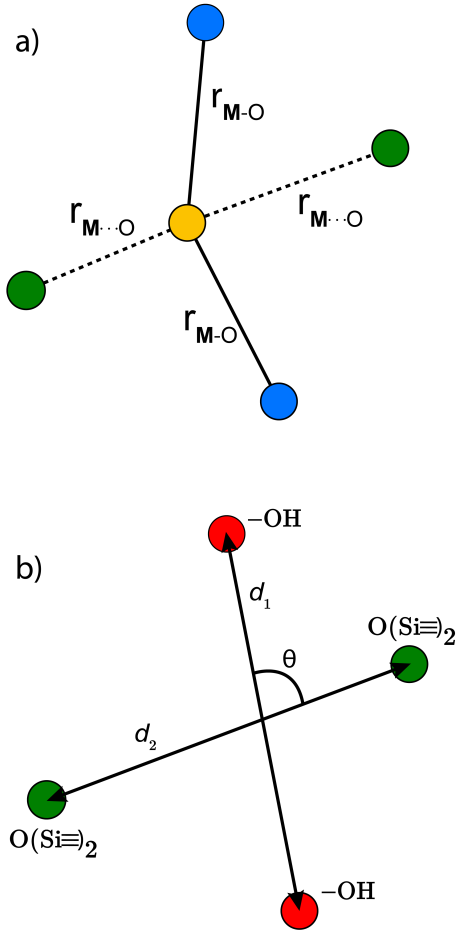

Figure 3.4: Bond lengths in the force field and in the optimization of the **M**-atom position. (b) Coordinates for describing the local environment around the grafting site. We have used three of the five ($2 \times 4 - 1$ (rotation) $- 2$ (translations)) peripheral environment coordinates in the initial kernel regression model.

3.5 Sites with non-uniform grafting barriers: a population balance perspective

As described in Sec. 3.2, an amorphous support will have a distribution of grafting sites with different grafting rates. As time progresses, the most reactive grafting sites will be consumed, while grafting sites with higher reaction barriers remain unreacted and

reduce the rate of further grafting. This situation can be modelled using the following population balance scheme:

$$\frac{d\rho(\Delta G^{\ddagger}, t)}{dt} = -\mathscr{k}(\Delta G^{\ddagger}, m)\rho(\Delta G^{\ddagger}, t). \tag{3.15}$$

Here $\rho(\Delta\hat{G}^{\ddagger}, t)$ is the population of unreacted vicinal silanol sites at time t with a barrier of $\Delta\hat{G}^{\ddagger}$, $\mathscr{k}(\Delta\hat{G}^{\ddagger}, m)$ is the rate at which the sites react (Eq. 3.1), and $m = [\mathbf{ML}_2]/\hat{V}_0^{-1}$ is the ratio of the concentration of the precursor $\mathbf{ML}_2$ in the gas phase to the reference concentration ($\hat{V}_0^{-1}$) at which $\Delta\hat{G}^{\ddagger}$ is computed. The rate of change of m is

$$\frac{dm}{dt} = -\int d\Delta G^{\ddagger}\rho(\Delta G^{\ddagger}, t)k(\Delta G^{\ddagger}, m) + m_G. \tag{3.16}$$

Here, the first term on the right-hand side is rate of consumption of $\mathbf{ML}_2$ due to the grafting reaction, and m_G is the rate at which $\mathbf{ML}_2$ is fed to the reactor. In some grafting experiments, the molecular complex is constantly replenished by evaporation from a reservoir, so that its gas phase concentration is always in equilibrium with its liquid reservoir.[50,58] In such cases, the $\mathbf{ML}_2$ concentration remains constant at its vapor pressure as grafting proceeds. Assuming constant m, Eq. 3.15 can be integrated to yield

$$\rho(\Delta G^{\ddagger}, t) = \rho_o(\Delta G^{\ddagger})\exp[-\frac{k_B T}{h}e^{-\beta\Delta G^{\ddagger}}mt]. \tag{3.17}$$

Here $\rho_0(\Delta\hat{G}^{\ddagger})$ is the initial population of vicinal silanol sites.

Defining non-dimensional time as:

$$\tau = \frac{k_B T}{h}\exp[-\beta\Delta G^{\ddagger}_{ref}t]. \tag{3.18}$$

leads to the population of unreacted vicinal silanol sites as a function of τ and grafting

free energy barrier:

$$\rho(\Delta G^{\ddagger}, \tau) = \rho_0(\Delta G^{\ddagger}) \exp[-e^{-\beta\alpha\Delta G^o} m\tau]. \tag{3.19}$$

3.6 Results and discussion

3.6.1 Evolution of grafting site population

A 1500×1500 lattice was randomly perturbed using the procedure outlined in Sec. 3.2.1. A total of 19368 grafting sites were identified. A metal atom was placed in each grafting site, and its position was optimized. The grafting free energy barrier was computed for each grafting site. A histogram of the results was constructed to approximate the initial distribution $\rho_o(\Delta\hat{G}^{\ddagger})$. Note that the horizontal axis depends on the choice of $\Delta\hat{G}^{\ddagger}_{ref}$ and $\Delta S^o/k_B$, i.e., different values of these parameters will shift the distribution left and right along the $\Delta\hat{G}^{\ddagger}$ axis. In a real system, *ab initio* calculations yield $\Delta\hat{G}^{\ddagger}$ and ΔS^o values for all grafting sites with no adjustable parameters, so there would be no arbitrary shift. Following this, Eq. 3.19 was used to compute the evolution of the unreacted grafting site population, Figure 3.5a.

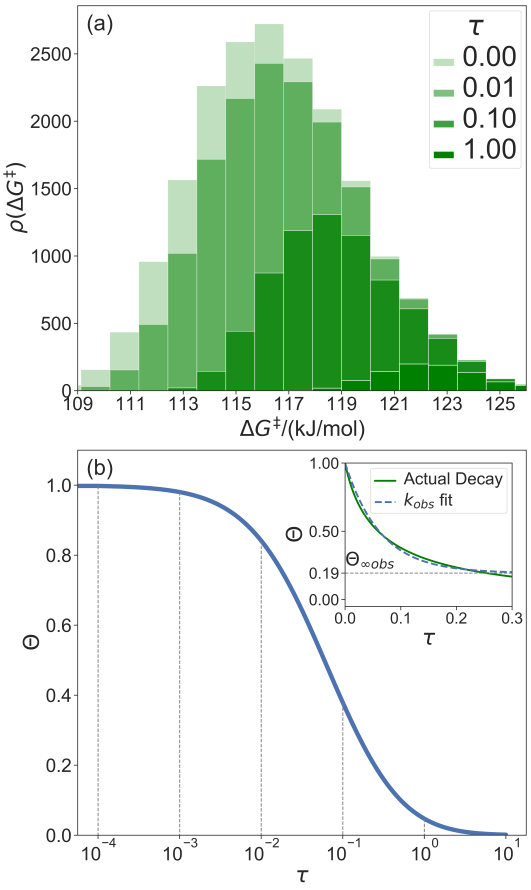

Figure 3.5: (a) Evolution of the unreacted vicinal silanol site population as a function of non-dimensional grafting time. (b) Fraction of unreacted vicinal silanol sites as a function of logarithmic time. The inset shows the evolution as a function of real time in the range $0 < \tau < 0.3$. It also includes an exponential decay model fit to this data.

The initial range of grafting barriers spans 23 kJ mol^{-1}. Grafting sites with the lowest barriers react first, so the distribution shifts to the right as grafting proceeds. The 23 kJ mol^{-1} width of the distribution causes the grafting sites to react at markedly different rates. The fastest grafting sites react in about $10^{-4}\tau$. Grafting is complete in about 10τ.

During a grafting experiment, the total number of grafted sites at any time can be measured, e.g., by monitoring the amount of HL released. The fraction of unreacted

vicinal silanol sites (relative to the total number of vicinal silanol sites) is:

$$\Theta = \frac{\int \rho(\Delta G^{\ddagger}, \tau) d\Delta G^{\ddagger}}{\int \rho(\Delta G^{\ddagger}, 0) d\Delta G^{\ddagger}}. \tag{3.20}$$

Figure 3.5b shows the evolution of the fraction of unreacted vicinal silanols (note the log scale). Grafting progress slows dramatically as the most reactive grafting sites vanish from the distribution. In an experiment, the reaction might seem complete when all the vicinal silanols with low barriers have reacted. The inset of Figure 3.5b shows how the data would appear if the fraction of unreacted silanols were monitored only for time 0 $< \tau <$ 0.3. The inset also shows a fit to the common pseudo-first-order kinetic model $\Theta = \Theta_{\infty}(1 - \Theta_{\infty}) \exp(-k_{obs}\tau)$ fraction of unreacted vicinal silanol sites and k_{obs} is an "apparent" grafting rate constant. Over the range $0 < \tau < 0.3$, the data appears to be approximately an exponential decay, thus one might infer that all silanols react with the same rate constant (kobs), and that 19% (from = 0.19) of the vicinal silanol sites are unreactive. However, all of the silanols (in this model) do react at exponentially longer time intervals. The final silanol sites react last because they are different. Therefore, they change the distribution of grafted sites, and may also change the catalytic activity. Hence, it is important to analyse grafting kinetics on a logarithmic time scale.

Predictions about catalytic activity require information about the abundance of grafted sites and their characteristics. Both the grafting kinetics and the catalytic turnover frequency at a particular grafted site depend on the local grafted site environment. However, the most readily grafted sites may not correspond to the most catalytically active sites. Therefore, predictions of the overall catalyst activity require predictions about grafting propensity and characteristics of the grafted sites. Chapter 4 develops tools for computing site-averaged kinetics starting from the grafted distribution.

3.6.2 Applying kernel regression to predict grafting barriers

The kernel regression model was trained on grafting barriers for 100 vicinal silanol sites randomly sampled from the set of all 19368 grafting sites using local coordinates described in Sec. 3.4. Justification for choosing a training set size of 100 is provided in Section B.2. A parity plot of the true $\Delta\hat{G}^{\ddagger}$ values and kernel regression $\Delta\hat{G}^{\ddagger}$ predictions is shown in Figure 3.6.

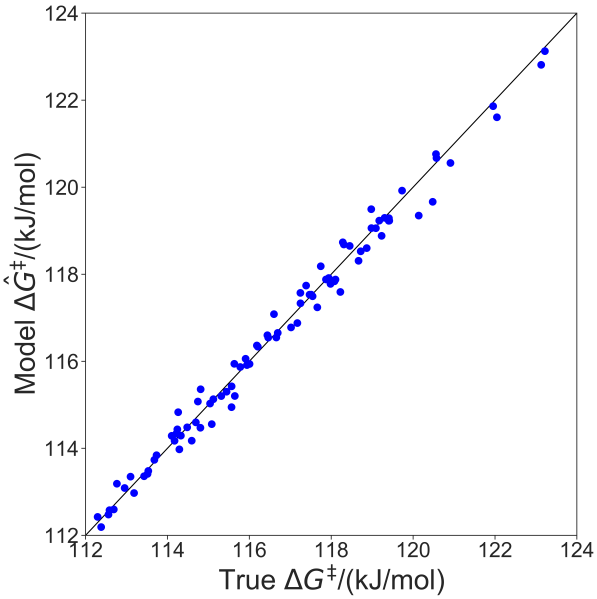

Figure 3.6: Parity plot showing predictions of grafting activation barriers by the kernel regression model trained on 100 grafting sites.

The model trained with 100 $\Delta\hat{G}^{\ddagger}$ calculations was used to predict grafting barriers for all 19368 grafting sites. After training, the only input information for each grafting site are its values of d_1, d_2, and θ. The residuals of the predictions are plotted as a distribution in Figure 3.7. Nearly all residuals are within ± 1 kJ mol^{-1}, and the standard deviation of the residual distribution is 0.48 kJ mol^{-1}.

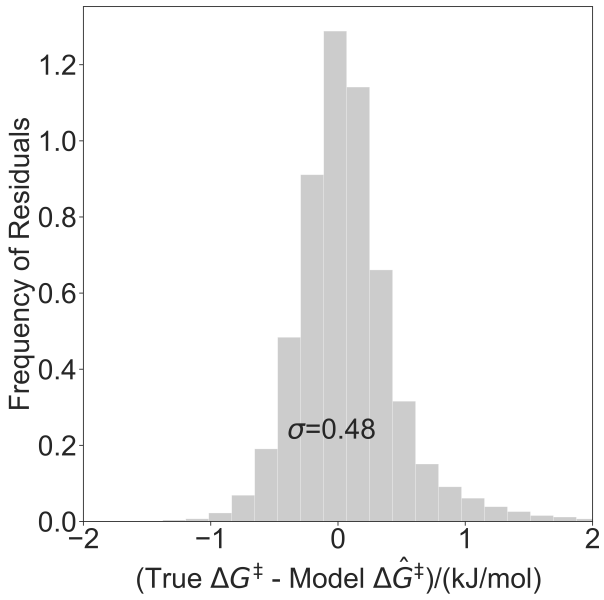

Figure 3.7: Distribution of residuals for a model trained on 100 grafting sites.

3.6.3 Identifying important local coordinates

The results in Sec. 3.6.2 used three of five coordinates to construct the kernel regression model. Three is already a relatively compact structural parameter set, but for this model it can be reduced further. To evaluate the importance of different combinations of local coordinates, the model was retrained by systematically excluding some coordinates. Table 3.2 shows R^2 values for fits with different coordinates. Figure 3.8 shows parity plots like the one in Figure 3.6, but for a model based only on d1, and for a model based on d_1 and d_2 (i.e., without θ).

The model trained using d_1 and d_2 ($R^2 = 0.99$) is comparable in accuracy to the model trained using all coordinates ($R^2 = 0.99$) Clearly, d_1 and d_2 are both important for describing barriers, but θ is inconsequential as its omission does not diminish the accuracy of the kernel regression model. We can also see that the model cannot be further simplified from d_1 and d_2 dependence. The models trained on only d_1 ($R^2 = 0.60$) and

Table 3.2: R^2 values of kernel regression models with different combinations of local coordinates)

Coordinates	$\mathbf{R^2}$
θ	-0.02
d_2	0.52
d_1	0.60
d_2, θ	0.52
d_1, θ	0.60
d_1, d_2	0.99
d_1, d_2, θ	0.99

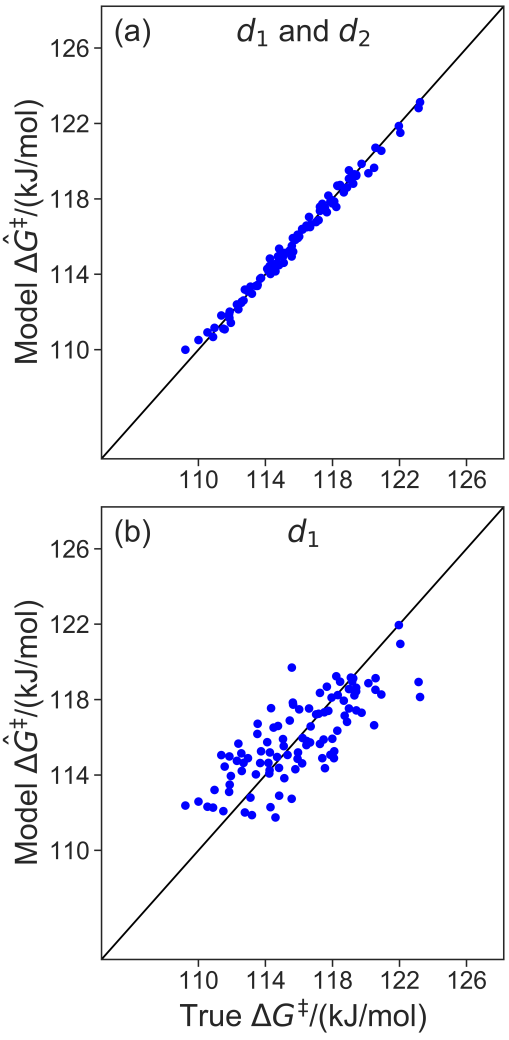

Figure 3.8: (a) Parity plot of the model trained with d_1 and d_2. (b) Parity plot of the model trained with d_1 only.

d_2 ($R^2 = 0.52$) have severely diminished accuracy.

Now, using just two coordinates, we can project the grafting free energy barriers onto a 2D plot, Figure 3.9. The barrier decreases monotonically with increasing d_1 or d_2. Therefore, grafting sites with large values of d_1 and d_2 react first, while grafting sites with small values of d_1 and d_2 react more slowly. We emphasize that, even with this simple model, it was not obvious a priori how structural characteristics would influence the grafting kinetics. The procedures in this paper should help to identify features of the most reactive silanol sites.

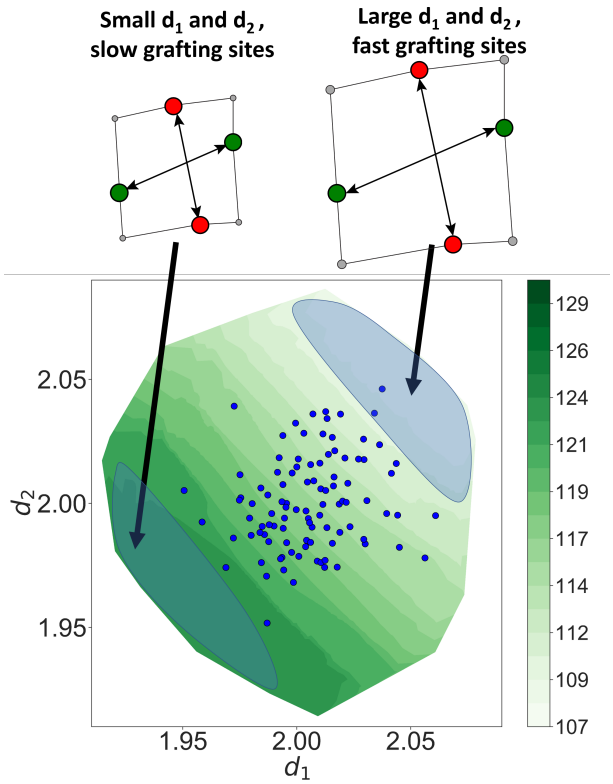

Figure 3.9: Model-predicted barriers as function of d_1 and d_2. Blue dots show training set grafting sites. The figure also shows the structures of active and inactive grafting sites. Grafting sites with smaller values of d_1 and d_2 have larger barriers, while grafting sites with larger values of d_1 and d_2 have smaller barriers.

3.6.4 Predicting the time evolving population of grafting sites

In this section, we recompute results from section 6.1, now using the kernel regression model. We use the model based only on d_1 and d_2 and trained on just 100 randomly sampled grafting sites to predict the evolving population of unreacted silanols. The results are shown in Figure 3.10a.

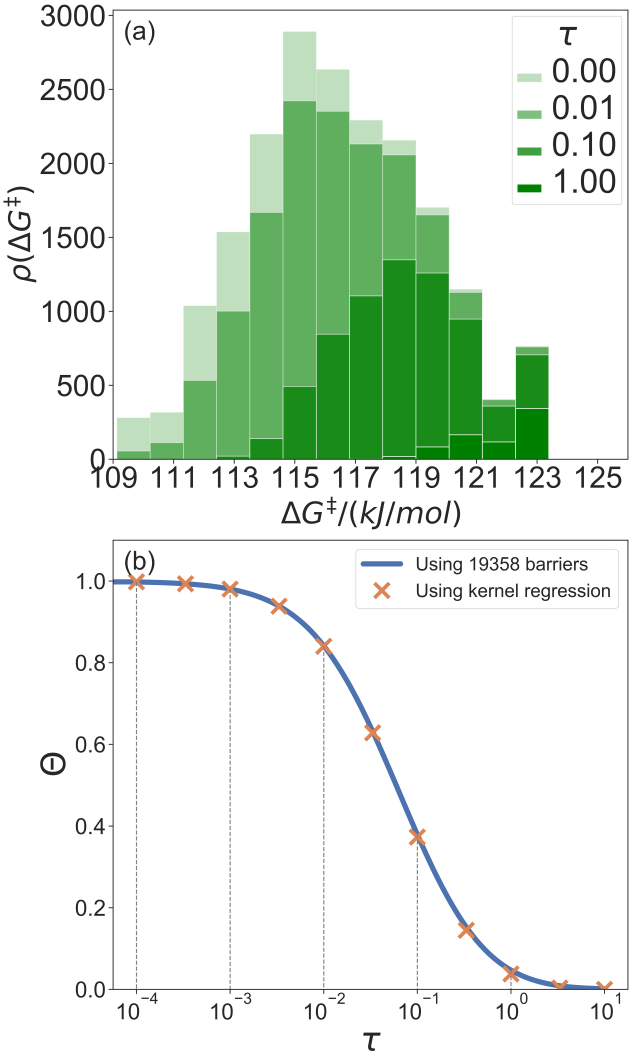

Figure 3.10: (a) Evolving population of grafting sites predicted using a kernel regression model trained on 100 grafting sites. (b) The predicted fraction of unreacted grafting sites as a function of logarithmic time.

The training set of 100 grafting sites does not include examples of grafting sites at the extreme fast and slow grafting limits. Accordingly, the trained model does not accurately predict grafting kinetics at the extreme fast and slow limits. Fortunately, the extreme tails account for only a small portion of the total grafting sites, so important properties like the overall grafting progress are still accurately predicted by the model, Figure 3.10b.

3.7 Conclusions

Several factors make *ab initio* rate calculations prohibitively difficult for single-atom catalysts grafted to amorphous supports such as silica. First, the quenched disorder of the support presents an unknown distribution of local environments. Second, grafted site abundances depend on differences in grafting kinetics at different grafting sites. Third, differences between the grafted sites can cause differences in their catalytic activity. Several investigators are working to overcome the first challenge.[71–74] This paper addresses the second challenge by combining transition state theory, kernel regression, and population balance models. Chapter 4 addresses the third challenge.

To illustrate and test the new methodology, we introduce a simple 2D disordered lattice model of amorphous silica. The model allows us to compute the grafting rate at nearly 20 thousand grafting sites to obtain essentially exact solutions for the evolving grafting/grafted site population during grafting. Then, we trained a kernel regression model to predict grafting rates from a training set of rate calculations at just 100 grafting sites. The regression model predicted barriers with ca. ± 0.5 kJ mol^{-1} accuracy on the test set of about 20 thousand grafting sites. We also showed how the kernel regression results can identify those grafting site characteristics that most strongly influence the grafting kinetics. Finally, the trained kernel regression model was used to predict the

evolving population of unreacted silanols.

In future work, we will use this framework with *ab initio* calculations and more realistic silica models to predict grafting rates and active site abundances during the preparation of real single-site catalysts on amorphous silica. Given a model of amorphous silica, the new algorithm should enable quantitative predictions about the grafting process and the grafted site distribution without assuming the characteristics of the most active or most abundant sites.

Bibliography

1. Morokuma, K. & Musaev, D. G. *Computational Modeling for Homogeneous and Enzymatic Catalysis: A Knowledge-Base for Designing Efficient Catalysis* (John Wiley & Sons, 2008).

2. Sperger, T., Sanhueza, I. A., Kalvet, I. & Schoenebeck, F. Computational Studies of Synthetically Relevant Homogeneous Organometallic Catalysis Involving Ni, Pd, Ir, and Rh: An Overview of Commonly Employed DFT Methods and Mechanistic Insights. *Chem. Rev.* **115,** 9532–9586. https://www.doi.org/10.1021/acs.chemrev.5b00163 (2015).

3. Goldsmith, B. R., Hwang, T., Seritan, S., Peters, B. & Scott, S. L. Rate-Enhancing Roles of Water Molecules in Methyltrioxorhenium-Catalyzed Olefin Epoxidation by Hydrogen Peroxide. *J. Am. Chem. Soc.* **137,** 9604–9616. https://www.doi.org/10.1021/jacs.5b03750 (2015).

4. Voth, G. *Computational approaches for studying enzyme mechanism* (Academic Press, 2016).

5. Garcia-Viloca, M., Gao, J., Karplus, M. & Truhlar, D. G. How Enzymes Work: Analysis by Modern Rate Theory and Computer Simulations. *Science* **303,** 186. https://www.doi.org/10.1126/science.1088172 (2004).

6. Tuñón, I. & Moliner, V. *Simulating enzyme reactivity: computational methods in enzyme catalysis* (Royal Society of Chemistry, 2016).

7. Hammer, B. & Nørskov, J. K. in, 71–129 (Academic Press, 2000). https://www.doi.org/10.1016/S0360-0564(02)45013-4.

8. Getman, R. B., Schneider, W. F., Smeltz, A. D., Delgass, W. N. & Ribeiro, F. H. Oxygen-Coverage Effects on Molecular Dissociations at a Pt Metal Surface. *Phys. Rev. Lett.* **102,** 076101. https://www.doi.org/10.1103/PhysRevLett.102.076101 (2009).

9. Greeley, J. Theoretical Heterogeneous Catalysis: Scaling Relationships and Computational Catalyst Design. *Annu Rev Chem Biomol* **7,** 605–635. https://www.doi.org/10.1146/annurev-chembioeng-080615-034413 (2016).

10. Saleheen, M. & Heyden, A. Liquid-Phase Modeling in Heterogeneous Catalysis. *ACS Catal.* **8,** 2188–2194. https://www.doi.org/10.1021/acscatal.7b04367 (2018).

11. Salciccioli, M., Stamatakis, M., Caratzoulas, S. & Vlachos, D. G. A review of multiscale modeling of metal-catalyzed reactions: Mechanism development for complexity and emergent behavior. *Chem. Eng. Sci.* **66,** 4319–4355. https://www.doi.org/10.1016/j.ces.2011.05.050 (2011).

12. Blaszkowski, S. R. & van Santen, R. A. Theoretical study of the mechanism of surface methoxy and dimethyl ether formation from methanol catalyzed by zeolitic protons. *J. Chem. Phys. B* **101,** 2292–2305 (1997).

13. Li, Y.-P., Head-Gordon, M. & Bell, A. T. Analysis of the Reaction Mechanism and Catalytic Activity of Metal-Substituted Beta Zeolite for the Isomerization of Glucose to Fructose. *ACS Catal.* **4,** 1537–1545. https://www.doi.org/10.1021/cs401054f (2014).

14. Newsome, D. & Coppens, M.-O. Molecular dynamics as a tool to study heterogeneity in zeolites - Effect of Na+ cations on diffusion of CO_2 and N_2 in Na-ZSM-5. *Chemical Engineering Science* **121,** 300–312. https://www.doi.org/10.1016/j.ces.2014.09.024 (2015).

15. McFarland, E. W. & Metiu, H. Catalysis by Doped Oxides. *Chem. Rev.* **113,** 4391–4427. https://www.doi.org/10.1021/cr300418s (2013).

16. Le Bahers, T., Rérat, M. & Sautet, P. Semiconductors Used in Photovoltaic and Photocatalytic Devices: Assessing Fundamental Properties from DFT. *J. Chem. Phys. C* **118,** 5997–6008. https://www.doi.org/10.1021/jp409724c (2014).

17. Li, F., Luo, S., Sun, Z., Bao, X. & Fan, L.-S. Role of metal oxide support in redox reactions of iron oxide for chemical looping applications: experiments and density functional theory calculations. *Energy Environ. Sci.* **4,** 3661–3667. https://www.doi.org/10.1039/C1EE01325D (2011).

18. Knott, B. C. *et al.* The Mechanism of Cellulose Hydrolysis by a Two-Step, Retaining Cellobiohydrolase Elucidated by Structural and Transition Path Sampling Studies. *J. Am. Chem. Soc.* **136,** 321–329. https://www.doi.org/10.1021/ja410291u (2014).

19. Masgrau, L. & Truhlar, D. G. The Importance of Ensemble Averaging in Enzyme Kinetics. *Acc. Chem. Res.* **48,** 431–438. https://www.doi.org/10.1021/ar500319e (2015).

20. Brunk, E., Arey, J. S. & Rothlisberger, U. Role of Environment for Catalysis of the DNA Repair Enzyme MutY. *J. Am. Chem. Soc.* **134,** 8608–8616. https://www.doi.org/10.1021/ja301714j (2012).

21. Peters, B. & Scott, S. L. Single Atom Catalysts on Amorphous Supports: A Quenched Disorder Perspective. *J. Chem. Phys.* **142,** 104708. https://www.doi.org/10.1063/1.4914145 (2015).

22. Goldsmith, B. R., Sanderson, E. D., Bean, D. & Peters, B. Isolated Catalyst Sites on Amorphous Supports: A Systematic Algorithm for Understanding Heterogeneities in Structure and Reactivity. *J. Chem. Phys.* **138,** 204105. https://www.doi.org/10.1063/1.4807384 (2013).

23. McDaniel, M. P. A Review of the Phillips Supported Chromium Catalyst and Its Commercial Use for Ethylene Polymerization. English. *Adv. Catal.* **53,** 123–606. https://www.doi.org/https://doi.org/10.1016/S0360-0564(10)53003-7 (2010).

24. Coperet, C. *et al.* Surface Organometallic and Coordination Chemistry toward Single-Site Heterogeneous Catalysts: Strategies, Methods, Structures, and Activities. *Chem. Rev.* **116,** 323–421. https://www.doi.org/10.1021/acs.chemrev.5b00373 (2016).

25. Buijink, J. K. F., van Vlaanderen, J. J. M., Crocker, M. & Niele, F. G. M. Propylene epoxidation over titanium-on-silica catalyst–the heart of the SMPO process. *Catal. Today* **93-95,** 199–204. https://www.doi.org/10.1016/j.cattod.2004.06.041 (2004).

26. Delley, M. F. *et al.* Proton Transfers Are Key Elementary Steps in Ethylene Polymerization on Isolated Chromium(III) Silicates. *Proc. Natl. Acad. Sci.* **111,** 11624–11629. https://www.doi.org/10.1073/pnas.1405314111 (2014).

27. Floryan, L., Borosy, A. P., Nunez-Zarur, F., Comas-Vives, A. & Coperet, C. Strain Effect and Dual Initiation Pathway in Cr(III)/SiO_2 Polymerization Catalysts from

Amorphous Periodic Models. English. *J. Catal.* **346,** 50–56. https://www.doi.org/10.1016/j.jcat.2016.11.037 (2017).

28. Espelid, Ø. & Børve, K. J. Molecular-Level Insight into Cr/Silica Phillips-Type Catalysts: Polymerization-Active Dinuclear Chromium Sites. *J. Catal.* **206,** 331–338. https://www.doi.org/10.1006/jcat.2001.3499 (2002).

29. Fong, A., Vandervelden, C., Scott, S. L. & Peters, B. Computational Support for Phillips Catalyst Initiation via Cr-C Bond Homolysis in a Chromacyclopentane Site. *ACS Catal.* **8,** 1728–1733. https://doi.org/10.1021/acscatal.7b03724 (2018).

30. Fong, A., Yuan, Y., Ivry, S. L., Scott, S. L. & Peters, B. Computational Kinetic Discrimination of Ethylene Polymerization Mechanisms for the Phillips (Cr/SiO_2) Catalyst. English. *ACS Catal.* **5,** 3360–3374. https://www.doi.org/10.1021/acscatal.5b00016 (2015).

31. Gierada, M. & Handzlik, J. Computational insights into reduction of the Phillips CrOx/SiO2 catalyst by ethylene and CO. *J. Catal.* **359,** 261–271. https://www.doi.org/10.1016/j.jcat.2018.01.014 (2018).

32. Guesmi, H. & Tielens, F. Chromium oxide species supported on silica: A representative periodic DFT model. *J. Phys. Chem. C* **116,** 994–1001. https://doi.org/10.1021/jp209680r (2012).

33. Ewing, C. S. *et al.* Impact of Support Interactions for Single-Atom Molybdenum Catalysts on Amorphous Silica. *Ind. Eng. Chem. Res.* **55,** 12350–12357. https://www.doi.org/10.1021/acs.iecr.6b03558 (2016).

34. Jystad, A. M., Biancardi, A. & Caricato, M. Simulations of Ammonia Adsorption for the Characterization of Acid Sites in Metal-Doped Amorphous Silicates. *J. Phys.*

Chem. C **121,** 22258–22267. https://www.doi.org/10.1021/acs.jpcc.7b08113 (2017).

35. Vansant, E. E., Van Der Voort, P. & Vrancken, K. C. *Characterization and Chemical Modification of the Silica Surface* (1995).

36. Brinker, C. J. & Scherer, G. W. *Sol-gel science: the physics and chemistry of sol-gel processing* (Academic press, 1990).

37. Bergna, H. E. & Roberts, W. O. *Colloidal silica: fundamentals and applications* (CRC Press, 2005).

38. Brückner, R. Properties and structure of vitreous silica. I. *J. Non-Cryst. Solids* **5,** 123–175. https://www.doi.org/10.1016/0022-3093(70)90190-0 (1970).

39. Brückner, R. Properties and structure of vitreous silica. II. *J. Non-Cryst. Solids* **5,** 177–216. https://www.doi.org/10.1016/0022-3093(71)90032-9 (1971).

40. Flörke, O. W. *et al. Silica* ISBN: 9783527306732. https://doi.org/10.1002/14356007 (John Wiley & Sons, 2000).

41. Atiqullah, M. *et al.* Influence of silica calcination temperature on the performance of supported catalyst SiO_2–nBuSn$Cl_{3/}$MAO/$(nBuCp)_2ZrCl_2$ polymerizing ethylene without separately feeding the MAO cocatalyst. *Appl. Catal., A* **320,** 134–143. https://www.doi.org/10.1016/j.apcata.2007.01.023 (2007).

42. Oschatz, M. *et al.* Effects of calcination and activation conditions on ordered mesoporous carbon supported iron catalysts for production of lower olefins from synthesis gas. *Catal Sci Technol* **6,** 8464–8473. https://www.doi.org/10.1039/C6CY01251E (2016).

43. Rimola, A., Costa, D., Sodupe, M., Lambert, J.-F. & Ugliengo, P. Silica Surface Features and Their Role in the Adsorption of Biomolecules: Computational Modeling and Experiments. *Chem. Rev.* **113,** 4216–4313. https://www.doi.org/10.1021/cr3003054 (2013).

44. Zhuravlev, L. T. The surface chemistry of amorphous silica. Zhuravlev model. *Colloids Surf., A* **173,** 1–38. https://www.doi.org/10.1016/S0927-7757(00)00556-2 (2000).

45. Sharma, S. K., Mammone, J. F. & Nicol, M. F. Raman investigation of ring configurations in vitreous silica. *Nature* **292,** 140–141. https://www.doi.org/10.1038/292140a0 (1981).

46. Brinker, C. J., Brow, R. K., Tallant, D. R. & Kirkpatrick, R. J. Surface structure and chemistry of high surface area silica gels. *J. Non-Cryst. Solids* **120,** 26–33. https://www.doi.org/10.1016/0022-3093(90)90187-Q (1990).

47. Humbert, B., Burneau, A., Gallas, J. P. & Lavalley, J. C. Origin of the Raman bands, D1 and D2, in high surface area and vitreous silicas. *J. Non-Cryst. Solids* **143,** 75–83. https://www.doi.org/10.1016/S0022-3093(05)80555-1 (1992).

48. Peri, J. B. & Hensley, A. L. The surface structure of silica gel. *J. Chem. Phys.* **72,** 2926–2933. https://www.doi.org/10.1021/j100854a041 (1968).

49. Taha, Z. A., Deguns, E. W., Chattopadhyay, S. & Scott, S. L. Formation of Digallium Sites in the Reaction of Trimethylgallium with Silica. *Organometallics* **25,** 1891–1899. https://www.doi.org/10.1021/om051034o (2006).

50. Fleischman, S. D. & Scott, S. L. Evidence for the Pairwise Disposition of Grafting Sites on Highly Dehydroxylated Silicas via Their Reactions with $Ga(CH_3)_3$. *J. Am. Chem. Soc.* **133,** 4847–4855. https://www.doi.org/10.1021/ja108905p (2011).

51. Abdillah, B., Rice, G. L. & Scott, S. L. Mono- and Dinuclear Silica-Supported Titanium(IV) Complexes and the Effect of TiOTi Connectivity on Reactivity. *J. Am. Chem. Soc.* **121,** 7201–7210. https://www.doi.org/10.1021/JA9829160 (1999).

52. Gao, X., Bare, S. R., Fierro, J. L. G., Banares, M. A. & Wachs, I. E. Preparation and in-Situ Spectroscopic Characterization of Molecularly Dispersed Titanium Oxide on Silica. *J. Chem. Phys. B* **102,** 5653–5666. https://www.doi.org/10.1021/jp981423e (1998).

53. Kytökivi, A. & Haukka, S. Reactions of HMDS, $TiCl_4$, $ZrCl_4$, and $AlCl_3$ with Silica As Interpreted from Low-Frequency Diffuse Reflectance Infrared Spectra. *J. Chem. Phys. B* **101,** 10365–10372. https://www.doi.org/10.1021/jp971822u (1997).

54. Deguns, E. W., Taha, Z., Meitzner, G. D. & Scott, S. L. An X-ray Absorption Study of Two VOCl3-Modified Silicas: Evidence for Chloride-Silica Interactions. *J. Chem. Phys. B* **109,** 5005–5011. https://www.doi.org/10.1021/jp045886y (2005).

55. Zhu, H. *et al.* VOx/SiO2 Catalyst Prepared by Grafting VOCl3 on Silica for Oxidative Dehydrogenation of Propane. *ChemCatChem* **7,** 3332–3339. https://www.doi.org/10.1002/cctc.201500607 (2015).

56. Jarupatrakorn, J. & Tilley, T. D. Silica-Supported, Single-Site Titanium Catalysts for Olefin Epoxidation. A Molecular Precursor Strategy for Control of Catalyst Structure. *J. Am. Chem. Soc.* **124,** 8380–8388. https://www.doi.org/10.1021/ja0202208 (2002).

57. Fraile, J. M., García, J. I., Mayoral, J. A. & Vispe, E. Catalytic sites in silica-supported titanium catalysts: silsesquioxane complexes as models. *J. Catal.* **233,** 90–99. https://www.doi.org/10.1016/j.jcat.2005.04.018 (2005).

58. Zhong, L. *et al.* Spectroscopic and structural characterization of Cr(II)/SiO_2 active site precursors in model Phillips polymerization catalysts. *J. Catal.* **293,** 1–12. https://www.doi.org/10.1016/j.jcat.2012.05.014 (2012).

59. Fukudome, K., Ikenaga, N.-o., Miyake, T. & Suzuki, T. Oxidative dehydrogenation of propane using lattice oxygen of vanadium oxides on silica. *Catal Sci Technol* **1,** 987–998. https://www.doi.org/10.1039/C1CY00115A (2011).

60. Samantaray, M. K. *et al.* Surface organometallic chemistry in heterogeneous catalysis. *Chem. Soc. Rev.* **47,** 8403–8437. https://www.doi.org/10.1039/C8CS00356D (2018).

61. Handzlik, J., Grybos, R. & Tielens, F. Structure of Monomeric Chromium(VI) Oxide Species Supported on Silica: Periodic and Cluster DFT Studies. *J. Chem. Phys. C* **117,** 8138–8149. https://www.doi.org/10.1021/jp3103035 (2013).

62. Cavalleri, M. *et al.* Analysis of silica-supported vanadia by X-ray absorption spectroscopy: Combined theoretical and experimental studies. *J. Catal.* **262,** 215–223. https://www.doi.org/10.1016/j.jcat.2008.12.013 (2009).

63. Khaliullin, R. Z. & Bell, A. T. A Density Functional Theory Study of the Oxidation of Methanol to Formaldehyde over Vanadia Supported on Silica, Titania, and Zirconia. *J. Chem. Phys. B* **106,** 7832–7838. https://www.doi.org/10.1021/jp014695h (2002).

64. Wang, T.-H. *et al.* The surprising oxidation state of fumed silica and the nature of water binding to silicon oxides and hydroxides. *Chem. Phys. Lett.* **501,** 159–165. https://www.doi.org/10.1016/j.cplett.2010.11.013 (2011).

65. Jaegers, N. R. *et al.* Investigation of Silica-Supported Vanadium Oxide Catalysts by High-Field 51V Magic-Angle Spinning NMR. *J. Chem. Phys. C* **121,** 6246–6254. https://www.doi.org/10.1021/acs.jpcc.7b01658 (2017).

66. Handzlik, J. Properties and metathesis activity of monomeric and dimeric Mo centres variously located on γ-alumina - A DFT study. *Surf. Sci.* **601,** 2054–2065. https://www.doi.org/10.1016/J.SUSC.2007.03.002 (2007).

67. Chung, L. W. *et al.* The ONIOM Method and Its Applications. *Chem. Rev.* **115,** 5678–5796. https://www.doi.org/10.1021/cr5004419 (2015).

68. Goumans, T. P. M., Catlow, C. R. A. & Brown, W. A. Hydrogenation of CO on a silica surface: An embedded cluster approach. *J. Chem. Phys.* **128,** 134709. https://www.doi.org/10.1063/1.2888933 (2008).

69. Handzlik, J. & Ogonowski, J. Structure of Isolated Molybdenum(VI) and Molybdenum(IV) Oxide Species on Silica: Periodic and Cluster DFT Studies. *J. Chem. Phys. C* **116,** 5571–5584. https://www.doi.org/10.1021/jp207385h (2012).

70. Gomes, J., Zimmerman, P. M., Head-Gordon, M. & Bell, A. T. Accurate Prediction of Hydrocarbon Interactions with Zeolites Utilizing Improved Exchange-Correlation Functionals and QM/MM Methods: Benchmark Calculations of Adsorption Enthalpies and Application to Ethene Methylation by Methanol. *J. Chem. Phys. C* **116,** 15406–15414. https://www.doi.org/10.1021/jp303321s (2012).

71. Ewing, C. S., Bhavsar, S., Veser, G., McCarthy, J. J. & Johnson, J. K. Accurate amorphous silica surface models from first-principles thermodynamics of surface dehydroxylation. *Langmuir* **30,** 5133–5141. https://doi.org/10.1021/la500422p (2014).

72. Ugliengo, P. *et al.* Realistic models of hydroxylated amorphous silica surfaces and MCM- 41 mesoporous material simulated by large-scale periodic B3LYP calculations. *Adv. Mater.* **20,** 4579–4583. https://www.doi.org/10.1002/adma.200801489 (2008).

73. Comas-Vives, A. Amorphous SiO_2 surface models: Energetics of the dehydroxylation process, strain, ab initio atomistic thermodynamics and IR spectroscopic signatures. *Phys. Chem. Chem. Phys.* **18,** 7475–7482. https://www.doi.org/10.1039/c6cp00602g (2016).

74. Tielens, F., Gervais, C., Lambert, J. F., Mauri, F. & Costa, D. Ab initio study of the hydroxylated surface of amorphous silica: A representative model. *Chem. Mater.* **20,** 3336–3344. https://www.doi.org/10.1021/cm8001173 (2008).

75. Peters, B., Scott, S. L., Fong, A., Wang, Y. & Stiegman, A. E. Reexamining the Evidence for Proton Transfers in Ethylene Polymerization. *Proc. Natl. Acad. Sci. USA* **112,** E4160–E4161. https://www.doi.org/10.1073/pnas.1422589112 (2015).

76. Peek, N. M. *et al.* Reassessment of the Electronic Structure of Cr(VI) Sites Supported on Amorphous Silica and Implications for Cr Coordination Number. *J. Chem. Phys. C* **122,** 4349–4358. https://www.doi.org/10.1021/acs.jpcc.7b12079 (2018).

77. Lwin, S., Li, Y., Frenkel, A. I. & Wachs, I. E. Nature of WOx Sites on SiO2 and Their Molecular Structure-Reactivity/Selectivity Relationships for Propylene Metathesis. *ACS Catal.* **6,** 3061–3071. https://www.doi.org/10.1021/acscatal.6b00389 (2016).

78. Peters, B. *Reaction Rate Theory and Rare Events* **20178817,** xiv, 619 pages (Elsevier, Amsterdam ; Cambrige, MA, 2017).

79. Nørskov, J. K., Studt, F., Abild-Pedersen, F. & Bligaard, T. *Fundamental Concepts in Heterogeneous Catalysis* https://books.google.com/books?id=BiZeBAAAQBAJ (Wiley, 2014).

80. Peters, B. Common Features of Extraordinary Rate Theories. *J. Chem. Phys. B* **119,** 6349–6356. https://www.doi.org/10.1021/acs.jpcb.5b02547 (2015).

81. Chorkendorff, I. & Niemantsverdriet, J. W. *Concepts of modern catalysis and kinetics* (John Wiley & Sons, 2017).

82. Boudart, M. & Djega-Mariadassou, G. *Kinetics of Heterogeneous Catalytic Reactions* https://books.google.com/books?id=iqf_AwAAQBAJ (Princeton University Press, Princeton, 2014).

83. Van Santen, R. A. & Neurock, M. *Molecular Heterogeneous Catalysis* https://www.doi.org/10.1002/9783527610846.ch2 (Wiley-VCH, Weinheim, Germany, 2007).

84. Jensen, F. *Introduction to Computational Chemistry* 624 (2007).

85. Leffler, J. E. Parameters for the Description of Transition States. *Science* **117,** 340–341. https://www.doi.org/10.1126/science.117.3039.340 (1953).

86. Mahalanobis, P. C. On the generalized distance in statistics. *Proc. Natl. Inst. Sci. India* **2,** 49–55. https://doi.org/10.1007/s13171-019-00164-5 (1936).

87. Hofmann, T., Schölkopf, B. & Smola, A. J. Kernel methods in machine learning. *Ann. Stat.* **36,** 1171–1220. https://www.doi.org/10.1214/009053607000000677 (2008).

88. Mohri, M., Rostamizadeh, A. & Talwalkar, A. *Foundations of machine learning* (MIT press, 2018).

89. Weinberger, K. Q. & Tesauro, G. Metric Learning for Kernel Regression. *J. Mach. Learn. Res.*, 8. http://proceedings.mlr.press/v2/weinberger07a.html (2007).

90. Strang, G. & Strang, S. *Linear Algebra and Its Applications* https://books.google.com/books?id=8QVdcRJyL2oC (Thomson, Brooks/Cole, 2006).

91. Nocedal, J. & Wright, S. *Numerical optimization* (Springer Science & Business Media, 2006).

92. Carey, C. J. & Tang, Y. *metric-learn.* https://metric-learn.github.io/metric-learn/ (2015).

Chapter 4

Site-averaged kinetics for catalysts on amorphous supports: An importance learning algorithm

Reproduced in part with permission from:

. Vandervelden, C. A., Khan, S. A., Scott, S. L. & Peters, B. Site-averaged kinetics for catalysts on amorphous supports: An importance learning algorithm. *React. Chem. Eng.* **5,** 77–86. https://doi.org/10.1039/c9re00356h (2020).

4.1 Introduction

A recent surge of interest in atomically-dispersed "single atom" catalysts is driven by their unique and potentially selective reactivity,[1–3] and by sustainability efforts that seek to minimize use of scarce elements and maximize atom economy.[4–6] Among single atom catalysts, those which are chemically bonded to a thermally robust oxide support like silica are especially resistant to deactivation by sintering.[7,8] Moreover, grafting strategies

that promote selective reaction of the catalyst precursor at specific surface sites may help to minimize differences between grafted metal sites. Well-studied catalysts that are comprised of single metal atoms grafted onto amorphous silica include chromocenes or chromates for olefin polymerization,[9–11] titanium and tantalum complexes for olefin epoxidation,[12] molybdates for methanol dehydration,[13] and vanadates for partial oxidation of methanol.[14]

Investigators have occasionally drawn comparisons between the metal atoms present in the active sites in enzymes, and metal atoms grafted onto silica surfaces.[12] There are similarities, but there are also important differences. Each enzyme molecule of a given type is the same, while each metal atom on amorphous silica resides in a unique ligand environment. These non-uniform environments can result in metal atoms with non-uniform catalytic properties, including a range of activities, selectivities, adsorption constants, and even different spectroscopic features. When the sites have variable activities, a minority of the sites may contribute most of the overall catalyst activity. Indeed, active site counting experiments confirm that only a small fraction of sites in a heterogeneous catalyst is typically active.[15–18] This poses an extraordinary difficulty in experimental as well as theoretical studies of these catalysts. Powerful characterization tools (NMR, EXAFS, IR, Raman, etc.) generally provide the strongest signals for the most common sites, and these are likely inactive.[11]

If we could understand the mechanisms of these catalysts, we might systematically work to improve them.[19] In some applications like olefin polymerization, where the catalysts are not recovered from the polymer product, one might even use mechanistic understanding to design catalysts with a desired activity distribution capable of generating polymer with a desired molecular weight distribution.

Chapter 3 introduced a method to predict the distribution of sites that emerges from grafting a precursor onto an amorphous support. The simple model system consisted of

a quenched-disordered lattice (to represent the amorphous silica support), surface functional groups (representing pairs or nests of hydroxyl groups) to which a metal complex can be grafted, and a microkinetic model for each grafted site with rate parameters that depend on the site characteristics. Much like in an *ab initio* study, computing activation barriers for the model system requires geometry optimizations of intermediates. Our realistic but simple model allowed us to focus on developing the importance sampling and machine learning tools, without being distracted by controversies about the mechanisms about the mechanisms of these catalysts.

Starting from the simple model and the grafted site population described in Chapter 3, this chapter aims to compute an average over sites to predict the overall kinetics. Since the turnover frequencies at individual sites vary exponentially with the activation energy, even a small variance in the activation energy leads to an enormous variance in site-specific activities. Such exponential averages are notoriously difficult to converge with standard sampling tools,[20–22] but importance sampling methods can dramatically accelerate convergence. The ideal importance sampling algorithm[23] requires activation energies for each site, but these activation energies are not known a priori. Each activation energy must be obtained through costly ab initio calculations. Because of this limitation, typical approaches calculate just one[24,25] or a small handful of sites[26–33] – far too few to converge site-averaged predictions of kinetic properties.[34] Kernel regression tools can use a modest set of *ab initio* calculations to predict activation energies that have not actually been computed. This chapter shows how importance sampling and machine learning can be combined to generate site-averaged predictions efficiently.

In the remainder of this chapter, we discuss model elementary steps and a rate law for a catalytic reaction with our simple model system. We briefly review the kernel regression tools (from Chapter 3) that predict activation energies. We combine the importance sampling and kernel regression tools into an "importance learning algorithm". We then

use the new algorithm to identify characteristics of highly active sites and to estimate site-averaged activation energies. Finally, we compare the efficiency of importance sampling estimates to straightforward sampling.

4.2 Model for amorphous support and grafted sites

Chapter 3 described the creation of a disordered, functionalized lattice model to approximate the non-uniform silanol sites and siloxane environments on the surface of amorphous SiO_2. That chapter also considered a kinetic model for grafting of metal atoms onto the silanol sites. All sites with two silanol neighbors and two siloxane neighbors on opposite sides were eligible grafting sites in the model. A schematic of the simple model is shown in Fig. 4.1.

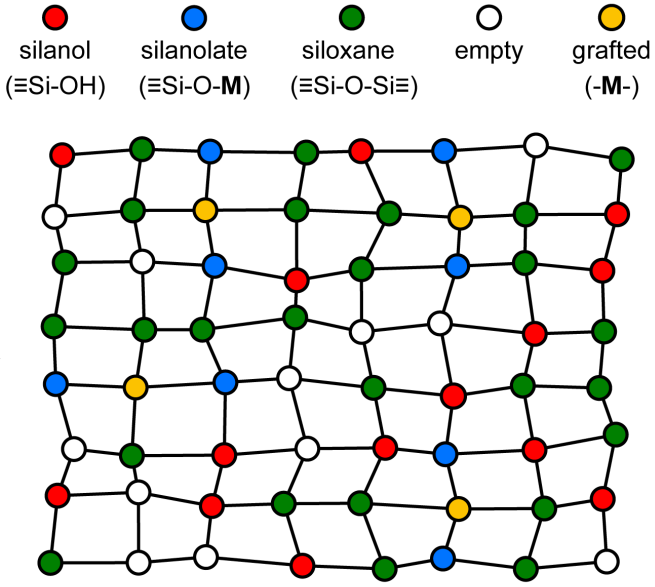

Figure 4.1: Quenched disorder lattice model. Sites with a grafted metal center are shown in gold.

This chapter uses the distribution of non-uniform grafted sites, like those shown in Fig. 4.1, as its starting point. We assume that grafting has occurred at all eligible

sites, but one could modify the starting distribution (using methods in Chapter 3) to investigate lower catalyst loadings.

The discussion below invokes bonds between metal atoms and adsorbates, as well as the oxygen atoms of the silanol and siloxane sites. However, the local environment of each site (before grafting and during catalysis) is described entirely by the positions of atoms in the silica support surrounding the metal center. The coordinates used to describe the local environment are shown in Fig. 4.2 They are: (i) the distance between siloxane groups, d_1, (ii) the distance between silanolate groups, d_2, and (iii) the angle between the silanolate and siloxane groups, θ.

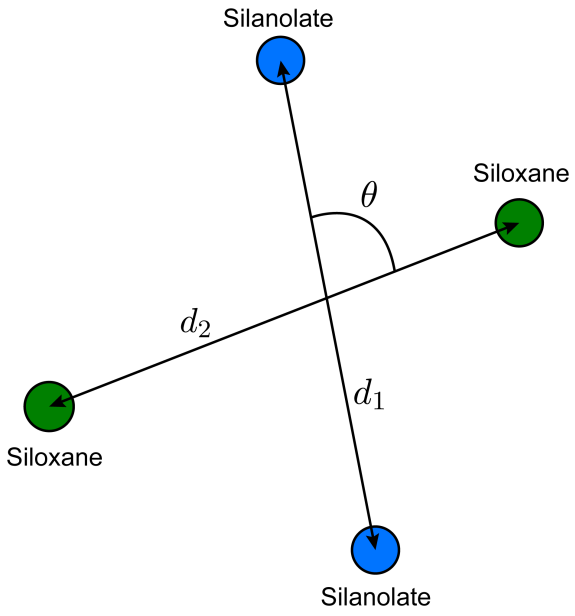

Figure 4.2: Coordinates used to describe the local environment of a grafting site.

The selected coordinates are nearly orthogonal in the sense that their gradients have little or no overlap. Note, however, that the coordinates are incomplete. For a grafting site on our two dimensional surface model, the four nearest neighbors are fully described by five internal coordinates ($8 - 2 \times$ (center of mass) $- 1 \times$ (rotation)). We use only three

coordinates in the kernel regression model, and the results below will show that just two of these coordinates are sufficient to predict site-averaged kinetics. We also emphasize that some calculations below involve other coordinates at intermediate stages, but that the overall kinetics and the kinetics of individual sites ultimately depends only on the coordinates in Fig. 4.2.

4.3 Model for catalysis at grafted sites

We consider a simple model of a catalyst site, $\mathbf{M}^*$, comprised of a metal center M and its surrounding support environment, *. We will consider the case in which the catalytic reaction at each site has the same rate-limiting step and the same most abundant surface intermediate (MASI). We further assume that the site does not deactivate. The model reaction has a simple Langmuir-Hinshelwood mechanism:

$$\mathbf{A} + \mathbf{M}^* \rightleftharpoons \mathbf{AM}^* \quad K(\mathbf{x})$$
$$\mathbf{AM}^* \rightarrow \mathbf{B} + \mathbf{M}^* \quad k_2$$

We further assume that

1. the equilibrium constant K for adsorption of reactant A depends on the local environment of site i, $\mathbf{x}_i$,

2. the adsorbed molecule $\mathbf{A}$ ($\mathbf{AM}^*$) is irreversibly converted into the gas phase product B and a bare site $\mathbf{M}^*$,

3. $K(\mathbf{x})c_{\mathbf{A}} \ll 1$ for all sites, so that the bare site is the MASI.

The bond strengths chosen in this work, described below, ensure that these three

assumptions are true for all sites. Fig. 4.3 depicts the Langmuir-Hinshelwood mechanism and the three simplifying assumptions for the simple model system in this work.

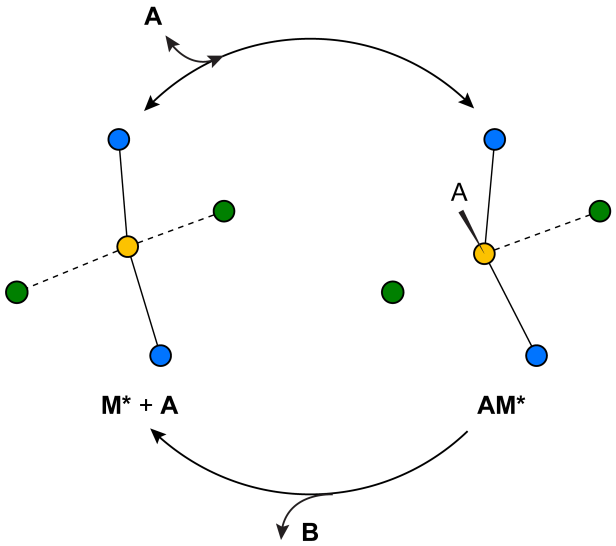

Figure 4.3: The equilibrated adsorption step and irreversible chemical reaction steps for the model reaction $\mathbf{A} \rightarrow \mathbf{B}$, and the $\mathbf{M}^*$ sites described in this work.

The Langmuir-Hinshelwood mechanism leads to a rate law of form

$$\dot{\imath} = \frac{k_2 K(\mathbf{x}) c_{\mathbf{A}}}{1 + K(\mathbf{x}) c_{\mathbf{A}}} \tag{4.1}$$

Because of assumption 3., the rate law simplifies to a power law rate expression of the form

$$\dot{\imath} = k(\mathbf{x}) c_{\mathbf{A}} \tag{4.2}$$

where the pseudo-first-order rate constant is:

$$k(\mathbf{x}) = k_2 K(\mathbf{x}) \tag{4.3}$$

Note that we have also assumed that the rate constant k_2 for the second step in the Langmuir-Hinshelwood mechanism is the same for all sites. In principal, k_2 could also

depend on $\mathbf{x}$, but a model for $k_2(\mathbf{x})$ would require additional parameters to create a model for the saddle region on the potential energy surface. The more elaborate model system with $\mathbf{x}$-dependence in k_2 would still lead to an apparent rate constant k_2K that is one function of $\mathbf{x}$.

The apparent rate constant $k(\mathbf{x})$ depends on the local site geometry through $K(\mathbf{x})$. The adsorption constant is

$$K(\mathbf{x}) = \exp\left[-\frac{\Delta H(\mathbf{x}) - T\Delta S}{k_B T}\right] \tag{4.4}$$

where $\Delta H(\mathbf{x})$ is a site-dependent adsorption enthalpy. $T\Delta S$ is assumed to be constant because its main contributions are the loss of translational and rotational freedom upon adsorption. The rate constant, according to transition state theory, will be of the form

$$k_2 = \frac{k_B T}{h} \exp\left[\frac{\Delta S^{\ddagger}}{k_B}\right] \exp\left[-\frac{\Delta H^{\ddagger}}{k_B T}\right] \tag{4.5}$$

Here, the entropy and enthalpy of activation for the reaction step are assumed to be the same for all sites.

The site-dependent enthalpy of adsorption, $\Delta H(\mathbf{x})$, is modeled by

$$\Delta H(\mathbf{x}) = V_{\mathbf{AM}*}(\mathbf{x}) - (V_{\mathbf{M}*}(\mathbf{x}) + \varepsilon_{\mathbf{A}} + k_B T) \tag{4.6}$$

where $\mathbf{x}$ is the position of $\mathbf{M}$, $V_{\mathbf{AM}^*}(\mathbf{x})$ is the energy with $\mathbf{A}$ chemisorbed to the metal site, $V_{\mathbf{M}^*}(\mathbf{x})$ is the energy of the bare metal site, $\varepsilon_{\mathbf{A}}$ is the gas phase energy of $\mathbf{A}$, and $k_B T$ is the PV contribution to the gas phase enthalpy of $\mathbf{A}$. The same Morse potentials that we used to model grafting (Chapter 3) are now used to describe the $\mathbf{M}-\mathrm{OSi}\equiv$ bond energies and $\mathbf{M}(\mathrm{OSi}\equiv)_2$ bond energies. Specifically, the individual interaction energies

are

$$\varepsilon_i(r) = D_i \left(1 - \exp\left[-a_i(r - r_{i,eq})^2\right]\right) - D_i \tag{4.7}$$

where i is the bond type, D_i is the bond dissociation energy, a_i is inversely related to the vibrational well width, r is the bond length, and $r_{eq,i}$ is its equilibrium bond length. The energy of the bare metal site is

$$V_{\mathbf{M}*}(\mathbf{x}) = \varepsilon_{\mathbf{M}-O}(r_1) + \varepsilon_{\mathbf{M}-O}(r_2) + \varepsilon_{\mathbf{M}\cdots O}(r'_1) + \varepsilon_{\mathbf{M}\cdots O}(r'_2) \tag{4.8}$$

where $\varepsilon_{\mathbf{M}-\mathrm{O}}(r_i)$ is the energy of the $\mathbf{M} - \mathrm{OSi} \equiv$ bonds, r_i is the metal-oxygen bond distance, $\varepsilon_{\mathbf{M}\cdots\mathrm{O}}(r'_i)$ is the energy of the $\mathbf{M}\cdots(\mathrm{OSi} \equiv)_2$ metal-siloxane bond, and r'_i is the metal-siloxane bond distance.

We model adsorption of **A** onto the grafted metal center as an **M-A** bond with energy $\varepsilon_{\mathbf{M}-\mathbf{A}}$. The length of the M-A bond is not explicitly optimized. Instead, we assume that the **M- A** bond displaces the longest and most weakly-coordinated siloxane ($\mathbf{M}\cdots(\mathrm{OSi} \equiv)_2$) from **M**. The displaced siloxane can still exert a repulsive interaction on **M**. We model the close-range repulsion with a Weeks-Chandler-Andersen potential:[35]

$$\varepsilon^{WCA}_{\mathbf{AM}\cdots\mathbf{O}}(r) = D_{\mathbf{AM}\cdots\mathbf{O}} \left(1 - \exp\left[-a_{\mathbf{AM}\cdots\mathbf{O}}(r - r_{\mathbf{AM}\cdots\mathbf{O},eq})^2\right]\right) \tag{4.9}$$

for $r \leq r_{\mathbf{AM}\cdots\mathrm{O,eq}}$ and $\varepsilon^{WCA}_{\mathbf{AM}\cdots\mathbf{O}}(r) = 0$ otherwise. Thus, the energy of state $\mathbf{AM}^*$ is

$$V_{\mathbf{AM}*}(\mathbf{x}) = \varepsilon_{\mathbf{M}-\mathbf{A}} + \varepsilon_{\mathbf{M}-O}(r_1) + \varepsilon_{\mathbf{M}-O}(r_2) + \varepsilon_{\mathbf{M}\cdots O}(r'_1) + \varepsilon^{WCA}_{\mathbf{M}\cdots O}(r^*) \tag{4.10}$$

where r^* is the longest $\mathbf{M}\cdots\mathrm{O}$ bond prior to the adsorption of **A**.

With these definitions, eqn. 4.6 presents a geometry optimization problem much like that encountered in *ab initio* calculations. The interior atoms must be optimized

subject to constraints on peripheral atoms around the metal center. The equilibrium configurations of $\mathbf{M}^*$ and $\mathbf{AM}^*$ are found by changing the M atom position with fixed silanolate and siloxane group positions to minimize 4.8 and 4.10, respectively. This procedure creates a collection of model sites with quenched disorder and limited local flexibility, somewhat like a real amorphous catalyst.

4.3.1 Parameter selection

The quenched disordered lattice was created by starting with a square lattice with spacing 1. Random displacements of the lattice sites were drawn from an isotropic 2D Gaussian distribution with $\sigma^2_{\text{lattice}} = 0.00022$ in the x and y directions. We used the same fractions of silanol, siloxane, and empty sites ($f_{\text{silanol}} = 0.3$, $f_{\text{siloxane}} = 0.3$, and $f_{\text{empty}} = 0.4$) as Chapter 3. All rate calculations in this work were performed for a temperature of 300 K and a reactant pressure of 1 atm. The metal-adsorbate bond dissociation energy was modeled as the Cr-C bond dissociation energy for a ($\equiv$ SiO)$_2$Cr(III) alkyl site – the widely accepted active site for Cr/SiO$_2$ olefin polymerization catalysts.[11,36] Based on DFT calculations (Section S1) and reported values for the Cr-C bond,[37] we set $\varepsilon_{\mathbf{M-A}} =$ 160 kJ/mol. A list of the parameters and their values are summarized in Table 4.1.

Table 4.1: Parameter values for the quenched disorder lattice, Langmuir-Hinshelwood mechanism, and model chemistry

Parameter	Value
T	300K
$P_{\mathbf{A}}$	1 atm
$\Delta H^{\ddagger}$	65 kJ/mol
$\sigma^2_{\text{lattice}}$	0.00022
f_{Silanol}	0.3
f_{Siloxane}	0.3
f_{Empty}	0.4
$D_{\mathbf{M}\cdots\text{O}}$	120 kJ/mol
$a_{\mathbf{M}\cdots\text{O}}$	1.3
$\hat{r}_{\mathbf{M}\cdots\text{O,eq}}$	1.16
$D_{\mathbf{M-O}}$	500 kJ/mol
$a_{\mathbf{M-O}}$	1.7
$\hat{r}_{\mathbf{M-O,eq}}$	1.0
$\varepsilon_{\mathbf{A}}$	0 kJ/mol
$\varepsilon_{\mathbf{M-A}}$	160 kJ/mol

4.3.2 Site-averaged kinetics

Each metal site has a unique environment, and the different environments lead to a distribution of kinetic properties. For example, the sites will exhibit a distribution of turnover frequencies and activation energies. In contrast, a conventional experiment measures just one site-averaged value for each kinetic property. In this Chapter 3, we focus on the site-averaged activation energy. From eqns. 4.2 - 4.5, the activation energy for site i is

$$E_a(\mathbf{x}_i) = -\frac{d \ln \textit{r}_i}{d\beta} = \Delta H(\mathbf{x}_\mathrm{i}) + \Delta H^\ddagger + 2k_B T \tag{4.11}$$

where $\beta = 1/k_B T$. A derivation of eqn. 4.11 can be found in Section C.2 of Appendix C. In this calculation, we assume that E_a, ΔS, $\Delta S^\ddagger$, and $\Delta H^\ddagger$ are not functions of temperature.[38] For ΔH, the temperature dependence from $k_B T$ (eqn. 4.6) is considered, but other temperature-dependent terms such as partition functions are ignored. (In practice, all of these properties will probably exhibit some temperature dependence.)

Naively, one might estimate $E_a(\mathbf{x})$ for a large sample of sites and then average them to obtain the site-averaged activation energy. This straightforward average does not give the correct value, even in the limit of large sample sizes. The correct site-averaged activation energy,[39] $\langle E_a \rangle_k$ is obtained from a derivative of the site-averaged rate:

$$\begin{aligned}
\langle E_a \rangle_k &\equiv -\partial \ln \langle \textit{r} \rangle / \partial\beta \\
&= -\frac{\partial}{\partial\beta} \ln \int d\mathbf{x} \rho(\mathbf{x}) k(\mathbf{x}) \prod\nolimits_i c_i^{\alpha_i} \\
&= -\frac{\int d\mathbf{x} \rho(\mathbf{x}) \partial k(\mathbf{x})/\partial\beta}{\int d\mathbf{x} \rho(\mathbf{x}) k(\mathbf{x})} \\
&= \frac{\int d\mathbf{x} \rho(\mathbf{x}) k(\mathbf{x}) \{E_a(\mathbf{x}) + \beta E_a(\mathbf{x}) \partial \ln E_a(\mathbf{x})/\partial\beta\}}{\int d\mathbf{x} \rho(\mathbf{x}) k(\mathbf{x})} \\
&= \langle E_a \{1 + \beta \cdot \partial \ln E_a/\partial\beta\} \rangle_{\rho(\mathbf{x})k(\mathbf{x})}
\end{aligned} \tag{4.12}$$

In this work, we ignore the temperature dependence of E_a. In practice, the rates at individual sites cannot be probed, nor are the temperature intervals in which the rates are measured wide enough to see definitive curvature in the Arrhenius plot. We also expect the correction to be small. Using E_a from eqn. 4.11, $E_a\beta\partial \ln E_a/\partial\beta = 2\beta^{-1}$, which will be relatively small compared to a typical $E_a(\mathbf{x})$. Moreover, we anticipate that $E_a\beta\partial \ln E_a/\partial\beta$ term will be similar across different sites, so that conclusions about characteristics of highly active and abundant sites will be unaffected. Using eqns. 4.2 - 4.5, the derivatives and integrations yield:

$$\langle E_a \rangle_k = \left\langle \Delta H(\mathbf{x}) + \Delta H^{\ddagger} + 2k_B T \right\rangle_k. \tag{4.13}$$

The subscript k indicates that the average is computed with probability weights $\rho(\mathbf{x})k(\mathbf{x})$, instead of $\rho(\mathbf{x})$. In practice, this average can be computed in two different ways.

The first strategy is to randomly choose sites from $\rho(\mathbf{x})$ and reweight each of them by $k(\mathbf{x})$ when computing the average:

$$\tilde{E}_a = \sum\nolimits_{i=1}^{n} k(\mathbf{x}_i)E_a(\mathbf{x}_i) \Big/ \sum\nolimits_i k(\mathbf{x}_i) \tag{4.14}$$

The numerator and denominator are both exponential averages. As shown in previous work,[34] this strategy usually requires an enormous sample size to converge.

The second strategy is to directly sample sites according to probability weight $\rho(\mathbf{x})k(\mathbf{x})$. This is difficult, because we do not know $k(\mathbf{x})$ precisely prior to performing *ab initio* calculations at $\mathbf{x}$. However, if such a sampling algorithm could be devised (see below), the site-averaged activation energy would become a simple arithmetic average:

$$\bar{E}_a = \frac{1}{n} \sum\nolimits_{i=1}^{n} E_a(\mathbf{x}_i). \tag{4.15}$$

This second strategy enables fast convergence to the site-averaged activation energy according to the central limit theorem. Confidence intervals on the precision of E_a follow from the usual statistical formulae

$$\langle E_a \rangle_k = \bar{E}_a \pm \frac{1}{\sqrt{n}} \hat{S}_{Ea} t_{X,n} \tag{4.16}$$

where $t_{X,n}$ is the student-t statistic for an $X\%$ confidence interval with sample size n, and where the standard error is:

$$\hat{S}^2_{E_a} = \frac{n}{n-1} \left\{ \overline{E^2_{a,i}} - \overline{E_{a,i}}^2 \right\}. \tag{4.17}$$

Of course, these estimates and error formulas do not account for systematic errors in the *ab initio* predictions. Moreover, to sample the distribution $\rho(\mathbf{x})k(\mathbf{x})$, we use a kernel regression model to predict $k(\mathbf{x})$ at sites that have not yet been investigated. The error formulas above also do not account for errors in the kernel regression estimates. In our calculations, the kernel regression errors are much smaller than the intrinsic width of the E_a-distribution, so they can probably be ignored. However, Section C.3 of Appendix C shows how the typical kernel regression errors could be included in cases where they are large enough to be important.

4.4 Kernel regression

To sample the distribution $\rho(\mathbf{x})k(\mathbf{x})$ starting from a large collection of sites, *i.e.*, from $\rho(\mathbf{x})$, we require preliminary estimates for $k(\mathbf{x})$ at each site. Given accurate calculations as training data at a modest collection of sites, kernel regression can estimate $E_a(\mathbf{x})$ at all the remaining sites.[40,41] The estimated activation energy at site with environment x_i

is a weighted average of the training data, eqn. 4.18:

$$\hat{E}_a(\mathbf{x}_i) = \frac{\sum_j E_a(\mathbf{x}_j) w_{ij} \left(d(\mathbf{x}_i, \mathbf{x}_j)\right)}{\sum_j w_{ij} \left(d(\mathbf{x}_i, \mathbf{x}_j)\right)} \tag{4.18}$$

Here $\hat{E}_a(\mathbf{x}_i)$ is the predicted activation energy, and the $E_a(\mathbf{x}_j)$ are computed activation energies. The w_{ij} are Gaussian kernels

$$w_{ij} = \exp[-d^2(\mathbf{x}_i, \mathbf{x}_j)] \tag{4.19}$$

that depend on a Mahalanobis distance,[42] d:

$$d^2(\mathbf{x}_i, \mathbf{x}_j) = (\mathbf{x}_i - \mathbf{x}_j)^T \mathbf{S} (\mathbf{x}_i - \mathbf{x}_j). \tag{4.20}$$

Here, $\mathbf{S}$ is a $\dim(\mathbf{x}) \times \dim(\mathbf{x})$ dimensional, positive definite, and symmetric matrix. The kernel regression model is trained by finding the elements of $\mathbf{S}$ which minimizes the leave-one-out loss to best fit the training data. We use Python library tools to implement the kernel regression.[43] Further details about the kernel regression procedures can be found in Section 3.3.

4.5 Importance learning algorithm

The sections above described rate calculations at individual sites, an importance sampling procedure, and a kernel regression (machine learning) procedure. This section integrates all of these components into one "importance learning" algorithm. Importance learning simultaneously accumulates training data, builds the kernel regression model, and focuses computational effort on kinetically important sites with low activation barriers. The algorithm is shown in Fig. 4.4.

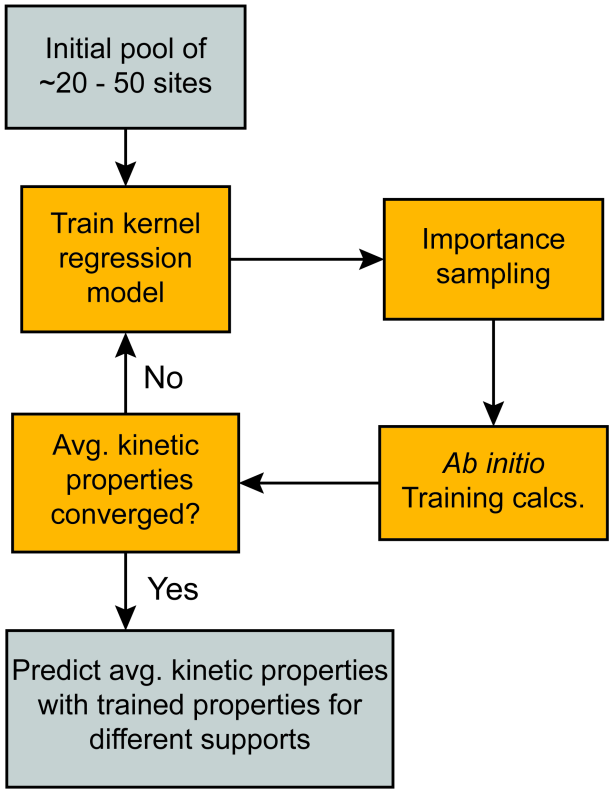

Figure 4.4: The combination of efficient sampling techniques and a machine learning model leads to the "importance learning" algorithm. A set of sites trains a model to learn characteristics of highly active (*i.e.*, important) sites. Efficient sampling techniques select active sites to improve the model and to efficiently predict average kinetic properties. A test for convergence terminates the algorithm when the confidence interval on the site-averaged activation energy shrinks to a prescribed narrow size. In our calculations, the threshold confidence interval was set to 0.75 kJ/mol.

Note that the importance sampling and kernel regression procedures mutually depend on each other. The kernel regression model guides the importance sampling to kinetically important sites. Meanwhile, the accumulated sample of sites and rate calculations teach kernel regression to make accurate preliminary rate predictions.

To compute kinetic properties, precise rate calculations for less active sites are not important, but we need their populations to predict kinetic properties like the overall rate and the fraction of active sites. Therefore, the kernel regression model should also learn to make approximate predictions for inactive sites. For this reason, the importance

learning algorithm begins with rate calculations at a collection of randomly sampled sites. We verified that an initial training set of 20-50 randomly chosen sites is adequate (see Section C.4 of Appendix C).

4.6 Results

Because the model system is extremely simple, an accurate site-averaged activation energy can be directly calculated without importance learning. Using results for ca. 20,000 sites, we computed the activation energy distribution:

$$\tilde{\rho}(E_a) = \int d\mathbf{x}\rho(\mathbf{x})\delta[E_a(\mathbf{x}) - E_a]. \tag{4.21}$$

and the $k(\mathbf{x})$-weighted activation energy distribution:

$$\tilde{\rho}_k(E_a) = \frac{\int d\mathbf{x}\rho(\mathbf{x})k(\mathbf{x})\delta[E_a(\mathbf{x}) - E_a]}{\int d\mathbf{x}\rho(\mathbf{x})k(\mathbf{x})}. \tag{4.22}$$

Fig. 4.5 shows the essentially exact distributions $\tilde{\rho}(E_a)$ and $\tilde{\rho}_k(E_a)$. The activation energy distribution has support[44] over a range of about 40 kJ/mol. The site-averaged activation energy is 40.4 kJ/mol, about 13 kJ/mol below the (incorrect) average without k-weighting. These results serve as benchmarks for testing the importance learning algorithm. To start the importance learning algorithm, we began with an initial training set of fifty randomly chosen sites. The initial kernel regression model was optimized to minimize the leave-one-out errors. Within this initial training set, the kernel regression model predicts activation energies with a standard error $\sigma \approx 0.8$ kJ/mol. Fig. 4.6 shows how the predicted activation energies compare to the true (precisely computed via eqn. 4.11) activation energies for individual sites. At each iteration of the importance learning algorithm, the activation energy distributions $\tilde{\rho}(E_a)$ and $\tilde{\rho}_k(E_a)$ can be predicted using

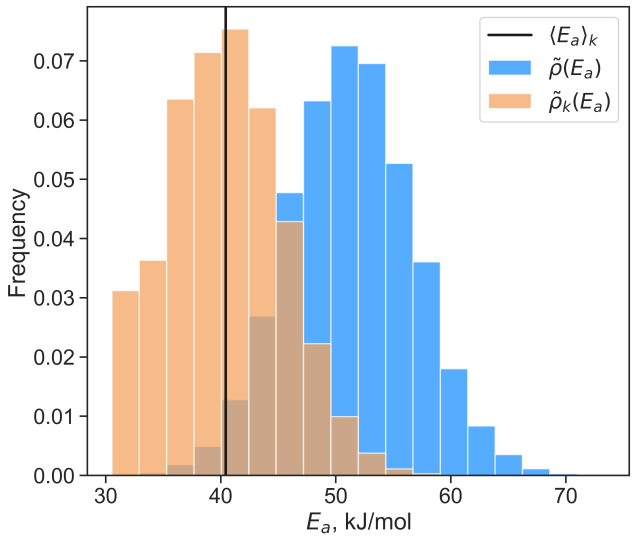

Figure 4.5: Distribution of activation energies (blue) and the rate-weighted activation energy distribution (orange). The solid line shows the site-averaged activation energy.

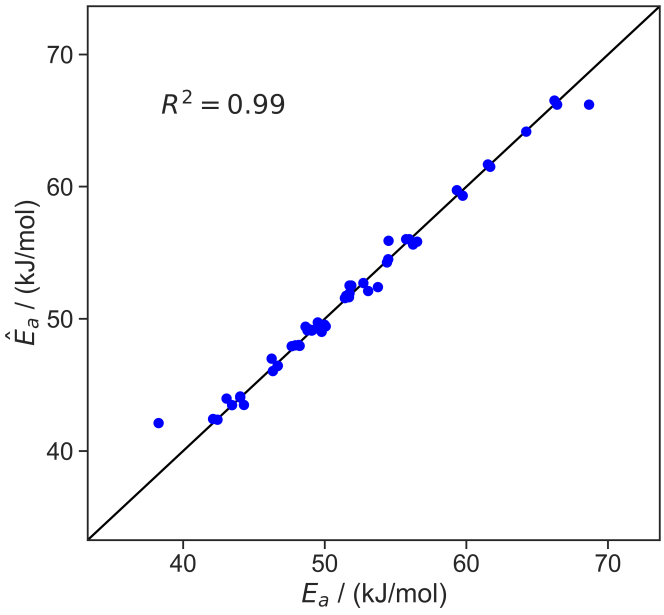

Figure 4.6: Parity plot of predicted activation barriers vs true activation barriers at individual sites. Predictions are from leave-one-out optimization of kernel regression models based on the initial training set of 50 sites. The residuals for all ca. 20,000 sites are approximately Gaussian distributed, with a standard deviation of approximately 0.7 kJ/mol (Figure C.1).

the kernel regression model. After each iteration, the new calculations are appended to the training set. As more training data is accumulated (primarily at low activation energies), the estimated E_a distributions should become more like the true distribution in the kinetically important range of activation energies. As a corollary, the site-averaged activation energy should also converge to the correct value. Fig. 4.7 shows the predicted distributions at the 0th and 28th iterations of importance learning (the latter being the iteration at which the standard error decreases below 0.75 kJ/mol). A rug shows that the activation energies of the importance sampled sites are indeed centered over the main support of $\tilde{\rho}_k(\hat{E}_a)$.

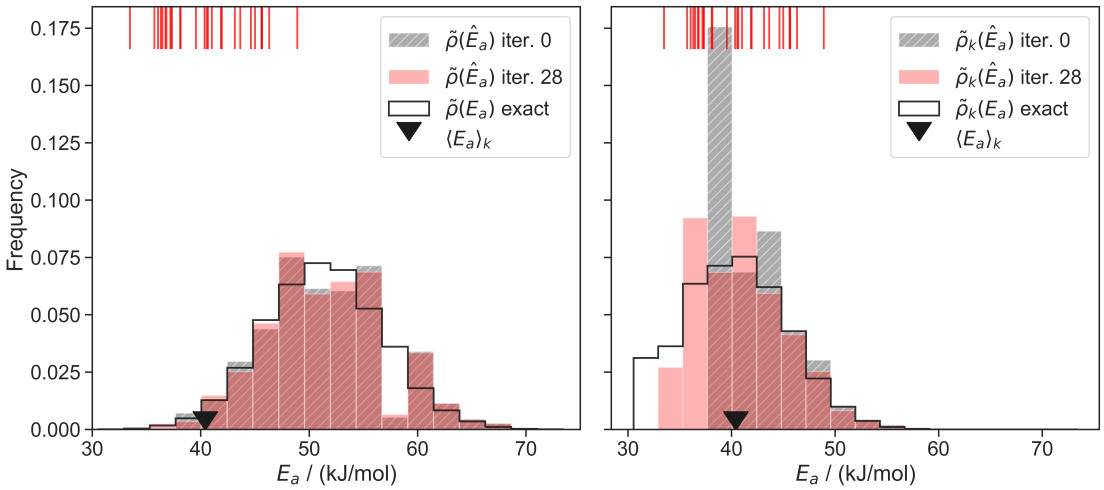

Figure 4.7: Model-predicted activation energy distribution for the unweighted (top) and k-weighted (bottom) distributions at iteration 0 (grey, hatched) and 28 (red) of the importance learning algorithm. Apparent activation energies of importance sampled sites are shown as a rug at the top of each plot. The ▼ symbol shows the correct site averaged E_a.

Prior to importance learning, the initial training set contained only one site with an activation energy under 40 kJ/mol. Importance learning discovers sites with activation energies below 40 kJ/mol, which dominate the overall kinetics. After 28 iterations of importance learning, the low activation energy tail of the predicted $\tilde{\rho}(\hat{E}_a)$ closely resembles

that of the exact $\tilde{\rho}(E_a)$. More importantly, the main support of the predicted $\tilde{\rho}_k(\hat{E}_a)$ closely resembles that of the exact $\tilde{\rho}_k(E_a)$. Both distributions are inaccurately predicted at high activation energies, but these sites make vanishingly small contributions to the observed kinetics. They only need to be counted in the normalization of $\tilde{\rho}(E_a)$ to predict the kinetic properties.

Fig. 4.8 shows the convergence of $\langle E_a \rangle_k$ estimates from importance sampling using standard errors. A higher degree of confidence could also be computed using eqn. 4.16.

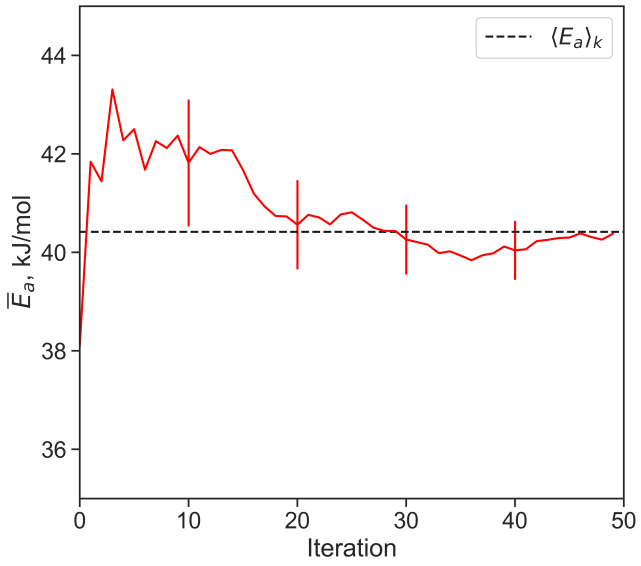

Figure 4.8: The importance learning algorithm converges to within 0.75 kJ/mol of the correct site-averaged $\overline{E}_a$ in 28 iterations. By comparison, a reweighted random sample requires about 200,000 samples to compute $\tilde{E}_a$ with the same level of confidence (Section C.5).

4.7 Identifying characteristics of active sites

In real applications, optimizing the Mahalanobis matrix is inexpensive compared to generating training data from *ab initio* calculations. Therefore, an importance learning calculation can include all potentially important coordinates. However, a central goal

of these calculations is to discover those few key characteristics that distinguish active from inactive sites. Intuition would suggest that the most important coordinates can be identified from the largest diagonal elements in the Mahalanobis matrix. The optimized matrix obtained in this work, using d_1, d_2, and θ, is:

$$\mathbf{S} = \begin{array}{c} \begin{matrix} \scriptstyle d_1 & \scriptstyle d_2 & \scriptstyle \theta \end{matrix} \\ \begin{bmatrix} 54370 & -39653 & -11 \\ -39653 & 29308 & 13 \\ -11 & 13 & 0 \end{bmatrix} \end{array} \tag{4.23}$$

Coordinates d_1 and d_2 have the largest diagonal elements, and they indeed have the strongest influence on site activity. The coordinates d_1 and d_2 correspond to silanolate – silanolate distances and siloxane – siloxane distances, respectively. In hindsight, these coordinates should have primary importance because the potential energies are defined in terms of these coordinates.

In general, the diagonal matrix elements are not reliable indicators of the most important structural characteristics. For example, the diagonal matrix elements change magnitude depending on the units used to represent the coordinates. In addition, diagonal matrix elements indicate sensitivity to local structural changes. They do not account for differences in the extent to which sites vary along different structural coordinates within the global ensemble of sites. Off-diagonal matrix elements may also be important. Large off-diagonal matrix elements may indicate that special combinations of the coordinates are important. Alternatively, off-diagonal elements may compensate for non-orthogonality or redundancy in the set of trial coordinates. The latter complications can be avoided by choosing coordinates that are orthogonal, in the sense:

$$\frac{\partial q_i}{\partial \mathbf{x}} \cdot \frac{\partial q_j}{\partial \mathbf{x}} \approx 0 \tag{4.24}$$

More general guidelines are that

1. Good coordinates should suffice to predict differences in activity over the region with support in distribution $\rho(\mathbf{x})k(\mathbf{x})$.

2. The kernel regression model should predict activation energies with errors that are much smaller than the range of activation energies in $\tilde{\rho}_k(E_a)$.

These two guidelines suggest ranking models according to the fraction of the actual E_a variance that is explained by the model. In linear regression, this is the familiar R^2 statistic. Models that include more input coordinates will generally give larger R^2 values, but small models are preferred, as long as they give accurate site-averaged rate predictions. The fit quality of the kernel regression models trained on different sets of coordinates are shown in Fig 4.9.

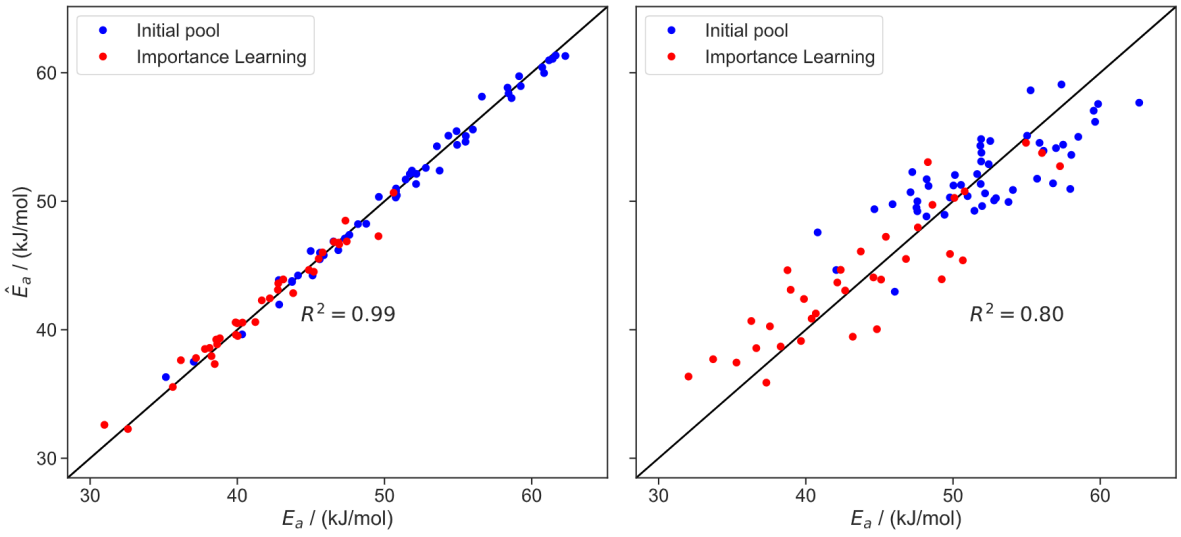

Figure 4.9: Parity plot of model trained with d_1, d_2 (top) and d_1, θ (bottom) at iteration 30 of the importance learning algorithm. As shown in Table 2, d_1 and d_2 are sufficient (without the extra variable θ) to allow kernel regression to predict activation energies across the range of values.

The R^2 values identify θ as a kinetically unimportant structural characteristic. The kernel regression model trained only on θ completely fails to make predictions based on

Table 4.2: R^2 values of trained model with different combination of local coordinates at iteration 30 of the importance learning algorithm.

Coordinates	R^2
d_1	0.80
d_2	0.16
θ	-0.03
d_1, d_2	0.99
d_1, θ	0.82
d_2, θ	0.34
d_1, d_2, θ	0.99

the local environment. Models based only on d_1 or d_2 begin to predict coarse trends in the activation energies. The model trained using d_1 and d_2 together makes extremely accurate predictions across the whole range of activation energies. Note that d_1 and d_2 are just two of the five total coordinates that define the local site environment. The model-predicted E_a is plotted as a function of d_1 and d_2 in Fig. 4.10. This plot reveals that d_1 and d_2 compensate for each other in active sites. Among sites with the same activation energy, one length increases while the other decreases. Fig. 4.10 also illustrates that the most active sites have shorter d_1 (silanolate-silanolate) distances and longer d_2 (O-O distance of the siloxane ligands) distances relative to the unperturbed distance of 2.00.

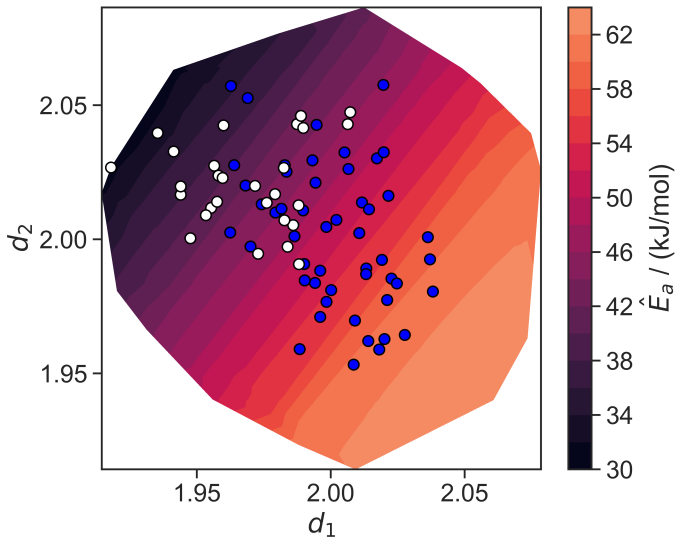

Figure 4.10: Activity of sites as function of the local environment. The upper plot shows the true barriers and the bottom plot shows the model-predicted barriers at iteration 30 of the importance learning loop. Blue points correspond to the initial pool and white points are importance sampled sites.

4.8 Conclusions

Several industrially important or promising catalysts are single metal atoms grafted onto an amorphous support such as silica. These catalysts tend to be poorly understood because the amorphous support gives each site a unique local environment. Moreover, the distribution of disordered environments around each site is quenched, history dependent, and thus largely unpredictable. Each site has a different activation energy, and the variance in activation energies is exponentially magnified in the distribution of activities. Accordingly, active sites tend to be rare, with less than 20% of sites accounting for most of the catalytic activity. The small fraction of active sites hampers both experimental characterization and theoretical modeling efforts.

This Chapter 3 presented an importance learning algorithm to overcome the theoretical challenges of modeling the activity of such catalysts. It combines machine learning

techniques (kernel regression) and importance sampling techniques (to focus effort on the most active and abundant sites). To illustrate the algorithm, we developed a simple model of a Langmuir-Hinshelwood reaction at sites on a quenched and disordered support. We used the algorithm to compute the site-averaged activation energy.

The algorithm rapidly converged estimates of the site-averaged E_a with uncertainties less than 0.75 kJ/mol, even though the individual sites in the model have activation energies that span a range of nearly 40 kJ/mol. Estimating the site-averaged E_a with the same level of confidence as importance learning requires through standard sampling methods requires 200,000 samples (compared to 75 samples in the importance learning algorithm) for this system. Furthermore, the kernel regression model generated by the algorithm can accurately predict the activation energies using just two structural characteristics of the local environment. The new importance learning algorithm, if combined with *ab initio* calculations and realistic models of amorphous silica, should enable the first rigorous site-averaged computational studies and quantitative predictions for this important family of catalysts.

Bibliography

1. Zhang, X., Shi, H. & Xu, B. Q. Catalysis by gold: Isolated surface Au_3^+ ions are active sites for selective hydrogenation of 1,3-butadiene over Au/ZrO_2 catalysts. *Angew. Chem., Int. Ed.* **44,** 7132–7135. https://www.doi.org/10.1002/anie.200502101 (2005).

2. Hackett, S. F. J. *et al.* High-activity, single-site mesoporous Pd/Al_2O_3 catalysts for selective aerobic oxidation of allylic alcohols. *Angew. Chem., Int. Ed.* **46,** 8593–8596. https://www.doi.org/10.1002/anie.200702534 (2007).

3. Wei, H. *et al.* FeOx -supported platinum single-atom and pseudo-single-atom catalysts for chemoselective hydrogenation of functionalized nitroarenes. *Nat. Commun.* https://www.doi.org/10.1038/ncomms6634 (2014).

4. Thomas, J. M., Raja, R. & Lewis, D. W. Single-site heterogeneous catalysts. *Angew. Chem., Int. Ed.* **44,** 6456–6482. https://www.doi.org/10.1002/anie.200462473 (2005).

5. Wang, A., Li, J. & Zhang, T. Heterogeneous single-atom catalysis. *Nat. Rev. Chem.* **2,** 65–81. https://doi.org/10.1038/s41570-018-0010-1 (2018).

6. Flytzani-Stephanopoulos, M. & Gates, B. C. Atomically Dispersed Supported Metal Catalysts. *Annu. Rev. Chem. Biomol. Eng.* https://doi.org/10.1146/annurev-chembioeng-062011-080939 (2012).

7. McDaniel, M. P. & Welch, M. B. The activation of the phillips polymerization catalyst: I. Influence of the hydroxyl population. *J. Catal.* **82,** 98–109. https://www.doi.org/10.1016/0021-9517(83)90121-5 (1983).

8. Maksasithorn, S., Praserthdam, P., Suriye, K. & Debecker, D. P. Preparation of super-microporous WO_3/SiO_2 olefin metathesis catalysts by the aerosol-assisted sol-gel process. *Microporous Mesoporous Mater.* **213,** 125–133. https://www.doi.org/10.1016/j.micromeso.2015.04.020 (2015).

9. Carrick Wayne, L. *et al.* Ethylene polymerization with supported bis(triphenylsilyl) chromate catalysts. *J. Polym. Sci., Part A-1: Polym. Chem.* **10,** 2609–2620. https://www.doi.org/10.1002/pol.1972.150100909 (1972).

10. Theopold, K. H. Organochromium(III) Chemistry: A Neglected Oxidation State. *Acc. Chem. Res.* **23,** 263–270. https://www.doi.org/10.1021/ar00176a005 (1990).

11. McDaniel, M. P. A Review of the Phillips Supported Chromium Catalyst and Its Commercial Use for Ethylene Polymerization. English. *Adv. Catal.* **53,** 123–606. https://www.doi.org/https://doi.org/10.1016/S0360-0564(10)53003-7 (2010).

12. Ruddy, D. A. & Tilley, T. D. Kinetics and mechanism of olefin epoxidation with aqueous H_2O_2 and a highly selective surface-modified TaSBA15 heterogeneous catalyst. *J. Am. Chem. Soc.* **130,** 11088–11096. https://www.doi.org/10.1021/ja8027313 (2008).

13. Shannon, I. J. *et al.* Metallocene-derived, isolated Mo(VI) active centres on mesoporous silica for the catalytic dehydrogenation of methanol. *J. Chem. Soc., Faraday Trans.* **94,** 1495–1499. https://www.doi.org/10.1039/a800054i (1998).

14. Vining, W. C., Strunk, J. & Bell, A. T. Investigation of the structure and activity of $VO_x/CeO_2/SiO_2$ catalysts for methanol oxidation to formaldehyde. English. *J. Catal.* **281,** 222–230. https://www.doi.org/10.1016/j.jcat.2011.09.024 (2012).

15. Amakawa, K. *et al.* In situ generation of active sites in olefin metathesis. *J. Am. Chem. Soc.* **134,** 11473. https://www.doi.org/10.1021/ja3011989 (2012).

16. McDaniel, M. P. & Martin, S. J. Poisoning Studies on Cr/Silica. 2. Carbon Monoxide. *J. Phys. Chem.* **95,** 3289–3293. https://doi.org/10.1021/j100161a059 (1991).

17. Chauvin, Y. & Commereuc, D. Chemical counting and characterization of the active sites in the rhenium oxide/alumina metathesis catalyst. *J. Chem. Soc., Chem. Commun.* **6,** 462–464. https://doi.org/10.1039/C39920000462 (1992).

18. Howell, J. G., Li, Y. P. & Bell, A. T. Propene Metathesis over Supported Tungsten Oxide Catalysts: A Study of Active Site Formation. *ACS Catal.* **6,** 7728–7738. https://doi.org/10.1021/acscatal.6b01842 (2016).

19. Brunelli, N. A. & Jones, C. W. Tuning acid-base cooperativity to create next generation silica-supported organocatalysts. *J. Catal.* **308,** 60–72. https://doi.org/10.1016/j.jcat.2013.05.022 (2013).

20. Baştuğ, T. & Kuyucak, S. Application of Jarzynski's equality in simple versus complex systems. *Chem. Phys. Lett.* **436,** 383–387. https://www.doi.org/10.1016/j.cplett.2007.01.078 (2007).

21. Bustamante, C., Liphardt, J. & Ritort, F. The Nonequilibrium Thermodynamics of Small Systems. *Phys. Today* **58,** 43–48. https://doi.org/10.1063/1.2012462 (2005).

22. Sear, R. P. Non-self-averaging nucleation rate due to quenched disorder. *J. Phys.: Condens. Matter* **24,** 052205. https://doi.org/10.1088/0953-8984/24/5/052205 (2012).

23. Wang, F. & Landau, D. P. Efficient, multiple-range random walk algorithm to calculate the density of states. *Phys. Rev. Lett.* **86,** 2050. https://doi.org/10.1103/PhysRevLett.86.2050 (2001).

24. Espelid, Ø. & Børve, K. J. Theoretical Models of Ethylene Polymerization over a Mononuclear Chromium(II)/Silica Site. *J. Catal.* **195,** 125–139. https://www.doi.org/10.1006/jcat.2000.2986 (2000).

25. Fong, A., Vandervelden, C., Scott, S. L. & Peters, B. Computational Support for Phillips Catalyst Initiation via Cr-C Bond Homolysis in a Chromacyclopentane Site. *ACS Catal.* **8,** 1728–1733. https://doi.org/10.1021/acscatal.7b03724 (2018).

26. Jystad, A. M., Biancardi, A. & Caricato, M. Simulations of Ammonia Adsorption for the Characterization of Acid Sites in Metal-Doped Amorphous Silicates. *J. Phys. Chem. C* **121,** 22258–22267. https://www.doi.org/10.1021/acs.jpcc.7b08113 (2017).

27. Floryan, L., Borosy, A. P., Nunez-Zarur, F., Comas-Vives, A. & Coperet, C. Strain Effect and Dual Initiation Pathway in Cr(III)/SiO_2 Polymerization Catalysts from Amorphous Periodic Models. English. *J. Catal.* **346,** 50–56. https://www.doi.org/10.1016/j.jcat.2016.11.037 (2017).

28. Handzlik, J. Properties and metathesis activity of monomeric and dimeric Mo centres variously located on γ-alumina - A DFT study. *Surf. Sci.* **601,** 2054–2065. https://www.doi.org/10.1016/J.SUSC.2007.03.002 (2007).

29. Guesmi, H. & Tielens, F. Chromium oxide species supported on silica: A representative periodic DFT model. *J. Phys. Chem. C* **116,** 994–1001. https://doi.org/10.1021/jp209680r (2012).

30. Fong, A., Yuan, Y., Ivry, S. L., Scott, S. L. & Peters, B. Computational Kinetic Discrimination of Ethylene Polymerization Mechanisms for the Phillips (Cr/SiO_2) Catalyst. English. *ACS Catal.* **5,** 3360–3374. https://www.doi.org/10.1021/acscatal.5b00016 (2015).

31. Delley, M. F. *et al.* Proton Transfers Are Key Elementary Steps in Ethylene Polymerization on Isolated Chromium(III) Silicates. *Proc. Natl. Acad. Sci.* **111,** 11624–11629. https://www.doi.org/10.1073/pnas.1405314111 (2014).

32. Gierada, M. & Handzlik, J. Active Sites Formation and Their Transformations During Ethylene Polymerization by the Phillips CrO_x/SiO_2 Catalyst. *J. Catal.* **352,** 314–328. https://www.doi.org/10.1016/j.jcat.2017.05.025 (2017).

33. Ewing, C. S., Bhavsar, S., Veser, G., McCarthy, J. J. & Johnson, J. K. Accurate amorphous silica surface models from first-principles thermodynamics of surface dehydroxylation. *Langmuir* **30,** 5133–5141. https://doi.org/10.1021/la500422p (2014).

34. Goldsmith, B. R., Peters, B., Johnson, J. K., Gates, B. C. & Scott, S. L. Beyond Ordered Materials: Understanding Catalytic Sites on Amorphous Solids. *ACS Catal.* **7,** 7543–7757. https://www.doi.org/10.1021/acscatal.7b01767 (2017).

35. Weeks, J. D., Chandler, D. & Andersen, H. C. Role of Repulsive Forces in Determining Equilibrium Structure of Simple Liquids. English. *J. Chem. Phys.* **54,** 5237–5247. https://doi.org/10.1063/1.1674820 (1971).

36. McGuinness, D. S., Davies, N. W., Horne, J. & Ivanov, I. Unraveling the Mechanism of Polymerization with the Phillips Catalyst. *Organometallics* **29,** 6111–6116. https://www.doi.org/10.1021/om100883n (2010).

37. Luo, Y.-R. *Comprehensive handbook of chemical bond energies* English (CRC Press, Boca Raton, 2007).

38. Peters, B. & Scott, S. L. Single Atom Catalysts on Amorphous Supports: A Quenched Disorder Perspective. *J. Chem. Phys.* **142,** 104708. https://www.doi.org/10.1063/1.4914145 (2015).

39. Wu, C., Schmidt, D. J., Wolverton, C. & Schneider, W. F. Accurate coverage-dependence incorporated into first-principles kinetic models: Catalytic NO oxidation on Pt (111). English. *J Catal* **286,** 88–94. ISSN: 0021-9517. %3CGo%20to%20ISI%3E://WOS:000300141300010 (2012).

40. Weinberger, K. Q. & Tesauro, G. Metric Learning for Kernel Regression. *J. Mach. Learn. Res.,* 8. http://proceedings.mlr.press/v2/weinberger07a.html (2007).

41. Hofmann, T., Schölkopf, B. & Smola, A. J. Kernel methods in machine learning. *Ann. Stat.* **36,** 1171–1220. https://www.doi.org/10.1214/009053607000000677 (2008).

42. Mahalanobis, P. C. On the generalized distance in statistics. *Proc. Natl. Inst. Sci. India* **2,** 49–55. https://doi.org/10.1007/s13171-019-00164-5 (1936).

43. Carey, C. J. & Tang, Y. *metric-learn* https://github.com/metric-learn/metric-learn, 2019. https://github.com/metric-learn/metric-learn.

44. Logan, J. D. *Applied mathematics* 3rd. **14204421,** 529. https://www.wiley.com/en-us/Applied%20Mathematics,%204th%20Edition-p-9781118475805 (Wiley-Interscience, Hoboken, N.J., 2006).

Chapter 5

Importance learning estimator for the site-averaged turnover frequency of a disordered solid catalyst

Reproduced in part with permission from:

. Vandervelden, C. A., Khan, S. A. & Peters, B. Importance learning estimator for the site-averaged turnover frequency of a disordered solid catalyst. *J. Chem. Phys.* **153,** 244120. https://doi.org/10.1063/5.0037450 (2020).

5.1 Introduction

Catalysts are essential for transforming chemical feedstocks into valuable products in the petrochemical,[1] pharmaceutical,[2] and food industries[3] – some of the largest sectors in the world economy. Much of catalysis research aims to identify the active sites and reaction mechanisms to engineer better catalysts.[4–7] Nearly all homogeneous catalysts and many heterogeneous catalysts have well-defined sites that are amenable to established

research techniques. For example, characterization techniques can probe the structure (XRD and NMR),[8–11] oxidation states (XANES and XPS),[12–14] and coordination environments (EXAFS and 2D NMR).[13,15] Likewise, DFT calculations based on sites with known structural characteristics can predict the structures and energies of intermediates and transition states.[16] These calculations are widely used to test specific mechanistic hypotheses against experimental data.[17–19]

Disordered heterogeneous catalysts present special challenges for experimental and computational studies.[20,21] Here we distinguish heterogeneous catalysts that exhibit quenched non-equilibrium disorder from those that exhibit dynamical disorder.[22] For example, dynamically disordered catalysts include small fluxional nanoparticles that rapidly interconvert between active and inactive forms within or between turnovers.[23–25] The steady-state abundances and turnover frequencies in a system with dynamical disorder follow from the theories of non-equilibrium thermodynamics[26] and rare events.[27,28] Though often costly and complicated, these systems are amenable to established rare events methods for computing rates and sampling ensembles of dynamically disordered states.[29]

Examples of catalysts that exhibit quenched disorder include metallic glasses,[30–32] high-entropy alloys,[33,34] mixed metal oxides,[35] and single metal atoms grafted to amorphous supports like silica or silica-alumina.[20,36–38] Each of these catalysts has sites with a distribution of permanent structural differences that lead to a distribution of different activities. Catalysts with quenched disorder pose special difficulties beyond the reach of established experimental and theoretical methods. Active site counting experiments for these catalysts show that only a small fraction of sites – usually fewer than 30% – are responsible for most of the catalytic turnovers.[39–42] Uncovering features of the most active sites is challenging because spectroscopic techniques probe the most common sites, which are likely inactive. The Phillips catalyst, Cr atoms on amorphous silica for ethylene polymerization, is perhaps most emblematic of these difficulties.[40] Despite its discovery

in 1951 and subsequent decades of research, the full catalytic cycle remains unknown and is still debated.[43–52]

Also on the theoretical side, amorphous catalysts present many challenges. Foremost among these, are questions about the structure and surface features of an amorphous solid. Even for amorphous silica, for which tremendous effort has been spent developing models,[53–60] we lack atomically resolved structural data to assess model accuracy. Moreover, the quenched disorder is a signature of the preparation history, so the distribution of structures is not defined by Boltzmann statistics and cannot be generated by standard Monte Carlo sampling techniques. Somehow, this unknown distribution must be sampled to compute site-averaged kinetic properties. A final difficulty is that accurate estimates of site-averaged kinetic properties require difficult-to-converge exponential averages.[61,62] Although a few studies have computed kinetics for large collections of sites, none of them have computed proper, site-averaged TOFs according to the correct theoretical expression.[61]

In the two previous chapters, we introduced a quenched-disordered lattice model as a platform to develop computational methods for amorphous catalysts. The quenched-disordered lattice model was inspired by the rings, silanols, and siloxanes on the surface of amorphous silica,[63] by grafting reactions for supported organometallics,[64–66] and by a Langmuir-Hinshelwood mechanism[67] with site-dependent kinetic parameters. In Chapter 3, the model was used to illustrate how a combination of population balance modeling and machine learning (kernel regression) techniques can predict how the population of grafted sites evolves in time. In Chapter 4, we started with a distribution of grafted sites and developed an "importance learning" algorithm to efficiently estimate the site-averaged activation energy, $\langle E_a \rangle_k$. Importance learning, the first to our knowledge, combination of importance sampling and machine learning required about 2500-times fewer samples to estimate $\langle E_a \rangle_k$ with the same uncertainty as random sampling with reweighting (see

Figure 4.8 and Section C.5).

In this chapter, we develop an efficient estimator for the site-averaged TOF, $\langle \dot{s} \rangle$. Starting from the quenched-disordered lattice model and final grafted site distribution from Chapter 3, this chapter aims to compute the site-averaged, absolute TOF. Like $\langle E_a \rangle_k$, computing $\langle \dot{s} \rangle$ also involves converging an exponential average. The efficient estimator samples sites with the same weights as importance learning, so *ab initio* calculations beyond those previously used to construct training sets for predicting E_a are unrequired. In the remainder of this chapter, we develop the theoretical properties of the efficient TOF estimator, we briefly review the quenched-disordered lattice model of an amorphous catalyst, and we illustrate the TOF estimator for the quenched-disordered catalyst model.

5.2 Efficient estimator for the site-averaged TOF

In this work, we show how the importance learning algorithm and its machine learning (ML) model, trained to be accurate for the most active sites, can estimate the absolute site-averaged TOF. No new training set calculations are required for the calculations below, and therefore (as in the $\langle E_a \rangle_k$ estimate) these calculations should be possible with a training set of ca. 100 sites.

We consider a catalyst where each site has a TOF with power-law dependence on concentrations C_j,

$$\dot{s}(\mathbf{x}) = k(\mathbf{x}) \prod_j {C_j}^{\alpha_j}. \tag{5.1}$$

Here, $k(\mathbf{x})$ is an Arrhenius-type rate constant which depends on the local environment,

$\mathbf{x}$,

$$k(\mathbf{x}) = A(\mathbf{x}) \exp[-\beta E_a(\mathbf{x})]. \tag{5.2}$$

Here, $\beta = 1/k_B T$. Note that both $A(\mathbf{x})$ and $E_a(\mathbf{x})$ may depend on the local environment. In Section 5.3 we show how assumptions like those implicit in eqns. 5.1 and 5.2 can arise from a simple model with a Langmuir-Hinshelwood reaction rate law. From eqn. 5.1, the site-averaged TOF can be written as

$$\begin{aligned} \langle r(\mathbf{x}) \rangle &= \int d\mathbf{x} k(\mathbf{x}) \rho(\mathbf{x}) \prod_j C_j^{\alpha_j} \\ &= \langle A(\mathbf{x}) \exp[-\beta E_a(\mathbf{x})] \rangle \prod_j C_j^{\alpha_j} \end{aligned} \tag{5.3}$$

where $\rho(\mathbf{x})$ is the density of sites with local structure $\mathbf{x}$. The quantity in brackets on the right side of eqn. 5.3 is $\langle k \rangle$, the site-averaged rate constant. Eqn. 5.3 assumes $\rho(\mathbf{x})$ is normalized, but the normalization will emerge naturally as a number of sites per support surface area. The average in equation 5.3 is deceptively difficult to compute because it is an exponential average. Specifically, the Arrhenius law within $k(\mathbf{x})$ amplifies the importance of sites with unusually small activation energies and diminishes the contribution of typical sites. Starting from $\langle k(\mathbf{x}) \rangle$ in eqn. (3),

$$\begin{aligned} \langle k(\mathbf{x}) \rangle &= \int d\mathbf{x} \rho(\mathbf{x}) A(\mathbf{x}) \exp[-\beta E_a(\mathbf{x})] \\ &= \langle A(\mathbf{x}) \rangle_{\rho(\mathbf{x}) \exp[-\beta E_a(\mathbf{x})]} \int d\mathbf{x} \rho(\mathbf{x}) \exp[-\beta E_a(\mathbf{x})] \\ &= \langle A(\mathbf{x}) \rangle_{\rho(\mathbf{x}) \exp[-\beta E_a(\mathbf{x})]} \langle \exp[-\beta E_a(\mathbf{x})] \rangle_{\rho(\mathbf{x})} \end{aligned} \tag{5.4}$$

where

$$\langle A(\mathbf{x})\rangle_{\rho(\mathbf{x})\exp[-\beta E_a(\mathbf{x})]} = \frac{\int d\mathbf{x}\rho(\mathbf{x})\exp[-\beta E_a(\mathbf{x})]A(\mathbf{x})}{\int d\mathbf{x}\rho(\mathbf{x})\exp[-\beta E_a(\mathbf{x})]} \tag{5.5}$$

In the second line of eqn. 5.4, we have multiplied and divided by the integral that remains on the right side to obtain an average of $A(\mathbf{x})$ in distribution $\rho(\mathbf{x})\exp[-\beta E_a(\mathbf{x})]$. In the third line, we have noted that the remaining integral was itself an average of $\exp[-\beta E_a(\mathbf{x})]$ in distribution $\rho(\mathbf{x})$.

Eqn. 5.4 is the central result of this chapter. It converts the difficult site-average of $k(\mathbf{x})$ into a product of two averages that are easily computed with importance learning. In the discussion below, we also make frequent reference to a projected distribution of activation energies: $\rho(E_a) = \int d\mathbf{x}\delta[E_a - E_a(\mathbf{x})]\rho(\mathbf{x})$. For example, note that

$$\begin{aligned}\langle\exp[-\beta E_a(\mathbf{x})]\rangle_{\rho(\mathbf{x})} &= \int d\mathbf{x}\rho(\mathbf{x})\exp[-\beta E_a(\mathbf{x})] \\ &= \int d\mathbf{x}\rho(\mathbf{x})\int dE_a\exp[-\beta E_a]\delta[E_a - E_a(\mathbf{x})] \\ &= \int dE_a\rho(E_a)\exp[-\beta E_a]\end{aligned} \tag{5.6}$$

So $\langle\exp[-\beta E_a(\mathbf{x})]\rangle_{\rho(\mathbf{x})}$ can be computed by sampling $\rho(\mathbf{x})$, or by integrating the distribution $\rho(E_a)$.

No new *ab initio* calculations are required to estimate $\langle A(\mathbf{x})\rangle_{\rho(\mathbf{x})\exp[-\beta E_a(\mathbf{x})]}$, because this average uses the same weights as importance learning. It can be directly computed as an arithmetic average of $A(\mathbf{x})$ at sites harvested from $\rho(\mathbf{x})\exp[-\beta E_a(\mathbf{x})]$ during the training procedure. Additional work is needed to study convergence properties of $\langle A(\mathbf{x})\rangle_{\rho(\mathbf{x})\exp[-\beta E_a(\mathbf{x})]}$ because the initially sampled data during training will not yet be representative of $\rho(\mathbf{x})\exp[-\beta E_a(\mathbf{x})]$. However, we expect $A(\mathbf{x})$ to be a relatively weak

function of $\mathbf{x}$ with a quickly converging average. The $\langle \exp[-\beta E_a] \rangle_{\rho(E_a)}$ average might still appear to pose a problem. Of course, the exact form of $\rho(E_a)$ is unknown and this is the reason we need methods beyond standard Monte Carlo importance sampling.

Fortunately, the importance learning algorithm trains the ML algorithm to compute the integrand in the calculation of $\langle \exp[-\beta E_a] \rangle_{\rho(E_a)}$ accurately and directly. First, we return to the full ensemble of sites, most of which will not be part of the training set and will have unknown properties. For this ensemble, we use the trained ML model to predict the distribution of activation energies. We denote the ML-predicted E_a distribution as $\hat{\rho}(\hat{E}_a)$, where the hats indicate that this object is an estimated distribution of estimated activation energies. Now, the exponential integral is

$$\begin{aligned} \langle \exp[-\beta E_a] \rangle_{\rho(E_a)} &\approx \langle \exp[-\beta \hat{E}_a] \rangle_{\hat{\rho}(\hat{E}_a)} \\ &= \frac{1}{N} \sum_i^N \exp[-\beta \hat{E}_a(\mathbf{x}_i)] \end{aligned} \tag{5.7}$$

Eqn. 5.7 is approximate because $\hat{\rho}(\hat{E}_a)$ is equal to $\rho(E_a)$ if and only if there are no errors in the ML model. Note that eqn. 5.7 is still an exponential average, but the ML model is trained to be accurate for sites that dominate the sum, and that evaluating the sum for large N is now trivial with the ML model.

In practice, errors in the ML model will propagate through the average, biasing the estimate. The bias arises because activation parameters from the ML model are scattered symmetrically around the true values, but the exponential magnifies contributions of errors on the low activation energy side. We can use residuals from the test set to correct for this bias. Assuming the errors of the ML model are normally distributed, the bias in the $\langle \exp[-\beta \hat{E}_a] \rangle$ calculation can be estimated through a similar procedure that we previously used to estimate the bias of $\langle \hat{E}_a \rangle_k$, Section C.3. A detailed derivation of

the bias correction can be found in Section D.1 of the supplementary information. The bias-corrected estimator, $\langle \exp[-\beta \hat{E}_a] \rangle_{B.C.}$ is

$$\langle \exp[-\beta \hat{E}_a] \rangle_{B.C.} = \exp[\frac{1}{2}(\beta \sigma_r)^2] \langle \exp[-\beta \hat{E}_a] \rangle_{\hat{\rho}(\hat{E}_a)} \tag{5.8}$$

Here, σ_r is the standard deviation of residual errors in the ML predictions. The residual distribution can be approximated from leave-one-out-predicted $\hat{E}_a$ values for sites in the test set. The supporting information shows that the test set residual distribution closely resembles the residual distribution of all sites, with standard deviations within 10% of each other, Figure D.1. In the remainder of the chapter, we use $\langle \exp[-\beta \hat{E}_a] \rangle$ in general reference to the theoretical average with distribution $\rho(\mathbf{x})$. Subscripts $\hat{\rho}(\hat{E}_a)$ and B.C. are used only when necessary to distinguish the raw importance learning estimates and bias corrected estimates.

5.3 Example calculation

Section 3.2.1 described a structurally disordered, functionalized lattice model to mimic the surface of amorphous SiO_2. As shown in Figure 5.1, sites in the model are designated as silanol, siloxane, or empty sites. Grafting sites are defined as empty sites with two silanol neighbors and two siloxane neighbors on opposite sides. As in Chapter 4, we assume that grafting has occurred at all grafting sites. The same kernel regression ML model for estimating activation energies via importance learning is here used to estimate $\langle \mathscr{k} \rangle$. The ML model uses three coordinates (see Figure 5.1) to describe the local environment around each site: (i) the distance between silanolate groups, d_1, (ii) the distance between siloxane groups, d_2, and (iii) the angle between the silanolate and siloxane groups, θ. Our previous work showed that these coordinates are nearly orthog-

onal and, despite being incomplete, they are sufficient to predict the kinetics at each site. Moreover, the coordinates describe site characteristics that remain fixed (quenched) while reactions occur at the site. A more involved discussion on coordinate selection can be found in Section 4.7.

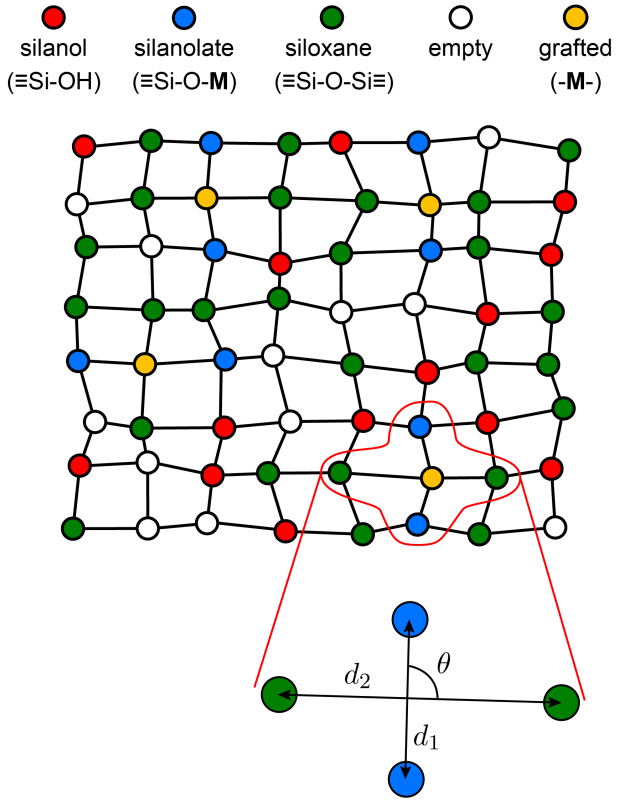

Figure 5.1: Quenched disorder lattice model. Coordinates d_1, d_2, and θ describe the local environment (region in red outline) around the active metal site, $\mathbf{M}^*$ (yellow).

5.3.1 Model of catalytic cycle

The model catalyst site, $\mathbf{M}^*$, as in our previous work, contains a metal center **M** and support environment *. A simple model Langmuir-Hinshelwood mechanism at each site has a quasi-equilibrated adsorption step and an irreversible, rate-liming step.

$$\mathbf{A} + \mathbf{M}^* \rightleftharpoons \mathbf{AM}^* \quad K(\mathbf{x})$$
$$\mathbf{AM}^* \rightarrow \mathbf{B} + \mathbf{M}^* \quad k_2$$

We assume that:

1. the equilibrium constant K for adsorption of reactant $\mathbf{A}$ depends on the local environment of site i, $\mathbf{x}_i$,

2. the second step irreversibly converts the adsorbed molecule $\mathbf{A}$ ($\mathbf{AM}^*$) into the gas phase product $\mathbf{B}$ and a bare site $\mathbf{M}^*$ with a uniform rate constant, k_2,

3. $K(\mathbf{x})c_{\mathbf{A}} \ll 1$ for all sites, so that the bare site $\mathbf{M}^*$ is the most abundant surface intermediate (MASI).

The Langmuir-Hinshelwood mechanism under these simplifying assumptions is shown in Figure 5.2.

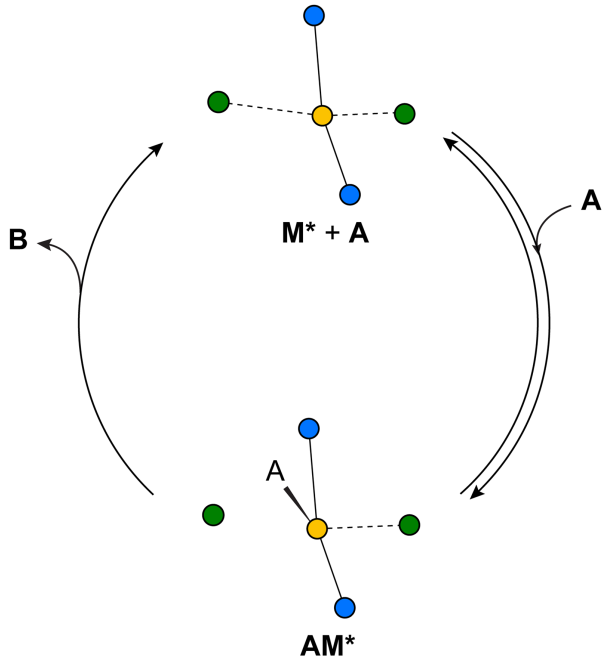

Figure 5.2: The quasi-equilibrated adsorption step and irreversible chemical reaction step for the model Langmuir-Hinshelwood reaction $\mathbf{A} \rightarrow \mathbf{B}$, with $\mathbf{M}^*$ and $\mathbf{AM}^*$ intermediates.

The simplified rate law under these assumptions is

$$\dot{\imath} \approx k(\mathbf{x}) c_{\mathbf{A}}, \tag{5.9}$$

where $k(\mathbf{x}) = k_2 K(\mathbf{x})$ is the apparent, pseudo-first-order rate constant. The apparent turnover frequency depends on the local site geometry $\mathbf{x}$ because the adsorption constant

$$K(\mathbf{x}) = \exp\left[-\frac{\Delta H(\mathbf{x}) - T\Delta S}{k_B T}\right] \tag{5.10}$$

depends on $\mathbf{x}$. Here $\Delta H(\mathbf{x})$ is a site-dependent adsorption enthalpy that we compute by minimizing the energies of states $\mathbf{M}^*$ and $\mathbf{AM}^*$ subject to the constrained geometry $\mathbf{x}$, much like the procedure for real *ab initio* calculations.[68,69] The siloxane and silanolate groups are also held fixed to mimic the approximate rigidity of a real amorphous oxide.

A transition state theory model was used for the rate constant,

$$k_2 = \frac{k_B T}{h} \exp\left[\frac{\Delta S^{\ddagger}}{k_B}\right] \exp\left[-\frac{\Delta H^{\ddagger}}{k_B T}\right], \tag{5.11}$$

where $\Delta S^{\ddagger}$ and $\Delta H^{\ddagger}$ are (in this simple model) uniform across all sites. A full description of the model and its parameters can be found in Section 4.3. The temperature dependent rate at each site can be summarized in terms of a site-specific activation energy. The activation energy at each site is

$$E_a(\mathbf{x}_i) = -\frac{d \ln k_i}{d\beta} = \Delta H(\mathbf{x}_\mathrm{i}) + \Delta H^{\ddagger} + 2k_B T \tag{5.12}$$

A full derivation of $E_a(\mathbf{x}_i)$ can be found in Appendix C.2. This simple model chemistry allows us to test the accuracy and efficiency of algorithms, as we can exactly compute site-averaged kinetics for the entire ensemble of sites.

5.3.2 Review of importance learning

Theoretical analyses show that contributions of individual sites to the site-averaged kinetic properties in a disordered are approximately $\rho(\mathbf{x}) \exp[-\beta E_a(\mathbf{x})]$. However, the distribution $\rho(\mathbf{x})$ and the structure-activation energy relationship $E_a(\mathbf{x})$ are both *a priori* unknown. Moreover, *ab initio* calculations are too expensive to straightforwardly sample thousands of sites, compute their kinetic properties, and properly reweight them.[20] Importance learning circumvents these problems through a combination of machine learning and importance sampling methods. The algorithm starts from calculated $E_a(\mathbf{x})$ values at a small pool of randomly sampled sites and a primitive model trained to predict $E_a(\mathbf{x})$ from this initial data. At each subsequent iteration, we importance sample the approximate $\rho(\mathbf{x}) \exp[-\beta E_a(\mathbf{x})]$ distribution, compute $E_a(\mathbf{x})$ at the new site, append the

new data to the training set, and retrain the machine learning model. The result is an adaptive importance sampling algorithm that iteratively focuses the training data and computational effort on those parts of the site ensemble that are most important to the site-averaged kinetic properties (Chapters 3 and 4).

The ML part of the importance learning algorithm is a simple kernel regression model[70,71] that uses activation energies from *ab initio* calculations of previous sites $\mathbf{x}_j$ ($j = 1, 2, 3, \ldots, n$) in a weighted average to estimate the activation energy of a new site with local environment $\mathbf{x}$

$$\hat{E}_a(\mathbf{x}) = \frac{\sum_j^n E_a(\mathbf{x}_j) w(\mathbf{x}, \mathbf{x}_j)}{\sum_j w(\mathbf{x}, \mathbf{x}_j)}. \tag{5.13}$$

Here, $\hat{E}_a(\mathbf{x})$ is the predicted activation energy, and the $E_a(\mathbf{x}_j)$ are computed activation energies in the training set. The $w(\mathbf{x}, \mathbf{x}_j)$ function is a Gaussian kernel:

$$w(\mathbf{x}, \mathbf{x}_j) = \exp[-d^2(\mathbf{x}, \mathbf{x}_j)], \tag{5.14}$$

that depends on the Mahalonobis distance,[72] d:

$$d^2(\mathbf{x}, \mathbf{x}_j) = (\mathbf{x} - \mathbf{x}_j)^T \mathbf{S} (\mathbf{x} - \mathbf{x}_j). \tag{5.15}$$

Here, $\mathbf{S}$ is a $\dim(\mathbf{x}) \times \dim(\mathbf{x})$ dimensional, positive definite, and symmetric matrix. The ML model was trained to fit the training data (the cumulative set of completed *ab initio* calculations) by optimizing elements of $\mathbf{S}$ to minimize the sum of leave-one-out losses, Section 3.3. The ML kernel regression-based procedure can intuitively be thought of as similarity-based interpolation. If a site has a similar local environment to a site in the training set, the Mahalanobis distance will be small and that site will have a large weight in the weighted average. For the model system in Chapter 4, importance learning

accelerated convergence to the correct activation energy by several orders of magnitude over standard sampling and reweighting procedures. The importance learning algorithm obtained $\langle E_a \rangle_k$ to within 0.75 kJ/mol of the correct site-averaged value with fewer than 100 training set calculations, Figure 4.8.

5.3.3 Site-averaged TOF for model amorphous catalyst

The site-averaged TOF for the model catalyst is given by inserting eqn. 5.9 into eqn. 5.3,

$$\langle \mathscr{t} \rangle = \langle k \rangle c_{\mathbf{A}} = \langle K(\mathbf{x}) k_2 \rangle c_{\mathbf{A}} \tag{5.16}$$

From eqns. 5.10 and 5.11, $k(\mathbf{x})$ can be expanded as

$$k(\mathbf{x}) = \frac{k_B T}{h} \exp\left[-\frac{\Delta H(\mathbf{x}) - T\Delta S}{k_B T}\right] \exp\left[-\frac{\Delta H^{\ddagger} - T\Delta S^{\ddagger}}{k_B T}\right] \tag{5.17}$$

The apparent rate constant can be converted to an Arrhenius form by using the definition of $E_a(\mathbf{x}_i)$ from eqn. 5.12,

$$\begin{aligned} k(\mathbf{x}) &= \frac{k_B T}{h} \exp\left[\frac{\Delta S + \Delta S^{\ddagger} + 2k_B}{k_B}\right] \exp\left[-\frac{\Delta H(\mathbf{x}) + \Delta H^{\ddagger} + 2k_B T}{k_B T}\right] \\ &= k_0 \exp[-\beta E_a(\mathbf{x})] \end{aligned} \tag{5.18}$$

Where $k_0 = k_B T h^{-1} \exp[(\Delta S + \Delta S^{\ddagger} + 2k_B)/k_B]$. In the first line, the rate constant was multiplied by $\exp[-2]\exp[2]$ to express the $k(\mathbf{x})$ in terms of $E_a(\mathbf{x})$. The average TOF is then

$$\begin{aligned} \langle \mathscr{t} \rangle &= \langle k_0 \exp[-\beta E_a(\mathbf{x})] \rangle c_{\mathbf{A}} \\ &= k_0 \langle \exp[-\beta E_a(\mathbf{x})] \rangle c_{\mathbf{A}} \end{aligned} \tag{5.19}$$

Eqn. 5.19 is a special case where the prefactor k_0 does not depend on the local environment only because of the simplicity of our model. For *ab initio* calculations on real amorphous catalysts, terms like ΔS and $\Delta S^{\ddagger}$ will have some dependence on $\mathbf{x}$ through

vibrational contributions in the partition function. The explicit dependence will likely depend on both the support type, the metal center, and the coordination environment. We expect the entropic contributions to be weaker functions of the local geometry than the enthalpic contributions. The calculations below focus on $\langle \lambda \rangle / k_0 = \langle \exp[-\beta \hat{E}_a] \rangle$ because the prefactor in our model is independent of $\mathbf{x}$. For reference, a histogram of $\rho(E_a)$ is shown in Figure 5.3.

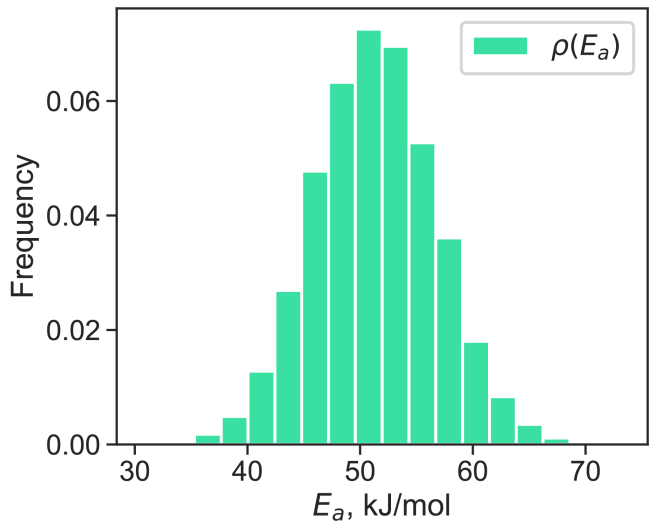

Figure 5.3: Histogram of the activation energy distribution, $\rho(E_a)$.

The site-averaged TOF was estimated using the same data from the importance learning algorithm in previous work. The ML model from importance learning, $\hat{\rho}(\hat{E}_a)$ is also used to approximate $\rho(E_a)$. Note that at each iteration, the ML model is retrained with the E_a of the importance sampled site appended to the training set. As the number of importance learning iterations increases, $\hat{\rho}(\hat{E}_a)$ and $\hat{\rho}(\hat{E}_a)\exp[-\beta \hat{E}_a]$ will become more accurate. The convergence of $\langle \exp[-\beta \hat{E}_a] \rangle$ is shown in Figure 5.4.

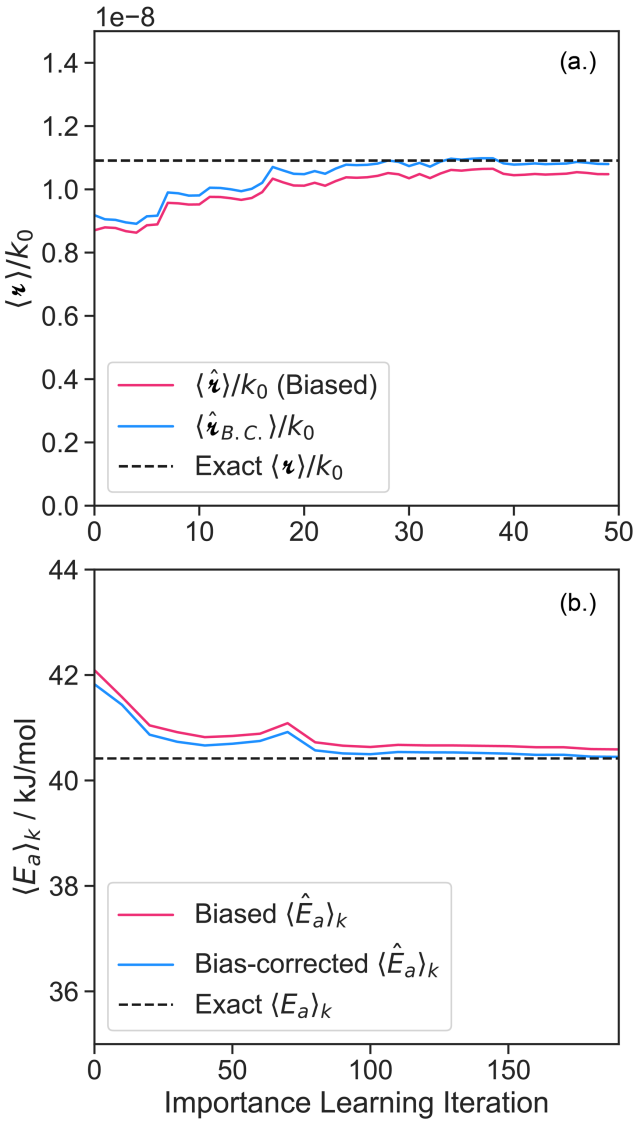

Figure 5.4: Figure 4: (a.) Convergence of $\langle \hat{r} \rangle / k_0 = \langle \exp[-\beta \hat{E}_a] \rangle$ using the ML model from different numbers of importance learning iterations. The red curve shows the biased $\langle \hat{r} \rangle / k_0$, computed according to eqn. 5.7. The blue curve corrects for bias, $\langle \hat{r}_{\text{B.C.}} \rangle / k_0$, using eqn. 5.8. (b.) The bias-corrected, site-averaged activation energy predicted by the ML model also quickly converges to the correct value. (Chapter 4 estimated $\langle \hat{E}_a \rangle_k$ by averaging the importance sampled sites.) From Appendix C.3 the bias-corrected $\langle \hat{E}_a \rangle_k$ estimate is $\langle \hat{E}_a \rangle_{k,B.C.} = \langle \hat{E}_a \rangle_k - \beta \sigma_r^2$.

The biased $\langle \hat{r} \rangle / k_0$ estimate continues to underestimate the rate after 50 importance learning iterations and even after 374 iterations, Figure D.2 and D.3. After just ca. 25

iterations of importance learning, the biased-corrected $\langle \hat{\boldsymbol{\imath}} \rangle / k_0$ estimate converges to the exact $\langle \boldsymbol{\imath} \rangle / k_0$ value. The biased-corrected $\langle \hat{\boldsymbol{\imath}} \rangle / k_0$ also underpredicts the bias for the first ca. 25 importance learning iterations. This occurs because the errors in the ML model are non-uniform across E_a. In the early iterations of importance learning, the errors of low-E_a sites will be larger than higher E_a sites from the dearth of data (Figure D.4). The errors of low-E_a sites are particularly important since they are exponentially magnified by eqn. 5.7. However, the number of these sites is not large enough to sizably contribute to σ_r in eqn. 5.8. As enough low-E_a sites are importance sampled, the ML model error becomes more uniform across E_a, and eqn. 5.8 correctly accounts for the bias, Figure D.5.

5.4 Conclusions

Ab initio calculations on single atom catalysts on amorphous supports have been limited by an inability to account for the non-equilibrium, preparation dependent, and quenched disordered ensemble of sites in predictions of kinetic properties. Every site also has a different local environment, different activation parameters, and kinetics that exponentially magnify the differences. Given a model of the amorphous solid catalyst, kinetic predictions that average over the site distribution with standard sampling methods require an intractable sample size for *ab initio* calculations. We first addressed these theoretical challenges with the importance learning algorithm, which converged an estimate of the site-averaged activation energy thousands of times faster than random sampling with reweighting.

This chapter extends our previous efforts by presenting an efficient estimator for the site-averaged absolute rate, $\langle \boldsymbol{\imath} \rangle / k_0$. We first showed how $\langle \boldsymbol{\imath} \rangle$ could be split into a product of judiciously weighted averages for $A(\mathbf{x})$ and $\exp[-\beta E_a(\mathbf{x})]$. Both averages

use the same information the importance learning algorithm uses to estimate the site-averaged activation energy, $\langle E_a \rangle_k$. Thus, $\langle \boldsymbol{z} \rangle$ can be computed concurrently with $\langle E_a \rangle_k$ during importance learning, without additional, expensive *ab initio* calculations. We illustrated the $\langle \boldsymbol{z} \rangle$-estimator using the same simple model of a Langmuir-Hinshelwood reaction on a support with quenched-disorder used to demonstrate importance learning $\langle E_a \rangle_k$. Estimates of $\langle \boldsymbol{z} \rangle$ rapidly converged within 1% of the exact value by iteration 30 of importance learning. We also showed how to correct for errors in ML model when computing $\langle \boldsymbol{z} \rangle$. The enormous acceleration affected by these new importance learning tools should enable the first *ab initio* studies of these catalysts with proper site-averaged rate predictions.

Bibliography

1. Matar, S., Mirbach, M. J. & Tayim, H. A. *Catalysis in Petrochemical Processes* 200. https://www.doi.org/10.1007/978-94-009-1177-2 (Kluwer Academic Publishers, Dordrecht, 1989).

2. Pollak, P. *Fine Chemicals: The Industry and the Business* 2nd, 280. https://books.google.com/books?id=yuxJGasHvkoC (Wiley, Boboken, New Jersey, 2011).

3. Patterson, H. B. W. *Hydrogenation of Fats and Oils - Theory and Practice* 2nd, 420 (AOCS Press, Urbana, 2009).

4. Nørskov, J. K. *et al.* The nature of the active site in heterogeneous metal catalysis. *Chem. Soc. Rev.* **37,** 2163–2171. https://www.doi.org/10.1039/b800260f (2008).

5. Goodman, E. D., Schwalbe, J. A. & Cargnello, M. Mechanistic Understanding and the Rational Design of Sinter-Resistant Heterogeneous Catalysts. *ACS Catal.* **7,** 7156–7173. https://www.doi.org/10.1021/acscatal.7b01975 (2017).

6. Chen, K. & Arnold, F. H. Engineering new catalytic activities in enzymes. *Nat. Catal.* **3,** 203–213. https://www.doi.org/10.1038/s41929-019-0385-5 (2020).

7. Jin, R., Li, G., Sharma, S., Li, Y. & Du, X. Toward Active-Site Tailoring in Heterogeneous Catalysis by Atomically Precise Metal Nanoclusters with Crystallographic

Structures. *Chem. Rev.* **121,** 567–648. https://www.doi.org/10.1021/acs.chemrev.0c00495 (2020).

8. Perego, G. Characterization of heterogeneous catalysts by X-ray diffraction techniques. *Catal. Today* **41,** 251–259. https://www.doi.org/10.1016/S0920-5861(98)00054-6 (1998).

9. Hargreaves, J. S. J. Powder X-ray diffraction and heterogeneous catalysis. *Crystallogr. Rev.* **11,** 21–34. https://www.doi.org/10.1080/08893110500078324 (2005).

10. Gutmann, T. *et al.* Solid-state NMR concepts for the investigation of supported transition metal catalysts and nanoparticles. *Solid State Nucl. Magn. Reson.* **55-56,** 1–11. https://www.doi.org/10.1016/j.ssnmr.2013.06.004 (2013).

11. Xu, J., Wang, Q. & Deng, F. Metal Active Sites and Their Catalytic Functions in Zeolites: Insights from Solid-State NMR Spectroscopy. *Acc. Chem. Res.* **52,** 2179–2189. https://www.doi.org/10.1021/acs.accounts.9b00125 (2019).

12. Venezia, A. M. X-ray photoelectron spectroscopy (XPS) for catalysts characterization. *Catal. Today* **77,** 359–370. https://www.doi.org/10.1016/S0920-5861(02)00380-2 (2003).

13. Nelson, R. C. & Miller, J. T. An introduction to X-ray absorption spectroscopy and its in situ application to organometallic compounds and homogeneous catalysts. *Catal. Sci. Technol.* **2,** 461–470. https://www.doi.org/10.1039/c2cy00343k (2012).

14. Shimizu, K. I., Kamiya, Y., Osaki, K., Yoshida, H. & Satsuma, A. The average Pd oxidation state in Pd/SiO 2 quantified by L 3-edge XANES analysis and its effects

on catalytic activity for CO oxidation. *Catal. Sci. Technol.* **2,** 767–772. https://www.doi.org/10.1039/c2cy00422d (2012).

15. Li, S. & Deng, F. Recent Advances of Solid-State NMR Studies on Zeolites. *Annu. Rep. NMR Spectrosc.* **78,** 1–54. https://www.doi.org/10.1016/B978-0-12-404716-7.00001-8 (2013).

16. Van Santen, R. A. & Neurock, M. *Molecular Heterogeneous Catalysis* https://www.doi.org/10.1002/9783527610846.ch2 (Wiley-VCH, Weinheim, Germany, 2007).

17. Nørskov, J. K., Bligaard, T., Rossmeisl, J. & Christensen, C. H. Towards the computational design of solid catalysts. *Nat. Chem.* **1,** 37–46. https://www.doi.org/10.1038/nchem.121 (2009).

18. Besora, M. & Maseras, F. Microkinetic modeling in homogeneous catalysis. *WIREs Comput. Mol. Sci.* **8,** e1372. https://www.doi.org/10.1002/wcms.1372 (2018).

19. Motagamwala, A. H., Ball, M. R. & Dumesic, J. A. Microkinetic analysis and scaling relations for catalyst design. *Annu. Rev. Chem. Biomol. Eng.* **9,** 413–450. https://www.doi.org/10.1146/annurev-chembioeng-060817-084103 (2018).

20. Goldsmith, B. R., Peters, B., Johnson, J. K., Gates, B. C. & Scott, S. L. Beyond Ordered Materials: Understanding Catalytic Sites on Amorphous Solids. *ACS Catal.* **7,** 7543–7757. https://www.doi.org/10.1021/acscatal.7b01767 (2017).

21. Zhang, Z., Zandkarimi, B. & Alexandrova, A. N. Ensembles of Metastable States Govern Heterogeneous Catalysis on Dynamic Interfaces. *Acc. Chem. Res.* **53,** 447–458. https://www.doi.org/10.1021/acs.accounts.9b00531 (2020).

22. Zwanzig, R. Rate Processes with Dynamical Disorder. *Acc. Chem. Res.* **23,** 148–152. https://www.doi.org/10.1021/ar00173a005 (1990).

23. Xing, X., Yoon, B., Landman, U. & Parks, J. H. Structural evolution of Au nanoclusters: From planar to cage to tubular motifs. *Phys. Rev. B* **74,** 165423. https://www.doi.org/10.1103/PhysRevB.74.165423 (2006).

24. Guedes-Sobrinho, D., Wang, W., Hamilton, I. P., Da Silva, J. L. F. & Ghiringhelli, L. M. (Meta-)stability and Core-Shell Dynamics of Gold Nanoclusters at Finite Temperature. *J. Phys. Chem. Lett.* **10,** 685–692. https://www.doi.org/10.1021/acs.jpclett.8b03397 (2019).

25. Guo, H., Sautet, P. & Alexandrova, A. N. Reagent-Triggered Isomerization of Fluxional Cluster Catalyst via Dynamic Coupling. *J. Phys. Chem. Lett.* **11,** 3089–3094. https://www.doi.org/10.1021/acs.jpclett.0c00548 (2020).

26. Christiansen, J. A. The Elucidation of Reaction Mechanisms by the Method of Intermediates in Quasi-Stationary Concentrations. *Adv. Catal.* **5,** 311–353. https://www.doi.org/10.1016/S0360-0564(08)60644-6 (1953).

27. Min, W. *et al.* Fluctuating enzymes: Lessons from single-molecule studies. *Acc. Chem. Res.* **38,** 923–931. https://www.doi.org/10.1021/ar040133f (2005).

28. Min, W., Xie, X. S. & Bagchi, B. Role of conformational dynamics in kinetics of an enzymatic cycle in a nonequilibrium steady state. *J. Chem. Phys.* **131,** 065104. https://www.doi.org/10.1063/1.3207274 (2009).

29. Peters, B. *Reaction Rate Theory and Rare Events* **20178817,** xiv, 619 pages (Elsevier, Amsterdam ; Cambrige, MA, 2017).

30. Tanaka, S. *et al.* A nanostructured skeleton catalyst: Suzuki-coupling with a reusable and sustainable nanoporous metallic glass Pd-catalyst. *Chem. Commun.* **27,** 5985–5987. https://www.doi.org/10.1039/c1cc10710k (2011).

31. Hasannaeimi, V. & Mukherjee, S. Noble-Metal based Metallic Glasses as Highly Catalytic Materials for Hydrogen Oxidation Reaction in Fuel Cells. *Sci. Rep.* **9,** 12136. https://www.doi.org/10.1038/s41598-019-48582-7 (2019).

32. Jia, Z. *et al.* Attractive In Situ Self-Reconstructed Hierarchical Gradient Structure of Metallic Glass for High Efficiency and Remarkable Stability in Catalytic Performance. *Adv. Funct. Mater.* **29,** 1807857. https://www.doi.org/10.1002/adfm.201807857 (2019).

33. Nellaiappan, S. *et al.* High-Entropy Alloys as Catalysts for the CO2 and CO Reduction Reactions: Experimental Realization. *ACS Catal.* **10,** 3658–3663. https://www.doi.org/10.1021/acscatal.9b04302 (2020).

34. Pedersen, J. K., Batchelor, T. A. A., Bagger, A. & Rossmeisl, J. High-entropy alloys as catalysts for the CO2 and CO reduction reactions. *ACS Catal.* **10,** 2169–2176. https://www.doi.org/10.1021/acscatal.9b04343 (2020).

35. Bui, L. & Bhan, A. Mechanisms for C-C bond cleavage and formation during acrolein production on a mixed metal oxide catalyst. *Appl. Catal., A* **546,** 87–95. https://www.doi.org/10.1016/j.apcata.2017.08.011 (2017).

36. Thomas, J. M., Raja, R. & Lewis, D. W. Single-site heterogeneous catalysts. *Angew. Chem., Int. Ed.* **44,** 6456–6482. https://www.doi.org/10.1002/anie.200462473 (2005).

37. Coperet, C. *et al.* Surface Organometallic and Coordination Chemistry toward Single-Site Heterogeneous Catalysts: Strategies, Methods, Structures, and Activities. *Chem. Rev.* **116,** 323–421. https://www.doi.org/10.1021/acs.chemrev.5b00373 (2016).

38. Wang, A., Li, J. & Zhang, T. Heterogeneous single-atom catalysis. *Nat. Rev. Chem.* **2,** 65–81. https://doi.org/10.1038/s41570-018-0010-1 (2018).

39. Chauvin, Y. & Commereuc, D. Chemical counting and characterization of the active sites in the rhenium oxide/alumina metathesis catalyst. *J. Chem. Soc., Chem. Commun.* **6,** 462–464. https://doi.org/10.1039/C39920000462 (1992).

40. McDaniel, M. P. A Review of the Phillips Supported Chromium Catalyst and Its Commercial Use for Ethylene Polymerization. English. *Adv. Catal.* **53,** 123–606. https://www.doi.org/https://doi.org/10.1016/S0360-0564(10)53003-7 (2010).

41. Amakawa, K. *et al.* Active Sites in Olefin Metathesis over Supported Molybdena Catalysts. *ChemCatChem* **7,** 4059–4065. https://www.doi.org/10.1002/cctc.201500725 (2015).

42. Howell, J. G., Li, Y. P. & Bell, A. T. Propene Metathesis over Supported Tungsten Oxide Catalysts: A Study of Active Site Formation. *ACS Catal.* **6,** 7728–7738. https://doi.org/10.1021/acscatal.6b01842 (2016).

43. Merryfield, R., McDaniel, M. & Parks, G. An XPS study of the Phillips Cr/silica polymerization catalyst. *J. Catal.* **77,** 348–359. https://www.doi.org/10.1016/0021-9517(82)90178-6 (1982).

44. Feher, F. J. & Blanski, R. L. Polyhedral oligometallasilasesquioxanes as models for silica-supported catalysts: Chromium attached to two vicinal siloxy groups. *J. Chem. Soc., Chem. Commun.,* 1614–1616. https://www.doi.org/10.1039/C39900001614 (1990).

45. Amor Nait Ajjou, J. & Scott, S. L. A kinetic study of ethylene and 1-hexene homo- and copolymerization catalyzed by a silica-supported Cr(IV) complex: Evidence for

propagation by a migratory insertion mechanism. *J. Am. Chem. Soc.* **122,** 8968–8976. https://www.doi.org/10.1021/ja001693m (2000).

46. McGuinness, D. S., Davies, N. W., Horne, J. & Ivanov, I. Unraveling the Mechanism of Polymerization with the Phillips Catalyst. *Organometallics* **29,** 6111–6116. https://www.doi.org/10.1021/om100883n (2010).

47. Conley, M. P. *et al.* Polymerization of ethylene by silica-supported dinuclear CrII-IIsites through an initiation step involving C=H bond activation. *Angew. Chem., Int. Ed.* **53,** 1872–1876. https://www.doi.org/10.1002/anie.201308983 (2014).

48. Peters, B., Scott, S. L., Fong, A., Wang, Y. & Stiegman, A. E. Reexamining the Evidence for Proton Transfers in Ethylene Polymerization. *Proc. Natl. Acad. Sci. USA* **112,** E4160–E4161. https://www.doi.org/10.1073/pnas.1422589112 (2015).

49. Gierada, M., Michorczyk, P., Tielens, F. & Handzlik, J. Reduction of chromia-silica catalysts: A molecular picture. *J. Catal.* **340,** 122–135. https://www.doi.org/10.1016/j.jcat.2016.04.022 (2016).

50. Handzlik, J., Grybos, R. & Tielens, F. Isolated Chromium(VI) Oxide Species Supported on Al-Modified Silica: A Molecular Description. *J. Phys. Chem. C* **120,** 17594–17603. https://www.doi.org/10.1021/acs.jpcc.6b05675 (2016).

51. Fong, A., Vandervelden, C., Scott, S. L. & Peters, B. Computational Support for Phillips Catalyst Initiation via Cr-C Bond Homolysis in a Chromacyclopentane Site. *ACS Catal.* **8,** 1728–1733. https://doi.org/10.1021/acscatal.7b03724 (2018).

52. Groppo, E., Martino, G. A., Piovano, A. & Barzan, C. The Active Sites in the Phillips Catalysts: Origins of a Lively Debate and a Vision for the Future. *ACS*

Catal. **8,** 10846–10863. https://www.doi.org/10.1021/acscatal.8b02521 (2018).

53. Van Ginhoven, R. M., Jónsson, H. & Corrales, L. R. Silica glass structure generation for ab initio calculations using small samples of amorphous silica. *Phys. Rev. B* **71,** 024208. https://www.doi.org/10.1103/PhysRevB.71.024208 (2005).

54. Gulmen, T. S. & Thompson, W. H. Testing a two-state model of nanoconfined liquids: Conformational equilibrium of ethylene glycol in amorphous silica pores. *Langmuir* **22,** 10919–10923. https://www.doi.org/10.1021/la062285k (2006).

55. Tielens, F., Gervais, C., Lambert, J. F., Mauri, F. & Costa, D. Ab initio study of the hydroxylated surface of amorphous silica: A representative model. *Chem. Mater.* **20,** 3336–3344. https://www.doi.org/10.1021/cm8001173 (2008).

56. Ugliengo, P. *et al.* Realistic models of hydroxylated amorphous silica surfaces and MCM- 41 mesoporous material simulated by large-scale periodic B3LYP calculations. *Adv. Mater.* **20,** 4579–4583. https://www.doi.org/10.1002/adma.200801489 (2008).

57. Ewing, C. S., Bhavsar, S., Veser, G., McCarthy, J. J. & Johnson, J. K. Accurate amorphous silica surface models from first-principles thermodynamics of surface dehydroxylation. *Langmuir* **30,** 5133–5141. https://doi.org/10.1021/la500422p (2014).

58. Comas-Vives, A. Amorphous SiO_2 surface models: Energetics of the dehydroxylation process, strain, ab initio atomistic thermodynamics and IR spectroscopic signatures. *Phys. Chem. Chem. Phys.* **18,** 7475–7482. https://www.doi.org/10.1039/c6cp00602g (2016).

59. Jystad, A. M., Biancardi, A. & Caricato, M. Simulations of Ammonia Adsorption for the Characterization of Acid Sites in Metal-Doped Amorphous Silicates. *J. Phys. Chem. C* **121,** 22258–22267. https://www.doi.org/10.1021/acs.jpcc.7b08113 (2017).

60. Tielens, F., Gierada, M., Handzlik, J. & Calatayud, M. Characterization of amorphous silica based catalysts using DFT computational methods. *Catal. Today* **354,** 3–18. https://www.doi.org/10.1016/j.cattod.2019.03.062 (2020).

61. Peters, B. & Scott, S. L. Single Atom Catalysts on Amorphous Supports: A Quenched Disorder Perspective. *J. Chem. Phys.* **142,** 104708. https://www.doi.org/10.1063/1.4914145 (2015).

62. Zhang, J., Hu, P. & Wang, H. Amorphous Catalysis: Machine Learning Driven High-Throughput Screening of Superior Active Site for Hydrogen Evolution Reaction. *J. Phys. Chem. C* **124,** 10483–10494. https://www.doi.org/10.1021/acs.jpcc.0c00406 (2020).

63. Devine, R. A. B. *The Physics and Technology of Amorphous SiO_2* https://books.google.com/books?id=8rbvAAAAMAAJ (Springer US, Boston, MA, 1988).

64. Abdillah, B., Rice, G. L. & Scott, S. L. Mono- and Dinuclear Silica-Supported Titanium(IV) Complexes and the Effect of TiOTi Connectivity on Reactivity. *J. Am. Chem. Soc.* **121,** 7201–7210. https://www.doi.org/10.1021/JA9829160 (1999).

65. Notestein, J. M., Iglesia, E. & Katz, A. Grafted Metallocalixarenes as Single-Site Surface Organometallic Catalysts. *J. Am. Chem. Soc.* **126,** 16478–16486. https://www.doi.org/10.1021/ja0470259 (2004).

66. Pelletier, J. D. A. & Basset, J.-M. Catalysis by Design: Well-Defined Single-Site Heterogeneous Catalysts. *Acc. Chem. Res.* **49,** 664–677. https://www.doi.org/10.1021/acs.accounts.5b00518 (2016).

67. Boudart, M. & Djega-Mariadassou, G. *Kinetics of Heterogeneous Catalytic Reactions* https://books.google.com/books?id=iqf_AwAAQBAJ (Princeton University Press, Princeton, 2014).

68. Goldsmith, B. R., Sanderson, E. D., Bean, D. & Peters, B. Isolated Catalyst Sites on Amorphous Supports: A Systematic Algorithm for Understanding Heterogeneities in Structure and Reactivity. *J. Chem. Phys.* **138,** 204105. https://www.doi.org/10.1063/1.4807384 (2013).

69. Fong, A., Yuan, Y., Ivry, S. L., Scott, S. L. & Peters, B. Computational Kinetic Discrimination of Ethylene Polymerization Mechanisms for the Phillips (Cr/SiO_2) Catalyst. English. *ACS Catal.* **5,** 3360–3374. https://www.doi.org/10.1021/acscatal.5b00016 (2015).

70. Weinberger, K. Q. & Tesauro, G. Metric Learning for Kernel Regression. *J. Mach. Learn. Res.,* 8. http://proceedings.mlr.press/v2/weinberger07a.html (2007).

71. Hofmann, T., Schölkopf, B. & Smola, A. J. Kernel methods in machine learning. *Ann. Stat.* **36,** 1171–1220. https://www.doi.org/10.1214/009053607000000677 (2008).

72. Mahalanobis, P. C. On the generalized distance in statistics. *Proc. Natl. Inst. Sci. India* **2,** 49–55. https://doi.org/10.1007/s13171-019-00164-5 (1936).

Chapter 6

Predicted Properties of Active Catalyst Sites on Amorphous Silica: Impact of Silica Pre-Optimization Protocol

6.1 Introduction

Amorphous silica is frequently used as a support for industrial heterogeneous catalysts. The term amorphous silica refers to several different materials, including silicas made by sol-gel synthesis, spray drying, pyrolysis, and precipitation methods.[1–5] The resulting supports are typically characterized to determine their silanol densities, but the precise atomic structure is unknown. Additionally, these materials "remember" their non-equilibrium preparation history, which also influences their catalytic properties.[6,7] Theoretical considerations suggest that, even within a single amorphous silica material, a distribution of structurally different sites gives a distribution of different activities.[8] Although there has been recent progress with simple model systems, (Chapters 3, 4, and 5), it remains unclear which structural features on the surface of real silica most directly

influence the activity of a supported catalyst.[9,10]

Many computational studies rely on "supermolecular" cluster models, where a portion of the amorphous silica is carved out from an extended-solid model and treated with standard quantum mechanical (QM) methods used for molecules. This approach has the advantage that high QM levels of theory can be used for modeling the catalytic site, contrary to periodic boundary conditions (PBC) approaches. Three types of disorder impact the computed activity of catalyst sites on amorphous silica in cluster models: quenched disorder,[8] dynamical disorder,[11] and procedural disorder. The effects of dynamical disorder have been examined in several modeling efforts.[12–18] A few recent computational studies examined the effects of quenched disorder.[9,19–21] To our knowledge the impact of procedural disorder, an easily overlooked artifact of cluster models for amorphous solids, has not previously been examined.

The disordered siloxane ring network in amorphous silica is quenched, *i.e.*, these features are locked-in by strong bonds that do not rearrange on the time scale of catalytic reactions.[22] In contrast, silanols on the surface of silica form dynamically disordered hydrogen bond networks, *i.e.*, these involve weak fluxional bonds that can rearrange quickly, perhaps even within the time scale of a single catalytic turnover. Note that the effects of hydrogen bond network rearrangements of liquid water,[23] ice,[24,25] and polar compounds adsorbed to metal surfaces[26] have already been extensively studied. The quenched and dynamical disorder contributions undoubtedly influence the activity of catalyst sites on real amorphous silicas. The quenched disorder gives each active site unique properties, while the dynamically disordered degrees of freedom influence the free energy of intermediates and transition states. Figure 6.1 shows a schematic of the energy landscape as a function of quenched and dynamically disordered degrees freedom.

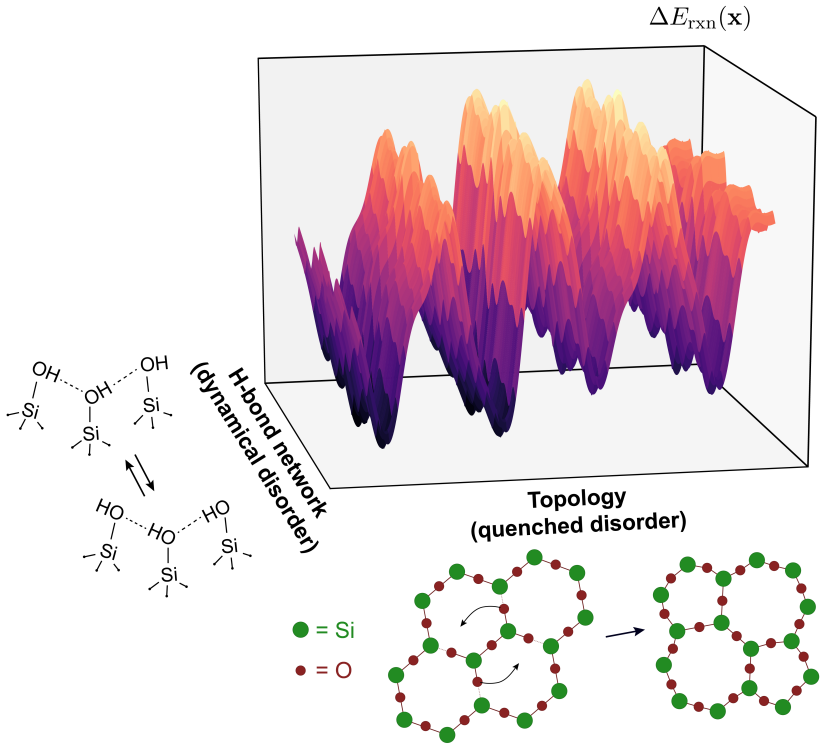

Figure 6.1: Schematic showing how the free energy of an intermediate depends on quenched and dynamically disordered degrees of freedom. Barriers to motion along the quenched degree of freedom are impassable at temperatures of catalyst operation. In contrast, barriers for motion along the dynamically disordered degrees of freedom are easily traversed at temperatures of catalyst operation.

Modeling of these catalysts proceeds in two steps: (1) creating models of amorphous silica surfaces with representative quenched and dynamical structural disorder, and (2) creating cluster models of the active sites on these surfaces that are amenable to accurate QM calculations for the thermodynamics and kinetics. Models of amorphous silica surfaces are typically created by melting 3D-periodic crystalline silica in a high temperature molecular dynamics (MD) simulation, rapidly quenching the silica to a lower temperature, cutting the bulk silica into slabs with 2D periodicity followed by a re-equilibration step, and creating surface ≡SiOH (silanol) groups.[19,27–31] In many cases, additional equilibration, annealing, and condensation steps are included to adjust the silanol orientation

and density. These additional steps are usually performed with the same MD empirical force fields because, unlike the small unit cell of crystalline materials like zeolites, the amorphous silica model typically contains thousands of Si and O atoms.[10] The details of these procedures vary widely. They give different bond angle and ring size distributions, and different proportions of geminal, vicinal, and isolated silanols. It is difficult to identify the best procedure given the lack of detailed structural data from experiments,[9,32] but we do not concentrate on this important issue here.

Procedural disorder stems from steps that follow the melt, quench, cut, and cap (MQCC) steps in the formation of amorphous silica, *i.e.*, after the creation of a quenched extended support model. Following creation of a classical amorphous silica model, a catalytic site is introduced, usually including at least one metal center,[9,33] and QM methods are employed to study the reactivity of the site, typically based on density functional theory (DFT).[34] Although periodic boundary conditions (PBC-DFT) calculations are possible, they require a large simulation cell to accurately capture the quenched disorder.[31] This limits the number of silica replicas that can be investigated and the accuracy of the level of theory that can be employed (*e.g.*, using accurate hybrid or double-hybrid functionals is not feasible). In fact, most studies only report results for a single model of an active site.

An alternative approach is to carve a cluster model from the classical slab, and treat it as a supermolecule.[19,35,36] This is reasonable because silica is an insulator and long-range electronic interactions should not have a considerable effect.[37,38] The size of the cluster can be adjusted to provide an acceptable cost-accuracy balance. The cluster size should be large enough so that reactants/intermediates/products interact with the catalytic sites in a realistic manner (including steric effects, electrostatic/dispersion attraction, and H-bonding).[39–41] However, the cluster model should also be small enough so accurate QM methods and basis sets remain computationally tractable. Clusters that

contain a few hundred atoms are often necessary, and cluster models with just two tetrahedral Si atoms are likely insufficient.[10] The procedures to create these cluster models of amorphous silica[33,42] resemble those used to create cluster models of zeolites.[43,44] The cluster encompasses all atoms within some cutoff away from a site of interest, all "peripheral" Si-O-Si linkages beyond the cutoff are cut, and dangling bonds are terminated with capping atoms like F, H, or OH groups. In most,[9,19,31,35,45] but not all cases,[46,47] the peripheral atoms are constrained during subsequent analyses of adsorption and reactivity to mimic the structural constraints imposed by the silica matrix. These procedures are largely conserved across different protocols in the literature,[31] but the protocols differ in other subtle and potentially important aspects, which lead to the procedural disorder introduced above.

For cluster models of zeolites, the peripheral atoms are positioned according to corresponding positions of atoms in the experimental zeolite structure.[38,48] This is not possible in amorphous silica models. Instead, most of the cluster is fixed at the geometry obtained as a snapshot from a classical low-temperature MD simulation. A relatively small portion surrounding the active site is relaxed with the QM Hamiltonian, *i.e.*, the "relaxed zone". Therefore, the interior atoms of the cluster relax subject to the perturbed peripheral positions and not to the positions from a QM optimization on the full system. For a given cluster model size and a given catalytic reaction, cluster models constructed as described above may appear to give a perfectly reasonable set of barriers and intermediate free energies. However, the location of the boundary between the MD fixed region and QM reactive/flexible region affects the results. Each time the radius of the relaxed zone is increased, new peripheral constraints are released and allowed to relax. These perturbed degrees of freedom tug on the interior atoms from longer distances as the relaxation radius grows. Presumably the force that a relaxing constraint exerts on the active site is attenuated by distance, but the number of perturbed degrees of freedom grows as

the radius grows. The convergence (if it may be assumed at all) involves a complicated interplay between elastic forces on a random network of bonds with somewhat random perturbations imposed at the periphery. We hypothesize that faster and smoother convergence of the QM reaction barriers and energies can be achieved by starting from a large amorphous silica cluster model that is pre-optimized with the QM Hamiltonian, as shown in Figure 6.2.

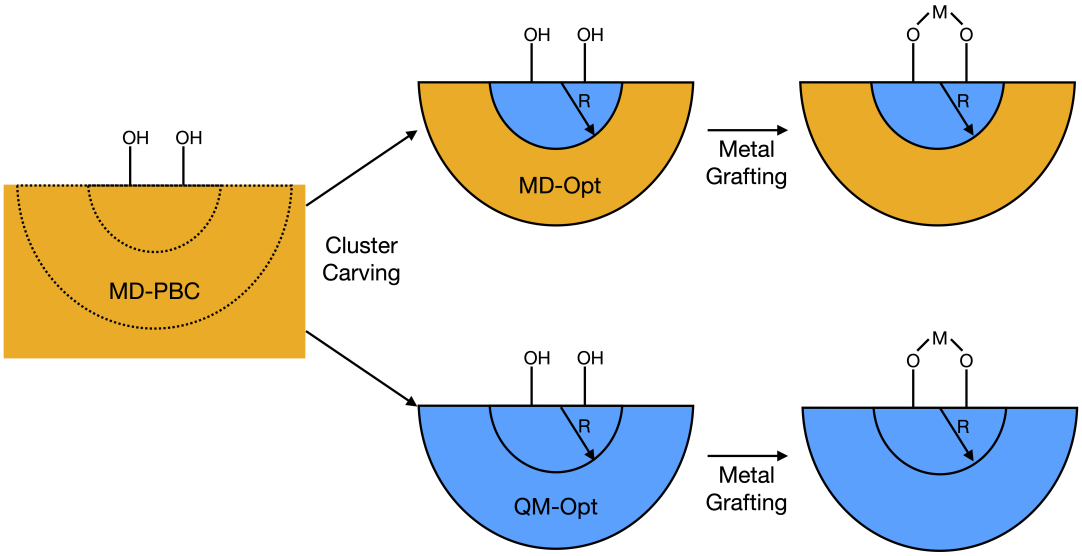

Figure 6.2: Schematic illustrating two different optimization protocols, MD-Opt and QM-Opt. In the MD-opt protocol, only the region within the radius R is relaxed with the QM Hamiltonian before and after grafting (in blue), while the rest is frozen at the MD geometry (in green). In the QM-Opt protocol, the whole cluster is pre-optimized at QM level, then the region within the radius R is relaxed again after grafting.

In this paper, we study the convergence of reaction energies vs. size of the relaxed zone, represented by the R radius in Figure 6.2, for clusters starting from the MD and QM pre-optimized structure. We call the two protocols "MD-Opt" and "QM-Opt", respectively, throughout the paper. This comparison is carried out using atomistic models treated at DFT level, and an empirical disordered lattice model that allows us to explore significantly larger cluster model sizes. We use the grafting reaction of a dioxo-Cr group, *i.e.*, the initial grafted site in the Phillips catalyst,[49] as an example. We also perform a

computational cost analysis of the two optimization protocols and a structural analysis of the active site based on the relaxation radius.

The paper is organized as follows. In Section 6.2.1, we introduce a disordered lattice model that allows analysis of convergence over long length scales. In Section 6.2.2 we review the atomistic SiO_2 cluster models. In Section 6.3, we compare how the energy of a grafting reaction converges with cluster model size for the MD-Opt and QM-Opt optimization protocols. For the atomistic SiO_2 models, we also compare the computational cost of the the QM-Opt and MD-Opt protocols. Finally, we compare the optimized structures of both protocols and examine which degrees of freedom in the atomistic cluster models are most labile. Finally, Section 6.4 summarizes the results and reports concluding remarks.

6.2 Computational Details

6.2.1 Disordered Lattice Model

The disordered lattice model (DLM) aims to mimic the qualitative characteristics of an amorphous support like silica and precursor grafting reactions. Like MD and MM calculations for atomistic models, reactant and product geometries in the DLM are identified by geometry optimizations. Because the DLM uses simple classical potentials, we can examine convergence with considerably larger cluster models than with DFT. The quenched disorder is modeled through a random network of elastic bonds, with different forcefield parameters corresponding to the "QM" and "MD" Hamiltonians.

The DLM initially starts as a square lattice of size $N \times (N-1) \times N/2$, where N is an even integer. Each node of the lattice occupies integer lattice positions (*e.g.*, [1, 1, 1]) and is analogous to an SiO_2 center in silica. The coordination environment of

the DLM (octahedral) differs from that of SiO_2 (tetrahedral), so we refer to the nodes as Σ centers. The octahedral (cubic) lattice greatly simplifies model construction and the DLM still exhibits quenched disorder like the real system. Each node is bonded to its neighbors. Then, disorder is created by perturbing each Σ center from their initial lattice position by a random vector drawn from a 3D, isotropic, normal distribution with variance σ^2_{disp}. The resulting irregular distances are taken as equilibrium distances in the MD Hamiltonian. The DLM also contains "surface hydroxyls", each represented as a single atom. The two surface hydroxyls are placed over the center of the DLM surface as shown in Figure 6.3. A metal atom (described by an empirical force field) is then grafted to these two hydroxyls.

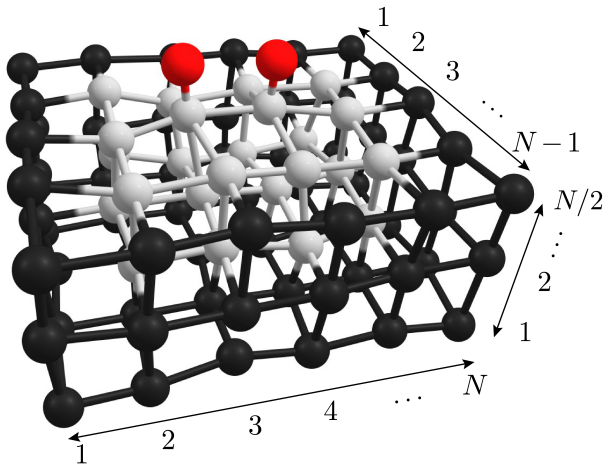

Figure 6.3: Sample DLM model with two surface OH groups. Red beads are surface OH groups, grey beads are Σ centers which are allowed to relax in structure optimizations, and black beads are peripheral capping groups whose positions are held fixed in structure optimizations. A small DLM with $N = 6$ is shown here for clarity. Results in this paper DLM models with $N > 10$.

Cluster models of the extended DLM slab are carved by including a specific number of Σ centers (as opposed to including atoms within a specific distance as for the atomistic SiO_2 models). We refer to the size of the cluster model as n_{shells}, where n_{shells} is an integer. Starting underneath and between the two central OH groups, a cluster model is

created by including all Σ centers n_{shells} lattice positions in the positive and negative x direction, $n_{shells}-1$ lattice positions in the positive and negative y direction, and $n_{shells}/2$ in the negative z direction. Figure 6.3 shows an example of carving a cluster model with $n_{shells} = 2$. Other examples of carving out cluster models with different sizes in shown in Figure E.1. The largest cluster model size is also related to the size of the DLM, $n_{shells} \leq N/2$.

We also define two configurations of the DLM. The first one corresponds to the minimum energy configuration of the Hamiltonian used to create the disordered lattice structure, akin to the MD Hamiltonian for an atomistic SiO_2 slab model. The second one corresponds to the minimum energy configuration of the QM Hamiltonian used to compute reaction energies. The minimum energy configuration of the MD Hamiltonian is *perturbed* relative to that from the QM Hamiltonian.

We mimic the two different minimum energy configurations in the DLM by using two different sets of equilibrium Σ-Σ distances. When the DLM was first created by random Gaussian displacements of the Σ centers from their lattice positions, every Σ-Σ bond acquired an initial length. We define these Σ-Σ distances as the perturbed-minimum-energy configuration (*i.e.*, the "MD" equilibrium model structure). The initial (MD) distribution of Σ-Σ distances is also Gaussian and has a variance related to that of the displacements, $\sigma^2_{dist} = 2\sigma^2_{disp}$. The factor of 2 appears because the distance involves 2 Σ centers being displaced. The equilibrium (QM) length for a given Σ-Σ bond is then assigned by re-sampling from the Gaussian distribution with mean distance of 1 and variance of $2\sigma^2_{dist}$. The equilibrium distance between the two Σ centers with surface OH groups is set by sampling $\mathcal{U}(0.77, 0.83)$, where $\mathcal{U}$ is a uniform distribution. We found that the grafting energy strongly depends on this equilibrium distance, and that an equilibrium distance less than $\hat{r} = 1$ led to a wide range of grafting energies. All Σ-Σ bonds have the same spring constant.

Lastly, we explain the model for grafting on the DLM, which allows us to compute a grafting energy of a cluster model carved from the DLM through geometry optimizations. The model uses simple classical potentials, commonly used in MD simulations. A schematic of the coordinates used for the potential is shown in Figure 6.4.

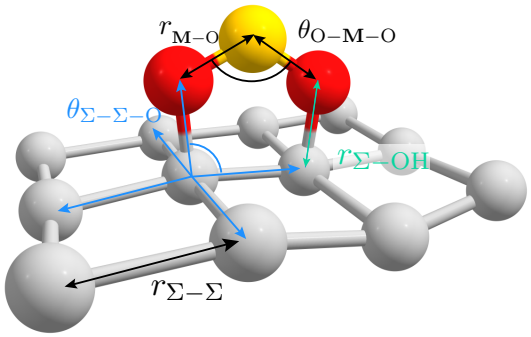

Figure 6.4: Schematics of coordinates used to model the grafting energetics. Grey beads are Σ centers allowed relax during structure optimizations the gold bead is the metal atom, a red beads represent surface O atoms.

Interactions between Σ centers are modeled with a harmonic potential,

$$V_{\Sigma\text{-}\Sigma}(\mathbf{r}) = \sum_{i \in \Sigma-\Sigma} k_i (r_i - r_i^{eq})^2 \tag{6.1}$$

where i runs over all nearest neighbors Σ-Σ bonds. Here, $\mathbf{r}$ is the configuration of the Σ centers and OH groups, k_i is the force constant for site i, r_i is the Σ-Σ bond length, and r_i^{eq} is the equilibrium length for the corresponding Σ-Σ bond. Note that each equilibrium Σ-Σ distance will be different for every bond to model structural disorder. The bond between Σ centers and surface hydroxyls is also described with a harmonic potential,

$$V_{\Sigma\text{-OH}}(\mathbf{r}) = \sum_{i \in \Sigma\text{-OH}} k_i (r_i - r_i^{eq})^2. \tag{6.2}$$

where the force constant and distances refer to a Σ center and OH group. The surface

OH groups are kept normal to the surface by

$$V_{\Sigma\text{-}\Sigma\text{-}\mathrm{OH}}(\mathbf{r}) = \sum_{i\in\Sigma\text{-}\Sigma\text{-}\mathrm{OH}} \frac{k_i}{4} \sum_{j\in\mathrm{NN}}^{4} (\theta_j - \theta^{eq}_{\Sigma\text{-}\Sigma\text{-}\mathrm{OH}})^2. \tag{6.3}$$

For each surface OH, the difference of the angles formed by the OH, basal Σ center, and 4 nearest neighbor (NN) Σ centers is taken with an equilibrium angle ($\theta^{eq}_{\Sigma\text{-}\Sigma\text{-}\mathrm{OH}}$), squared, then averaged.

For grafting of a metal atom **M** on the surface, a Morse potential is used to describe the two **M**-O bonds,

$$V_{\mathbf{M}\text{-}\mathrm{O}}(\mathbf{r}) = \sum_{i\in\mathbf{M}\text{-}\mathrm{O}}^{2} D_{\mathbf{M}\text{-}\mathrm{O}}(1 - \exp[-a_{\mathbf{M}\text{-}\mathrm{O}}(r_i - r_i^{eq})])^2 - D_{\mathbf{M}\text{-}\mathrm{O}}. \tag{6.4}$$

An O-**M**-O angle term is also added

$$V_{\mathrm{O}\text{-}\mathbf{M}\text{-}\mathrm{O}}(\mathbf{r}) = k_{\mathrm{O}\text{-}\mathbf{M}\text{-}\mathrm{O}}(\theta_{\mathrm{O}\text{-}\mathbf{M}\text{-}\mathrm{O}} - \theta^{eq}_{\mathrm{O}\text{-}\mathbf{M}\text{-}\mathrm{O}})^2. \tag{6.5}$$

The O-**M**-O angle is chosen such that the Σ-O groups pucker outwards, straining the Σ-O angles in $V_{\Sigma\text{-}\Sigma\text{-}\mathrm{OH}}(\mathbf{r})$. The degree of the strain depends on the local environment at the grafting site. Lastly, an Σ-O-**M** angle term is added

$$V_{\Sigma\text{-}\mathrm{O}\text{-}\mathbf{M}}(\mathbf{r}) = k_{\Sigma\text{-}\mathrm{O}\text{-}\mathbf{M}}(\theta_{\Sigma\text{-}\mathrm{O}\text{-}\mathbf{M}} - \theta^{eq}_{\Sigma\text{-}\mathrm{O}\text{-}\mathbf{M}})^2 \tag{6.6}$$

Here, $k_{\Sigma\text{-}\mathrm{O}\text{-}\mathbf{M}}$ is the force constant, $\theta_{\Sigma\text{-}\mathrm{O}\text{-}\mathbf{M}}$ is the angle between **M**, the midpoint of the two O atoms, and the midpoint of the two Σ groups bonded to the O atoms (Figure E.6). The DLM energy before ($V_B(\mathbf{r})$) and after ($V_G(\mathbf{r})$) grafting is

$$V_B(\mathbf{r}) = V_{\Sigma\text{-}\Sigma}(\mathbf{r}) + V_{\Sigma\text{-}\mathrm{OH}}(\mathbf{r}) + V_{\Sigma\text{-}\Sigma\text{-}\mathrm{OH}}(\mathbf{r}). \tag{6.7}$$

$$\begin{aligned} V_G(\mathbf{r}) =& V_{\Sigma\text{-}\Sigma}(\mathbf{r}) + V_{\Sigma\text{-OH}}(\mathbf{r}) + V_{\Sigma\text{-}\Sigma\text{-OH}}(\mathbf{r}) \\ &+ V_{\mathbf{M}\text{-O}}(\mathbf{r}) + V_{\text{O-}\mathbf{M}\text{-O}}(\mathbf{r}) + V_{\Sigma\text{-O-}\mathbf{M}} \end{aligned} \tag{6.8}$$

The grafting energy of the disordered lattice model, $\Delta E_{G,DLM}$, is computed by

$$\Delta E_{G,DLM} = \min[V_G] + 2E_{\mathbf{HL}} - (\min[V_B] + E_{\mathbf{ML}_2}). \tag{6.9}$$

where $\min[\cdot]$ denotes the energy-minimized potential, obtained by a geometry optimization. The values of $2E_{\mathbf{HL}}$ and $E_{\mathbf{ML}_2}$ were chosen such that $\Delta E_{G,DLM} = -50$ kJ mol^{-1} for a perfect (ordered) lattice. Finally, we study the convergence of the results with cluster size by defining

$$\Delta\Delta E_{G,DLM}(n_{shells}) = \Delta E_{G,DLM}(n_{shells}) - \Delta E_{G,DLM}(\infty) \tag{6.10}$$

In practice, $\Delta E_{G,DLM}(\infty)$ is the $\Delta E_{G,DLM}$ for the largest possible cluster from the DLM, which exceeds the length scale for the dependence of the grafting energy on the boundary condition. This is quantitatively confirmed in the plots in Figure E.8. Note that Eq. 6.10 eliminates contributions from dynamical and quenched disorder, so only variance from procedural disorder remains.

Equilibrium bond distances, bond angles, and force constants were obtained from DFT calculations on a simple SiO_2 cluster model and dioxoCr(VI)/SiO_2 cluster model. Force constants were obtained by performing relaxed scans on these two cluster models. A full description of the cluster models, computational details, fitting procedures, and resulting parameters is given in Section E.1 The list of parameters and equilibrium values is given in Table E.1 Geometry optimizations on the DLM were performed using the truncated Newton method,[50] a Hessian-free method designed for optimizing non-linear

functions with many degrees of freedom. For convergence criteria, the absolute error in $\mathbf{r}_{\text{opt}}$ between optimization iterations was required to be less than 1.25×10^{-8} (dimensionless distance) and the absolute error in $V_i(\mathbf{r}_{\text{opt}})$ between optimization iterations was required to be less than 1.25×10^{-7} kJ mol^{-1}. The optimization was performed in Python with SciPy.[51] The optimized structures were confirmed as minima by ensuring all forces are near zero and the Hessian of optimized geometries is positive definite. The Jacobian and Hessian of the forcefield were both computed via automatic differentiation with JAX.[52]

6.2.2 Atomistic Cluster Models

The atomistic cluster models provide a more realistic representation of the Cr-doped sites on the amorphous silica. Therefore, we use an approach similar to that we used to create the METal doped Amorphous SIlica Library, METASIL.[19] We start with an amorphous silica surface created using molecular dynamics (MD) simulations. This was obtained beginning from a unit cell of β-cristobalite crystal containing 5103 atoms; the crystal was then heated to 8000 K, after which the simulation cell was expanded in the z- dimension to create a slab geometry. Following equilibration at this high temperature for 0.5 ns, the system was cooled down quickly to maintain the disordered structure; a cooling rate of 25 K/ps was used. The MD simulations were carried out using the LAMMPS software,[53] and the BKS force field[27,54,55] was used to describe the interactions within the silica. The two surfaces of the slab created in this procedure were then functionalized with hydroxyl groups. Specifically, silanol groups were created by choosing strained Si-O bonds based on a distance criteria for the bond, $r > 1.8$Å, and proximity to the surface. Each strained Si-O bond selected in this way was broken and an OH (H) group added to the Si (O) atom, so that the functionalization maintains the charge

neutrality of the surface. The functionalization was followed by an equilibration step at 298 K, which allows the relaxation of the silanol groups and their rearrangements in a stable H-bonding network. The final structure is obtained by taking a snapshot after equilibration is achieved. The resulting surfaces have a silanol density of about 4 nm^{-2}, which is consistent with experimental data.[56,57] The structure resulting from this procedure is not exactly equivalent to a geometry optimization with the same classical force field (FF) as that used for the dynamics, but it should be fairly close because the FF contains steep harmonic potential terms.

From this initial large simulation cell, we select ten sites to be doped with the metal, five from each side of the slab. These are the same sites that we used in METASIL for doping with Zr, Nb, and W.[19,58–61] The metal dopant in this work, Cr, is grafted between a pair of silanol groups, SiOH. When clusters do not contain a central SiOH pair, a water is added across the longest Si-O bond of the central silicon atom. The center of mass (COM) of the two oxygens within this central pair is used as the center of the cluster. Each model contains approximately 175 non-H atoms on average, as for the METASIL structures. Eight out of ten grafting sites are on vicinal silanols and the remaining two are on isolated silanols that are at an appropriate distance for inserting the metal. Although the distribution of vicinal silanols is likely different than that of isolated silanols in the real material, thus affecting the corresponding grafting distributions, this is not a fundamental issue here. In fact, the optimization protocol should be independent of the site distribution, and it is interesting to consider both types of grafting sites. Therefore, we include results on the effect of procedural disorder only on the vicinal silanol grafting sites as well as on the whole collection of sites. Furthermore, although ten sites would not be sufficient for modeling the site distribution and the effective kinetics of the grafting process,[7] they are sufficient to illustrate trends in the effects of procedural disorder introduced by the choice of optimization protocol.

In the pre-optimization protocol (QM-Opt), all of the atoms are relaxed except the capping -OH groups, which are kept fixed at the initial positions. Grafting energies obtained with the largest relaxed zone are close to the bulk limit, as shown in Figure E.9. In the non-pre-optimized case (MD-Opt), only the region within a radius R from the grafting site (*i.e.*, the COM of the central silanol discussed above) is allowed to relax, shown schematically in Figure 6.2. A Cr center is grafted on the two central SiOH, formally corresponding to the chemical reaction:

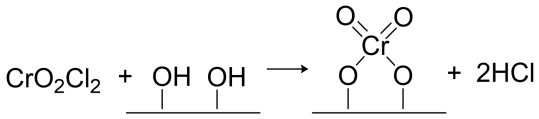

(6.11)

where the two inner species represent the undoped and doped clusters, respectively. We consider a range of radii for the relaxed zone: $R = 4, 5, \ldots, R_{max}$ Å, with $R_{max} = 10$ Åfor three clusters, $R_{max} = 11$ Åfor four clusters, and $R_{max} = 12$ Åfor three clusters. In the MD-Opt protocol, the region within the radius R is relaxed before and after grafting. An example of a Cr-doped cluster is shown in Figure 6.5.

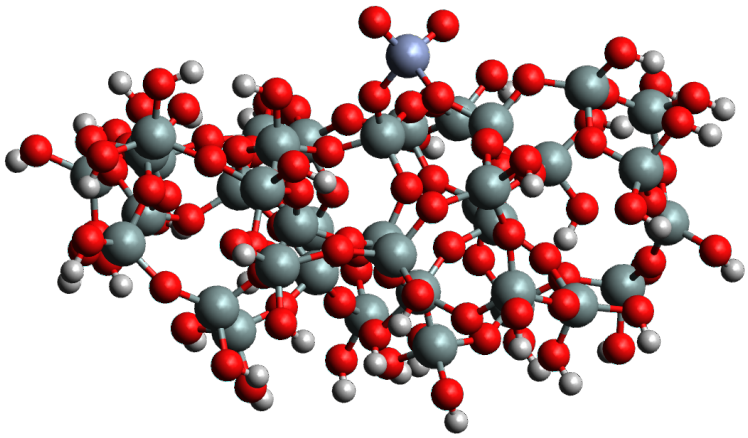

Figure 6.5: Example of an atomistic Cr-doped silica cluster.

All DFT calculations were performed with a development version of the GAUSSIAN

suite of programs.[62] The B3LYP hybrid functional and Grimme's D3 dispersion were chosen for consistency with the procedure used to build METASIL.[63,64] Cr is treated with the Def2TZVP basis set,[65] the oxo and SiOH groups on the surface are treated with 6-31++g(d,p), and the remaining atoms with 6-31G(d). The grafting energy, ΔE_G, and the relative grafting energy, $\Delta\Delta E_G$, are calculated as:

$$\Delta E_G = (E_G + 2E_{HCl}) - (E_B + E_{Cr}) \tag{6.12}$$

$$\Delta\Delta E_G(R) = \Delta E_G(R) - \Delta E_G(R_{max}) \tag{6.13}$$

where E_B and E_G are the energies of the clusters before and after grafting, respectively, and E_{Cr} is the energy of CrO_2Cl_2. $\Delta E_G(R_{max})$ is the grafting energy when the entire cluster (except the capping -OH) is allowed to relax, and $\Delta E_G(R)$ is the grafting energy where the atoms within the region of radius R are allowed to relax. The expressions in Eqs. 6.12-6.13 are equivalent to those for the DLM in Eqs. 6.9-6.10. The $\Delta\Delta E_G$ values in Eqs. 6.13 and 6.10 are the principal quantities for the scope of this study as they filter out any dependence on the site and grafting energy distributions and focus only on the procedural disorder.

Beyond the grafting energy, the atomistic clusters can provide valuable structural information on the Cr sites. Specifically, we can investigate how the grafting energy is affected by all three forms of disorder discussed in the Introduction. For such comparison, it is useful to introduce two small models of Cr sites based on grafting on vicinal and isolated silanols, shown in Figure 6.6, since both types of site are represented in the large clusters. We identified two important structural parameters that define a Cr site: the dihedral angles θ and ϕ depicted in the figure. We perform rigid and relaxed scans of

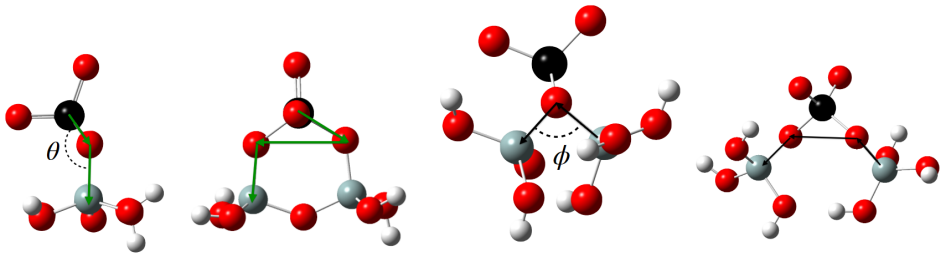

Figure 6.6: Front and side views of the small models for grafting on vicinal (a-b) and neighboring non-vicinal (c-d) silanols. The dihedral angles used for scan are also defined: Cr-O-O-Si (a-b) and Si-O-O-Si (c-d) dihedral angles, θ and ϕ, respectively. Cr is represented as a black ball, O as red, Si as gray, and H as white.

these two angles for the small models in Figure 6.6 and for the ten large clusters. A comparison of the scans for the two sets of model clusters allows us to discuss the effect of the quenched disorder on the structure and grafting energy of the metal precursor.

6.3 Results

6.3.1 Protocol Comparison

For the disordered lattice model, a distribution of sites was created by generating 100 slabs with edge lengths [18 × 17 × 9] with a single pair of silanols over the center. The grafting energy for an effectively infinite slab was computed by allowing the maximum number of shells to relax. The grafting energy distribution of the slab models is shown in Figure 6.7. The distribution is peaked around -40 kJ mol^{-1}, 10 kJ mol^{-1} above the grafting energy of an ordered, crystalline lattice, and extends to about -20 kJ mol^{-1} for a range of about 30 kJ mol^{-1}.

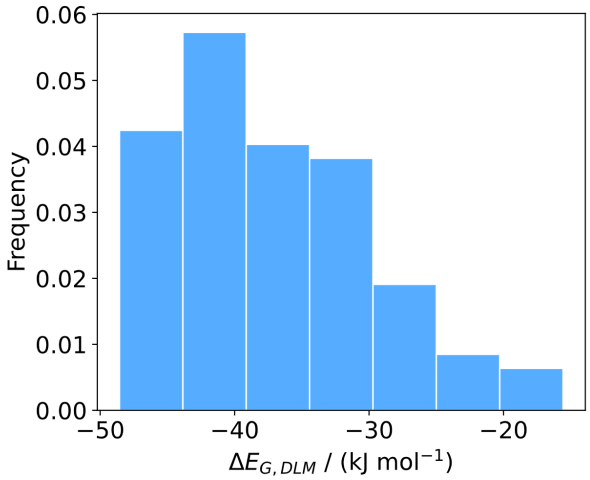

Figure 6.7: Distribution of grafting energies for 100 disordered lattice models, all with the maximum cluster size of 8 shells.

We performed geometry optimizations for cluster models of size $n_{shells} = 2 - 8$ using the two optimization protocols. For the QM-Opt protocol, the lattice was pre-optimized by allowing all 8 inner shells of the ungrafted lattice to relax before carving clusters and fixing the terminal atoms. For all subsequent optimizations, centers outside the relaxation zone were constrained according to their pre-optimized positions. For the

MD-Opt protocol, peripheral capping atoms were simply held constrained to the initial configuration (*i.e.*, their perturbed-minimum-energy configuration).

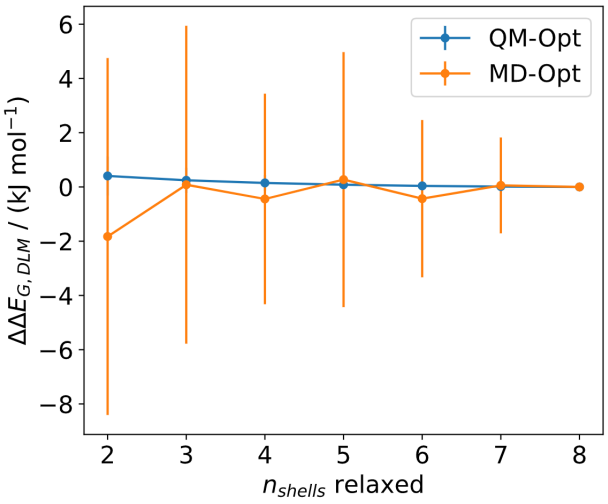

Figure 6.8: Average deviation from exact grafting energy ($\Delta\Delta E_{G,DLM}$) for the QM-Opt (blue) MD-Opt (orange) protocol for different sized DLM cluster models. Errors bars are the standard deviation.

Figure 6.8 reports the average $\Delta\Delta E_{G,DLM}$ of the two protocols, computed via Eq. 6.10. The figure shows that when the DLM is pre-optimized to the minimum-energy configuration before constraining peripherals atoms, $\Delta\Delta E_{G,DLM}$ converges smoothly and with low variation. Conversely, with the MD-Opt protocol, $\Delta\Delta E_{G,DLM}$ converges slowly and with large variability. The sample standard deviations of $\Delta\Delta E_{G,DLM}$ are reported in Table 6.1. The $\Delta\Delta E_{G,DLM}$ values for the MD-Opt protocol have sample standard deviations 1 order of magnitude larger than those for the QM-Opt protocol. The standard deviation of $\Delta\Delta E_{G,DLM}$ values is ca. 1.8 kJ mol^{-1} for the MD-Opt protocol even at $n_{shells} = 7$. These results suggest that procedural disorder can become significant, on a scale comparable to that of the energy difference between sites due to the quenched disorder (here $\pm$10 kJ mol^{-1}) even for large clusters.

Table 6.1: Sample standard deviation ($\hat{s}_{MD}$ and $\hat{s}_{QM}$, kJ mol^{-1}) of $\Delta\Delta E_{G,DLM}$ values from the DLM. Rows correspond to different cluster model sizes and columns correspond to different protocols

n_{shells}	$\hat{s}_{MD}$	$\hat{s}_{QM}$
2	0.70	6.58
3	0.45	5.86
4	0.27	3.88
5	0.15	4.70
6	0.08	2.90
7	0.03	1.77
8	0.00	0.00

Lastly, we compare the degree of strain around the metal center for the two optimization protocols. The strain of the support can be characterized by the root mean square difference (RMSD) of the Σ-Σ bond lengths, defined as:

$$\text{RMSD} = \sqrt{\sum_{i \in \Sigma\text{-}\Sigma} [r_i(n_{shells}) - r_i(\infty)]^2}. \tag{6.14}$$

Figure 6.9 shows the Σ-Σ bond length RMSD for different cluster model sizes and the two optimization protocols. For a given cluster model size, the RMSD is computed for all bonds in the first three shells relative to the largest cluster model. The RMSD converges smoothly for both optimization protocols, but the QM-Opt cluster models have RMSD values ca. 2 orders of magnitude smaller than the MD-Opt clusters.

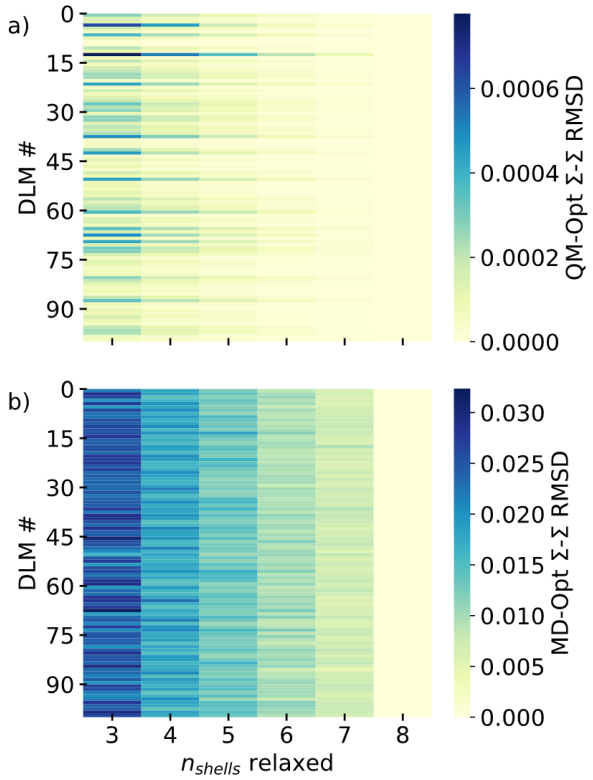

Figure 6.9: RMSD values of Σ-Σ bond lengths for DLM cluster models of different sizes, see Eq. 6.14. RMSD values are computed using only the first 3 shells of Σ-Σ bonds of a given cluster model size are used. a) shows RMSD values for the pre-optimized cluster models and b) shows RMSD for the non-pre-optimized cluster models. Note that scales of the two color bars are different.

The grafting energy convergence shown in Figure 6.8 is likely a direct result from the RMSD convergence of Figure 6.9. When cluster models are pre-optimized, the RMSD is low because the Σ centers are already near their minimum-energy configuration. Thus, the grafting energy converges rapidly and smoothly. For non-pre-optimized cluster models, the Σ centers are at a *perturbed* minimum-energy configuration. Because the peripheral atoms are held fixed in structure optimizations, the Σ centers cannot fully relax to their minimum-energy configuration, imparting a greater degree of strain on the metal site. The greater degree of strain is not only an additional (and non-physical) source of variance in the grafting energy, but also leads to erratic convergence of the grafting

energy.

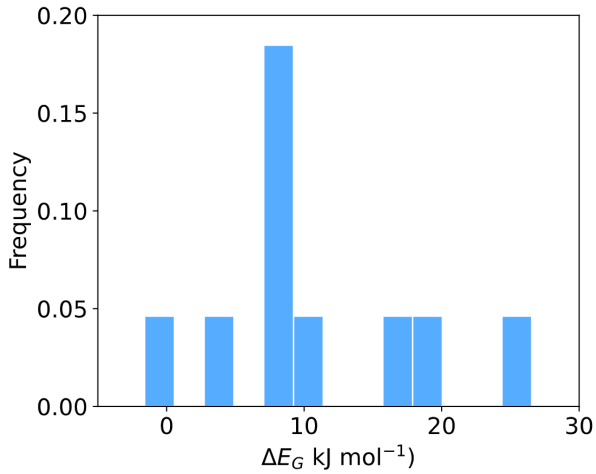

Figure 6.10: Distribution of $\Delta E_G(R_{max})$ for the ten atomistic clusters treated at DFT level.

The distribution of grafting energies for the fully-relaxed atomistic cluster models, $\Delta E_G(R_{max})$, is reported in Figure 6.10. For the eight clusters where grafting occurs on a pair of vicinal silanols, two minima for the metal site can be found, and Figure 6.10 reports the grafting energy distribution for the lowest energy minima. Interestingly, the two stable site structures are found at all values of R with the QM-Opt protocol, but only for radii $R > 5$ Åwith the MD-Opt protocol. This limitation for the MD-Opt protocol at short radii is due to the rigidity of the MD structure, which prevents the formation of the second stable minimum configuration. The average $\Delta E_G(R_{max})$ is 10.6 kJ mol^{-1}, with a standard deviation of 8.2 kJ mol^{-1}, and a median of 8.2 kJ mol^{-1}. As for the DLM, the large variations in the grafting energy are due to the quenched disorder in the local structure of the amorphous silica.

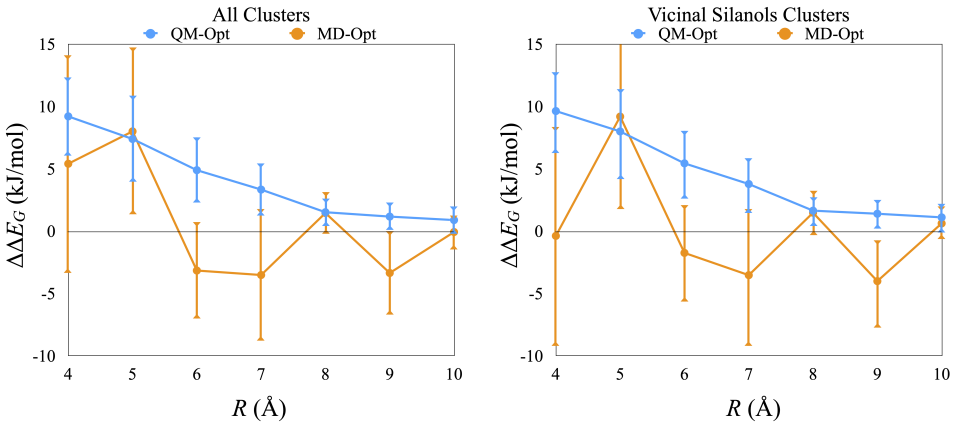

Figure 6.11: Average $\Delta\Delta E_G$ of the ten atomistic clusters (left) and the eight clusters with vicinal-silanols grafting sites (right) plotted as the relaxation radius R increases for the QM-Opt (blue) and MD-Opt (orange) protocols. The vertical bars are the standard deviation of the sample.

The $\Delta\Delta E_G$ plot in Figure 6.11 shows that the QM-Opt protocol results in a smooth convergence of ΔE_G with the length of the relaxation radius R. This is independent on whether we consider only vicinal-silanol grafting sites (right plot) or the whole collection of clusters (left plot). The $\Delta\Delta E_G$ values do not go to 0 at $R = 10$ Åbecause 7 out of the 10 clusters have $R_{max} > 10$ Å. Nonetheless, the average $|\Delta\Delta E_G| < 1$ kJ mol^{-1} at $R = 10$ Å, and it is 1.5 kJ mol^{-1} at $R = 8$ Å, a reasonable compromise between accuracy and computational cost for the cluster relaxation radius. At the same time, this value is larger than the 6 Åpreviously recommended for the creation of doping sites.[20,66] All $\Delta\Delta E_G$ values are positive for all clusters and all values of R, consistent with the DLM results in Figure 6.8. This indicates that the grafting energy is consistently overestimated compared to $\Delta E_G(R_{max})$, which is reasonable because for $R < R_{max}$ the doped structure is not at the minimum while the undoped structure is.

On the other hand, the MD-Opt protocol leads to large shifts in ΔE_G and erratic $\Delta\Delta E_G$ values that can even become negative, see Figure 6.11. The average $\Delta\Delta E_G$ is comparable to that obtained with the QM-Opt protocol once R reaches 10 Å, but large

standard deviation values persist even at large R values. This indicates that strained structural features in the initial MD structures significantly affect the doping site for certain clusters even at large relaxation radii. In one case, for cluster 4 at $R = 7$ Å, a peripheral silanol group dehydrates, leading to a water molecule and a siloxane group (the grafting energy for this cluster is not included in the plot in Figure 6.11). The water molecule is not released at $R = 6$ Åbecause the strained silanol group is frozen, and at $R = 8$ Åbecause enough atoms are relaxed so that the silanol group can rearrange to a more favorable orientation. As for the DLM, the variation in $\Delta\Delta E_G$, even at large R, is comparable in magnitude with the differences in grafting energy due to the quenched disorder (compare Figures 6.10 and 6.11).

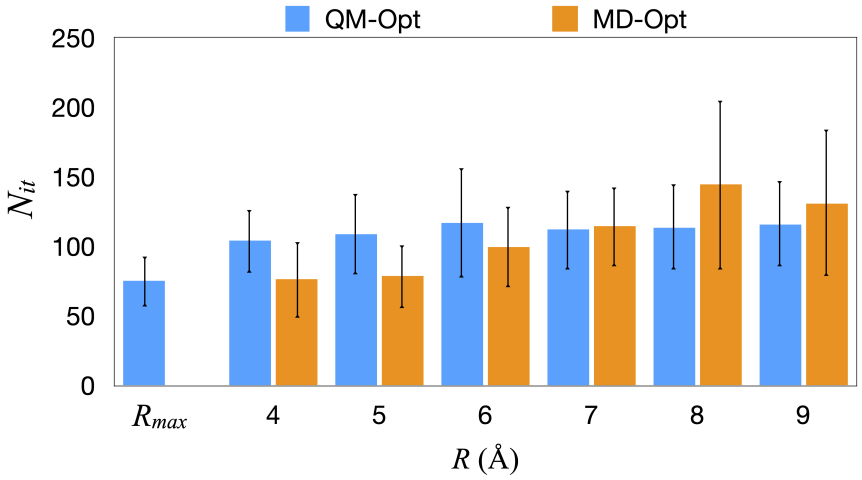

Figure 6.12: Average number of geometry optimization iterations for the ungrafted and grafted clusters with the QM-Opt (blue) and MD-Opt (orange) protocols. The number of iterations for ungrafted and grafted clusters are first summed, then averaged. The R_{max} bar corresponds to the QM pre-optimization step before grafting, and it is reported for reference. The averages are taken over the ten clusters and the standard deviations are represented by the black bars.

A reasonable concern with the QM-Opt protocol is the extra computational cost associated with the initial relaxation of the full structure (minus the capping groups) before metal grafting. We estimate the cost as the average sum of iterations (N_{it}) for

the geometry optimizations of doped and undoped clusters at every R with the two protocols, reported in Figure 6.12. The figure separately reports the average number of iterations to pre-optimize the undoped structures at R_{max}, *i.e.*, the first step in the QM-Opt protocol for grafting calculations. The blue bars in the figure are computed as the (average) sum of the "R_{max}" iterations and the number of iterations required after grafting. The N_{it} value can be used as a proxy to approximate the computational cost. The cost of the QM-Opt protocol is essentially the same for all values of R. On the other hand, the MD-Opt protocol is less computationally intensive at small values of R, but there is a crossing point at $R = 7$, near the R value where the $\Delta\Delta E_G$ becomes sufficiently small, see Figure 6.11. The combination of a smoother energy convergence and comparatively smaller computational cost at larger radii indicates that QM-Opt is the preferred protocol.

6.3.2 Structural Analysis

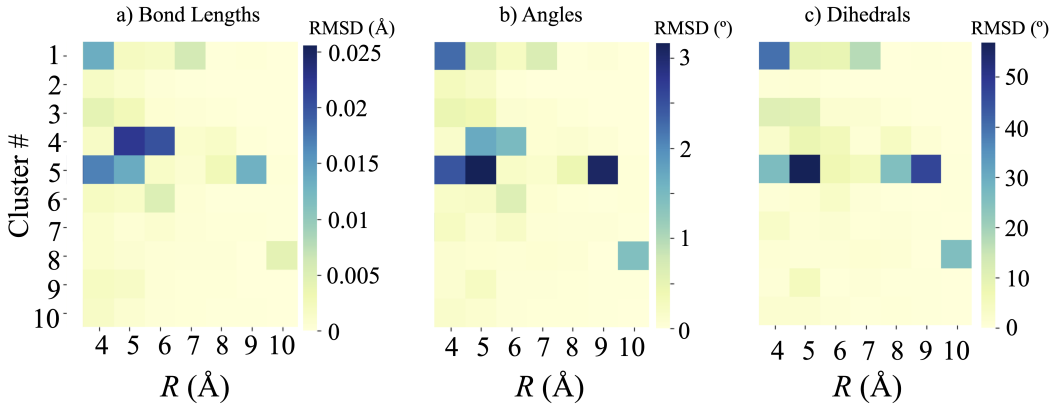

Figure 6.13: Heat maps of the RMSD, see Eq. 6.14, of the a) bond lengths, b) bond angles, and c) dihedrals of the atoms within a 3 Åradius from the Cr site as R increases, obtained with the QM-Opt protocol (only the lowest-energy configurations are included).

The convergence of the cluster structure with R can be also discussed in terms of geometrical parameters, not only the grafting energy. Figure 6.13 reports the root mean square deviations (RMSD) with respect to R_{max} of bond lengths, angles, and dihedrals of the centers within the 3 Åradius from the metal center as R increases for the QM-Opt clusters. The RMSD of the bond lengths and angles are small at all values of R but especially when $R \geq 8$ Å, with changes less than 0.015 Åand 3°, respectively. The dihedral angles RMSD is small ($0° - 4°$) for most clusters at $R > 8$ Å, but more significant changes ($10° - 20°$) are observed at smaller radii. Cluster 8 shows a deviation of ca. 30° at higher R values. The primary contribution to this large RMSD value in Figure 6.13c is the θ dihedral, see Figure 6.6.

The heat maps in Figure 6.13 suggest that dihedral angles are the structural parameters with the largest degree of variability. More specifically, the dihedral angles θ and ϕ defined in Figure 6.6 associated with the Cr sites are the key parameters, as one would expect given that the metal coordinates to the silica surface only through two bonds. We investigate this geometrical flexibility by using the small models in Figure 6.6 and comparing the results with those for the large clusters. Using the small model in Figure 6.6c-d, we first performed a relaxed scan of the grafting energy as a function of the ϕ angle, reported in Figure E.11. This figure presents two minima corresponding to an "eclipsed" configuration with ϕ close to 0° and a "gauche" configuration at $\phi = 95°$, shown pictorially in Figure E.12. The eclipsed configuration is equivalent to the structure found in vicinal-silanol grafting sites, see Figure 6.6a-b. In fact, the eclipsed structure is found in the eight large clusters with vicinal-silanols grafting sites ($-45° < \phi < 45°$) while the gauche structure is found in the two large clusters with isolated-silanol grafting sites ($90° < \phi < 100°$).

Now that we have isolated these two configurations, we perform a rigid scan along the θ dihedral angle for the small clusters, using the vicinal-silanol grafting model for the

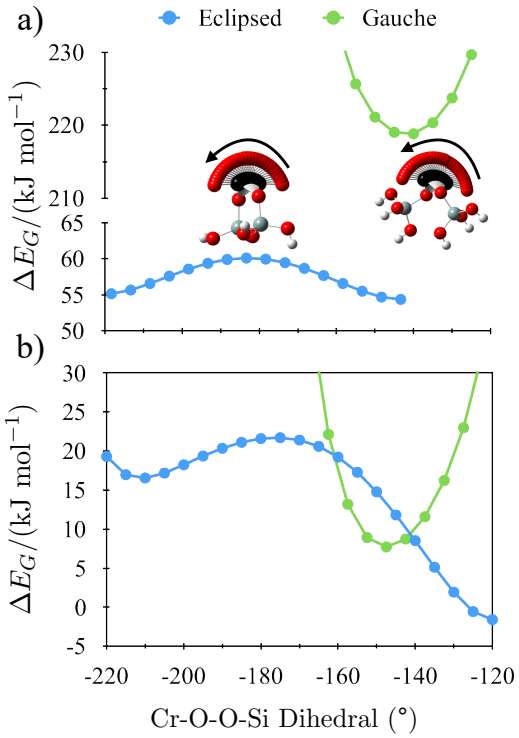

Figure 6.14: Rigid scan of ΔE_G as a function of the dihedral angle θ (5° increments) for the two small (a) and two large clusters (b), representative of the eclipsed (blue) and gauche (green) configurations.

eclipsed configuration and the isolated-silanol grafting model for the gauche configuration (with ϕ fixed at 95°). We also performed the same rigid scan for two representative large cluster models, and both scans are shown in Figure 6.14. The eclipsed configuration shows two stable minima for the Cr position (one on either side of the plane defined by the two Si−O linker groups). However, while these two minima are degenerate for the small model, they are not for the large cluster because of the different interaction of the CrO_2 group with the surrounding amorphous silica support. On the other hand, the gauche configuration shows a single minimum in both the small model and the large cluster. The grafting energies are comparable between the two types of sites in the large clusters while they are significantly different in the small models, and the metal grafting is considerably more favorable on the large clusters than on the small models. This

indicates that the interaction with the silica surface considerably stabilizes the Cr sites.

We report relaxed scans along the θ dihedral angle of the large clusters in Figure E.13. The eight clusters with the eclipsed configurations show barriers ranging around 4–18 kJ mol^{-1}. There are two types of eclipsed structures, those with near-degenerate double minima ($|\Delta E_G^{ec1} - \Delta E_G^{ec2}| < 5$ kJ mol^{-1}) and those with non-degenerate double minima ($|\Delta E_G^{ec1} - \Delta E_G^{ec2}| > 7$ kJ mol^{-1}). The eclipsed structures with near-degenerate grafting energies have the CrO_2 site oriented perpendicularly relative to the surface, so that the interaction with the local silica environments is similar on either side. The clusters with non-degenerate grafting energies have the CrO_2 site parallel to the surface, leading to a preferential interaction with the silica environment when the Cr group is more embedded in the silica surface. The two clusters with the metal site in the gauche configuration (isolated-silanols grafting) have only one stable structure and larger ΔE_G values compared to those in the eclipsed configuration (vicinal-silanols grafting), consistent with the results in Figure 6.14.

One limitation of the large clusters created in this study is the lack of an extended H-bonded network. This is due to the silanol density on the initial MD slab used to create the clusters (4 SiOH/nm^2). While this situation is consistent with experimental data,[56,57] other studies have shown that grouping of several silanol groups is possible.[67] Nevertheless, it will be important in the future to also study how the dynamical disorder is influenced by the fixed atom constraints.

6.4 Conclusions

Typically, a large number of models sites is necessary to estimate site-averaged reaction rates for amorphous catalysts,[7] even when efficient importance learning algorithms are employed (Chapters 4 and 5). Beyond the real dynamical fluctuations and quenched

disorder differences between catalyst sites on doped amorphous silica, there are also easily overlooked procedural disorder artifacts. The goal of this study is to determine a robust approach to build cluster models of these catalysts to enable accurate QM calculations, starting from amorphous silica slabs created with classical MD simulations. Grafting of CrO_2 onto silica, *i.e.* preparation of the Phillips catalyst, was used as an example reaction. Specifically, we examine how computed ΔE_G values depend on cluster model size and boundary conditions. We use two model classes for the analysis: an illustrative but simplified disordered lattice model and an atomistic cluster model treated at DFT level. The former system allows us to investigate very large structures, close to the bulk limit, while the latter system provides a more realistic system with complications of real QM calculations. For example, as detailed in Section 6.3, we find two different minimum energy configurations when CrO_2 is grafted at all vicinal silanols, but only one energy minimum when CrO_2 is grafted at neighboring, non-vicinal silanols.

We test two optimization protocols: one where the grafting is based on the structures obtained directly from the MD simulation, MD-Opt, and one where the undoped cluster is pre-optimized with the target (DFT) level of theory, QM-Opt. As discussed in Section 6.2, our analysis eliminates the effects of quenched and dynamical disorder, isolating the effects of different procedural steps. Specifically, we examine effects of different radii for the relaxed regions and different Hamiltonians used to specify the peripheral constrained region around each cluster model. Pre-optimization with the target (QM) Hamiltonian for a large region around the active site leads to structures and reaction energy predictions that converge quickly and smoothly with cluster size. In contrast, clusters optimized with the target (QM) Hamiltonian, but with boundary constraints from the MD simulations (MD-Opt protocol) exhibit slow, highly variable, and erratic convergence with cluster size. In some cases, we found that labile dihedral angles could lead to multiple stable configurations with the QM-Opt protocol and not with the MD-Opt. For both the DLM

and the atomistic DFT model, see Figures 6.8 and 6.11, we find that pre-optimization of the MD structures provides a better computational protocol for the creation of the active site models. The change in grafting energy with the radius of the optimized region, $\Delta\Delta E_G$, shown in Figures 6.8 and 6.11 for the DLM and DFT models, converges smoothly with R when using the pre-optimization protocol with either model system. Furthermore, the error standard deviation for different models is also significantly reduced with the pre-optimization protocol.

We also examine structural aspects of the geometries obtained with the pre-optimization protocol and find that the torsional degrees of freedom of the CrO_2 group are the most flexible aspect of the entire cluster. If the pair of O−Si linker groups that bind the metal are approximately coplanar, a conformation that is common in vicinal-silanol grafting sites and that we called eclipsed in Figure E.12a-b, two stable orientations of the CrO_2 group are found. In the small cluster models, the interconversion barrier is relatively small, about 6 kJ mol^{-1} as shown in Figure 6.14a. In the large clusters, different interactions with the silica on either side of the linker groups plane may result in one of the two minima being considerably more stable than the other, see Figures 6.14b and E.13. When the metal is grafted to two isolated silanols that are in a gauche configuration, see Figure E.12, only one stable CrO_2 conformation is possible and the grafting energy tends to be larger than that for the most stable eclipsed conformer, as shown in Figures 6.14b and E.13.

The pre-optimization comes at the cost of relaxing a large portion of the cluster, which in principle might considerably increase the computational effort. We find that $\Delta\Delta E_G$ becomes sufficiently small (of the order of 1.5 kJ mol^{-1}) for $R \geq 8$ Å. Significantly, at these R values the QM-Opt protocol has a lower computational cost than the MD-Opt protocol, see Figure 6.12. The extra computational effort expended in optimizing the ungrafted silica at the QM level is more than balanced by the reduction in computational

effort to optimize the grafted catalyst site on the QM-pre-optimized cluster. These findings should help to create a large number of cluster models for computational analysis of amorphous catalysts, and to obtain results that are nearly converged with respect to cluster size, while minimizing artifacts introduced by the computational protocol.

Bibliography

1. White, L. & Duffy, G. STAFF-INDUSTRY COLLABORATIVE REPORT Vapor-Phase Production of Colloidal Silica. *Ind. Eng. Chem.* **51,** 232–238. https://pubs.acs.org/doi/abs/10.1021/ie51394a019 (Mar. 1959).

2. Rahman, I. A. & Padavettan, V. Synthesis of Silica nanoparticles by Sol-Gel: Size-dependent properties, surface modification, and applications in silica-polymer nanocompositesa review. *J. Nanomater.* **2012,** 132424. https://doi.org/10.1155/2012/132424 (2012).

3. Garrett, P. R. *Defoaming: Theory and industrial applications* 329. https://doi.org/10.1201/9781315140827 (CRC Press, Boca Raton, 1992).

4. Barthel, H., Rösch, L. & Weis, J. *Fumed Silica - Production, Properties, and Applications* 761–778. https://doi.org/10.1002/9783527620777.ch91a (2005).

5. Ghimire, P. P. & Jaroniec, M. Renaissance of Stöber method for synthesis of colloidal particles: New developments and opportunities. *J. Colloid Interface Sci.* https://doi.org/10.1016/j.jcis.2020.10.014 (2020).

6. Vansant, E. E., Van Der Voort, P. & Vrancken, K. C. *Characterization and Chemical Modification of the Silica Surface* (1995).

7. Goldsmith, B. R., Peters, B., Johnson, J. K., Gates, B. C. & Scott, S. L. Beyond Ordered Materials: Understanding Catalytic Sites on Amorphous Solids. *ACS Catal.* **7,** 7543–7757. https://www.doi.org/10.1021/acscatal.7b01767 (2017).

8. Peters, B. & Scott, S. L. Single Atom Catalysts on Amorphous Supports: A Quenched Disorder Perspective. *J. Chem. Phys.* **142,** 104708. https://www.doi.org/10.1063/1.4914145 (2015).

9. Goldsmith, B. R., Sanderson, E. D., Bean, D. & Peters, B. Isolated Catalyst Sites on Amorphous Supports: A Systematic Algorithm for Understanding Heterogeneities in Structure and Reactivity. *J. Chem. Phys.* **138,** 204105. https://www.doi.org/10.1063/1.4807384 (2013).

10. Ewing, C. S., Bhavsar, S., Veser, G., McCarthy, J. J. & Johnson, J. K. Accurate amorphous silica surface models from first-principles thermodynamics of surface dehydroxylation. *Langmuir* **30,** 5133–5141. https://doi.org/10.1021/la500422p (2014).

11. Zwanzig, R. Rate Processes with Dynamical Disorder. *Acc. Chem. Res.* **23,** 148–152. https://www.doi.org/10.1021/ar00173a005 (1990).

12. Johannessen, T., Larsen, J. H., Chorkendorff, I., Livbjerg, H. & Topsøe, H. Catalyst dynamics: consequences for classical kinetic descriptions of reactors. *Chem. Eng. J.* **82.** FRONTIERS IN CHEMICAL REACTION ENGINEERING, 219–230. https://doi.org/10.1016/S1385-8947(00)00338-7 (2001).

13. Xing, X., Yoon, B., Landman, U. & Parks, J. H. Structural evolution of Au nanoclusters: From planar to cage to tubular motifs. *Phys. Rev. B* **74,** 165423. https://www.doi.org/10.1103/PhysRevB.74.165423 (2006).

14. Hammes, G. G., Benkovic, S. J. & Hammes-Schiffer, S. Flexibility, Diversity, and Cooperativity: Pillars of Enzyme Catalysis. *Biochemistry* **50,** 10422–10430. https://doi.org/10.1021/bi201486f (2011).

15. Bhattacharya, S., Levchenko, S. V., Ghiringhelli, L. M. & Scheffler, M. Stability and Metastability of Clusters in a Reactive Atmosphere: Theoretical Evidence for Unexpected Stoichiometries of $Mg_M\mathbf{O}_x$. *Phys. Rev. Lett.* **111,** 135501. https://link.aps.org/doi/10.1103/PhysRevLett.111.135501 (13 Sept. 2013).

16. Wang, Y.-G., Yoon, Y., Glezakou, V.-A., Li, J. & Rousseau, R. The Role of Reducible Oxide–Metal Cluster Charge Transfer in Catalytic Processes: New Insights on the Catalytic Mechanism of CO Oxidation on Au/TiO2 from ab Initio Molecular Dynamics. *J. Am. Chem. Soc.* **135,** 10673–10683. https://doi.org/10.1021/ja402063v (2013).

17. Goldsmith, B. R. *et al.* Two-to-three dimensional transition in neutral gold clusters: The crucial role of van der Waals interactions and temperature. *Phys. Rev. Materials* **3,** 016002. https://link.aps.org/doi/10.1103/PhysRevMaterials.3.016002 (1 Jan. 2019).

18. Zhang, J., Hu, P. & Wang, H. Amorphous Catalysis: Machine Learning Driven High-Throughput Screening of Superior Active Site for Hydrogen Evolution Reaction. *J. Phys. Chem. C* **124,** 10483–10494. https://www.doi.org/10.1021/acs.jpcc.0c00406 (2020).

19. Jystad, A. M., Biancardi, A. & Caricato, M. Simulations of Ammonia Adsorption for the Characterization of Acid Sites in Metal-Doped Amorphous Silicates. *J. Phys. Chem. C* **121,** 22258–22267. https://www.doi.org/10.1021/acs.jpcc.7b08113 (2017).

20. Handzlik, J. Application of the ONIOM (QM/QM) method in the study of molybdena-silica system active in olefin metathesis. *Int. J. Quantum Chem.* **107,** 2111–2119. https://www.doi.org/10.1002/qua.21397 (2007).

21. Tranca, D. C., Wojtaszek-Gurdak, A., Ziolek, M. & Tielens, F. Supported and inserted monomeric niobium oxide species on/in silica: a molecular picture. en. *Phys. Chem. Chem. Phys.* **17,** 22402–22411. https://doi.org/10.1039/C5CP03450G (2020) (2015).

22. Lichtenstein, L. *et al.* The atomic structure of a metal-supported vitreous thin silica film. *Angew. Chem., Int. Ed.* **116,** 20429–20432. https://doi.org/10.1002/anie.201107097 (2012).

23. Smith, J. D. *et al.* Energetics of Hydrogen Bond Network Rearrangements in Liquid Water. *Science* **306,** 851–853. https://doi.org/10.1126/science.1102560 (2004).

24. Pan, D. *et al.* Surface energy and surface proton order of the ice Ih basal and prism surfaces. *Journal of Physics Condensed Matter* **22,** 074209 (2010).

25. Smit, W. J. *et al.* Excess Hydrogen Bond at the Ice-Vapor Interface around 200 K. *Physical Review Letters* **119,** 133003 (2017).

26. Nordlund, D. *et al.* Sensitivity of x-ray absorption spectroscopy to hydrogen bond topology. *Phys. Rev. B* **80,** 233404. https://link.aps.org/doi/10.1103/PhysRevB.80.233404 (23 Dec. 2009).

27. Gulmen, T. S. & Thompson, W. H. Testing a two-state model of nanoconfined liquids: Conformational equilibrium of ethylene glycol in amorphous silica pores. *Langmuir* **22,** 10919–10923. https://www.doi.org/10.1021/la062285k (2006).

28. Ugliengo, P. *et al.* Realistic models of hydroxylated amorphous silica surfaces and MCM- 41 mesoporous material simulated by large-scale periodic B3LYP calculations. *Adv. Mater.* **20,** 4579–4583. https://www.doi.org/10.1002/adma.200801489 (2008).

29. Tielens, F., Gervais, C., Lambert, J. F., Mauri, F. & Costa, D. Ab initio study of the hydroxylated surface of amorphous silica: A representative model. *Chem. Mater.* **20,** 3336–3344. https://www.doi.org/10.1021/cm8001173 (2008).

30. Comas-Vives, A. Amorphous SiO_2 surface models: Energetics of the dehydroxylation process, strain, ab initio atomistic thermodynamics and IR spectroscopic signatures. *Phys. Chem. Chem. Phys.* **18,** 7475–7482. https://www.doi.org/10.1039/c6cp00602g (2016).

31. Tielens, F., Gierada, M., Handzlik, J. & Calatayud, M. Characterization of amorphous silica based catalysts using DFT computational methods. *Catal. Today* **354,** 3–18. https://www.doi.org/10.1016/j.cattod.2019.03.062 (2020).

32. Ewing, C. S. *et al.* Impact of Support Interactions for Single-Atom Molybdenum Catalysts on Amorphous Silica. *Ind. Eng. Chem. Res.* **55,** 12350–12357. https://www.doi.org/10.1021/acs.iecr.6b03558 (2016).

33. Sautet, P. & Delbecq, F. Catalysis and surface organometallic chemistry: A view from theory and simulations. *Chem. Rev.* **110,** 1788–1806. https://doi.org/10.1021/cr900295b (2010).

34. Chen, B. W. J., Xu, L. & Mavrikakis, M. Computational Methods in Heterogeneous Catalysis. *Chem. Rev.* **121,** 1007–1048. https://doi.org/10.1021/acs.chemrev.0c01060 (2021).

35. Handzlik, J. & Ogonowski, J. Structure of Isolated Molybdenum(VI) and Molybdenum(IV) Oxide Species on Silica: Periodic and Cluster DFT Studies. *J. Chem. Phys. C* **116,** 5571–5584. https://www.doi.org/10.1021/jp207385h (2012).

36. Handzlik, J., Grybos, R. & Tielens, F. Structure of Monomeric Chromium(VI) Oxide Species Supported on Silica: Periodic and Cluster DFT Studies. *J. Chem. Phys. C* **117,** 8138–8149. https://www.doi.org/10.1021/jp3103035 (2013).

37. Van Santen, R. A. & Kramer, G. J. Reactivity Theory of Zeolitic Broensted Acidic Sites. *Chem. Rev.* **95,** 637–660. https://doi.org/10.1021/cr00035a008 (1995).

38. in. *Catalysis: An Integrated Approach* (eds van Santen, R., van Leeuwen, P., Moulijn, J. & Averill, B.) 433–457 (Elsevier, 1999). https://doi.org/10.1016/S0167-2991(99)80012-3.

39. Sauer, J. Molecular models in ab initio studies of solids and surfaces: from ionic crystals and semiconductors to catalysts. *Chem. Rev.* **89,** 199–255. https://doi.org/10.1021/cr00091a006 (1989).

40. Sauer, J., Ugliengo, P., Garrone, E. & Saunders, V. R. Theoretical Study of van der Waals Complexes at Surface Sites in Comparison with the Experiment. *Chem. Rev.* **94,** 2095–2160. https://doi.org/10.1021/cr00031a014 (1994).

41. Van Santen, R. A. & Neurock, M. *Molecular Heterogeneous Catalysis* https://www.doi.org/10.1002/9783527610846.ch2 (Wiley-VCH, Weinheim, Germany, 2007).

42. Catlow, C. R., French, S. A., Sokol, A. A. & Thomas, J. M. Computational approaches to the determination of active site structures and reaction mechanisms in heterogeneous catalysts. *Philos. Trans. R. Soc. A: Math. Phys. Eng. Sci.,* 913–936 (2005).

43. Fermann, J. T. *et al.* Modeling proton transfer in zeolites: Convergence behavior of embedded and constrained cluster calculations. *J. Chem. Theory Comput.* **1,** 1232–1239 (2005).

44. Migues, A. N., Muskat, A., Auerbach, S. M., Sherman, W. & Vaitheeswaran, S. On the rational design of zeolite clusters. *ACS Catal.* **5,** 2859–2865. https://doi.org/10.1021/cs501827p (2015).

45. Fong, A., Yuan, Y., Ivry, S. L., Scott, S. L. & Peters, B. Computational Kinetic Discrimination of Ethylene Polymerization Mechanisms for the Phillips (Cr/SiO_2) Catalyst. English. *ACS Catal.* **5,** 3360–3374. https://www.doi.org/10.1021/acscatal.5b00016 (2015).

46. Moses, A. W. *et al.* Spectroscopically distinct sites present in methyltrioxorhenium grafted onto silica-alumina, and their abilities to initiate olefin metathesis. *J. Am. Chem. Soc.* **129.** https://doi.org/10.1021/ja072707s (2007).

47. Rimola, A., Fabbiani, M., Sodupe, M., Ugliengo, P. & Martra, G. How Does Silica Catalyze the Amide Bond Formation under Dry Conditions? Role of Specific Surface Silanol Pairs. *ACS Catal.* **8,** 4588–4568. https://doi.org/10.1021/acscatal.7b03961 (2018).

48. Curtiss, L. & Gordon, M. *Computational Materials Chemistry: Methods and Applications* ISBN: 9781402021176. https://books.google.com/books?id=u-IUSSTSrqcC (Springer Berlin, 2006).

49. McDaniel, M. P. A Review of the Phillips Supported Chromium Catalyst and Its Commercial Use for Ethylene Polymerization. English. *Adv. Catal.* **53,** 123–606. https://www.doi.org/https://doi.org/10.1016/S0360-0564(10)53003-7 (2010).

50. Nash, S. G. Preconditioning of Truncated-Newton Methods. *SIAM J. Comput.* **6,** 599–616. https://doi.org/10.1137/0906042 (3 1985).

51. Virtanen, P. *et al.* SciPy 1.0: Fundamental Algorithms for Scientific Computing in Python. *Nat. Methods* **17,** 261–272 (2020).

52. Bradbury, J. *et al.* JAX: composable transformations of Python+NumPy programs. Version 0.1.55. http://github.com/google/jax (2018).

53. Plimpton, S. Fast Parallel Algorithms for Short-Range Molecular Dynamics. *J. Comp. Chem.* **117,** 1–19 (1995).

54. Van Beest, B. W. H., Kramer, G. J. & van Santen, R. A. Force fields for silicas and aluminophosphates based on ab initio calculations. *Phys. Rev. Lett.* **64,** 1955–1958. https://doi.org/10.1103/PhysRevLett.64.1955 (16 1990).

55. Gulmen, T. S. & Thompson, W. Model silica pores with controllable surface chemistry for molecular dynamics simulations. *MRS Proc.* **899** (2005).

56. Ramírez, A., Lopez, B. L. & Sierra, L. Study of the Acidic Sites and Their Modifications in Mesoporous Silica Synthesized in Acidic Medium under Quiescent Conditions. *J. Phys. Chem. B* **107,** 9275–9280. https://doi.org/10.1021/jp0351472 (2003).

57. Wang, T.-H. *et al.* The surprising oxidation state of fumed silica and the nature of water binding to silicon oxides and hydroxides. *Chem. Phys. Lett.* **501,** 159–165. https://www.doi.org/10.1016/j.cplett.2010.11.013 (2011).

58. Jystad, A. & Caricato, M. Computational Multinuclear NMR Characterization of Metal-Doped Amorphous Silica Catalysts. *Chem. Mater.* **30,** 7813–7822. https://doi.org/10.1021/acs.chemmater.8b03257 (2018).

59. Wu, J.-F. *et al.* Correlation of Active Site Precursors and Olefin Metathesis Activity in W-Incorporated Silicates. *ACS Catal.* **8,** 10437–10445. https://doi.org/10.1021/acscatal.8b03263 (2018).

60. Wu, J.-F. *et al.* Enhanced Olefin Metathesis Performance of Tungsten and Niobium Incorporated Bimetallic Silicates: Evidence of Synergistic Effects. *ChemCatChem* **12,** 2004–2013. https://doi.org/10.1002/cctc.201902131 (2020).

61. Jystad, A., Leblanc, H. & Caricato, M. Surface Acidity Characterization of Metal-Doped Amorphous Silicates via Py-FTIR and ^{15}N NMR Simulations. *J. Phys. Chem. C* **124,** 15231–15240. https://doi.org/10.1021/acs.jpcc.0c03292 (2020).

62. Frisch, M. J. *et al. Gaussian Development Version Revision J.11* 2020.

63. Becke, A. D. Density-functional thermochemistry. III. The role of exact exchange. *J. Chem. Phys.* **98,** 5648–5652 (1993).

64. Grimme, S., Antony, J., Ehrlich, S. & Krieg, H. A consistent and accurate ab initio parametrization of density functional dispersion correnction (DFT-D) for the 94 elements H-Pu. *J. Chem. Phys.* **132,** 154104 (2010).

65. Weigend, F. & Ahlrichs, R. Balanced basis sets of split valence, triple zeta valence and quadruple zeta valence quality for H to Rn: Design and assessment of accuracy. *Phys. Chem. Chem. Phys.* **7,** 3297–3305 (2005).

66. Handzlik, J. Properties and metathesis activity of monomeric and dimeric Mo centres variously located on γ-alumina - A DFT study. *Surf. Sci.* **601,** 2054–2065. https://www.doi.org/10.1016/J.SUSC.2007.03.002 (2007).

67. Schrader, A. M. *et al.* Surface chemical heterogeneity modulates silica surface hydration. en. *Proc. Natl. Acad. Sci.* **115,** 2890–2895. http://www.pnas.org/lookup/doi/10.1073/pnas.1722263115 (2020) (Mar. 2018).

Appendix A

Supporting information for Computational Support for Phillips Catalyst Initiation via Cr-C Bond Homolysis in a Chromacyclopentane Site

A.1 Cluster model structure

The structure of the cluster model was obtained by performing an unconstrained gas phase optimization of **^{5}I** using the computational methodology described in the Chapter 2. The peripheral OH groups were held fixed for all subsequent calculations.

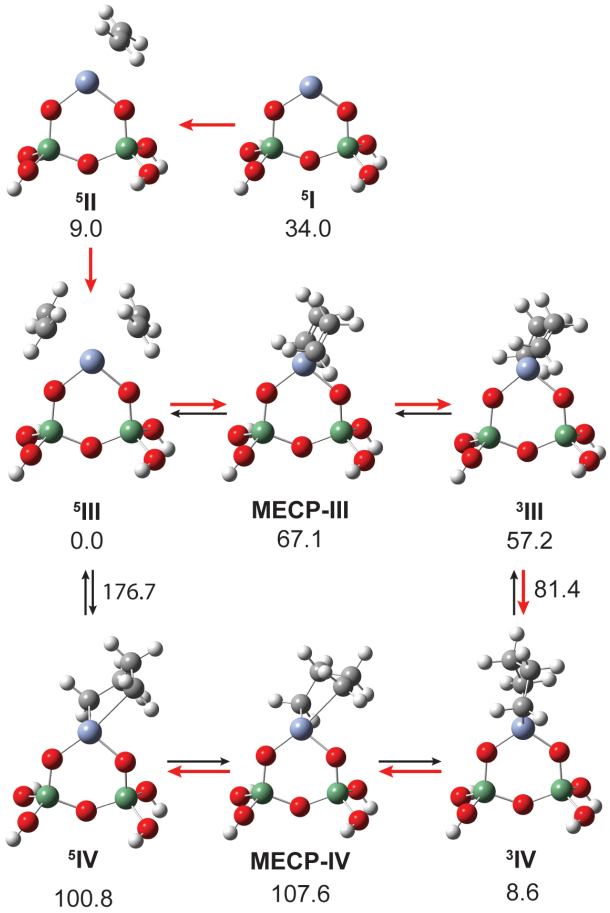

Figure A.1: Ball-and-stick representation of stationary points from Figure 1, illustrating geometry changes that occur due to spin state crossings for the *bis*(ethylene)Cr(II) complex and chromacyclopentane site. Free energies (kJ/mol) are given relative to **^{5}III**, at 373 K. Colored arrows show the preferred path.

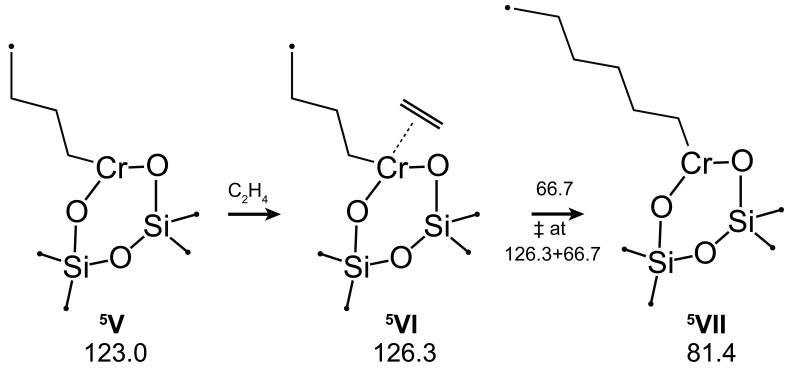

Figure A.2: Stationary points in ethylene insertion at Cr for a growing tethered alkyl radical. Free energies (kJ/mol) for all species are given relative to the *bis*(ethylene)Cr(II) complex, ^{5}**III**, at 373 K. ^{5}**V**, tethered *n*-butyl radical; ^{5}**VI**, ethylene complex with tethered *n*-butyl radical; ^{5}**VII**, tethered *n*-hexyl radical.

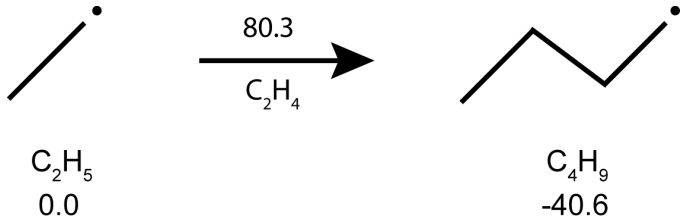

Figure A.3: Reaction of ethylene with ethyl radical. Free energies (kJ/mol) for all species are given relative to the ethyl radical, C_2H_5•, at 373 K. The free energy barrier approximates that for reaction of the tethered radical ^{5}**V** with ethylene to increase the length of the alkyl radical chain.

A.2 Irreversibility of initiation by *n*-butyl-bridged Cr(III) formation

All free energies quoted in the manuscript use the OH terminated cluster. However, we used a different cluster in calculations (only discussed in the SI) to ensure the formation of ^{3}**BB** is effectively irreversible. Our assumption is that ethylene insertion into the C-Cr bonds of the ^{3}**BB** site will begin before ^{3}**BB** can revert to the tethered radical (^{5}**V**). To test this assumption with calculations, we needed a model that included two adjacent Cr sites. The model of these sites was changed in three respects:

1. The capping hydroxyl groups were replaced by fluorine atoms. This change was made to avoid hydrogen-bonding interactions between capping groups of adjacent $^{5}\mathbf{I}$ sites, to simplify the geometry optimizations, and to ensure that the capping atoms from one cluster model do not interact with the Cr atom on the adjacent cluster.

2. The basis set 6-31G was used for the F atoms to better mimic the size of oxygen and its electronegativity in an extended silica framework. Goldsmith et al. found that this basis set best matches the deprotonation energy of $HOSiF_3$ (ca. 1405 kJ/mol) to the deprotonation energy of a silsesquioxane (1412 kJ/mol) modeled using B3LYP/LANL2DZ for the non-fluorine atoms.[1] The positions of the F atoms were found by optimizing an unconstrained, bare Cr(II) species ($^{5}\mathbf{I.F}$), as we did for the OH capped cluster model, $^{5}\mathbf{I}$.[2]

3. Once the isolated site with F-capping atoms was optimized, we created an *n*-butyl bridged pair of sites with the F-capping atoms ($^{3}\mathbf{BB.F}$). To ensure that the individually optimized site geometries were not altered during the $^{3}\mathbf{BB.F}$ optimization, we fixed the F-F bond lengths, F-F-F angles, and F-F-F-F dihedral angles within the individual clusters. In this manner, the optimization effectively determines the ideal distance and orientation of two rigid $^{5}\mathbf{I.F}$ sites to support the formation of an *n*-butyl bridge. Species capped with fluorine atoms are denoted $^{\mathbf{Y}}\mathbf{X.F}$, where $\mathbf{X}$ designates the species, $\mathbf{Y}$ is its spin state, and $\mathbf{F}$ indicates that the dangling bonds are capped by fluorine atoms. The optimized model $^{5}\mathbf{I.F}$ is shown in Figure A.4. A comparison of key geometric parameters with the OH-capped cluster, $^{5}\mathbf{I}$, is shown in Table A.1.

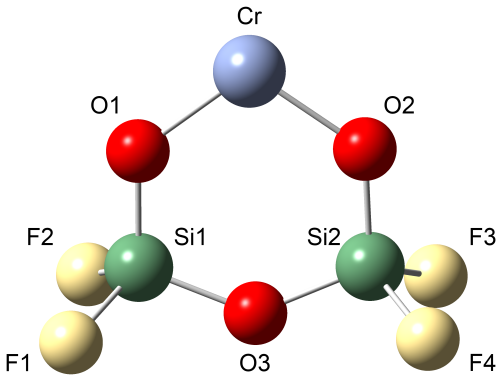

Figure A.4: Cr(II) cluster model **^{5}I.F**, with F capping atoms. Color scheme: Blue: Cr; Red: O, Green: Si; Yellow: F.

Table A.1: Comparison of key bond lengths (Å) and angles (deg.) in the cluster models **^{5}I** and **^{5}I.F**

	^{5}I	**^{5}I.F**
∠ O1-Cr-O2	109.78	107.54
∠ O3-Si1-O1	107.94	111.44
∠ O2-Si2-O3	107.9	111.41
∠ Si1-O3-Si2	139.25	134.89
r(Cr-O1)	1.82	1.84
r(Cr-O2)	1.82	1.84

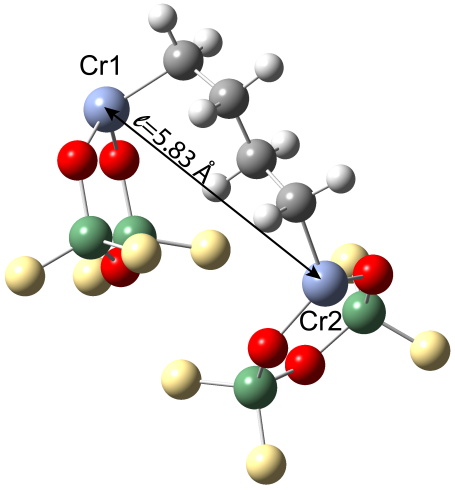

Figure A.5: Stationary point for the *n*-butyl-bridged Cr(III) clusters. The Cr-Cr distance is 5.83 Å. Color scheme: Blue: Cr; Red: O, Green: Si; Yellow: F; Grey: C; White: H.

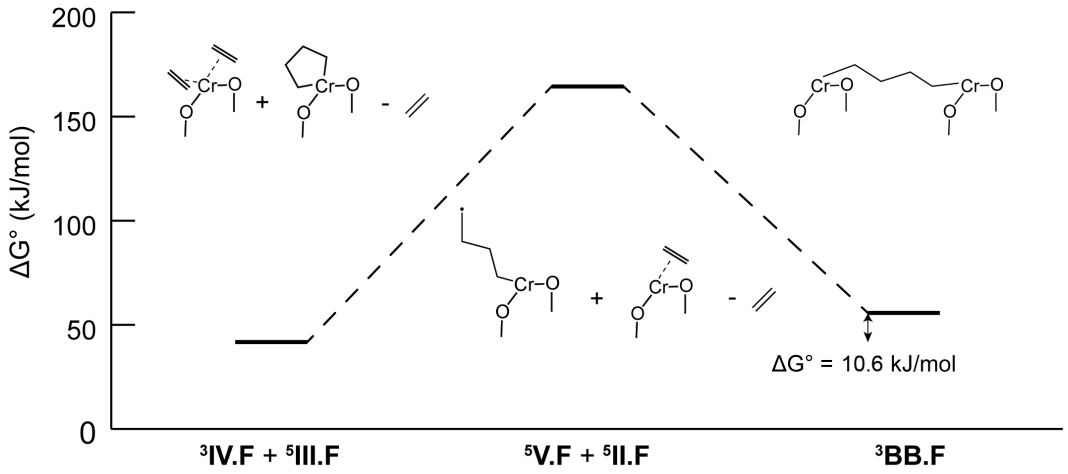

Figure A.6: Free energy diagram for **^{3}BB.F** formation from **^{5}IV.F** and **^{5}III.F**, using cluster models capped with fluorine atoms (Figure A.4). The estimated free energy barrier is 119.2 kJ/mol, in agreement with the estimated barrier in Figure 2.2 (123.4 kJ/mol). The free energy barrier for the reverse reaction (from **^{3}BB.F** to **^{5}V.F** + **^{5}II.F**) is 108 kJ/mol. Based on the previous work, the free energy barrier to insert ethylene into C-Cr bonds like those in site **^{3}BB.F** is about 80 kJ/mol. We therefore conclude that (on most sites) formation of *n*-butyl bridges between Cr(III) sites leads to irreversible initiation.

Note that information in Table A.2 can be used to estimate the overall barrier entirely

from calculations based on the F-capped cluster model. The overall barrier for initiation from F-capped sites is 160 kJ/mol (from the free energies of ^{5}**V.F** and ^{5}**III.F**). This estimate is 28 kJ/mol higher than the 132 kJ/mol barrier obtained based on OH-capped cluster calculations. The sensitive dependence of rates to subtle structural and electronic differences between sites illustrates the uncertainty in all findings based on single-site calculations. The sensitivity to subtle structural and electronic differences also suggests that the real catalyst (with many different sites) may present sites that cannot initiate by tethered homolysis and, perhaps, sites that initiate much faster than predicted by our calculations.

A.3 A kinetic model for initiation of paired Cr sites

Here we develop an approximate kinetic model to predict the rate at which sites activate starting from fully reduced Cr(II) sites ^{5}**I** in the presence of ethylene. The rate of initiation depends on the free energy differences between states, the free energy barriers between states, and the density of Cr atoms, as described in the main text. The derivation requires a few additional definitions. Let $\theta_D(t)$ be the fraction of "dormant" (D) Cr sites that have not yet been activated at time t. Also define conditional probabilities (fractional coverages) within the dormant population as

$$\theta_{\mathbf{X}|D} \equiv \text{probability of being in state } \mathbf{X} \text{ given in population D} \tag{A.1}$$

According to our DFT calculations, the bottleneck during initiation is the rate-determining (adiabatic) transition state for the creation of the tethered n-butyl radical ^{5}**V** from state ^{5}**IV**. Once formed, the n-butyl radical ^{5}**V** must have a neighbor in state ^{5}**II** or ^{5}**I** to create the n-butyl-bridged ^{3}**BB** site. The standard free energy of site ^{5}**II** at 373 K is 25

kJ/mol lower than that of site $^{5}\mathbf{I}$. Therefore, the probability of finding the neighboring site in state $^{5}\mathbf{I}$ is negligible compared to the probability of finding a neighboring site in state $^{5}\mathbf{II}$. The DFT calculations predict that the most abundant dormant intermediate is state $^{5}\mathbf{III}$, with a standard free energy that is approximately 9 kJ/mol lower than all other dormant states. Accordingly, we can approximate that

$$\begin{aligned} \theta_{^{5}\mathbf{III}|D} \equiv & \text{ fraction of dormant sites in state } ^{5}\mathbf{III} \\ \approx & \, 1.0 \end{aligned} \tag{A.2}$$

with all other dormant sites having relatively small fractional coverages. Based on a quasi-equilibrium approximation for other dormant states (all before the bottleneck), the fractional (conditional) coverages of other key dormant states are

$$\begin{aligned} \theta_{^{5}\mathbf{IV}|D} \equiv & \text{ fraction of dormant sites in state } ^{5}\mathbf{IV} \\ = & \, K_{^{5}\mathbf{III}\rightarrow{}^{5}\mathbf{IV}} \cdot \theta_{^{5}\mathbf{III}|D} \\ \approx & \, e^{-(100.8\,\mathrm{kJ/mol})/\mathrm{k_B T}} \cdot 1.0 \end{aligned} \tag{A.3}$$

and

$$\begin{aligned} \theta_{^{5}\mathbf{II}|D} \equiv & \text{ fraction of dormant sites in state } ^{5}\mathbf{IV} \\ = & \, \theta_{^{5}\mathbf{III}|D}/(K_{^{5}\mathbf{II}\rightarrow{}^{5}\mathbf{III}} P_{C2H4}) \\ \approx & \, (e^{(+9.0kJ/mol)/k_B T} \cdot P_{C2H4})^{-1} \end{aligned} \tag{A.4}$$

The free energy calculations that were used to compute $K_{^{5}\mathbf{III}\rightarrow{}^{5}\mathbf{IV}}$ and $K_{^{5}\mathbf{II}\rightarrow{}^{5}\mathbf{III}}$ were performed at 373 K and 1 atm, so the numerical value of the ethylene pressure $P_{C_2H_4}$ will have units of atm.

The rate at which the elongated Cr-C bond in site $^{3}\mathbf{IV}$ undergoes homolysis can be

estimated using a simple transition state theory expression:

$$\begin{aligned} k_{^5\mathbf{IV}\rightarrow{}^5\mathbf{V}} \equiv\ & \text{rate constant for Cr - C bond homolysis from state } {}^5\mathbf{IV} \\ \approx\ & \frac{k_B T}{h} e^{-(123.0-100.8)(kJ/mol)/k_B T} \end{aligned} \tag{A.5}$$

More accurate rate expressions could be obtained by (1) finding the actual saddle point on the potential energy surface for n-butyl radical migration from one Cr atom to the other, and/or (2) by performing a variational transition state theory calculation as outlined by Fong et al.[3] The results of these more elaborate calculations will vary from one site to another. Here we proceed to develop a simple and approximate model based on the properties of the one cluster model from our DFT calculations.

The quantities above can be used to develop a kinetic model in two ways: (1) by considering individual dormant sites or (2) by explicitly considering pairs of dormant Cr sites within the maximum length ℓ of the n-butyl bridge. A mean field kinetic model based on the number of individual dormant sites must incorporate, for each site, the same non-zero probability of having a neighboring dormant Cr site within distance ℓ. Thus, a mean field kinetic model with irreversible initiation must eventually activate all sites. To avoid this limitation of the mean field model, we start with an explicit estimate of the number of dormant pairs of Cr sites. Using Poisson statistics (eqn. 2.1 from Chapter 2), the number of pairs of sites separated by a distance ℓ or less is

$$n_P(0) = n \cdot \lambda \exp[-\lambda]/2 \tag{A.6}$$

where $\lambda = \pi \ell^2 \sigma_{Cr}$, and where n is the total number of Cr sites. At a typical industrial Phillips catalyst loading of $\sigma_{Cr} \leq 0.4$ Cr atoms/nm^2 and using $\ell \approx 5.8$ Å, about 27% of Cr sites are paired (based on $\lambda \exp[-\lambda] = 0.27$). Note that by using $\lambda \exp[-\lambda]$, we ignore sites with multiple neighbors within distance ℓ. These multiply-paired sites are

already rare (ca. 7 %, from $\lambda^2 \exp[-\lambda]/2! + \lambda^3 \exp[-\lambda]/3! + \cdots$) at typical catalyst loadings and they become even rarer at lower loadings. Moreover, a site with multiple nearby neighbors (see Figure A.7) can only form an n-butyl bridge to one neighbor, so some of the "extra" neighbors may not become active sites.

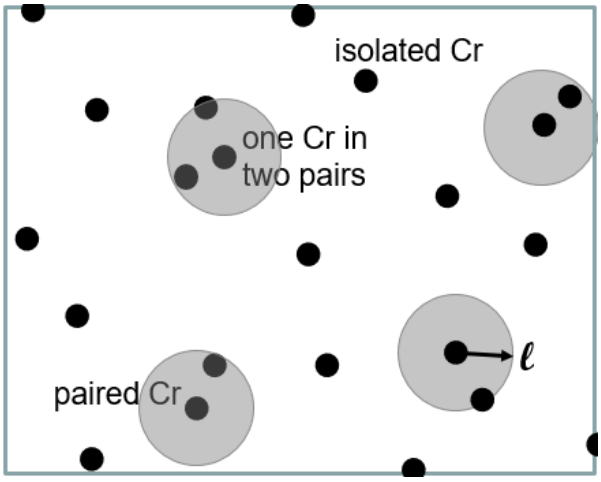

Figure A.7: Cr sites on the SiO_2 surface may be isolated, paired, or multiply paired, depending on the number of neighboring Cr sites within a distance ℓ. Gray circles of radius ℓ in the diagram highlight four of the paired Cr sites. Our kinetic model does not account for multiply paired Cr atoms, which become more common as the Cr loading σ_{Cr} increases.

The rate at which dormant pairs of Cr sites become active is given by

$$\frac{dn_P}{dt} = -2 \cdot \theta_{^5\mathbf{IV}|D} \theta_{^5\mathbf{II}|D} k_{^5\mathbf{IV}\rightarrow{}^5\mathbf{V}} p_b \cdot n_P \tag{A.7}$$

where p_b is the probability that an n-butyl radical attaches to a neighboring Cr site rather than re-forming the original chromacyclopentane. We assume that $p_b \approx 1/2$. Using expressions A.1 – A.6 in A.7 gives

$$\frac{dn_P}{dt} = \frac{k_B T}{h} e^{-(132 kJ/mol)/k_B T} \frac{1}{P_{C2H4}} \cdot n_P \tag{A.8}$$

where 132 kJ/mol is the computed standard free energy difference for the net reaction

$^{3}\mathbf{IV} + {}^{5}\mathbf{III} \longrightarrow {}^{5}\mathbf{V} + {}^{5}\mathbf{II} + C_2H_4(g)$. Equation A.9 identifies an initiation time scale, *i.e.*, an induction time starting from the fully reduced $^{5}\mathbf{I}$ sites.

$$\tau_{ind} = P_{C2H4} \Big/ \left(\frac{k_B T}{h} e^{-(132kJ/mol)/k_B T} \right) \tag{A.9}$$

Based on the computed free energies, the induction time for initiation is 108 hours at 373 K and 1 atm of ethylene. The experimentally observed induction time is on the order of 1 hour for a catalyst that has been pre-reduced by CO to Cr(II)/SiO_2. For example, see Figure 16 in McDaniel's review in Adv. Catal.[4] The predicted induction time is about 100 times longer than the observed induction time. The discrepancy, modest by DFT standards, can be explained by errors in free energy calculations of about 15 kJ/mol, comparable to the mean absolute deviation for state-of-the-art DFT calculations.[5]

Equation A.8 is easily solved to obtain the number of dormant pairs as a function of time

$$n_P(t) = n_P(0) e^{-t/\tau_{ind}} = \frac{1}{2} n\lambda \exp[-\lambda] e^{-t/\tau_{ind}} \tag{A.10}$$

There are two sites per pair (at low coverage), so the number of active sites as a function of time is

$$2(n_P(0) - n_P(t)) = n\lambda \exp[-\lambda](1 - e^{-t/\tau_{ind}}) \tag{A.11}$$

Finally, the fraction of active sites as a function of time (ignoring multiply paired sites) is

$$\lambda \exp[-\lambda](1 - e^{-t/\tau_{ind}}) \tag{A.12}$$

with $\lambda = \pi \ell^2 \sigma_{Cr}$. Figure 2.3 from Chapter 2 (reproduced here) shows the predicted fraction of active sites as a function of time.

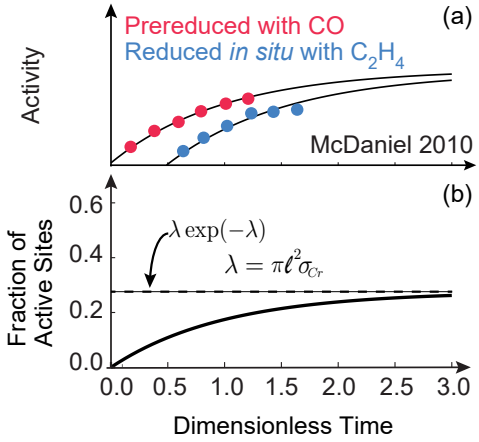

Figure A.8: Equations A.2-A.12 show the predicted fraction of active sites for $\sigma_{Cr} \leq 0.4$ Cr atoms / nm^2 (ignoring multiply paired sites). We emphasize that Figure A.8 only predicts the rate of initiation via the tethered homolysis mechanism. Other processes may also contribute to the total number of active sites, as described in the main text.

A.4 On enlarging the chromacycle prior to homolysis to extend its reach

As noted in the main text, chromacyclopentane ring expansion prior to homolysis could extend the reach of the radical-terminated chain to more distant Cr(II) sites (Figure A.9). Ethylene inserts into the chromacyclopentane ^{3}**IV** to give a chromacycloheptane ^{3}**VIII** with an overall free energy barrier of 157 kJ/mol, relative to ^{5}**III**. Further expansion to form a chromacyclononane ^{3}**IX** is prohibitively slow with a barrier of 189 kJ/mol. Cr-C bond homolysis in the chromacycloheptane ^{3}**VIII** requires an activation free energy of only about 122 kJ/mol. The distance between the Cr and the radical carbon chain end increases to 7.58 Å. However, the chromacycloheptane homolysis step competes with faster termination by intramolecular H-atom transfer. The latter pathway, with a barrier of only 114 kJ/mol, yields 1-hexene and regenerates the inactive bare ^{5}**I** site. Thus any chromacycle expansion events before the homolysis step will more likely

create an ethylene oligomer and an inactive site, rather than two active sites for polymerization. Moreover, the limiting step in this oligomerization cycle (from **^{3}IV** to **^{3}VIII** via ethylene insertion) requires 157 kJ/mol, which is 25 kJ/mol more than if Cr-C bond homolysis had occurred directly from **^{3}IV**. We conclude that this path is not important for initiation.

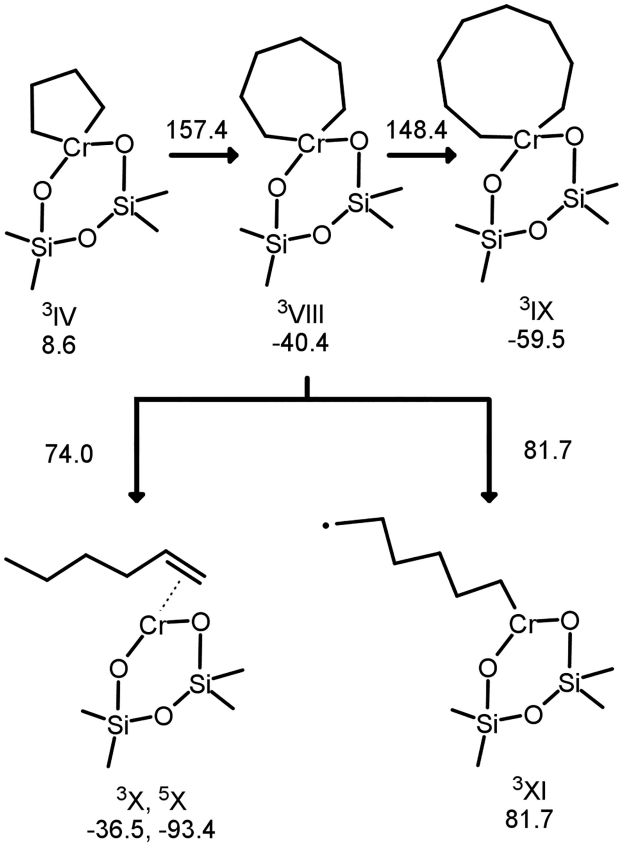

Figure A.9: Stationary points in metallacycle expansion, termination to 1-alkene, and Cr-C bond homolysis to a tethered radical. Free energies (kJ/mol) for all species are given relative to the *bis*(ethylene)Cr(II) complex, **^{5}III**, at 373 K. Numbers next to arrows represent free energies of transition states. **^{3}IV**, chromacyclopentane; **^{3}VIII**, chromacycloheptane; **^{3}IX**, chromacyclononane; **^{3}X**, (1-hexene)Cr(II) complex from intramolecular H-atom transfer; **^{3}VII**, tethered n-hexyl radical. Note: the triplet spin (1-hexene)Cr(II) complex, **^{3}X**, can later form a quintet spin (1-hexene)Cr(II) complex **^{5}X** that has an even lower free energy of -93.4 kJ/mol.

A.5 Approximate critical pore size calculation

Here we approximate the minimum silica pore size that is susceptible to fracture by polymer generation. The Griffith's equation[6] (eq A.13) relates the depth of a slit pore (a) to the Young's modulus (E), the interfacial energy (γ), and the fracture stress σ:

$$\sigma\sqrt{a} = \sqrt{2E\gamma/\pi} \tag{A.13}$$

To estimate the maximum stress that can be generated by polymerization, we equate $\Delta G = \sigma\Delta V$. The change in Gibbs free energy of reaction is 47 kJ/mol and the change in volume, ΔV, can be estimated as the inverse of the number of ethylene chains per unit volume, ρ^{-1}. Substitution of these terms yields $\sigma = \rho\Delta G$. Based on a value of $\rho = 34581$ mol/m^3 and $\Delta G = 47$ kJ/mol, the maximum stress generated is 1.63 GPa. Applying $\sigma = 1.63$ GPa, $\gamma = 1$ J/m^2, and $E = 62$ GPa into eq A.13, ethylene polymerization can crack silicas with slit pores deeper than $a = 15$ nm.

In experiments using siliceous Cr-SBA-15, Aguado et al.[7] showed that ethylene polymerization can fracture pores with diameters greater than 15 nm, given the walls are sufficiently thin. Their experiments and our calculation suggest that 15 nm be loosely identified as a critical pore size. However, the agreement between these estimates is probably coincidental, since the pore geometry in SBA-15 is very different from the notch/slit pore geometry in the Griffith model.

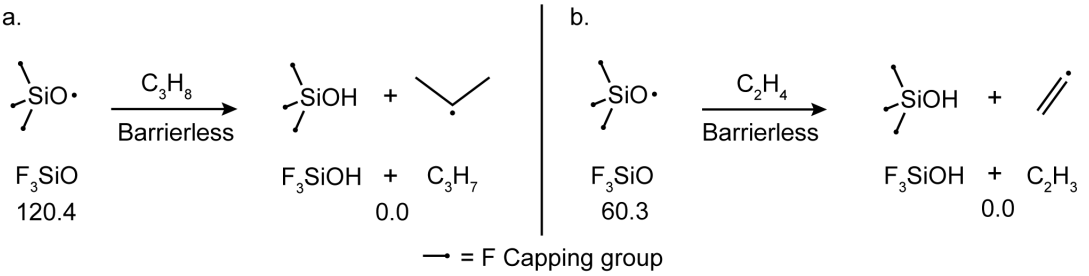

Figure A.10: Dangling bonds formed from fracturing can abstract an H atom from propane (a.) and ethylene (b.). which could react with Cr(II) sites to create active alkylCr(III) sites. F_3SiO and polyethylene model dangling bonds and polyethylene, respectively. Free energies (kJ/mol) are given relative to the products of schemes (a.) and (b.) and are downhill for both cases. These reactions are expected to have small barrier heights based on other studies of H atom abstractions involving hydroxyl radicals and hydrocarbons.[8]

Table A.2: Spin contamination before (S2) and after annihilation (S2A) of highest spin contaminant and the number of imaginary frequencies (N_ω) for each stationary point; energies in Hartrees

Species	Energy	S2	S2A	N_ω	Species	Energy	S2	S2A	N_ω
^{5}I	-2512.9	6.0150	6.0000	0	**^{5}TS[III-IV]**	-2310.1	6.0867	6.0015	1
^{5}I.F	-2248.8	6.0131	6.0000	0	**^{3}TS[III-IV]**	-2310.1	2.0652	2.0018	1
^{5}II	-2231.5	6.0127	6.0000	0	**^{3}TS[IV-VIII]**	-2388.7	2.9221	2.1571	1
^{5}II.F	-2327.4	6.0114	6.0000	0	**^{5}TS[VI-VII]**	-2388.7	6.0638	6.0008	1
^{5}III	-2310.1	6.0123	6.0000	0	**^{3}TS[VI-VII]**	-2388.7	3.0632	2.1313	1
^{5}III.F	-2406	6.0114	6.0000	0	**^{3}TS[VIII-IX]**	-2467.3	2.9398	2.1701	1
^{3}II	-2231.5	2.1102	2.0017	0	**^{3}TS[VIII-X]**	-2388.7	2.0826	2.0024	1
^{3}III	-2310.1	2.0463	2.0007	0					
^{3}III.F	-2405.9	2.0495	2.0006	0	**MECP-III**	-2310.1			
^{5}IV	-2310.1	6.0649	6.0006	0	**MECP-IV**	-2310.1			
^{5}IV.F	-2405.9	6.0774	6.0007	0					
^{3}IV	-2310.2	2.0803	2.0028	0	C_2H_3	-77.899	0.7638	0.7501	0
^{3}IV.F	-2406	2.1045	2.0047	0	C_2H_4	-78.587	0.0000	0.0000	0
^{5}V	-2310.1	6.0647	6.0007	0	C_2H_5	-79.157	0.7544	0.7500	0
^{5}V.F	-2406	6.0768	6.0008	0	C_3H_7	-118.48	0.7547	0.7500	0
^{3}V	-2310.1	3.0562	2.1297	0	C_3H_8	-119.15	0.0000	0.0000	0
^{5}VI	-2388.7	6.0701	6.0009	0	$n-C_4H_9$	-157.79	0.7544	0.7500	0
^{3}VI	-2388.7	3.0677	2.1426	0	$C_4H_9{}^+C_2H_4$	-236.38	0.7544	0.7500	0
^{5}VII	-2388.7	6.0625	6.0007	0	$C_4H_8{}^+C_2H_5$	-236.38	0.7544	0.7500	0
^{3}VII	-2388.7	3.0617	2.1276	0	**^{2}TS[C_2H_5+C_2H_4-C_4H_9]**	-157.74	0.7911	0.7503	1
^{3}VIII	-2388.8	2.0774	2.0025	0	**^{2}TS[C_4H_9+C_2H_4-C_4H_8 + C_2H_5]**	-236.33	0.8401	0.7512	1
^{3}IX	-2467.4	2.0837	2.0029	0					
^{5}X	-2388.8	6.0124	6.0000	0					
^{3}X	-2388.8	2.1094	2.0016	0					
^{3}BB.F	-4654.9	4.0813	4.5123	0					

Table A.3: Computed energies (kJ/mol), enthalpies (kJ/mol), entropies (kJ/mol), and Gibbs free energies (kJ/mol) of reaction and activation at 373.15 K

	ΔE	ΔH	$T\Delta S$	ΔG	$\Delta E^{\ddagger}$	$\Delta H^{\ddagger}$	$T\Delta S^{\ddagger}$	$\Delta G^{\ddagger}$
^{5}**I**+$C_2H_4 \rightarrow$ ^{5}**II**	-83.8	-76.5	-52.2	-24.3				
^{5}**I.F**+$C_2H_4 \rightarrow$ ^{5}**II.F**	-102.1	-90.0	-68.0	-22.0				
^{5}**II**+$C_2H_4 \rightarrow$ ^{5}**III**	-68.1	-61.0	-52.1	-8.9				
^{5}**II.F** $C_2H_4 \rightarrow$ ^{5}**III.F**	-79.1	-71.8	-62.8	-9.1				
^{3}**II**+$C_2H_4 \rightarrow$ ^{3}**III**	-64.8	-54.9	-54.5	-0.4				
^{5}**II** $\rightarrow$ ^{3}**II**	44.1	41.1	-7.6	48.7				
^{5}**III** $\rightarrow$ ^{3}**III**	47.3	47.2	-10.0	57.2				
^{5}**III.F** $\rightarrow$ ^{3}**III.F**	66.9	62.6	-11.2	73.7				
^{5}**III** $\rightarrow$ ^{5}**IV**	88.7	86.2	-14.6	100.8	186.0	177.3	0.5	176.7
^{5}**III.F** $\rightarrow$ ^{5}**IV.F**	109.8	104.1	-13.1	117.2				
^{3}**III** $\rightarrow$ ^{3}**IV**	-56.2	-55.6	-7.1	-48.6	19.9	17.2	-7.0	24.2
^{3}**III.F** $\rightarrow$ ^{3}**IV.F**	-35.6	-39.1	-7.1	-32.0				
^{3}**IV** $\rightarrow$ ^{5}**IV**	97.6	94.7	2.5	92.2				
^{3}**IV.F** $\rightarrow$ ^{5}**V.F**	126.7	121.4	11.2	110.2				
^{5}**IV** $\rightarrow$ ^{5}**V**	35.0	32.2	9.9	22.2				
^{3}**IV** $\rightarrow$ ^{3}**V**	131.9	126.4	11.2	115.2				
^{3}**IV** $\rightarrow$ ^{3}**VIII**	-127.6	-113.9	-64.8	-49.0	89.1	89.9	-59.0	148.8
^{5}**V** $\rightarrow$ ^{5}**VI**	-58.3	-50.6	-53.8	3.2				
^{3}**V** $\rightarrow$ ^{3}**VI**	-57.3	-49.7	-51.6	1.9				
^{5}**VI** $\rightarrow$ ^{5}**VII**	-56.8	-50.5	-5.6	-44.8	60.2	57.8	-8.9	66.7
^{3}**VI** $\rightarrow$ ^{3}**VII**	-57.0	-50.8	-6.8	-44.0	60.0	57.6	-11.0	68.7
^{3}**VIII** $\rightarrow$ ^{3}**IX**	-99.8	-88.4	-69.3	-19.0	129.0	129.1	-59.6	188.8
^{3}**VIII** $\rightarrow$ ^{3}**X**	9.1	9.9	5.9	4.0	114.3	105.2	-9.2	114.4
^{3}**X** $\rightarrow$ ^{5}**X**	-53.7	-50.0	6.9	-57.0				
^{3}**VIII** $\rightarrow$ ^{3}**VII**	145.2	139.8	17.7	122.1				
^{3}**BB.F** + C_2H_4	-27.8	-24.7	83.9	-108.6				
$^{2}C_2H_5 + C_2H_4 \rightarrow {}^{2}C_4H_9$	-113.0	-100.3	-59.7	-40.6	21.5	25.9	-54.4	80.3
$^{2}C_4H_9 + C_2H_4 \rightarrow$ C_4H_8 + $^{2}C_2H_5$	-13.2	-13.2	-1.3	-11.9	118.0	102.5	-27.0	129.5

Bibliography

1. Goldsmith, B. R., Sanderson, E. D., Bean, D. & Peters, B. Isolated Catalyst Sites on Amorphous Supports: A Systematic Algorithm for Understanding Heterogeneities in Structure and Reactivity. *J. Chem. Phys.* **138,** 204105. https://www.doi.org/10.1063/1.4807384 (2013).

2. Fong, A., Yuan, Y., Ivry, S. L., Scott, S. L. & Peters, B. Computational Kinetic Discrimination of Ethylene Polymerization Mechanisms for the Phillips (Cr/SiO_2) Catalyst. English. *ACS Catal.* **5,** 3360–3374. https://www.doi.org/10.1021/acscatal.5b00016 (2015).

3. Fong, A., Peters, B. & Scott, S. L. One-Electron-Redox Activation of the Reduced Phillips Polymerization Catalyst, via Alkylchromium (IV) Homolysis: A Computational Assessment. English. *ACS Catal.* **6,** 6073–6085. https://www.doi.org/10.1021/acscatal.6b01728 (2016).

4. McDaniel, M. P. A Review of the Phillips Supported Chromium Catalyst and Its Commercial Use for Ethylene Polymerization. English. *Adv. Catal.* **53,** 123–606. https://www.doi.org/https://doi.org/10.1016/S0360-0564(10)53003-7 (2010).

5. Harvey, J. N. On the Accuracy of Density Functional Theory in Transition Metal Chemistry. *Ann. Rep. Prog. Chem. C* **102,** 203–226. https://www.doi.org/10.1039/B419105F (2006).

6. Griffith, A. A. The Phenomena of Rupture and Flow in Solids. *Philos. Trans. R. Soc., A* **221,** 163. https://www.doi.org/10.1098/rsta.1921.0006 (1921).

7. Aguado, J., Calleja, G., Carrero, A. & Moreno, J. Morphological Modifications of Cr/SBA-15 and Cr/Al-SBA-15 Ethylene Polymerization Catalysts: Influence on Catalytic Behaviour and Polymer Properties. *Microporous Mesoporous Mater.* **131,** 294–302. https://www.doi.org/10.1016/j.micromeso.2010.01.006 (2010).

8. Hu, W.-P., Rossi, I., Corchado, J. C. & Truhlar, D. G. Molecular Modeling of Combustion Kinetics. The Abstraction of Primary and Secondary Hydrogens by Hydroxyl Radical. *J. Phys. Chem. A* **101,** 6911–6921. https://www.doi.org/10.1021/jp970188h (1997).

Appendix B

Supporting information for Grafting catalysts onto amorphous supports: from elementary steps to site populations via kernel regression

B.1 Parameters in model of grafting barriers and lattice displacements

B.1.1 Grafting temperature and dimensionless precursor concentration (m)

The grafting temperature was chosen to be 298.15 K (room temperature). The ratio of the ML_2 concentration in the gas phase to the reference concentration ($\hat{V}_0^{-1}$), $m = [\mathbf{ML_2}]/\hat{V}_0^{-1}$, was set to the ratio of CrO_2Cl_2 vapor pressure at 298.15 K (20 Torr) to

atmospheric pressure (760 Torr), giving $m = 0.026$.

B.1.2 DFT computational details

$D_{\mathbf{M}-O}$, $D_{\mathbf{M}\cdots O}$, $a_{\mathbf{M}-O}$, $a_{\mathbf{M}\cdots O}$, and $\Delta G^{\ddagger}_{ref}$ were set using density functional theory (DFT) calculations. All DFT calculations were performed with the ωB97X-D functional.[1] The def-2TZVP basis set[2] was used for chromium and the TZVP basis set[3,4] was used for all other atoms. The Berny algorithm, as implemented in Gaussian 16, was used to find minima and transition states.[5] The RMS and maximum forces were required to be less than 3.00×10^{-4} Hartrees/Bohr and 4.50×10^{-4} Hartrees/Bohr, respectively, while the RMS and maximum displacements were required to be less than 1.20×10^{-3} Bohr and 1.80×10^{-3} Bohr respectively. Transition states were required to have one imaginary frequency.

To make a reference site for DFT calculations, the bis(silanolato)chromium(II) cluster was optimized and its peripheral atom positions were held fixed for all subsequent computations to mimic a rigid support, Fig. B.1.[6]

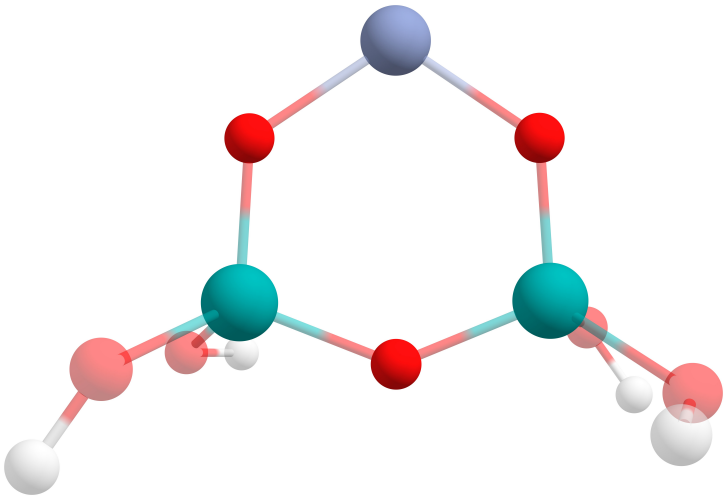

Figure B.1: The optimized bis(silanolato)chromium(II) cluster. Color scheme: oxygen (red), hydrogen (white), silicon (blue), and chromium (purple). Peripheral atoms (fixed) are transparent.

B.1.3 Morse potential parameters

The M-O bond strength ($D_{\mathbf{M}-O}$) was calculated by removing the Cr atom from the bis(silanolato) chromium(II) and performing a single-point energy calculation, Fig. B.2. $D_{\mathbf{M}-O}$ was calculated using

$$D_{\mathbf{M}-O} = E_{II} + E_{Cr} - E_{I}. \tag{B.1}$$

Here E_{II} is the electronic energy of structure II, E_{Cr} is the electronic energy of a Cr atom, and E_I is the electronic energy of the bis(silanolato)chromium(II) cluster (structure I). We get $D_{\mathbf{M}-O}$=524.4 kJ/mol.

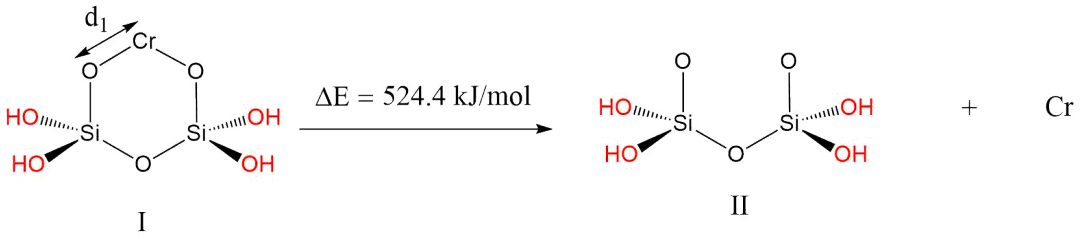

Figure B.2: Calculation of the M-O bond strength. Electronic energies of the optimized Cr(II) cluster (left) and cluster with dissociated Cr (right). Peripheral atoms (fixed) are red. d1 is used as the displacement variable in a Morse potential model (below).

The Morse potential width (a) can be related to the force constant by a second-order Taylor expansion of $V(r)$ around the equilibrium bond length (r_{eq}):

$$V(r) \approx \frac{d^2V}{dr^2}\frac{(r-r_{eq})^2}{2!} = k\frac{(r-r_{eq})^2}{2!} = Da^2(r-r_{eq})^2 \tag{B.2}$$

Here, k is the force constant. The zeroth-order term of the taylor expansion evaluates to 0 by construction, while the first derivative evaluates to 0 because r_{eq} corresponds to the minimum of the potential energy surface. Thus, $a = [k/2D]^{0.5}$. The force constant was computed using DFT by calculating the second derivative of the potential energy with

respect to the Cr-O bond length (d_1). We obtain $k_{\mathbf{M}-O} = 0.2063$ Ha/Bohr and $a_{\mathbf{M}-O} = 1$. Here $a_{\mathbf{M}-O}$ was non-dimensionalized by d_1. The non-dimensionalized equilibrium bond distance for the M-O bond ($r_{\mathbf{M}-O,eq}$) was set to 1.

To calculate the $\mathbf{M}\cdots O$ bond strength ($D_{\mathbf{M}\cdots O}$), a water molecule was adsorbed on the bare Cr cluster, and the cluster was reoptimized while keeping the positions of the peripheral atoms fixed, Fig. B.3. The bond strength of the $\mathrm{Cr}\cdots\mathrm{OH_2}$ bond was calculated using

$$D_{\mathbf{M}\cdots O} = E_I + E_{H_2O} - E_{III} \tag{B.3}$$

Here E_I is the electronic energy of structure I, E_{H_2O} is the electronic energy of the optimized water molecule, and E_{III} is the electronic energy of structure III. We get $D_{\mathbf{M}\cdots O} = 117$ kJ/mol.

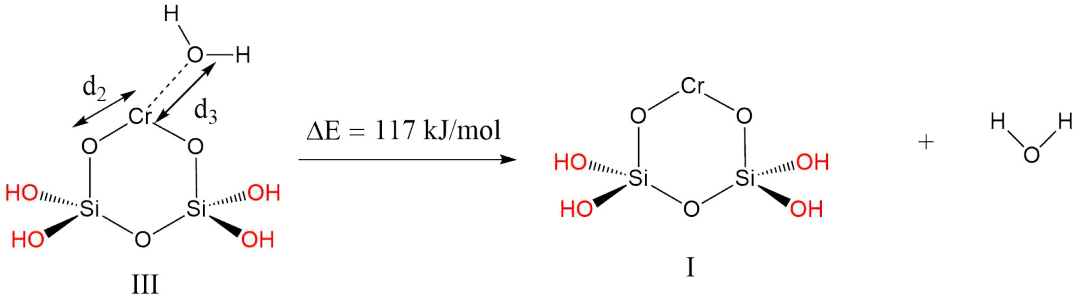

Figure B.3: Calculation of the $\mathrm{M}\cdots\mathrm{O}$ bond strength. Electronic energies of the Cr cluster with $\mathrm{H_2O}$ adsorbed (left) and the bare Cr cluster and $\mathrm{H_2O}$ in the gas phase (right). Peripheral atoms (fixed) are red. d_2/d_3 was used to compute $r_{M\cdots O,eq}$ and d_3 was used as a displacement variable in the Morse potential model for $\mathrm{M}\cdots\mathrm{O}$.

$k_{\mathbf{M}\cdots O}$ was computed as the second derivative of the energy of structure III with respect to the $M\cdots O$ bond length (d_3). We get $k_{\mathbf{M}\cdots O} = 0.054$ Ha/Bohr and $a_{\mathbf{M}\cdots O} = 2.3$ (Eq. (B.2)). Here $a_{\mathbf{M}\cdots O}$ was non-dimensionalized by d_3 (Fig. B.3).

The non-dimensionalized equilibrium $k_{\mathbf{M}\cdots O}$ bond length ($r_{\mathbf{M}\cdots O,eq}$) was set to d_3/d_2. This yields $r_{\mathbf{M}\cdots O,eq} = 1.16$.

B.1.4 Lattice displacements

The lattice points were displaced by drawing dispalcements according to a bivariate Gaussian distribution using the numpy.random.multivariate_normal function in python:[7]

$$p(\boldsymbol{x}, \boldsymbol{\mu}, \boldsymbol{\Sigma}) = \frac{1}{2\pi|\boldsymbol{\Sigma}|^{\frac{1}{2}}} exp(\frac{1}{2}(\boldsymbol{x}-\boldsymbol{\mu})^T\boldsymbol{\Sigma}^{-1}(\boldsymbol{x}-\boldsymbol{\mu})) \tag{B.4}$$

Here Σ is a 2×2 dimensional covariance matrix, $\boldsymbol{\mu} \in \boldsymbol{R}_2$ is the mean, and $\boldsymbol{x} \in \boldsymbol{R}_2$ is a 2D random variable representing displacement of lattice points. The covariance matrix was set equal to a scalar diagonal matrix

$$\boldsymbol{\Sigma} = \sigma^2_{lattice} I. \tag{B.5}$$

Here I is the 2×2 identity matrix. $\sigma^2_{lattice}$ was set to 0.00022 and the value of $\boldsymbol{\mu}$ was set to (0,0).

B.1.5 ϵ_{HL}, V_*, ΔPV, and ΔS^o to compute grafting free energy

From Eq. B.4, it follows that the grafting energy for a site on the unperturbed lattice is given by

$$\Delta E_{unperturbed} = 2\epsilon_{\boldsymbol{HL}} - (V_* + 2\epsilon_{\boldsymbol{ML}}) + V_{\boldsymbol{M}*}(\boldsymbol{x}_{unperturbed}). \tag{B.6}$$

Here V_{M*} is obtained by optimizing the metal position in a site on an unperturbed lattice. Similarly, from Eq. 3.8 it follows that the grafting free energy on an unperturbed site is given by

$$\Delta G^o_{unperturbed} = 2\epsilon_{\boldsymbol{HL}} - (V_* + 2\epsilon_{\boldsymbol{ML}}) + V_{\boldsymbol{M}^*}(\boldsymbol{x}_{unperturbed}) + \Delta PV - T\Delta S^o. \tag{B.7}$$

Rearranging Eq. B.7, we get

$$2\epsilon_{\boldsymbol{HL}} - (V_* + 2\epsilon_{\boldsymbol{ML}}) + \Delta PV - T\Delta S^o = \Delta G^o_{unperturbed} - V_{\boldsymbol{M}^*}(\boldsymbol{x}_{unperturbed}) \tag{B.8}$$

Using Morse potential parameters from Section B.1.3, we obtain $V_{\boldsymbol{M}^*}(\boldsymbol{x}_{unperturbed}) = -1259.57$ kJ/mol. To make grafting favorable for a reference site, $\Delta G^o_{unperturbed}$ was set equal to -30 kJ/mol. This yields $2\epsilon_{HL} - (V_* + 2\epsilon_{ML} + \Delta PV - T\Delta S^o) = 1229.56$ kJ/mol. ϵ_{HL}, V_*, ϵ_{ML}, ΔPV, and ΔS^o always occur together in the combination on the LHS of Eq. B.8, therefore they do not need to be determined separately.

B.1.6 Reference free energy barrier and linear free energy relation ($\Delta G^{\ddagger}_{ref}$)

The LFER for an unperturbed site is given by

$$\Delta G^{\ddagger}_{unperturbed}(\boldsymbol{r}) = \Delta G^{\ddagger}_{ref} + \alpha \Delta G^o_{unperturbed}(\boldsymbol{r}). \tag{B.9}$$

$\Delta G^{\ddagger}_{unperturbed}(\boldsymbol{r})$ was set equal to the DFT-computed activation barrier for CrO_2Cl_2 grafting to a vicinal disilanol model site at 1 atm pressure of CrO_2Cl_2 (Fig. B.4).

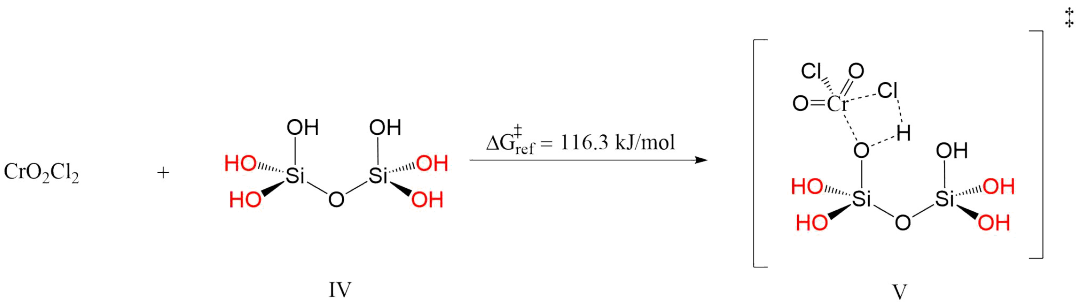

Figure B.4: Calculation of the reference free energy barrier. Free energies of CrO_2Cl_2 in the gas phase with the vicinal silanol site (left) and the transition state for CrO_2Cl_2 grafting to the vicinal silanol site (right). Free energies are at 1 atm CrO_2Cl_2 and 298.15 K. Peripheral atoms (fixed) are red.

Using $\Delta G^{o}_{unperturbed} = -30$ kJ/mol (Section B.1.5) and solving for $\Delta G^{\ddagger}_{ref}$ we get

$$\Delta G^{\ddagger}_{ref} = 131.3 kJ/mol. \tag{B.10}$$

B.2 Effect of training set size on test set error

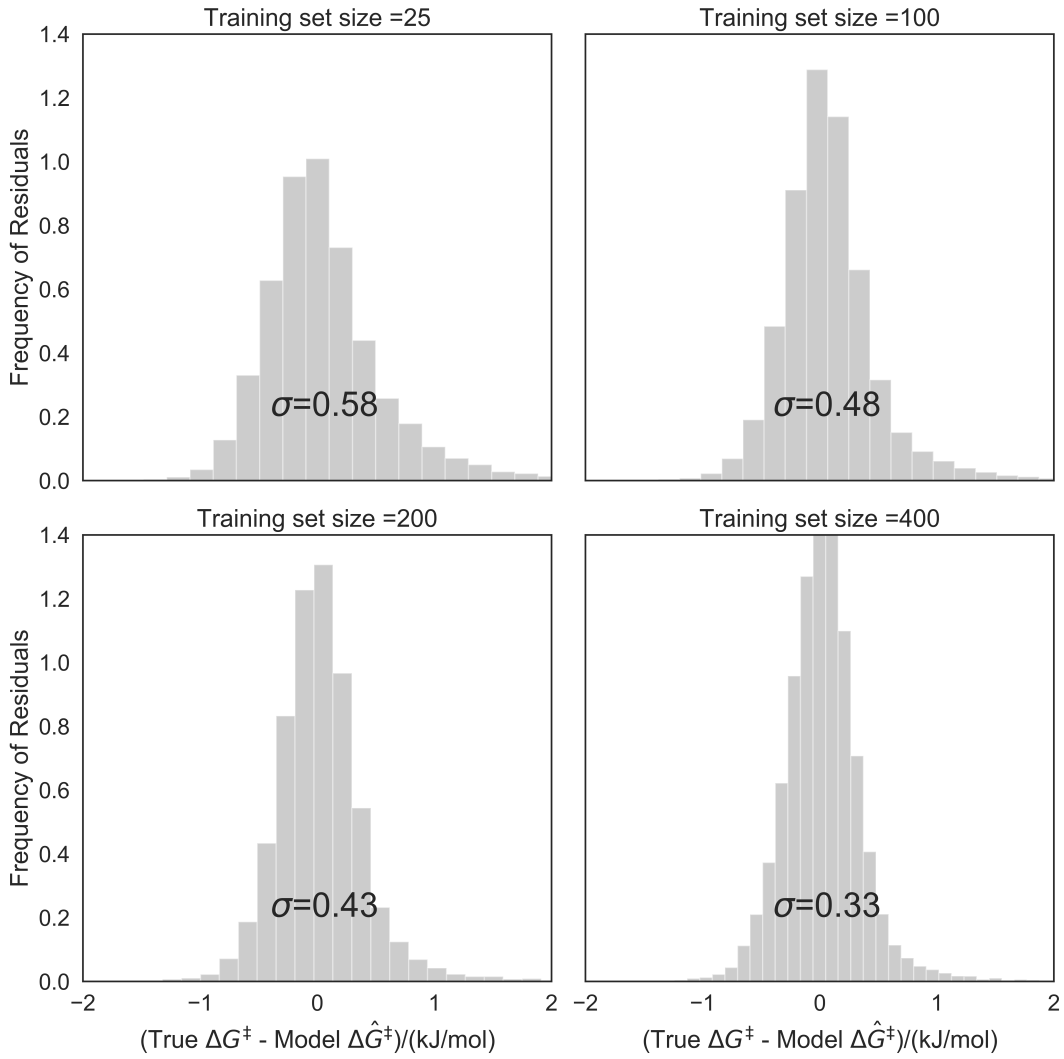

Figure B.5: Residual distributions for predicted grafting barriers as a function of training set size for all $\approx 20,000$ sites. As expected, the width of the residual distribution decreases on increasing the training set size.

Bibliography

1. Chai, J.-D. & Head-Gordon, M. Long-range corrected hybrid density functionals with damped atom-atom dispersion corrections. *Phys. Chem. Chem. Phys.* **10,** 6615–6620. https://www.doi.org/10.1039/B810189B (2008).

2. Feller, D. The role of databases in support of computational chemistry calculations. *J. Comput. Chem.* **17,** 1571–1586. https://www.doi.org/10.1002/(SICI)1096-987X(199610)17:13%3C1571::AID-JCC9%3E3.0.CO;2-P (1996).

3. Schuchardt, K. L. *et al.* Basis Set Exchange: A Community Database for Computational Sciences. *J. Chem. Inf. Model.* **47,** 1045–1052. https://www.doi.org/10.1021/ci600510j (2007).

4. Godbout, N., Salahub, D. R., Andzelm, J. & Wimmer, E. Optimization of Gaussian-type basis sets for local spin density functional calculations. Part I. Boron through neon, optimization technique and validation. *CJC University of Calgary 50th Anniversary Virtual Issue* **01,** 560–571. https://doi.org/10.1139/v92-079 (1992).

5. Frisch, M. J. *et al.* Gaussian16. Gaussian Inc. Wallingford CT 2016.

6. Fong, A., Yuan, Y., Ivry, S. L., Scott, S. L. & Peters, B. Computational Kinetic Discrimination of Ethylene Polymerization Mechanisms for the Phillips (Cr/SiO_2) Catalyst. English. *ACS Catal.* **5,** 3360–3374. https://www.doi.org/10.1021/acscatal.5b00016 (2015).

7. Oliphant, T. E. Guide to NumPy. *CreateSpace Independent Publishing Platform* (2015).

Appendix C

Supporting information for Site-averaged kinetics for catalysts on amorphous supports: An importance learning algorithm

C.1 Strength of M-A bond

The **M-A** bond strength in the quenched-disordered lattice model was chosen to approximately match the Cr-C bond strength for an alkylchromium(III) site on SiO_2. We started from a *bis*(silanolato)chromium(II) cluster model, which has been used in previous studies of Cr/SiO_2 catalysts.[1,2] Labile siloxane coordination was modeled by binding a water molecule. The **M-A** bond strength was calculated according to Scheme S1 and density functional theory calculations, and was computed as $\varepsilon_{\mathbf{M\text{-}A}} = 160$ kJ/mol. We chose a one-electron redox pathway (as opposed to a two-electron redox pathway) to ensure a strong bond energy for the chemisorption step. We stress that the bond strength

was chosen only to ensure a realistic model. The model is not intended make accurate predictions for Cr/SiO_2 olefin polymerization catalysts.

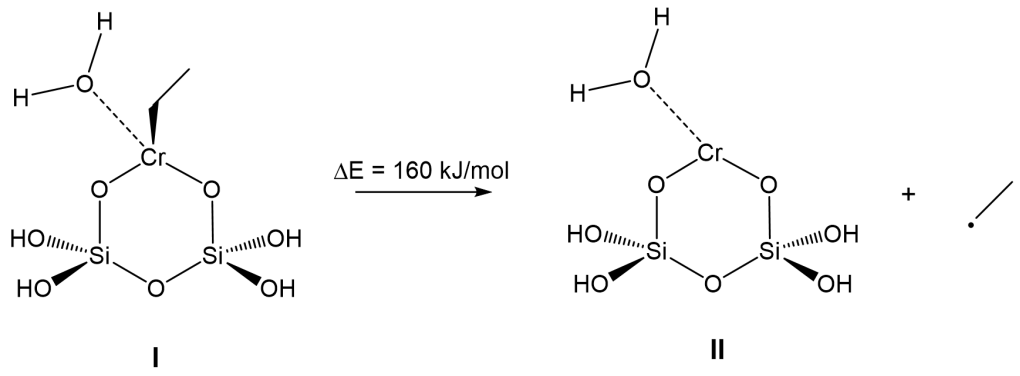

DFT calculations were carried out using Gaussian16.[3] All energies were calculated with the range-separated density functional, ωB97X-D.[4] The def2-TZVP basis set was used for Cr[5] and TZVP was used for C, H, O, and Si atoms.[6] All minima have zero imaginary frequencies. The peripheral OH atoms of the cluster model were also held constrained to model the geometric constraints of an extended silica network. The peripheral atom constraints were found by optimizing the bare Cr(II) cluster. The same peripheral atom constraints were applied to structures **I** and **II**. Cartesian coordinates of the optimized clusters are tabulated below Table SC.1.

Table C.1: Spin contamination before (S2) and after annihilation (S2A) of highest spin contaminant; energies in Hartrees

Species	Energy	S2	S2A
I	-2229.395021	6.0107	6.0000
II	-2308.613831	3.8158	3.7506
C3H7	-157.7869992	0.7544	0.7500

C.2 Derivation of apparent activation energy

In this section, a formula for the apparent activation energy of a site, $E_a(\mathbf{x}_i)$, is derived. The apparent activation energy for site i is given by

$$E_a(\mathbf{x}_i) = -\frac{d \ln \reflectbox{r}_i}{d\beta} \tag{C.1}$$

From eqns. 4.2 - 4.5, the turnover frequency (TOF) of a site, $\reflectbox{r}_i$, can be expressed as

$$\reflectbox{r}_i = k_2 K(\mathbf{x}_i) c_{\mathbf{A}} = \frac{k_B T}{h} \exp\left[-\frac{\Delta H^{\ddagger} - T\Delta S^{\ddagger}}{k_B T}\right] \exp\left[-\frac{\Delta H(\mathbf{x}_i) - T\Delta S}{k_B T}\right] c_{\mathbf{A}} \tag{C.2}$$

Taking the natural logarithm of the eqn. C.2, grouping temperature dependent terms, and simplifying yields

$$\ln \reflectbox{r}_i = \ln c_{\mathbf{A}} - \ln h + \frac{\Delta S + \Delta S^{\ddagger}}{k_B} - \beta \Delta H(\mathbf{x}_i, \beta) - \beta \Delta H^{\ddagger} - \ln \beta \tag{C.3}$$

where $\beta = 1/k_B T$. From eqn. 4.6, $\Delta H(\mathbf{x}_i)$ is temperature dependent through kBT. Taking the derivative of eqn. C.3 gives

$$E_a(\mathbf{x}_i) = \frac{d}{d\beta} \beta \Delta H(\mathbf{x}_i, \beta) + \Delta H^{\ddagger} + k_B T \tag{C.4}$$

Inserting eqn. 4.6 into $\Delta H(\mathbf{x}_i)$ to evaluate the derivative gives

$$\begin{aligned} \frac{d}{d\beta} \beta \Delta H(\mathbf{x}_i, \beta) &= \frac{d}{d\beta} [\beta V_{\mathbf{AM}*}(\mathbf{x}_i) - \beta V_{\mathbf{M}*}(\mathbf{x}_i) + 1] \\ &= V_{\mathbf{AM}*}(\mathbf{x}_i) - V_{\mathbf{M}*}(\mathbf{x}_i) \\ &= \Delta H(\mathbf{x}_i) + k_B T \end{aligned} \tag{C.5}$$

Thus, $E_a(\mathbf{x}_i)$ can be written as

$$E_a(\mathbf{x}_i) = \Delta H(\mathbf{x}_\mathrm{i}) + \Delta H^{\ddagger} + 2k_B T \tag{C.6}$$

C.3 Propagation of kernel regression model uncertainty in estimating $\langle E_a \rangle_k$

Site-averaged kinetics are estimated by importance sampling the activation energy distribution with E_a values obtained from the trained kernel regression model. Since errors in the kernel regression model propagate through the $\langle E_a \rangle_k$ calculation (beyond sampling error and error from ab initio calculations), the kernel regression model contributes additional errors. Here, we show that the regression errors, even when unbiased, will systematically bias the $\langle E_a \rangle_k$ estimate toward lower activation energy. We also show how this bias can be quantified and corrected to obtain $\langle E_a \rangle_k$ estimates with only sampling and ab initio calculation errors. Let the distribution of kernel regression activation energies be $\hat{\rho}(\hat{E}_a)$. rhoEaHat can be related to the E_a distribution, $\rho(E_a)$, by

$$\tilde{\rho}(\hat{E}_a) = \int dE_a \tilde{\rho}(E_a) P(\hat{E}_a | E_a) \tag{C.7}$$

Here, $P(\hat{E}_a|E_a)$ is the distribution of the model-predicted activation barriers around the true activation barriers, and the integral is over the all possible E_a values. The site averaged activation energy from $\hat{\rho}(\hat{E}_a)$ is

$$\langle \hat{E}_a \rangle_k = \frac{\int d\hat{E}_a \hat{E}_a e^{-\beta \hat{E}_a} \tilde{\rho}(\hat{E}_a)}{\int d\hat{E}_a e^{-\beta \hat{E}_a} \tilde{\rho}(\hat{E}_a)} \tag{C.8}$$

where $\beta = 1/k_B T$, and T is the operating temperature of the catalyst. Combining eqns C.7 and C.8 yields

$$\langle \hat{E}_a \rangle_k = \frac{\int \int d\hat{E}_a dE_a \hat{E}_a e^{-\beta \hat{E}_a} P(\hat{E}_a | E_a)}{\int \int d\hat{E}_a dE_a e^{-\beta \hat{E}_a} P(\hat{E}_a | E_a)} \tag{C.9}$$

Assuming $\hat{\rho}(\hat{E}_a)$ is normally distributed around $\rho(E_a)$ with a standard deviation of σ_g gives:

$$\tilde{\rho}(\hat{E}_a) = \int_{-\infty}^{+\infty} dE_a \tilde{\rho}(E_a) \frac{1}{\sqrt{2\pi}\sigma_g} \exp \frac{\left(\hat{E}_a - E_a\right)^2}{2\sigma_g^2}. \tag{C.10}$$

Combining eqns C.7 and C.10 and simplifying yields:

$$\langle \hat{E}_a \rangle_k = \frac{\int dE_a \tilde{\rho}(E_a) \int_{-\infty}^{+\infty} d\hat{E}_a \hat{E}_a \exp\left[\frac{\left(\hat{E}_a - E_a\right)^2}{2\sigma_g^2} - \beta \hat{E}_a\right]}{\int dE_a \tilde{\rho}(E_a) \int_{-\infty}^{+\infty} d\hat{E}_a \exp\left[\frac{\left(\hat{E}_a - E_a\right)^2}{2\sigma_g^2} - \beta \hat{E}_a\right]}. \tag{C.11}$$

The two integrals in eqn. C.11 have closed-form solutions:

$$\int_{-\infty}^{+\infty} d\hat{E}_a \hat{E}_a \exp\left[\frac{\left(\hat{E}_a - E_a\right)^2}{2\sigma_g^2} - \beta \hat{E}_a\right] = \sqrt{2\pi}\sigma_g (E_a - \beta {\sigma_g}^2) \exp\left[\frac{\beta^2 {\sigma_g}^2}{2} - \beta E_a\right] \tag{C.12}$$

and

$$\int_{-\infty}^{+\infty} d\hat{E}_a \exp\left[\frac{\left(\hat{E}_a - E_a\right)^2}{2\sigma_g^2} - \beta \hat{E}_a\right] = \sqrt{2\pi}\sigma_g \exp\left[\frac{\beta^2 {\sigma_g}^2}{2} - \beta E_a\right] \tag{C.13}$$

Introducing eqns. C.12 and C.13 into eqn. C.11 and simplifying gives

$$\langle \hat{E}_a \rangle_k = \frac{\int dE_a \tilde{\rho}(E_a)(E_a - \beta {\sigma_g}^2) e^{-\beta E_a}}{\int dE_a \tilde{\rho}(E_a) e^{-\beta E_a}} \tag{C.14}$$

From eqn. C.8, it can be seen that

$$\left\langle \hat{E}_a \right\rangle_k = \langle E_a \rangle_k - \beta {\sigma_g}^2 \tag{C.15}$$

Kernel regression errors (σ_g) can be used to estimate the error in the kernel regression model predicted k-weighted activation barrier ($\langle E_a \rangle_k$) using eqn. C.15. We can estimate typical size of kernel regression errors using the training set error.

C.4 Test set and training set statistics

The set of randomly sampled sites used to train the kernel regression model should sufficiently sample the main support of $\rho(E_a)$ to properly normalize $\hat{\rho}(\hat{E}_a)$ for predicting kinetic properties. Once the main support of $\rho(E_a)$ is sufficiently sampled, additional sites do not improve the normalization of $\hat{\rho}(\hat{E}_a)$ and require additional, costly structure optimizations. Figure C.1 shows the leave-one-out parity plot of the kernel regression plot trained on 25, 50, 75, and 100 randomly sampled sites.

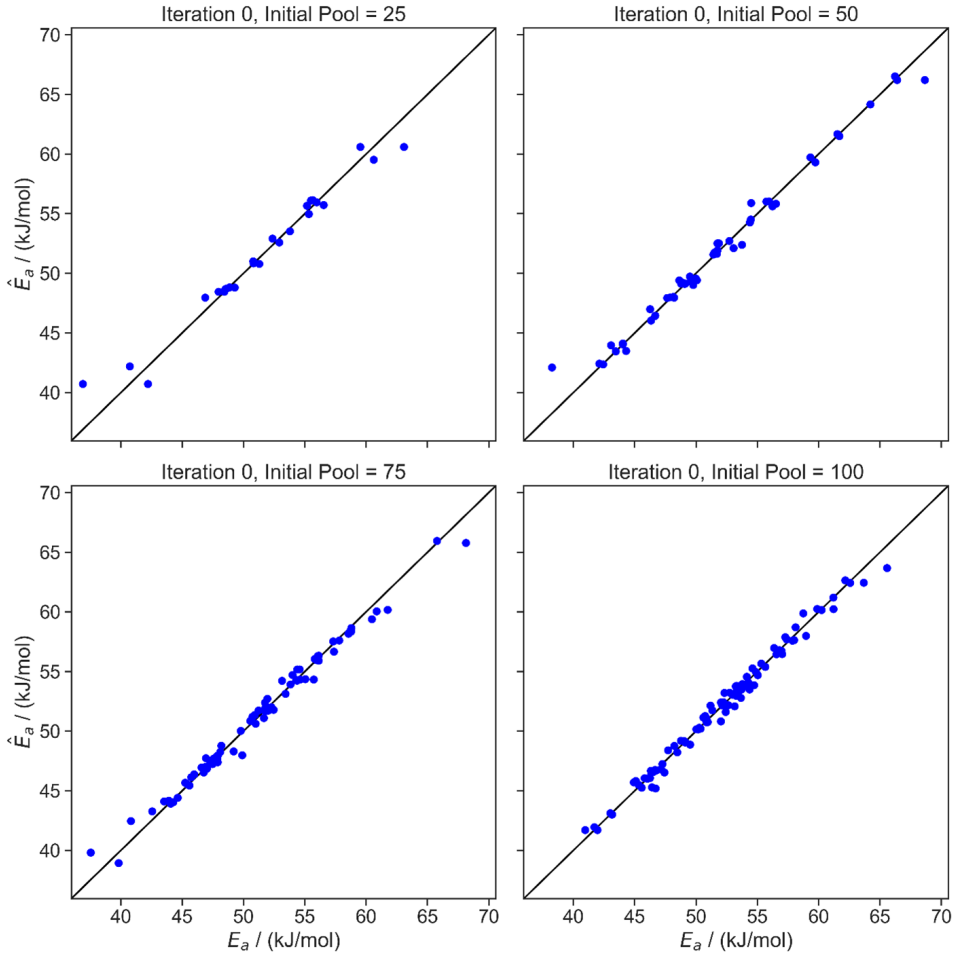

Figure C.1: Parity plot of kernel regression model trained on different initial pool sizes. An initial pool of 50 randomly selected sites samples the main support of $\rho(E_a)$.

Errors in the kernel regression model should be smaller than the width of $\rho(E_a)$ to accurately importance sample $\hat{\rho}(\hat{E}_a)$. Therefore, the initial pool should contain a set of sites with diverse local environments and activation energies to effectively train the kernel regression model. Residual distributions of all ca. 20,000 sites are shown for the kernel regression model trained on 25, 50, 75, and 100 randomly sampled sites in Figure C.2.

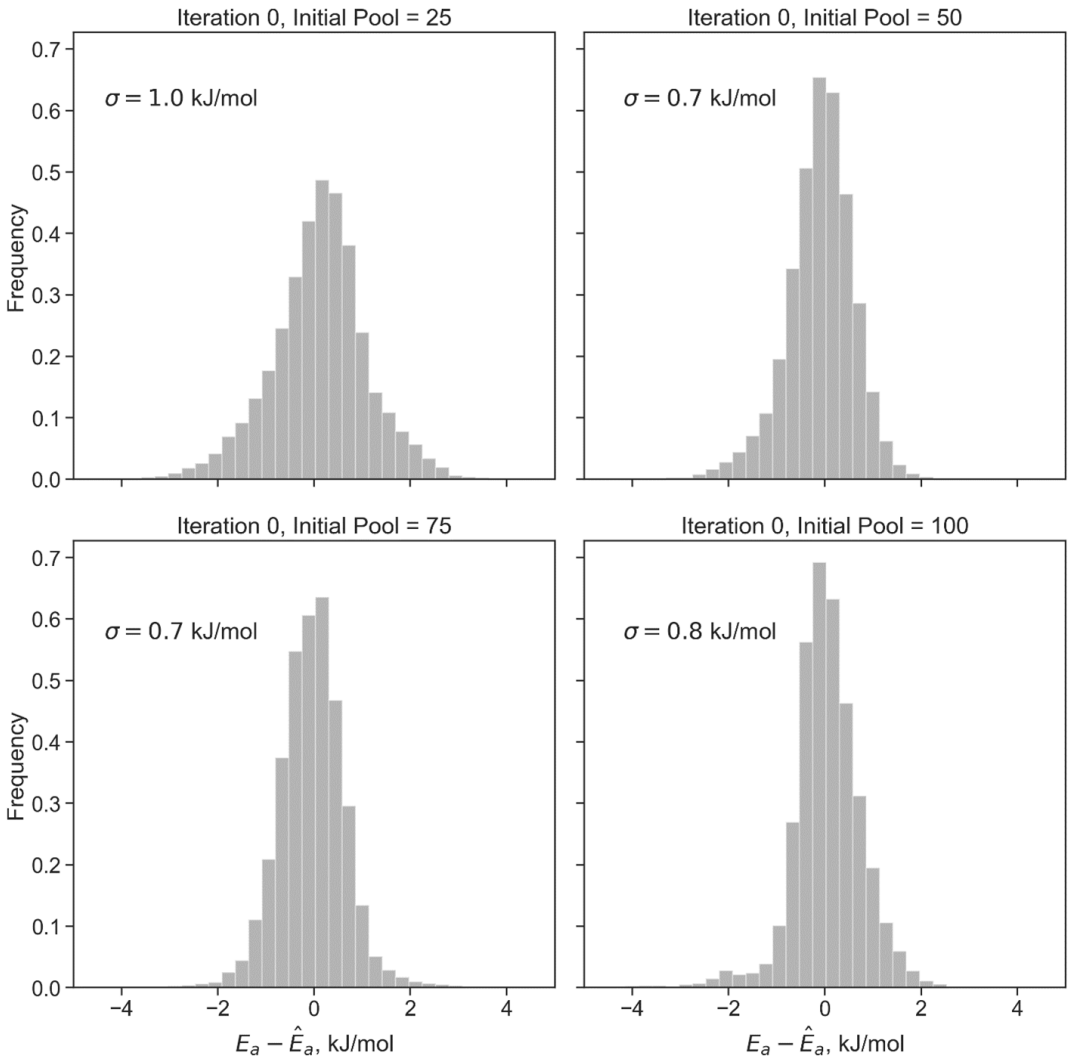

Figure C.2: Kernel regression model residual distribution for all ca. 20,000 sites with different initial pool sizes. For all initial pool sizes, the standard error is within 1.0 kJ/mol which is ca. 40 times smaller than the range of $\hat{\rho}(\hat{E}_a)$. The standard error does not decrease for initial pool sizes greater than 50.

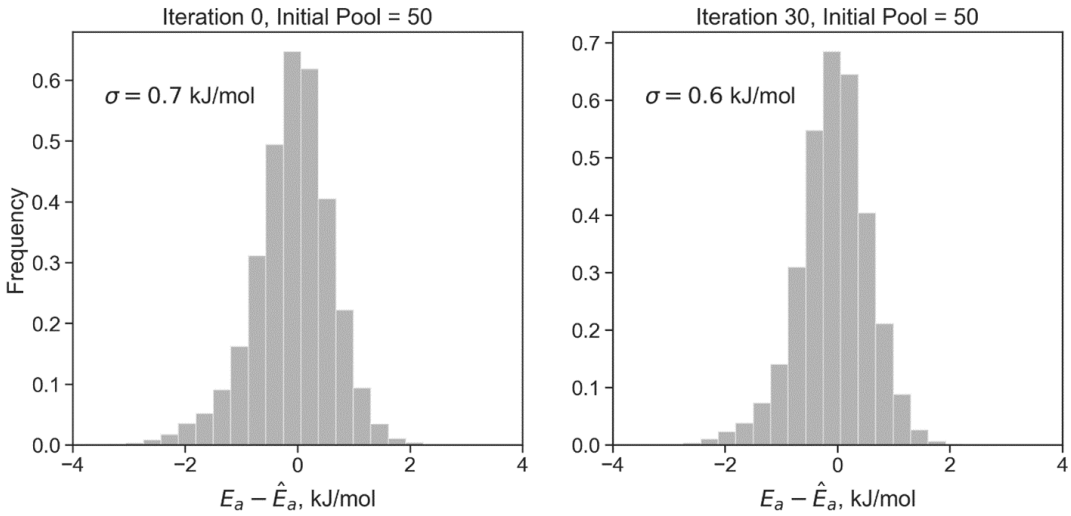

Figure C.3: Distribution of residuals for iterations 0 (left) and 30 (right) of the importance learning algorithm.

C.5 Number of samples required to estimate $\tilde{E}_a$ with the same precision $\overline{E}_a$

The $\overline{E}_a$ estimator from the importance learning algorithm (eqn. 4.15) quickly converges to the correct site averaged activation energy because sites are sampled with weights $\rho(\mathbf{x})\exp[-\beta E_a(\mathbf{x})]$. Alternatively, the $\tilde{E}_a$ estimator randomly samples sites with weights $\rho(\mathbf{x})$ and computes a ratio of exponential averages (eqn. 4.14). The reweighted estimator will require many more samples to converge to a precise estimate. In this section, the relative variance for the $\tilde{E}_a$ estimator is derived and the number of samples required to estimate $\tilde{E}_a$ with the same level of confidence as $\overline{E}_a$ is computed.

From eqn. 4.14, $\tilde{E}_a$ is computed by

$$\begin{aligned}\tilde{E}_a &= \sum_{i=1}^{n} k(\mathbf{x}_i)E_a(\mathbf{x}_i) \Big/ \sum_i k(\mathbf{x}_i) \\ &= \frac{\widetilde{kE}_a}{\tilde{k}}\end{aligned} \tag{C.16}$$

Both $\widetilde{kE}_a$ and $\tilde{k}$ are random variables for a given sample size, so their ratio is also a random variable. Assuming $\tilde{k}$ and $\widetilde{kE}_a$ are independent and uncorrelated, the sample variance of $\tilde{E}_a$ can be approximated by:

$$\sigma^2_{\tilde{E}_a} \approx \left(\frac{\partial \tilde{E}_a}{\partial \widetilde{kE}_a}\right)^2 \sigma^2_{\widetilde{kE}_a} + \left(\frac{\partial \tilde{E}_a}{\partial \tilde{k}}\right)^2 \sigma^2_{\tilde{k}} \tag{C.17}$$

Evaluating the derivatives and dividing by $\tilde{E}_a$ yields the relative sample variance

$$\frac{\sigma^2_{\tilde{E}_a}}{\tilde{E}_a^2} = \frac{\sigma^2_{\widetilde{kE}_a}}{\left(\widetilde{kE}_a\right)^2} + \frac{\sigma^2_{\tilde{k}}}{\tilde{k}^2} \tag{C.18}$$

The relative sample variance can be related to the relative variance by the central limit theorem:[7]

$$\frac{\sigma^2_{\widetilde{kE}_a}}{\left(\widetilde{kE}_a\right)^2} + \frac{\sigma^2_{\tilde{k}}}{\tilde{k}^2} = \frac{1}{N}\left[\frac{\sigma^2_{kE_a}}{\langle kE_a\rangle^2} + \frac{\sigma^2_k}{\langle k\rangle^2}\right]_{\rho(\mathbf{x})} \equiv \left.\frac{\sigma^2_{\langle E_a\rangle_k}}{\langle E_a\rangle_k^{\,2}}\right|_{\rho(\mathbf{x})} \tag{C.19}$$

where N is the number of samples. The right most equality with subscript $\rho(\mathbf{x})$ indicates that C.19 estimates the relative variance in the E_a estimate as computed with a sample from $\rho(\mathbf{x})$. The number of random samples required to match the uncertainty of the $\overline{E}_a$ estimator from the importance learning algorithm is found by equating the relative uncertainties of the two estimators:

$$\left.\frac{\sigma^2_{\langle E_a\rangle_k}}{\langle E_a\rangle_k^{\,2}}\right|_{k(\mathbf{x})\rho(\mathbf{x})} = \left.\frac{\sigma^2_{\langle E_a\rangle_k}}{\langle E_a\rangle_k^{\,2}}\right|_{\rho(\mathbf{x})} \tag{C.20}$$

Inserting eqn. C.19 in the right hand side of C.20 and solving for N yields

$$N = \left[\frac{\sigma^2_{\langle E_a\rangle_k}}{\langle E_a\rangle_k^{\,2}}\right]^{-1}_{k(\mathbf{x})\rho(\mathbf{x})} \left[\frac{\sigma^2_{kE_a}}{\langle kE_a\rangle^2} + \frac{\sigma^2_k}{\langle k\rangle^2}\right]_{\rho(\mathbf{x})} \tag{C.21}$$

The relative uncertainty in the $\overline{E}_a$ estimator is (0.75 kJ/mol) / (40.5 kJ/mol) = 1.85 %.

Since $\rho(E_a)$ can be precisely calculated for our simple model, $\sigma^2_{kE_a}/\langle kE_a\rangle^2$ and $\sigma^2_k/\langle k\rangle^2$ can be computed exactly. Evaluating eqn. C.21 gives

$$N = (0.0185)^{-2} \times (28.1 + 41.2) \approx 200,000 \tag{C.22}$$

Therefore, the reweighting estimator $\tilde{E}_a$ requires about 200,000 sites for the same level of confidence that the importance learning estimator $\overline{E}_a$ achieved with less than 100 sites.

Bibliography

1. Fong, A., Yuan, Y., Ivry, S. L., Scott, S. L. & Peters, B. Computational Kinetic Discrimination of Ethylene Polymerization Mechanisms for the Phillips (Cr/SiO_2) Catalyst. English. *ACS Catal.* **5,** 3360–3374. https://www.doi.org/10.1021/acscatal.5b00016 (2015).

2. Fong, A., Vandervelden, C., Scott, S. L. & Peters, B. Computational Support for Phillips Catalyst Initiation via Cr-C Bond Homolysis in a Chromacyclopentane Site. *ACS Catal.* **8,** 1728–1733. https://doi.org/10.1021/acscatal.7b03724 (2018).

3. Frisch, M. J. *et al.* Gaussian16. Gaussian Inc. Wallingford CT 2016.

4. Chai, J.-D. & Head-Gordon, M. Long-range corrected hybrid density functionals with damped atom-atom dispersion corrections. *Phys. Chem. Chem. Phys.* **10,** 6615–6620. https://www.doi.org/10.1039/B810189B (2008).

5. Weigend, F. & Ahlrichs, R. Balanced Basis Sets of Split Valence, Triple Zeta Valence and Quadruple Zeta Valence Quality for H to Rn: Design and Assessment of Accuracy. *Phys. Chem. Chem. Phys.* **7,** 3297–3305. https://www.doi.org/10.1039/b508541a (2005).

6. Schäfer, A., Horn, H. & Ahlrichs, R. Fully optimized contracted Gaussian basis sets for atoms Li to Kr. *J. Chem. Phys.* **97,** 2571–2577. https://www.doi.org/10.1063/1.463096 (1992).

7. Logan, J. D. *Applied mathematics* 3rd. **14204421,** 529. https://www.wiley.com/en-us/Applied%20Mathematics,%204th%20Edition-p-9781118475805 (Wiley-Interscience, Hoboken, N.J., 2006).

Appendix D

Supporting Information for: Importance learning estimator for the site-averaged turnover frequency of a disordered solid catalyst

D.1 Propagation of kernel regression model uncertainty in computing $\langle \exp[-\beta \hat{E}_a] \rangle$

The site-averaged TOF is estimated from activation energies predicted by the trained ML model. Importance sampling selectively adds low E_a sites to the training set, improving model accuracy in this region. However, errors in the ML model will propagate through the average, biasing the estimate. Here, we show how to quantify this bias and correct $\langle \exp[-\beta \hat{E}_a] \rangle$ estimates with only sampling and *ab initio* calculation errors. Let the distribution of ML-predicted activation energies be $\hat{\rho}(\hat{E}_a)$. We can relate $\hat{\rho}(\hat{E}_a)$ to

the E_a distribution, $\rho(E_a)$, by

$$\hat{\rho}(\hat{E}_a) = \int dE_a \rho(E_a) P(\hat{E}_a|E_a) \tag{D.1}$$

Here, $P(\hat{E}_a|E_a)$ is the distribution of the model-predicted activation barriers around the true activation barriers, and the integral is over all possible E_a values. The exponential average from $\hat{\rho}(\hat{E}_a)$ is

$$\langle \exp[-\beta \hat{E}_a] \rangle_{\hat{\rho}(\hat{E}_a)} = \int d\hat{E}_a \hat{\rho}(\hat{E}_a) \exp[-\beta \hat{E}_a] \tag{D.2}$$

where $\beta = 1/k_B T$, and T is the operating temperature of the catalyst. Combining eqns. D.1 and D.2 yields

$$\langle \exp[-\beta \hat{E}_a] \rangle_{\hat{\rho}(\hat{E}_a)} = \int \int dE_a d\hat{E}_a \rho(E_a) P(\hat{E}_a|E_a) \exp[-\beta \hat{E}_a] \tag{D.3}$$

Assuming $\exp[-\beta \hat{E}_a]$ is normally distributed around $\rho(E_a)$ with a standard deviation of σ_r gives

$$\hat{\rho}(\hat{E}_a) = \int_{-\infty}^{+\infty} dE_a \rho(E_a) \frac{1}{\sqrt{2\pi}\sigma_r} \exp \frac{\left(\hat{E}_a - E_a\right)^2}{2\sigma_r^2}. \tag{D.4}$$

Combining and rearranging eqn. D.3 and eqn. D.4 yields:

$$\langle \exp[-\beta \hat{E}_a] \rangle_{\hat{\rho}(\hat{E}_a)} = \int dE_a \rho(E_a) \int_{-\infty}^{+\infty} d\hat{E}_a \frac{1}{\sqrt{2\pi}\sigma_r} \exp[-\beta \hat{E}_a] \exp \frac{\left(\hat{E}_a - E_a\right)^2}{2\sigma_r^2} \tag{D.5}$$

The definite integral in eqn. D.5 has a closed-form solution:

$$\begin{aligned} \langle \exp[-\beta \hat{E}_a] \rangle_{\hat{\rho}(\hat{E}_a)} &= \exp\left[\frac{1}{2}(\beta\sigma_r)^2\right] \int dE_a \rho(E_a) \exp[-\beta E_a] \\ &= \exp\left[\frac{1}{2}(\beta\sigma_r)^2\right] \langle \exp[-\beta E_a] \rangle_{\rho(E_a)} \end{aligned} \tag{D.6}$$

Because the ML model is a weighted average of the training set, the ML model cannot make estimates outside the range of activation energies in the training set. As a result, low E_a sites which are below the range of the training set are almost always over-predicted, and $\langle \exp[-\beta \hat{E}_a] \rangle$ is underpredicted. The biased corrected estimator, $\langle \exp[-\beta \hat{E}_a] \rangle_{B.C.}$, is then

$$\langle \exp[-\beta \hat{E}_a] \rangle_{B.C.} = \exp[\frac{1}{2}(\beta\sigma_r)^2] \langle \exp[-\beta \hat{E}_a] \rangle \tag{D.7}$$

Kernel regression errors, σ_r, can be estimated from residuals of the test set, Figure D.1.

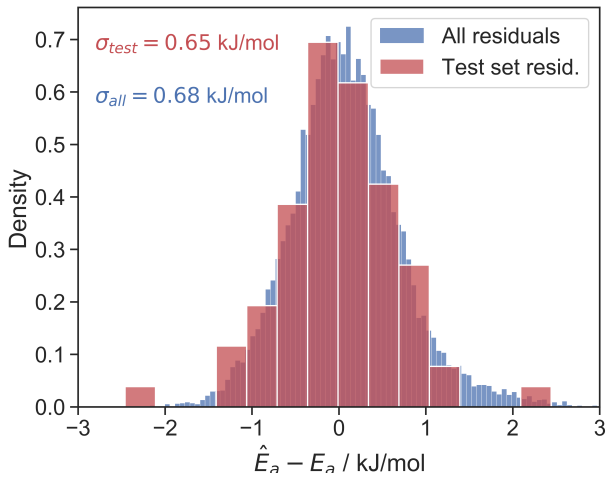

Figure D.1: Histograms of the residual $(\hat{E}_a - E_a)$ distribution of the test set (*i.e.* the leave-one-out predictions of the training set, red) and residual distribution for all ca. 20,000 sites (blue) at iteration 25 of importance learning. The standard deviations of the two histograms are also shown.

D.2 Convergence properties of $\langle \exp[-\beta \hat{E}_a] \rangle$

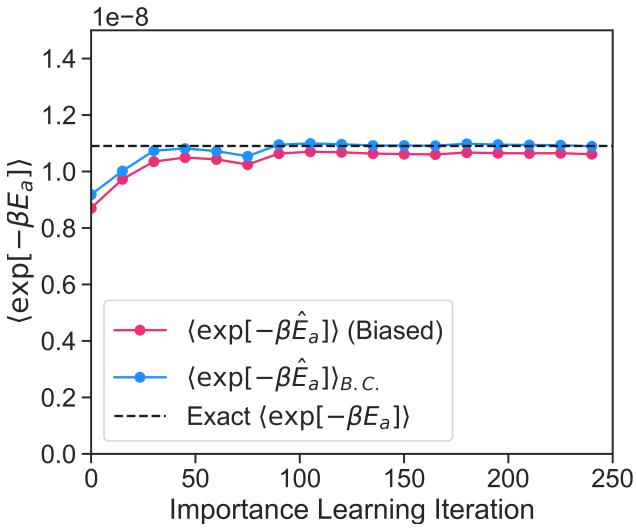

Figure D.2: Convergence of $\langle \hat{\boldsymbol{z}} \rangle / k_0 = \langle \exp[-\beta \hat{E}_a] \rangle$, for 374 importance learning iterations. Estimates are plotted every 11 iterations. The red curve shows the biased $\langle \hat{\boldsymbol{z}} \rangle / k_0$, computed according to eqn. 5.7, and is slightly biased due to errors in the ML model. The blue curve computes $\langle \hat{\boldsymbol{z}}_{B.C.} \rangle / k_0$ using $\hat{E}_a$ and also corrects for the bias, eqn. 5.8.

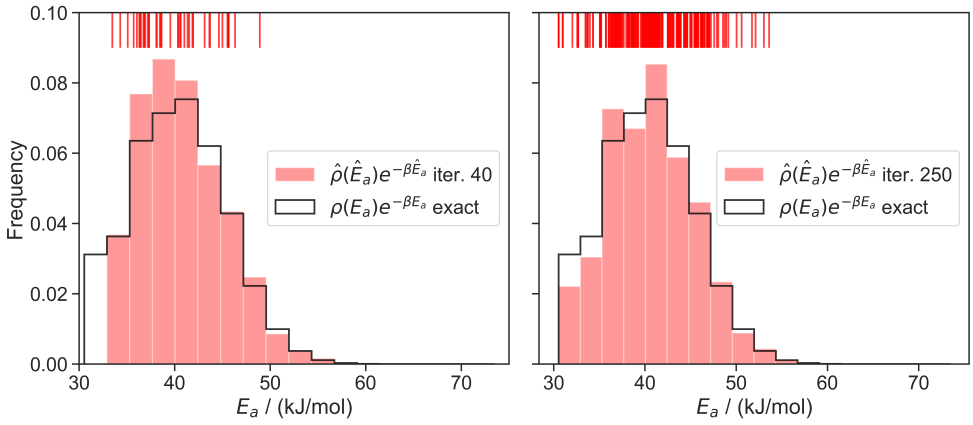

Figure D.3: Exact (grey outline) and model-predicted (red) exponentially weighted E_a distributes after 40 (left) and 374 (right) importance learning iterations. Note that no sites in the lowest E_a bin have been importance sampled at iteration 40, so the ML model is unable to make accurate predictions in that E_a interval.

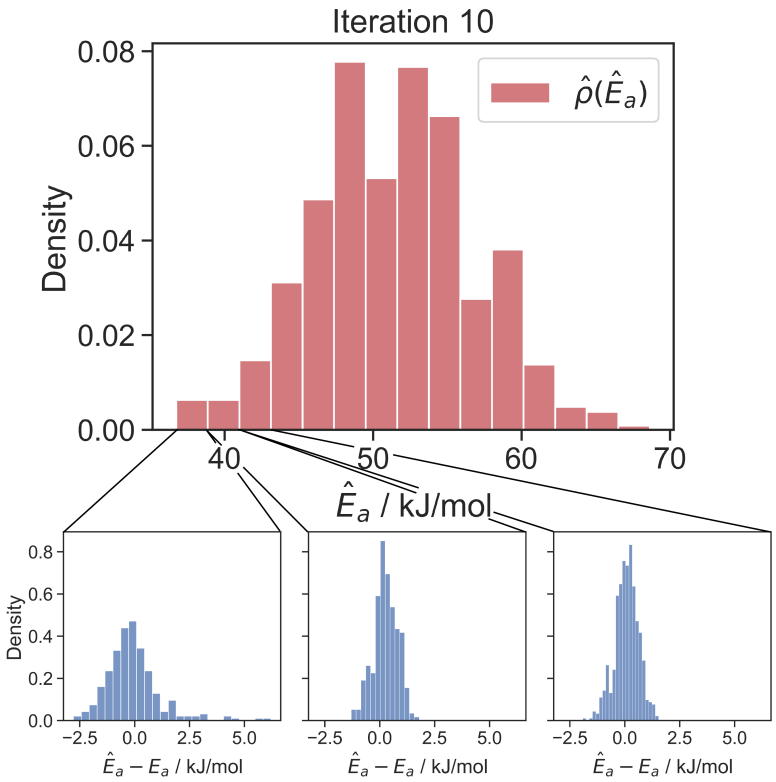

Figure D.4: Histogram of $\hat{E}_a$ for all sites after 10 importance learning iterations (red, top). The blue histograms below are residuals for all sites in the selected bin. Note the residual distributions are non-uniform across bins.

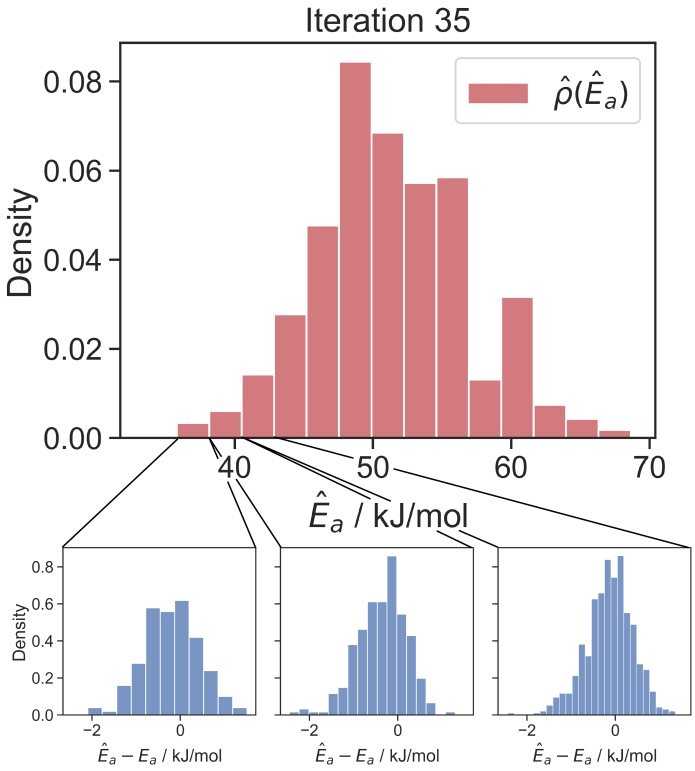

Figure D.5: Histogram of $\hat{E}_a$ for all sites after 35 importance learning iterations (red, top). The blue histograms below are residuals for all sites in the selected bin. Note the residual distributions are non-uniform across bins.

Appendix E

Supporting Information for: Predicted Properties of Active Catalyst Sites on Amorphous Silica: Impact of Silica Pre-Optimization Protocol

This supporting information contains the details for the parameterization of the DLM (section E.1), plots for the change in ΔE_G with the cluster size (section E.2), and plots of ΔE_G relaxed scans as a function of the dihedral angles θ and ϕ as defined in the main text (section E.3).

E.1 Force constant parameterization

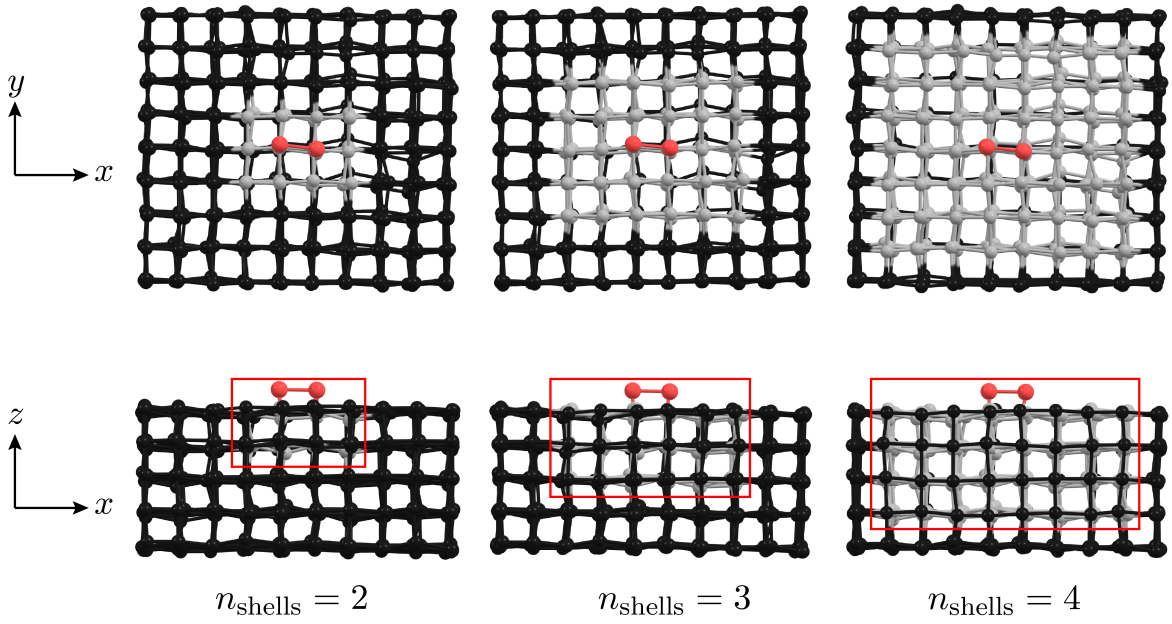

Figure E.1: Different sized cluster models carved from the DLM. A red box is drawn around around the grey beads in the $x - z$ plane for clarity.

The force constants used for the DLM potential were parameterized from relaxed scan DFT calculations of simple cluster models, Figure E.2. The coordinates scanned are shown with arrows.

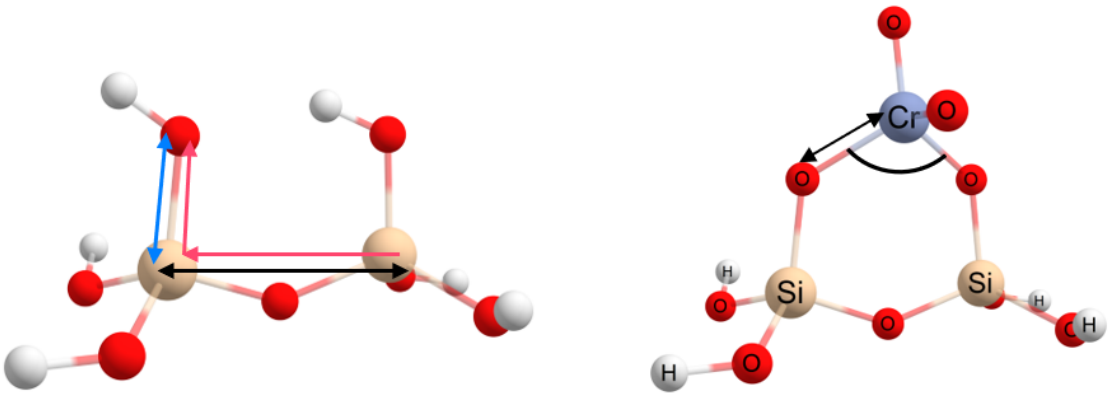

Figure E.2: Cluster models of SiO_2 and grafted dioxoCr(VI)/SiO_2. LeftA7: Si-OH coordinate scanned (blue arrow), Si-Si-OH coordinate scanned (red arrows), Si-Si coordinate scanned (black arrow). RightA7: The **M**-O bond is modeled as the Cr-O bond and the O-**M**-O angle is modeled by the O-Cr-O angle.

The configuration of peripheral capping OH groups was obtained by performing an unconstrained optimization of the dioxoCr(VI) species. The peripheral OH configuration was applied to the SiO_2 model. For all subsequent DFT calculations, the peripheral OH atom configuration was held fixed to mimic the rigidity of bulk SiO_2. The harmonic potentials were fit to the electronic energy of the relaxed scan calculations. The following harmonic potential was fit using the Levenberg-Marquardt algorithm in Python with the Scipy package,

$$V_i(x) = k_i(x_i - x_i^{eq})^2 \tag{E.1}$$

Where k is the force constant that is fitted, x is the value of coordinate i (*i.e.*, a distance or angle), and x_i^{eq} is the equilibrium value of the coordinate i. Only the value of k_i was fit to the scan data. The value of x_i^{eq} was set to the DFT energy-minimized value. Results for $k_{\Sigma\text{-OH}}$, $k_{\Sigma\text{-}\Sigma}$, $k_{\Sigma\text{-}\Sigma\text{-OH}}$, and $k_{\text{O-M-O}}$ are shown in Figure E.3.

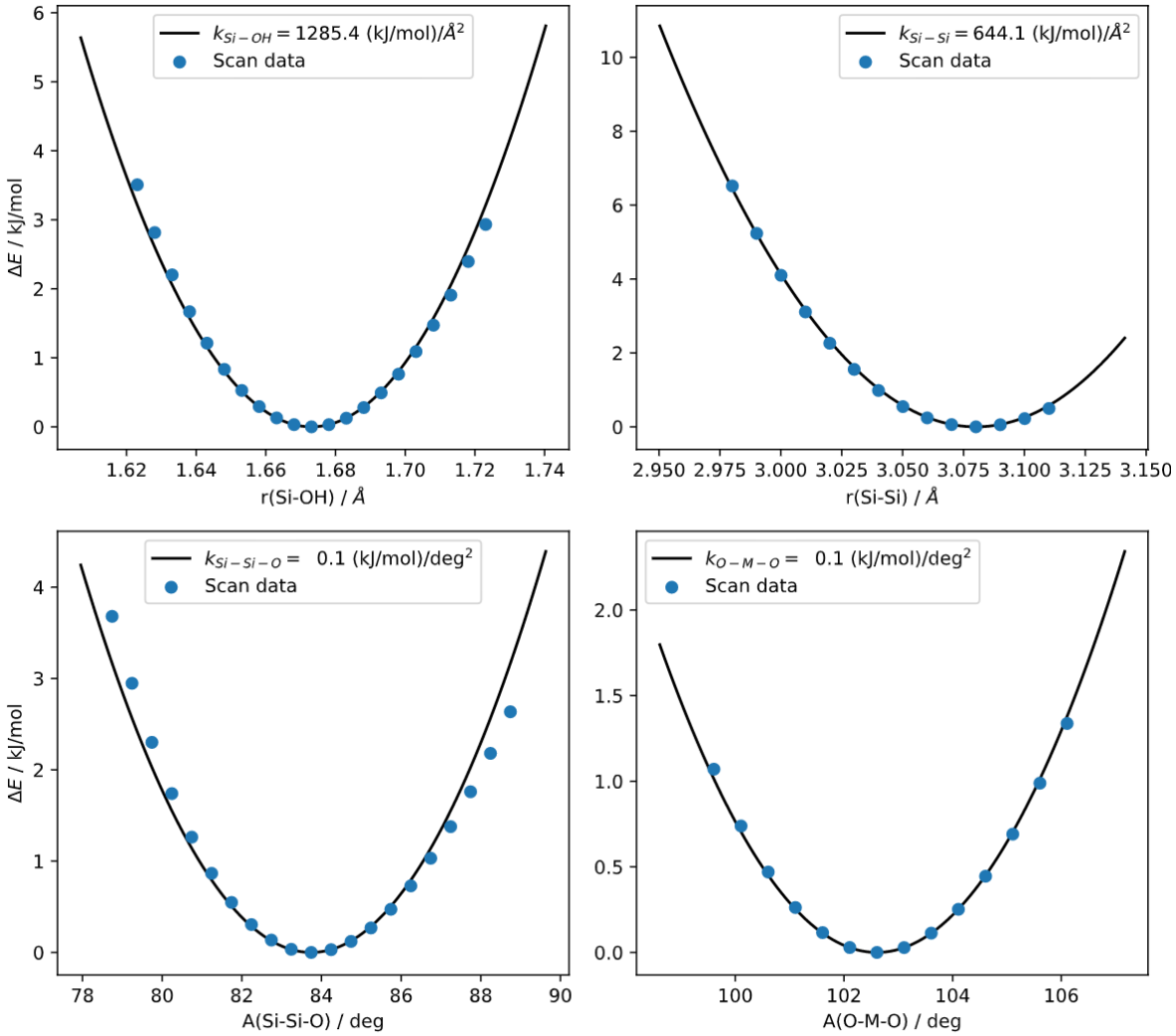

Figure E.3: Fit results of harmonic potentials to relaxed DFT scans of various coordinates.

The **M**-O bond energy was fit to a Morse potential,

$$V_i(r) = D_i(1 - \exp[a_i(r_i - r_i^{eq})])^2 - D_i. \tag{E.2}$$

Here D_i is the dissociation energy and a_i is a force constant-like value for coordinate i. In addition to scanning the **M**-O bond length, the dissociation energy was computed according to Scheme S1. We get $D_{\text{M-O}} = 325$ kJ/mol.

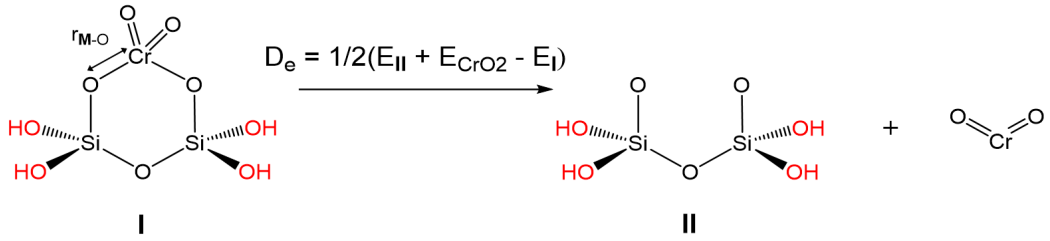

Figure E.4: Scheme to calculate **M**-O dissociation energy. Note the dissociation energy is divided by two because two **M**-O bonds are broken. Peripheral atoms (fixed) are red. $r_{\mathbf{M}-O}$ is used as the displacement variable in the Morse potential model.

We get $a_{\mathbf{M}-O} = 1.92$ Å^{-1}. The fit to the scan data is shown in Figure E.5.

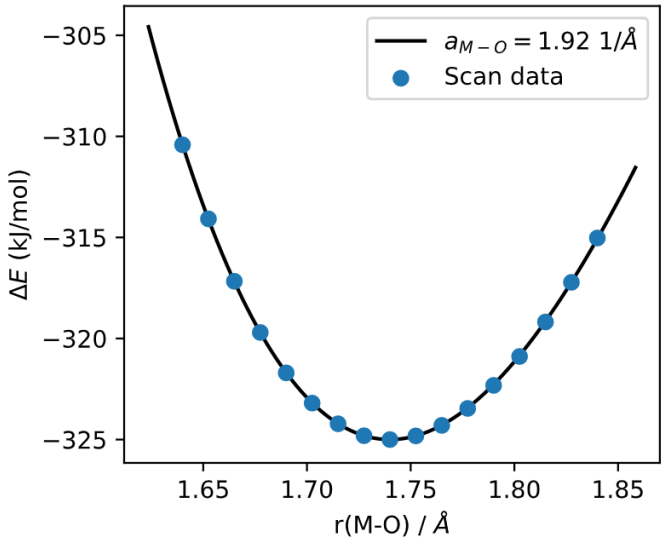

Figure E.5: Fit of the $a_{\mathbf{M}\text{-}\mathrm{O}}$ parameter to the relaxed DFT scan.

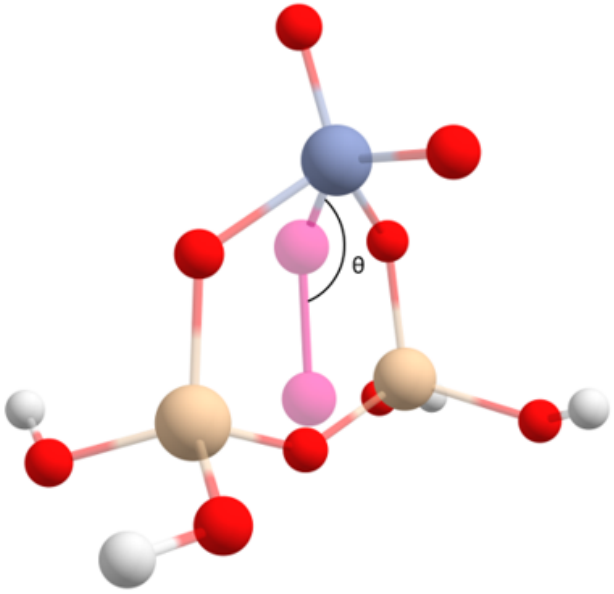

Figure E.6: Angle between the midpoint of the two Si atoms, two silanolate O atoms, and Cr.

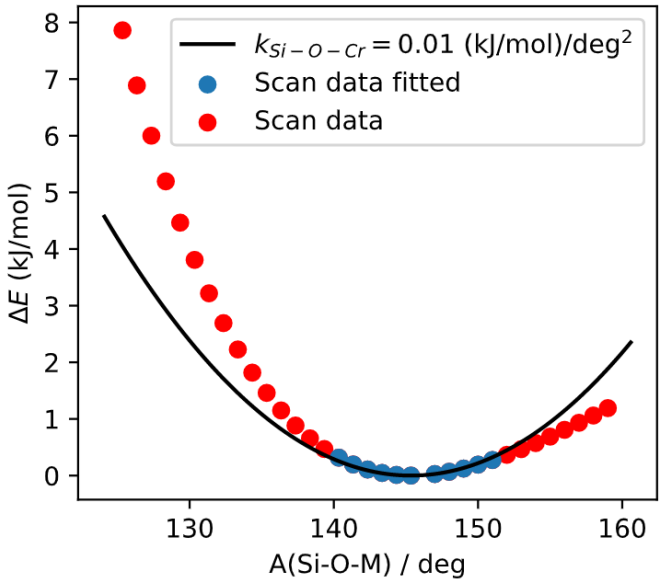

Figure E.7: Fit of the relaxed scan. Because the DFT-computed scan is anharmonic, only the angles near the equilibrium angle were fit. Capturing the complex, anharmonic nature of this potential is unimportant because this coordinate is orthogonal to all other coordinates. Thus, this coordinate will always relax to the equilibrium value during structure optimizations. A potential for this coordinate is included because it is otherwise a free mode, which corresponds to a near-zero eigenvalue of the Hessian of V_G (equation 6.8). The near-zero eigenvalue was sometimes negative, which made it difficult to confirm if the Hessian of an optimized cluster model was positive-definite (*i.e.*, the structure was successfully minimized).

Table E.1: Parameters used in DLM model

Parameter	Value	Unit
N	18	-
$\hat{r}$	3.02	Å
σ_{disp}	0.07	$\hat{r}$
$k_{\Sigma\text{-}\Sigma}$	6111	kJ mol^{-1} $\hat{r}^{-2}$
$k_{\Sigma\text{-OH}}$	12195	kJ mol^{-1} $\hat{r}^{-2}$
$r^{eq}_{\Sigma\text{-OH}}$	0.63	$\hat{r}$
$k_{\Sigma\text{-}\Sigma\text{-OH}}$	0.127	kJ mol^{-1} deg^{-2}
$\theta^{eq}_{\Sigma\text{-}\Sigma\text{-OH}}$	90	deg
$k_{\text{O-}\mathbf{M}\text{-O}}$	0.113	kJ mol^{-1} deg^{-2}
$\theta^{eq}_{\text{O-}\mathbf{M}\text{-O}}$	120	deg
$D_{\mathbf{M}\text{-O}}$	325	kJ mol^{-1}
$r^{eq}_{\mathbf{M}\text{-O}}$	0.627	$\hat{r}$
$a_{\mathbf{M}\text{-O}}$	5.92	$\hat{r}^{-1}$
$k_{\Sigma\text{-O-}\mathbf{M}}$	0.01	kJ mol^{-1} deg^{-2}
$\theta^{eq}_{\Sigma\text{-O-}\mathbf{M}}$	145	deg
T	300	K

E.2 Finite size effects and geometry optimization

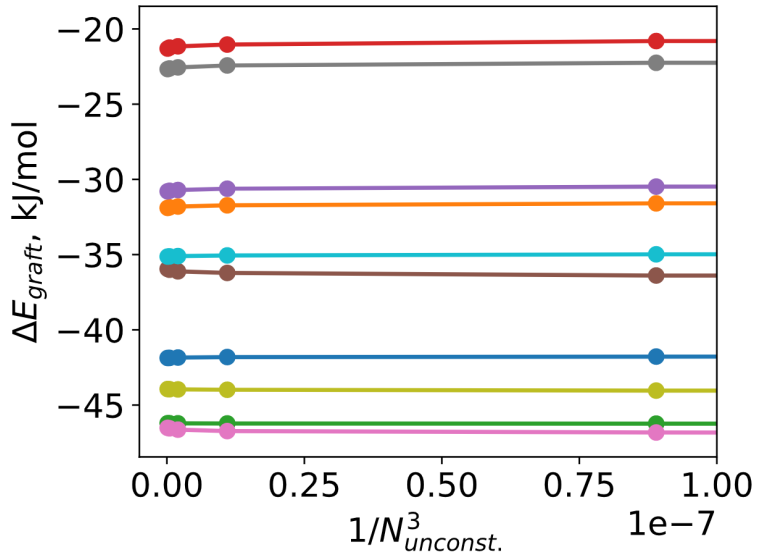

Figure E.8: Grafting energy versus the inverse cube of the number of unconstrained Σ centers allowed to relax for 10 randomly selected DLM slabs.

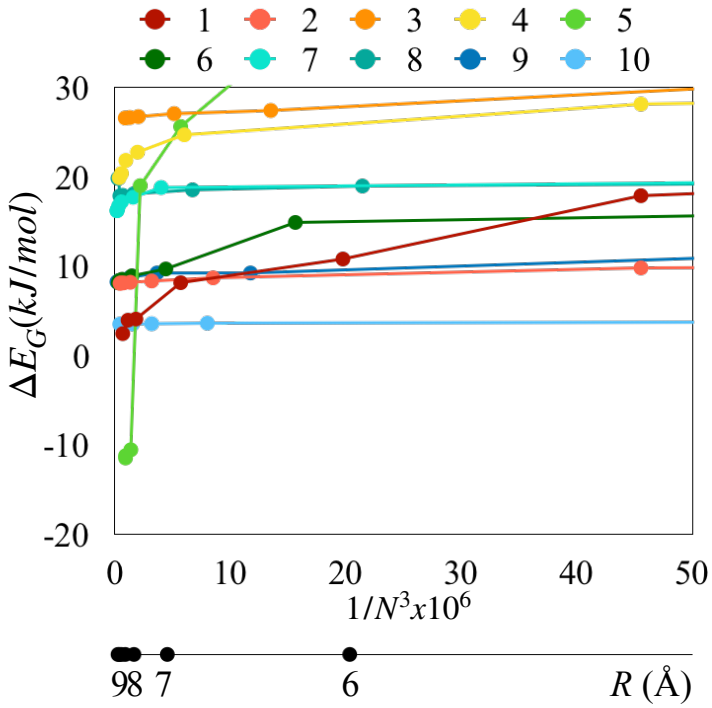

Figure E.9: Grafting energy versus the inverse cube of the number of unconstrained atoms (N) allowed to relax for the ten atomistic clusters obtained with the QM-Opt protocol. The line below shows approximately the corresponding value of R.

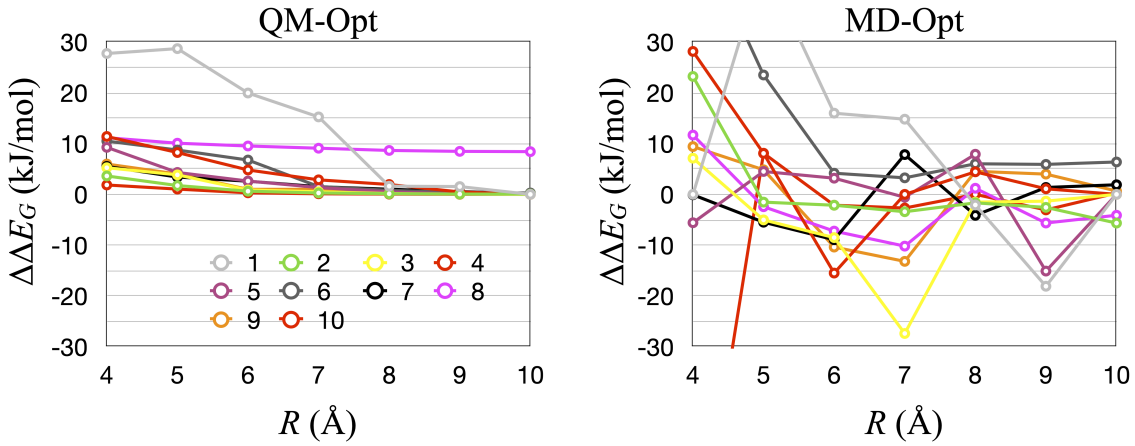

Figure E.10: Plots of $\Delta\Delta E_G$ as a function of the radius R (Å) of the relaxed zone for the ten atomistic clusters with the QM-Opt (left) and MD-Opt (right) protocols.

E.3 Dihedral angle scans

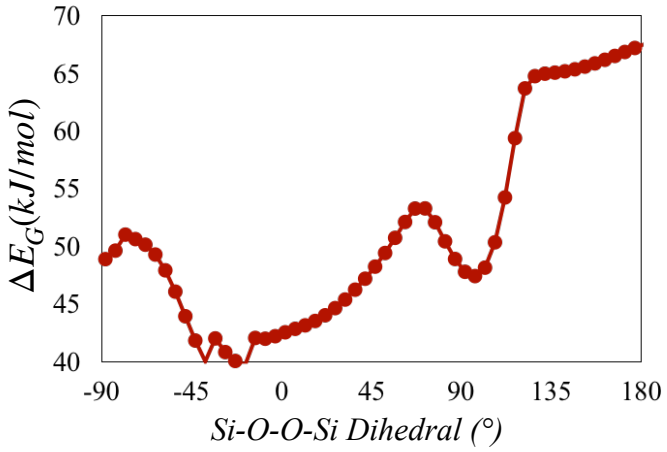

Figure E.11: Relaxed scan of ΔE_G as a function of the ϕ dihedral angle (5° increments) for the small cluster shown in Figure 6.6c-d.

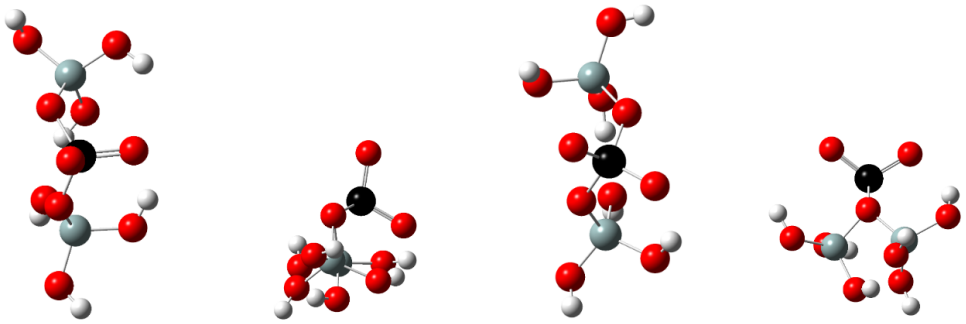

Figure E.12: Top and side views of the "eclipsed" (a-b) and "gauche" (c-d) configurations corresponding to the minima in Figure E.11. Cr is represented as a black ball, O as red, Si as gray, and H as white.

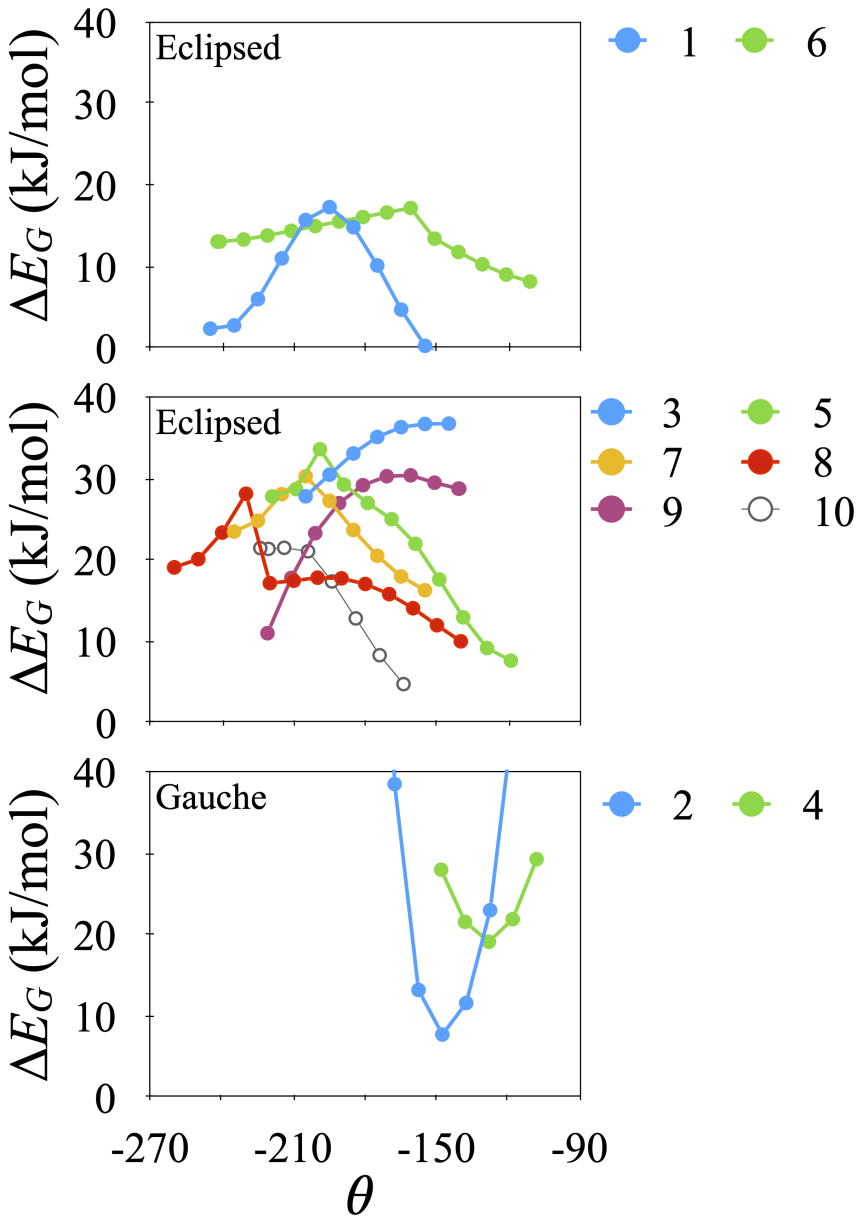

Figure E.13: Relaxed ΔE_G scans as a function of the θ dihedral angle for the ten large clusters. Top: clusters with near-degenerate double minima (vicinal-silanol grafting); middle: clusters with non-degenerate double minima (vicinal-silanol grafting); bottom: clusters with a single minimum (isolated-silanol grafting).